Confinement and grafting of ionic liquids in mesoporous ceramic membranes for the selective transport of CO2

Marie-Alix Pizzoccaro

THÈSE
Pour obtenir le grade de Docteur

Issued by **Université de Montpellier**

Prepared in the graduate school of Sciences Chimiques Balard
(ED 459)
And research unit Institut Européen des Membranes
(UMR 5635)

Speciality : **Chemistry and Physical Chemistry of Materials**

Presented by **Marie-Alix PIZZOCCARO**

Confinement and grafting of ionic liquids in mesoporous ceramic membranes for the selective transport of CO_2

Defending on 27 November 2017 in front of the esteemed jury comprising of

Mr David FARRUSSENG, CNRS Research Director IRCELyon, Villeurbanne (France)	President of the jury
Mrs Vera MEYNEN, Research Professor, University of Antwerp, Antwerp (Belgium)	Reviewer
Mrs Margarida COSTA GOMES, Professor, Blaise Pascal University, Clermont-Ferrand (France)	Reviewer
Mr Richard D. NOBLE, Professor, Colorado University, Boulder (United-State)	Examiner
Mrs Anne JULBE, CNRS Research Director IEM/Montpellier University, Montpellier (France)	Thesis director
Mr Gilles GUERRERO, Maître de Conférences, ICGM/Montpellier University, Montpellier (France)	Thesis advisor
Mr Martin DROBEK, CNRS Researcher IEM/Montpellier University, Montpellier (France)	Invitee
Mr André AYRAL, Professor, IEM/Montpellier University, Montpellier (France)	Invitee
Mr Peter HESEMANN, CNRS Research Director ICGM/Montpellier University, Montpellier (France)	Invitee

Thèse pour obtenir le grade de Docteur

Délivré par **Université de Montpellier**

Préparée au sein de l'école doctorale Sciences Chimiques Balard
(ED 459)
Et de l'unité de recherche - Institut Européen des Membranes
(UMR 5635)

Spécialité : **Chimie et physico-chimie des matériaux**

Présentée par **Marie-Alix Pizzoccaro**

Confinement et greffage de liquides ioniques dans des membranes céramiques mésoporeuses pour le transport sélectif du CO_2

Soutenue le 27 novembre 2017 devant le jury composé de

M. David FARRUSSENG Directeur de Recherche CNRS, IRCELyon, Villeurbanne (France)	Président du Jury
Mme Vera MEYNEN, a/Professeur, Université d'Anvers, Anvers (Belgique)	Rapporteur
Mme Margarida COSTA GOMES, Professeur, Université Blaise Pascal, Clermont-Ferrand (France)	Rapporteur
M. Richard D. NOBLE, Professeur, Université du Colorado, Boulder (Etats-Unis)	Examinateur
Mme Anne JULBE, Directeur de Recherche CNRS, IEM/ Université de Montpellier, Montpellier (France)	Directrice de thèse
M. Gilles GUERRERO, Maître de Conférences, ICGM/ Université de Montpellier, Montpellier (France)	Co-encadrant
M. Martin DROBEK, Chargé de Recherche CNRS, IEM/ Université de Montpellier, Montpellier (France)	Invité
M. André AYRAL, Professeur, IEM/ Université de Montpellier, Montpellier (France)	Invité
M. Peter HESEMANN, Directeur de Recherche CNRS, ICGM/ Université de Montpellier, Montpellier (France)	Invité

À Bertty,

"I cannot fix on the hour, or the spot, or the look, or the words which laid the foundation of my love for you. It is too long ago. I was in the middle before I knew I had begun."

"Je ne puis vous fixer ni le jour ni le lieu, pas plus que vous dire le regard ou les paroles qui ont éveillé mon amour pour vous. Il y a vraiment trop longtemps. J'étais déjà loin sur la route avant de m'apercevoir que je m'étais mis en marche.

Adapté de Jane Austen, Pride and Prejudice

A mes parents, ma grand-mère, et ma marraine.

ABSTRACT

In competition with amines, ionic liquids (ILs) are known to interact strongly and reversibly with acid gases, making supported IL-membrane (SILMs) versatile materials for use in CO_2 membrane separation applications. It is possible to finely tune SILMs properties for CO_2 adsorption/separation by tailoring the characteristics of both the support (*e.g., porosity, surface area, composition, etc.)* and the ionic liquid (*cations and anions*).

Up to now, nanoporous polymer supports have been favored for preparing SILMs, in spite of their relative instability during continuous separation processes in the presence of acidic gases. Recently, porous ceramic supports have been considered due to their excellent thermal and mechanical resistance. Most of the SILMs are prepared by impregnation/infiltration of IL in the pores of ceramic support leading to the formation of composite membrane materials with either a physisorbed or mechanically trapped IL in the support. Despite their promising performance, such SILMs exhibit inherent limitations such as facile IL disarrangement, heterogeneous distribution, and limited stability upon ageing.

In this Ph.D work, carried out in collaboration between the Institut Européen des Membranes (IEM) and the Institut Charles Gerhardt de Montpellier (ICGM), a new generation of SILMs has been developed in which ILs are confined within the pores of a mesoporous ceramic support by chemical grafting. The membranes are prepared in three steps:

i) Synthesis and characterization of new ILs bearing a coupling function which allow the grafting on the surface of ceramic oxide supports and determination of the CO_2 absorption capacity of the new ILs developed;

ii) Development and/or optimization of relevant synthesis protocols for grafting ILs on/in γ-alumina powders and physico-chemical characterizations of the as-obtained hybrid materials;

iii) Transfer of the optimized grafting protocols on commercial porous ceramic support with γ-alumina top-layer to produce Grafted Ionic Liquid Membranes (GILMs) and evaluate their performance for selective CO_2 transport.

An original research strategy, based on new ionic liquids and innovative membrane concepts has been addressed in this work, illustrating the contribution of a multi-step approach towards the development of membrane systems for CO_2 separation.

RÉSUMÉ

En compétition avec les alcanolamines, les liquides ioniques (LIs) sont connus pour interagir fortement et de façon réversible avec des gaz acides. Les propriétés remarquables des LIs ont conduit à la réalisation de '*Supported Ionic Liquid Membranes*' (SILMs) qui sont des systèmes continus attractifs pour la séparation de gaz, et notamment du CO_2. Dans les SILMs, il est possible d'adapter les propriétés d'adsorption/séparation en modifiant les caractéristiques du support (*e.g. composition, structure poreuse, surface spécifique, etc*.) et du LI (*nature des cations et anions*).

En dépit de leur relative instabilité dans les procédés de séparation de gaz acides, les supports nanoporeux polymériques sont classiquement utilisés pour préparer des SILMs. Récemment, les supports céramiques poreux ont été considérés pour la réalisation de SILMs en raison de leurs excellentes résistances thermique et mécanique. La plupart de ces systèmes sont préparés par imprégnation/infiltration des LIs dans les pores du support céramique. Ce protocole conduit à la formation de matériaux composites dans lesquels le LI est physiquement piégé dans le support, mais souvent avec une distribution hétérogène du LI et une stabilité limitée dans le temps.

Dans ce travail de thèse, réalisé en collaboration entre l'Institut Européen des Membranes (IEM) et l'Institut Charles Gerhardt de Montpellier (ICGM), nous avons développé une nouvelle génération de SILMs, dans lesquelles le LI est confiné dans les pores d'un support en céramique mésoporeux, par greffage chimique. La préparation de ces systèmes se fait en trois étapes :

i) Synthèse et caractérisation de nouveaux LIs portant des fonctions de couplage pour assurer leur greffage en surface des pores de la membrane céramique et détermination de la capacité d'absorption du CO_2 des différents LIs synthétisés;

ii) Optimisation des paramètres de greffage de ces LIs sur des poudres modèles de γ-Al_2O_3 et caractérisation des matériaux hybrides obtenus avec mise en évidence du greffage;

iii) Transfert du protocole de greffage optimisé sur des membranes céramiques commerciales γ-alumine (fabrication de Grafted Ionic Liquid Membranes - GILMs) et évaluation de leurs performances pour le transport sélectif du CO_2.

Ce travail, basé sur une approche originale associant de nouveaux liquides ioniques et un nouveau concept de membrane à base de liquide ionique supporté, montre, au travers de plusieurs exemples, l'intérêt d'une approche multi-étapes pour le développement de systèmes membranaires de séparation du CO_2.

ACKNOWLEDGEMENTS

This Ph.D work was carried out in collaboration between the Institut Européen des Membranes (UMR 5635 - CNRS/UM/ENSCM) and the Institut Charles Gerhardt de Montpellier (ICGM), team CMOS (UMR 5253 - CNRS/UM/ENSCM).

First and foremost I want to thank my Thesis director and advisor, *Dr. Anne JULBE*, CNRS Research Director at the Institut Européen des Membranes and *Dr. Gilles GUERRERO*, Maître de conférences at the ICGM. *Anne*, I cannot thank you enough for your guidance and all the encouragement you bestowed upon me during these last three years. The joy and enthusiasm you have for research was contagious and motivational for me, even during the toughest times in the Ph.D. *Gilles*, your guidance helped me throughout both my research and writing. I couldn't have wished for a better advisor and mentor for my Ph.D study. The multitude of meetings I had with the both of you have shaped not only this Ph.D work but also my scientific personality. May you find here, the expression of my sincere friendship.

I also would like to thank *Dr. Vera MEYNEN* (University of Antwerp, Antwerpen Belgium), *Prof. Richard D. NOBLE* (University of Colorado, Boulder, USA), *Dr. David FARRUSSENG* (IRCELyon, Villeurbanne) and *Prof. Margarida COSTA GOMES*, (University of Blaise Pascal, Clermont-Ferrand) for agreeing to review my Ph.D work and for being a part of my Ph.D examination committee.

Thank you, *Dr. Martin DROBEK* for supervising me and for your suggestions. Thank you for your advice and guidance in my professional and personal life.

A very special gratitude goes out to *Prof. Richard D. NOBLE* (University of Colorado, Boulder, USA) who gave me with the opportunity to join his team as an intern, and who gave me access to the laboratory and research facilities. Without his precious support it would have been impossible to conduct this research.

Thank you to *Dr. David FARRUSSENG* and *Dr. Cécile DANIEL*, from the IRCELyon, Villeurbanne for the valuable discussion on the gas sorption measurements and for the analysis carried out.

I want to extend my thanks to *Prof*. *Gilles SILLY* (University of Montpellier) for this enriching collaboration in solid-state NMR analysis. Thank you for your time and ideas.

I also would like to thank *Prof. André AYRAL* for his concern and advice during all the Ph.D. Thank you for all the stimulating research discussions and of course all the evening jokes.

My sincere thanks also goes to *Dr. Matthew G. COWAN*, (University of Canterbury, New Zeland) for your patience in training me on gas solubility measurements and answering my questions whenever I asked. Thank you for your precious tips to write/destroy/rewrite/correct some part of the manuscript and encouraging me to give the best I can.

A special thanks to *Mr. Eddy PETIT,* from the IEM and to *Dr. Philippe GAVEAU*, from the ICGM. I had so many doubts during my work, and you were always there to support me, help me conduct the characterizations and solve the surprising results.

For the ionic liquid preparations, thank you to *Mr. Guillaume GRACY* and *Dr. Franck MARTIN* from the SIKEMIA Company. I have appreciated your collaboration, advice for the synthesis and of course for providing me with some of the reactants.

I use this opportunity to extend my thanks to all the interns which have contributed to this work, Sandra MUNOZ PINA, Louën BRUN, Tom DELAGE, and Dorian CADARIO, and also to the staffs and colleagues of IEM and ICGM specially, to *Mr. Bertrand REBIERE* and *Mr Didier COT* for helping me with EDX and SEM analysis, to *Mr. Jim CARTIER* and *Dr. Christophe CHARMETTE* for all the gas permeation tests.

Last but not the least, I would like to thank my friends and family for their support throughout my thesis. To my sisters, brother and parents, without you, I would not have been able to do this. At the end, I would like to express my gratitude to my husband, Bertty, who stayed awake with me during those sleepless nights and was always my number one support.

Table of contents

General Introduction

In the past few decades, membrane-based separation processes have undergone enormous progress and have proved their potential as promising systems for the post-combustion CO_2 capture technologies. There has been more focus given to the synthesis of membranes and investigation of their performance (*selectivity vs flux*) and stability (*i.e. high temperature, high pressure..*) in order to obtain a system that is competitive with other CO_2 capture methods (*i.e. absorption by amine-based solvents or ammonia, adsorption by solids, calcium cycles or cryogenics*).

Recently the **ionic liquid (IL)-based membranes** have gained an increasing attention because of the specifically attractive features of ILs such as a limited vaporization, coupled with good chemical and thermal stability [1,2,3]. Also, ILs can interact strongly and reversibly with CO_2, making the **supported ionic liquid membranes** (SILMs) attractive systems for gas separation applications. Among the developed IL-based membranes, the SILMs based on porous ceramic support present good CO_2 separation performance [4-6]. Such SILMs are made of a porous solid support impregnated with an IL, which is held by capillary forces within the pores and eventually on the top-surface (Figure G.I.1). However, the SILMs are mechanically unstable, and the IL is easily "blown out" of most support materials under a pressure gradient.

To overcome these issues a new generation of SILMs has been recently developed which is composed of ILs chemically grafted on the outer surface and within the pores of mesoporous or microporous ceramic supports [7] (Figure G.I.1). The preparation of these **Grafted Ionic Liquid Membranes (GILMs)** requires a precise control of the covalent bonds formation between the ILs and the surface functional groups of the ceramic support and up to now it has been scarcely studied in the literature.

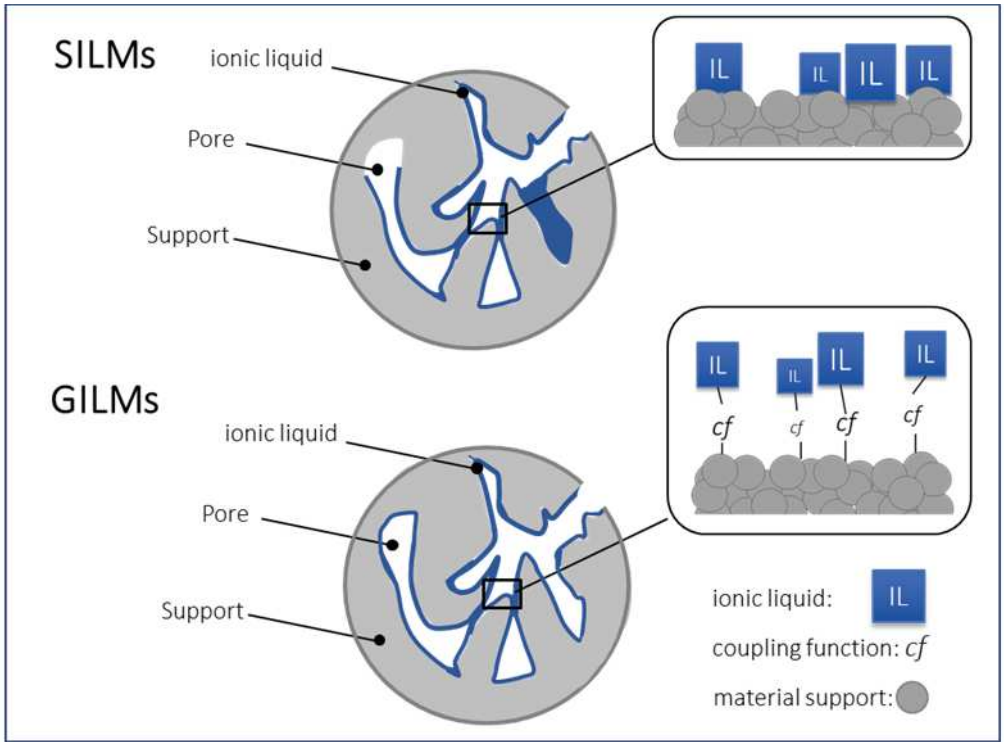

Figure G.I.1. Schematic representation of the porous network in the SILMs and GILMs IL-based membranes.

Generally speaking, grafted ILs materials are common hybrid systems used for a range of applications including catalysis [7,9], chromatography [10,11] and gas sorption [12,13]. These types of systems have been defined by Fehrmann *et al.* [14], as Supported Ionic Liquids (SILs) and refer to either inert or catalytically active covalently bound ILs monolayers. In these materials, the IL does not act as a bulk-IL anymore but as a surface modifier. As reported by the authors, tailoring the chemical nature of the support, as well as its microstructure (*i.e., pore size, size distribution, specific surface area),* govern IL grafting and its distribution on the support surface. Covalent linking of ILs on a ceramic oxide support appears as an attractive strategy to fine-tune solid materials with outstanding properties for CO_2 adsorption and improved long-term stability.

Several functionalized imidazolium-based ILs have been reported in the literature with coupling functions such as trimethoxysilyl, thiol-, ether-, carboxylic acid-, amino- and hydroxyl-groups [15]. Each of these coupling functions is adapted for being grafted on a pre-functionalized support. Vangeli *et al.* [13] selected the trimethoxysilyl group to react with the hydroxyl groups of silica-based materials pre-treated with a piranha solution[1]. The grafting reaction has been performed in two steps: *(i) grafting of a silylated precursor and (ii) quaternarization with 1-methylimidazole, yielding the imidazolium species.* We have to note that, despite several analytical methods conducted, the demonstration of both the quaternarization reaction and grafting remain rather unclear. Moreover, the silane coupling agents are very sensitive to hydrolysis and tend to undergo homocondensation reactions with

[1] mixture of sulfuric acid (H_2SO_4) and hydrogen peroxide (H_2O_2).

formation of Si-O-Si bonds leading to polycondensation reactions of the coupling agent molecules to the detriment of the simple grafting reaction. In fact, the silanization process can evolve toward the formation of bulky organosilane entities and leave in parallel a portion of the unaffected surface hydroxyls groups as shown in Scheme GI.1.

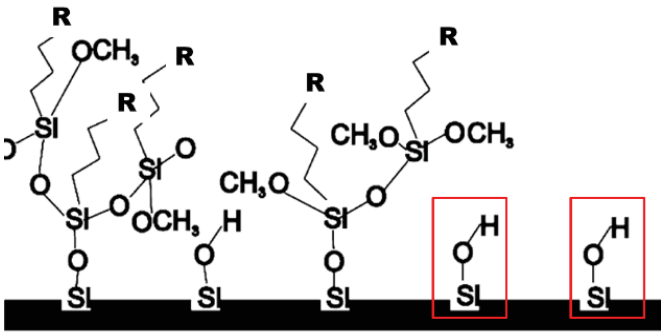

Scheme GI.1. Silanization process evolving toward the formation of bulky organosilane entities.

γ-Al_2O_3 is a commonly used mesoporous ceramic support, and its hydroxylated surface is attractive for anchoring or grafting active species for either gas separation or heterogeneous catalysis [16]. The chemical modification of γ-Al_2O_3 powders with organosilanes has been largely investigated in the literature [17,18]. As an alternative to silanization, grafting reactions could also be realized with phosphonate or phosphinate coupling functions. Randon *et al.* [19], have linked phosphoric acid and alkyl phosphonic acid to the surface of both titania and zirconia membranes to improve their performance for the ultrafiltration of BSA proteins. Caro *et al.* [20], modified γ-Al_2O_3 membrane top-layers with alkyl/aryl phosphonic acids, producing membranes with a hydrophilic or hydrophobic top-layer. Guerrero *et al.* [21,22], demonstrated the possibility to graft phenylphosphonic acid and its ester derivatives on both γ-Al_2O_3 and TiO_2 powders. The surface bonding modes were investigated by both diffuse reflectance infrared spectroscopy (DRIFT) and ^{31}P solid-state MAS NMR spectroscopy [21,22]. The same authors also patented a process for modifying an inorganic substrate with organophosphorus coupling agents, relevant for antibacterial applications. In this work, imidazolium-based ILs with phosphonyl functional groups were used for their intrinsic antimicrobial properties [23]. It could be thus concluded that the grafting of phosphonate-based ILs on a relevant membrane support appears as a promising strategy for the development of GILMs. In addition, it must be noted that, unlike their alkoxysilane analogues, phosphonate-based compounds cannot react together by homo-condensation thus ensuring the sole formation of homogeneously grafted monolayers.

Objectives of the thesis:

This Ph.D. reseach work has been carried out in collaboration between the Institut Européen des Membranes and the Institut Charles Gerhardt in Montpellier. It targets the design and fabrication of new γ-alumina hybrid membranes containing a grafted ionic liquid in their pores to efficiently and sustainably extract the CO_2 contained in mixtures with other gases such as N_2 or CH_4.

After a deep literature survey and some preliminary tests, our research was organized in three phases:

i) Synthesis of selected ILs with relevant coupling functions and investigation of the CO_2 absorption properties of the synthesized ILs.

ii) Optimization of the grafting parameters of these LIs on model powders of γ-Al_2O_3 and characterization of the hybrid materials obtained.

iii) Transfer of the optimized grafting protocol to commercial γ-Al_2O_3 ceramic membranes in order to produce Grafted Ionic Liquid Membranes (GILMs) and evaluate their performance for selective CO_2 transport.

Thesis outlines

This thesis is divided into 4 chapters and a general conclusion. Chapter I introduces the context and motivation of this research work, general concepts on CO_2 separation technologies, as well as a concise description of the IL-based membranes, including their preparation methods and CO_2 transport and separation performance.

The subsequent chapters of the thesis focus on the different steps involved in the design of a new generation of supported ionic liquid membranes. Chapter II focuses on the design of phosphonate-based ILs for CO_2/light-gas separation applications. Chapter III is dedicated to the controlled grafting of these ILs on γ-Al_2O_3 powders for the CO_2 capture. Chapter IV is dedicated to the preparation of grafted ionic liquid γ-Al_2O_3 membranes and the evaluation of their performance for CO_2 separation.

Introduction Générale

Au cours des dernières décennies, les procédés de séparation membranaires ont bénéficié d'énormes avancées et ont prouvé leur fort potentiel pour les technologies de capture du CO_2 après combustion. L'accent a été mis sur la synthèse des membranes et sur les études de leurs performances (sélectivité vs flux) et de leur stabilité (id. haute température, haute pression ...) afin d'obtenir un système compétitif vis-à-vis des autres méthodes de capture du CO_2 telles que l'absorption par les solvants à base d'amine ou d'ammoniac, l'adsorption par les solides, les cycles de calcium ou la cryogénie.

Récemment, les membranes incorporant des liquides ioniques (LI) ont fait l'objet d'un grand intérêt en raison des caractéristiques spécifiques des LIs telles qu'une pression de vapeur quasiment nulle, associée à une bonne stabilité chimique et thermique [1,2,3]. En outre, les LIs peuvent interagir de manière forte et réversible avec les gaz acides comme le CO_2, ce qui rend attrayants leur utilisation dans le développement de membranes à base de liquides ioniques compatibles pour les applications de séparation des gaz. Parmi les types de membranes développées à base de LIs, les Supported Ionic Liquid Membranes (SILMs) présentent de bonnes performances pour la séparation du CO_2 [4-6]. Ces SILMs sont constituées d'un support céramique poreux imprégné d'un LI maintenu par des forces capillaires sur la surface interne et/ou externe du support (figure G.I.1). De telles membranes sont constituées d'un support solide poreux imprégné de LI maintenu par des forces capillaires à l'intérieur des pores et éventuellement en surface (figure G.I.1). Cependant, les SILMs présentent une stabilité mécanique faible, et le LI peut être facilement expulsé hors des pores du support sous l'effet d'un gradient de pression.

Pour surmonter ce problème, une nouvelle génération de SILMs, les Grafted Ionic Liquid Membranes (GILMs), a récemment été développée en greffant chimiquement les LI sur la surface externe et dans les pores de supports céramiques mésoporeux ou microporeux [7] (Figure G.I.1).

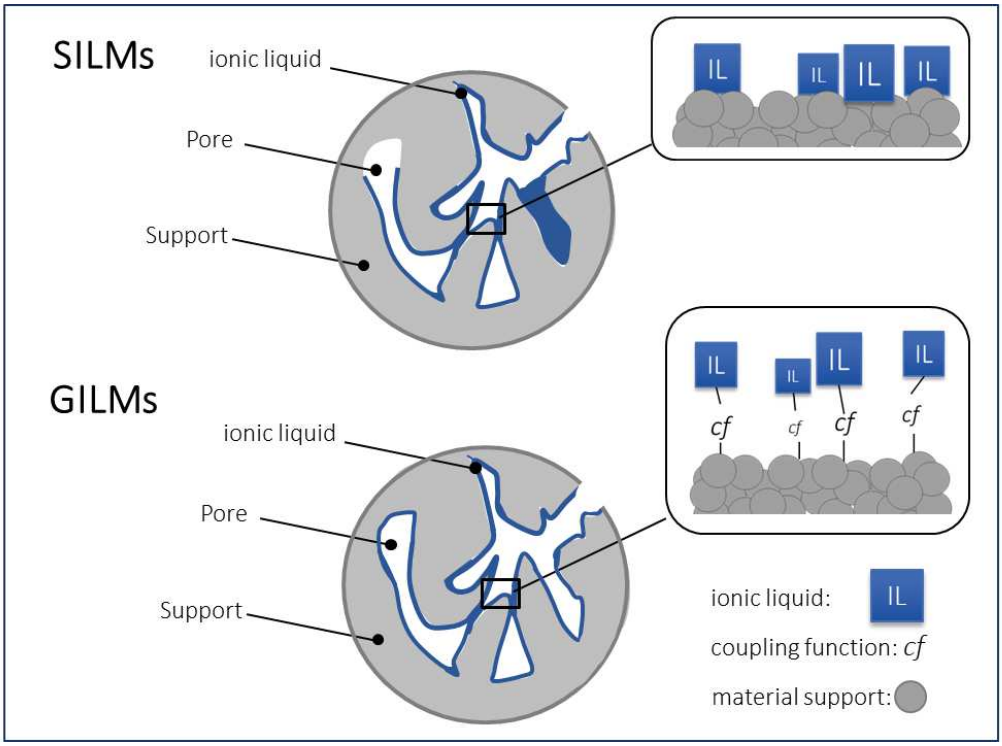

Figure G.I.1. Représentation schématique du réseau poreux dans des membranes de type SILMs et GILMs.

De manière générale, les matériaux hybrides à base de LIs greffés sont utilisés pour une large gamme d'applications incluant par exemple la catalyse [8,9], la chromatographie [10,11] et la sorption gazeuse [12,13]. Ces types de systèmes nommés par Fehrmann *et al.* [14], « Supported Ionic Liquids » (SILs) se réfèrent à des monocouches inertes ou catalytiquement actives de LIs liés chimiquement par liaisons ionocovalentes avec le support. Dans ces matériaux, le LI se comporte comme un agent de couplage, un modificateur de surface. Comme l'ont signalé les auteurs, la nature chimique du support ainsi que sa microstructure (*i.e., la taille des pores, la distribution des tailles, la surface spécifique*) régissent le mécanisme et la nature du greffage du LI ainsi que sa répartition sur la surface du support. La formation de liaisons ionocovalentes entre le LI et le support céramique apparaît comme une stratégie intéressante pour générer des matériaux hybrides solides présentant des propriétés remarquables pour l'adsorption du CO_2 avec une bonne stabilité mécanique, chimique et thermique à long terme.

Divers LIs sont rapportés dans la littérature comme agents de couplage à base de sels d'imidazolium fonctionnalisés. Ces LIs présentent des fonctions de couplage telles que les fonctions alcoxysilanes, thiol, éther, acide carboxylique, amine et hydroxyle [15]. Chacune de ces fonctions de couplage étant adaptée pour être greffée sur une certaine nature de support. Par exemple, Vangeli *et al.* [13], décrivent le greffage d'une silice, prétraitée par un mélange piranha[2], par un précurseur silylé porteur d'une fonction d'ancrage triméthoxysilyl qui réagit avec les groupes hydroxyles de surface. Dans une deuxième étape, l'agent de couplage silylé est quaternarisé avec le 1-méthylimidazole afin d'obtenir l'espèce imidazolium de surface.

[2] Mélange de H_2SO_4 et H_2O_2.

Cependant, malgré les différentes analyses menées, la mise en évidence de la réalisation de la réaction de quaternarisation ainsi que du mode d'ancrage restent non clarifiées. Qui plus est, les agents de couplage silanes sont très sensibles à l'hydrolyse et sujets à des réactions d'homocondensation avec formation de liaisons Si-O-Si menant à des réactions de polycondensation des molécules d'agents de couplage entre elles au détriment de la simple réaction de greffage. Le processus de silanisation peut donc évoluer vers la formation d'entités organosilanes volumineuses et laisser en parallèle une partie des hydroxyles de surface disponibles comme indiqué sur le schéma GI.1.

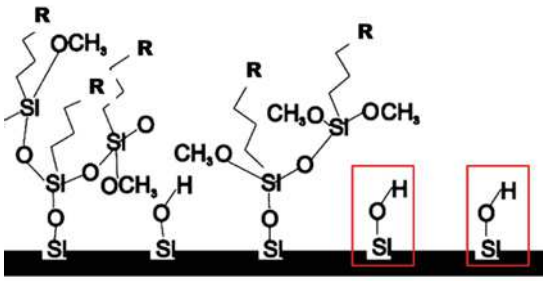

Scheme GI.1. Procédé de silanisation évoluant vers la formation d'espèces organosilane par polycondensation.

L'alumine γ (γ-Al_2O_3) est un support céramique mésoporeux couramment utilisé dans les procédés membranaires permettant par le biais de ses groupements hydroxyls de surface d'ancrer des espèces actives pour la séparation des gaz ou la catalyse hétérogène [16]. La modification chimique de poudres de γ-Al_2O_3 avec des agents de couplage organosilanes a été largement étudiée dans la littérature [17,18]. La modification de surface par des agents de couplage phosphonates ou phosphinates, moins sensibles à l'hydrolyse, a également été décrite comme alternative. Randon *et al.* [19], ont greffé l'acide phosphorique et un acide arylphosphoniques produisant ainsi des membranes présentant des propriétés de surface hydrophiles ou hydrophobes. Caro *et al.* [20], ont modifié la surface de membranes γ-Al_2O_3 avec des acides alkyl/arylphosphoniques, produisant ainsi des membranes à surface hydrophile ou hydrophobe. Guerrero *et al.* [21, 22], ont démontré la possibilité de greffer l'acide phénylphosphonique et ses dérivés phosphonates de diéthyle et phosphonates de triméthylsilyl sur des poudres de γ-Al_2O_3 et de TiO_2. Les modes de liaison des unités phosphonates à la surface ont été étudiés à la fois par spectroscopie infrarouge et par spectroscopie RMN solide ^{31}P [21, 22]. Les mêmes auteurs ont décrit un procédé de modification d'un substrat inorganique avec des agents de couplage organophosphorés portant des fonctions imidazolium permettant de préparer des surfaces antimicrobiennes [23]. Le greffage de LIs fonctionnalisés par des unités phosphonates semble être une stratégie prometteuse pour la préparation de GILMs sur supports oxydes de type alumine. En outre, il est à noter que, contrairement à leurs analogues les alcoxysilanes, les composés à base de phosphonate ne peuvent réagir ensemble par homocondensation, ce qui permet de garantir la formation de monocouches greffées homogènes.

Objectifs de la thèse

Ce travail de thèse a été réalisé en collaboration entre l'Institut Européen des Membranes et l'Institut Charles Gerhardt à Montpellier. Il cible la conception et la réalisation de nouvelles membranes hybrides à base d'alumine γ incorporant un liquide ionique greffé sur la surface des pores de l'alumine pour assurer de façon efficace et durable la séparation du CO_2 contenu dans des mélanges avec d'autres gaz tels que de N_2 ou CH_4.

Après une étude bibliographique et quelques essais préliminaires, nos travaux de recherche ont été organisés en trois phases :

i) Synthèse et caractérisation de LIs portant des fonctions de couplage phosphonates et détermination de la capacité d'absorption du CO_2 par les LIs synthétisés.

ii) Optimisation des paramètres de greffage de ces LIs sur des poudres modèles de γ-Al_2O_3 et caractérisation des matériaux hybrides obtenus.

iii) Transfert du protocole de greffage optimisé sur des membranes céramiques commerciales à base de γ-Al_2O_3 pour évaluation de leurs performances pour le transport sélectif du CO_2.

Organisation de la thèse

Cette thèse est divisée en 4 chapitres et se termine par une conclusion générale. Le chapitre I présente le contexte et les motivations, les concepts généraux sur les technologies de séparation du CO_2, ainsi qu'une description concise des membranes à base de LIs, y compris leurs méthodes de préparation et leurs performances pour le transport et la séparation du CO_2.

Les chapitres suivants de la thèse se concentrent sur les différentes étapes impliquées dans la conception d'une nouvelle génération de membranes liquides ioniques supportées. Le chapitre II est axé sur la conception des LIs fonctionnalisé par des groupements phosphonates pour des applications de séparation CO_2/gaz léger. Le chapitre III présente le greffage des LIs développés au chapitre 2 sur une poudre de γ-Al_2O_3, et la caractérisation des matériaux obtenus pour la sorption du CO_2. Enfin, le chapitre IV est consacré à la préparation de membranes hybrides et leur évaluation pour la séparation du CO_2.

References

1. L.C. Tomé, I.M. Marrucho, Ionic liquid-based materials: a platform to design engineered CO_2 separation membranes, *Chem. Soc. Rev*., 2016, *45(10),* 2785-2824.
2. M.G. Cowan, D.L. Gin, R.D. Noble, Poly(ionic liquid)/Ionic Liquid Ion-Gels with high "free" ionic liquid content: platform membrane materials for CO_2/light gas separations, *Acc. Chem. Res.,* 2016, *49(4)*, 724-732.
3. J. Wang, J. Luo, S. Feng, H. Li, Y. Wan, X. Zhang, Recent development of ionic liquid membranes, *Green Energy & Environment*, 2016, *1(1)*, 43-61.
4. J.J. Close, K. Farmer, S.S. Moganty, R.E. Baltus, CO_2/N_2 separations using nanoporous alumina-supported ionic liquid membranes: Effect of the support on separation performance, *J. Membrane. Sci.,* 2012, *390-391*, 201-210.
5. S.D. Hojniak, I.P. Silverwood, A.L. Khan, I.F.J. Vankelecom, W. Dehaen, S.G. Kazarian, K. Binnemans, Highly Selective Separation of Carbon Dioxide from Nitrogen and Methane by Nitrile/Glycol-Difunctionalized Ionic Liquids in Supported Ionic Liquid Membranes (SILMs), *J. Phys. Chem. B*., 2014, *118(26),* 7440-7749.
6. S.D. Hojniak, A.L. Khan, O. Hollo, B. Kirchner, I.F.J. Vankelecom, W. Dehaen, K. Binnemans, Separation of Carbon Dioxide from Nitrogen or Methane by Supported Ionic Liquid Membranes (SILMs): Influence of the Cation Charge of the Ionic Liquid, *J. Phys. Chem. B.,* 2013, *117(14),* 15131-15140.
7. O.C. Vangeli, G.E. Romanosa, K.G. Beltsios, D. Fokas, C.P. Athanasekou, N.K. Kanellopoulos, Development and characterization of chemically stabilized ionic liquid membranes-Part I: Nanoporous ceramic supports, *J. Membrane. Sci.,* 2010, *365,* 366-377.
8. C.P. Mehnert, Supported ionic liquid catalysis, C*hem. Eur. J.,* 2004, *11(1)*, 50-56.
9. C. Van Doorslaer, J. Wahlen, P. Mertens, K. Binnemans, D. De Vos, Immobilization of molecular catalysts in supported ionic liquid phases, *Dalton. T.,* 2010, *39(36)*, 8377-8390.
10. H. Qiu, M. Takafuji, X. Liu, S. Jiang, H. Ihara, Investigation of π –π and ion-dipole interactions on 1-allyl-3-butylimidazolium ionic liquid-modified silica stationary phase in reversed-phase liquid chromatography, *J. Chromatogr. A.,* 2010, *1217(32),* 5190-5196.
11. V. Pino, A.M. Afonso, Surface-bonded ionic liquid stationary phases in high-performance liquid chromatography-A review, *Anal. Chim. Acta*., 2012, *714*, 20-37.
12. A.V. Perdikaki, O.C. Vangeli, G.N. Karanikolos, K.L. Stefanopoulos, K.G. Beltsios, P. Alexandridis, N.K. Kanellopoulos, G.E. Romanos, Ionic Liquid-Modified Porous Materials for Gas Separation and Heterogeneous Catalysis, *J. Phys. Chem. C.,* 2012, *116(31),* 16398-16411.
13. O.C. Vangeli, G.E. Romanos, K.G. Beltsios, D. Fokas, E.P. Kouvelos, K.L. Stefanopoulos, N.K. Kanellopoulos, Grafting of imidazolium based ionic liquid on the pore surface of nanoporous materials - Study of physicochemical and thermodynamic properties, *J. Phys. Chem. B.,* 2010, *114*(19), 6480-6491.
14. R. Fehrmann, M. Haumann, A. Riisager, Introduction. In *Supported Ionic Liquids: Fundamentals and Applications*, 1st ed.; Fehrmann, R.; Riisager, A. & Haumann, M.; Wiley-VCH Verlag GmbH & Co. KGaA, Publisher: Weinheim, Germany, 2014, pp. 1-9.
15. B. Xin, J. Hao, Imidazolium-based ionic liquids grafted on solid surfaces, *Chem. Soc. Rev.,* 2014, *43(20)*, 7171-7187.
16. A. Julbe, D. Farrusseng, C. Guizard, Porous ceramic membranes for catalytic and reactors and overview and new ideas, *J. Membrane. Sci.,* 2001, *181(1)*, 3-20.
17. S. Alami-Younssi, C. Kiefer, A. Larbot, M. Persin, J. Sarrazin, Grafting γ-alumina microporous membranes by organosilanes: Characterisation by pervaporation, *J. Membrane. Sci*., 1998, *143(1-2),* 27-36.

18. C. Leger, H.L. De Lira, R. Paterson, Preparation and properties of surface modified ceramic membranes. Part III. Gas permeation of 5 nm alumina membranes modified by trichloro-octadecylsilane, *J. Membrane. Sci.,* 1996, *120(2)*, 187-195.
19. J. Randon, P. Blanc, R. Paterson, Modification of ceramic membrane surfaces using phosphoric acid and alkyl phosphonic acids and its effects on ultrafiltration of BSA protein, *J. Membrane. Sci.,* 1995, *98(1-2)*, 119-129.
20. J. Caro, M. Noack, P. Kölsch, Chemically modified ceramic membranes. *Microporous and Mesoporous Mater.,* 1998, *22(1-3)*, 321-332.
21. G. Guerrero, P.H. Mutin, A. Vioux, Organically modified aluminas by grafting and sol–gel processes involving phosphonate derivatives, *J. Mater. Chem.,* 2001, *11(12),* 3161-3165.
22. G. Guerrero, P.H. Mutin, A. Vioux, Anchoring of Phosphonate and Phosphinate Coupling Molecules on Titania Particles, *Chem. Mater.,* 2001, *13(11)*, 4367-4373.
23. P.H. Mutin, G. Guerrero, J. Almaric. (issued Nov 19, 2013) *Patent n° US 8586758 B2.* Preparation of an inorganic substrate having antimicrobial properties. Assignees: Centre National de la Recherche Scientifique, Paris (FR); Université Montpellier II Sciences et Techniques du Languedoc, Montpellier (FR).

Chapter I. Bibliographic study

This chapter describes in detail the context and motivation of the present thesis, the background and general concepts of the CO_2 post-combustion capture and the progressive development of the state of the art of ionic liquid (IL)-based materials as a new alternative for the preparation of CO_2-selective membranes.

Chapter I. Bibliographic study

I.1. Introduction

As reported by the International Energy Agency, Energy-related carbon dioxide (CO_2) emissions are the majority of global greenhouse gas (GHG) emissions [1]. The fight against climate change has become a defining feature in energy policymaking, but the implications are overwhelming. Even if the emission goals promised by countries under the United Nations Framework Convention on Climate Change (UNFCCC) are reached, the world would still leave with 13.7 billion tonnes of CO_2 (or 60%) above the level needed to remain on track for just 2°C warming by 2035 [1].

The CO_2 emissions could be lowered in two ways. First, by lowering emissions on the consumption side through reduced consumption, substitution and improved efficiency [2]. Second, by lowering CO_2 emissions on the supply side, e.*g., by switching electricity generation from fossil fuels to renewables* [3], or deploying *carbon capture and storage* [4]. **Carbon capture and storage (CCS)**, also known as *carbon sequestration* involves a broad range of technologies and techniques that enable: **i) capture** of CO_2 from fossil fuel combustion or industrial processes, **ii) transport** of CO_2 via ships or pipelines, and **iii)** CO_2 **storage** in suitable storage medium such as depleted oil and gas reservoirs, deep coal beds, mined carverns/salt domes or in deep saline aquifers [5].

Despite of the extensive research efforts to produce energy from renewable sources, fossil fuels remain the major source of energy and are predicted to remain in this position for at least the next couple of decades. Hence, there is still a great interest in the development of different CCS strategies to limit CO_2 emissions from the current energy sources.

Among the CO_2 capture and separation technologies, the most widely applied are the post-combustion capture, the oxyfuel combustion, the pre-combustion capture, and the supercritical CO_2 cycles (Figure I. 1). The amine-based post-combustion capture (PCC) is today the most developed CO_2 capture technology. Even if a significant progress has been made by technology vendors to reduce the energy penalty associated with amine sorbent regeneration [6], new cost-effective and high-performance technologies still need to be researched, and consequently, the design of new materials with the ability to efficiently and sustainably separate CO_2 from other gases should be developed.

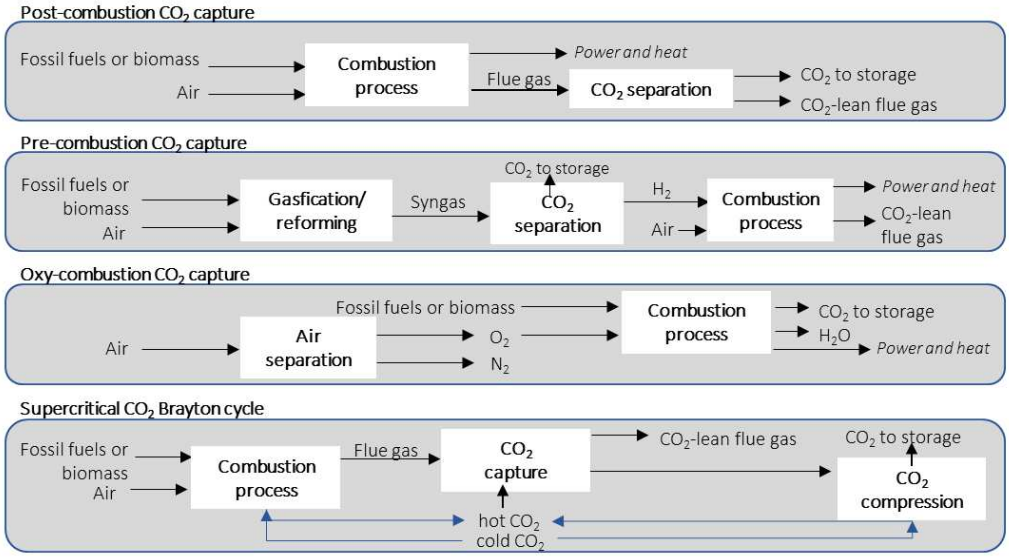

Figure I. 1. CO_2 capture technologies adapted from [7] and [8].

In the vast majority of cases, CO_2 must be separated from other gases such as methane (CH_4) (*e.g., natural gas sweetening*) and nitrogen (N_2) (*e.g., power plant flue streams*). In addition, CO_2 is often mixed

with various impurities from the fuel, such as: nitrous oxides (NOx = NO, NO_2), sulfur oxides (SOx = SO_2, SO_3), hydrogen sulfide (H_2S), carbon monoxide (CO), organic vapours (*e.g. volatile alcohols*), heavy metals or water [9,10].

Four CO_2 capture/separation technologies are identified as particularly promising for the CO_2 emission reductions: ***i)*** *cryogenic distillation,* ***ii)*** *absorption by solvents,* ***iii)*** *solids adsorption, and* ***iv)*** *membrane separations.* The principles of these techniques are briefly described below.

I.1.1. Cryogenic distillation

Cryogenic distillation is a technology which has been implemented for oxygen production in oxyfuel combustion. This technology is a physical gas separation method which provides high purity CO_2, especially from CO_2/N_2 and CO_2/CH_4 mixtures. The separation principle is similar to standard distillation: it is based on the difference in boiling points *(i.e., CO_2 (b.p. = -57 °C), N_2 (-196 °C), CH_4 (-164 °C))* and on a multistep cooling and condensation process. The low-temperature demand and occurrence of a phase transition (gas to liquid CO_2) make this very efficient separation process particularly energy intensive.

I.1.2. Solvent absorption

The CO_2 absorption solvents can be either physical or chemical absorbers (or absorbents).

Physical CO_2 absorbers:

Physical absorbents are typically ethers, alcohols or carbonyl compounds which can either form hydrogen bonds with CO_2 molecules or interact by Lewis acid-base interactions. This type of absorption requires a low operating temperature and high pressure. On an industrial level the most widely applied absorption processes are Selexol, Sectisol, Purisol and Fluor process [4,7].

Chemical CO_2 absorbers:

Amines solutions (alkylamines functionalized with –OH groups) are the most commonly used chemical absorbents [11], typically, composed of primary amines (*e.g., monoethanolamine*), secondary amines (*e.g.,diethanolamine or diisopropanolamine*) and tertiary amines (*e.g., methyldiethanolamine*) (Figure I. 2). These solvents present a high reactivity and good absorption capacity which can be increased when they are blended [12]. Despite of their performance, the use of amines remains of a high environmental and economic concern due to their corrosive nature, volatility and high energy demand for regeneration.

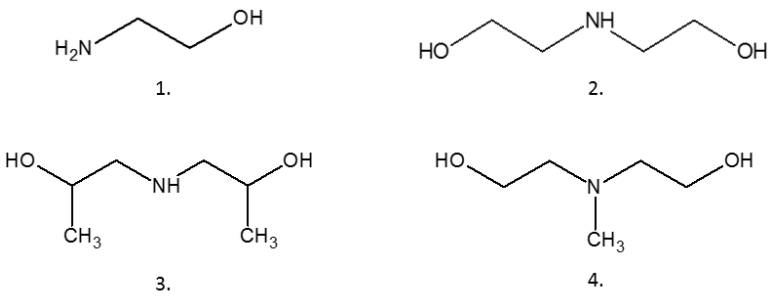

Figure I. 2. Structure of typical alkanolamines used in gas sweetening: 1. Monoethanolamine, 2. diethanolamine, 3. diisopropanolamine, 4. N-methyldiethanolamine.

I.1.3. Adsorption with porous solids

Compared to solvent-based absorption systems, the CO_2 adsorption processes with porous solids present some advantages such as : easy operation, rapid adsorption rates, low system corrosion, almost

no leaks and toxic chemicals contaminations, and low energy demand for adsorbent regeneration [13-16]. After the CO_2 capture, different methods can be employed to regenerate the adsorbent such as: **i)** vacuum and pressure swing adsorption (VSA and PSA), **ii)** temperature swing adsorption (TSA), **iii)** electric swing adsorption (ESA), **iv)** simulated moving bed, and **v)** purge displacement [16].

The principle of this technology is based on the CO_2 adsorption by physisorption into porous materials. The best adsorbents should have high CO_2 adsorption capacity and selectivity, fast adsorption/desorption kinetics, good mechanical properties, high thermal and chemical stability, and low costs for their synthesis. The porous materials typically employed in adsorption processes are often molecular sieve materials. Exemple of microporous adsorbents for CO_2 adsorption include aluminosilicates, titanosilicates, activated carbons [15], metal organic frameworks and zeolites [13]. Despite of the recent progress in the preparation of the above microporous materials, additional research focusing on reducing their synthesis costs, improving their stability and their working conditions are still needed for broadening their industrial implementation.

I.1.4. Membrane technology

Membranes are selective barriers between two media, which can preferentially pass one or more components under the effect of a driving force (Figure I. 3). Membrane processes can be applied to a large variety of fluid separations and they are now considered as an emerging key-separation technology for a number of industrial applications [17]. The separation of gas mixtures by membrane processes is based on the physical or chemical interaction of gases with the membrane.

As depicted in Figure I. 3., when a gas mixture (feed) is fed at one side of a membrane, some components of the mixture permeate through the membrane and reach the opposite side (permeate) while the other components are retained (retentate) [17].

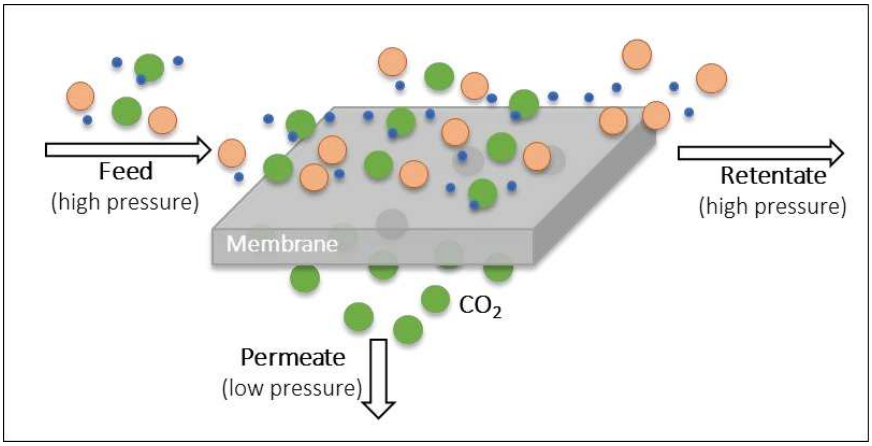

Figure I. 3. Schematic representation of a continuous membrane gas separation process.

Membrane technology is considered as a potentially powerful tool for CO_2 capture/separation processes from both economical and technological points of view [17]. In fact, the inherent simplicity of membranes can bring many advantages compared to other conventional separation technologies, namely the small scale and versatility of the equipment, relatively low environmental impact, ease of incorporation into existing processes, low energy consumption and low operating costs [18].

Nevertheless, to fully compete with well-established separation processes, additional efforts must be made to develop membranes with: **i)** high permeability and selectivity to specific gases, **ii)** good

thermal/chemical resistance, and **iii)** sufficient mechanical stability for withstanding the harsh environments of separation processes [9,10].

Gas separation membranes can be either dense or porous, organic (*e.g., polymeric membranes*), or inorganic (*e.g., ceramic oxide, non oxides, carbon, metals...*) or composite (*e.g., Mixed Matrix Membranes, Supported Ionic Liquid Membranes*) [10].

I.1.5. Conclusion

All the CO_2 capture/separation technologies described previously offer many advantages and disadvantages which have to be considered for the development of sustainable CO_2 capture/separation processes (Table I.1). As mentioned in the introduction, the amine-based post-combustion capture (PCC) is today the most largely used CO_2 capture technology. However, ionic liquids (ILs) are also known to interact strongly and reversibly with acid gases, thus making supported IL-materials promising candidates which could be used in either absorptive or membrane separation applications. Ionic liquids (ILs) are organic-based "molten salts" that exhibit liquid-like properties at ambient temperature and pressure. These compounds have low vapor pressure, high-temperature stability, and synthetic control over their structures and properties. Regarding gas transport, ILs have high CO_2 permeability, due to liquid-like diffusivity, and high CO_2/N_2 selectivity, due to solubility selectivity. A number of studies has been undertaken to develop new IL-based membranes [19-21], and currently, the goal is to design attractive membrane structures with both high CO_2 selectivity and permeability. Before describing the state of art IL-based membranes, the nature of ILs has to be addressed in more details.

Table I.1. Comparison of currently used worldwide CO_2 separation processes [19].

Process	Most suitable application	Main advantages	Main disadvantages
Cryogenic distillation	Gas stream with >75% CO_2	Very high purity CO_2	Very high energy cost
Adsorption	Various CO_2 streams a high pressure	High energy efficiency Low capital cost Good CO_2 separation	Severely lowered CO_2 capacity in the presence of other gases or water
Physical absorption	High pressure streams with high CO_2 content	No corrosion problems	Low efficiency Relatively high cost
Chemical absorption	Various CO_2 streams	High selectivity Up to 100% capture efficiency	Very high energy cost Low CO_2 loading Use of volatile solvents Corrosion problems
Membranes	Streams with high CO_2 concentrations	Small and uncomplicated installations Energy efficient Inexpensive in exploitation	Selectivity vs. permeability trade off (either high selectivity or high permeability feasible)

I.2. Ionic liquids

Ionic liquids (ILs) are molten salts with an extremely broad class of cations and anions which can be organic or not with a melting point less than 100°C. There are many possible combinations for a couple of cation-anions, and each new product may provide new properties and applications. Ionic liquids are composed of voluminous and unsymmetrical cations such as aromatic systems (*e.g.*, *imidazolium, pyridinium*) or ammonium and phosphonium cations. Predominant anion species include halides (*e.g.*, *chloride, bromide*), carboxylate anions (*e.g., acetate*), fluorinated anions (*e.g.*, *bis(trifluoromethylsulfonyl)imide, trifluoromethane sulfonate, trifluoroacetate*) and nitrile-containing anions (*tricyanomethanide*). The most common cations and anions are presented in Figure I. 4.

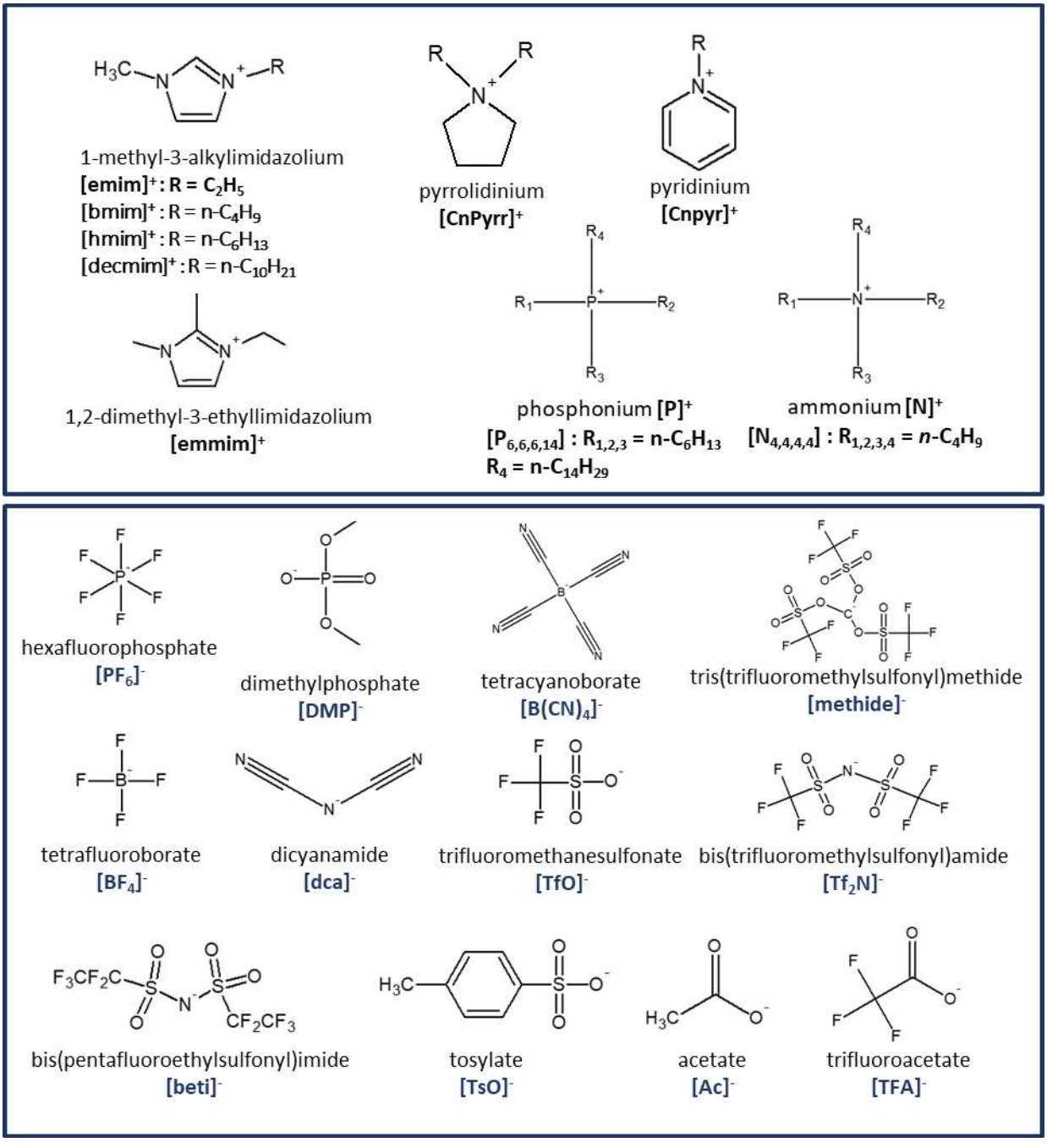

Figure I. 4. Abbreviations and chemical structures of the main cations and anions in common ILs.

Acronyms of ILs are composed of abbreviated names of both cations and anions placed next to one another in square brackets. For example, [emim][Tf_2N] is used for the common IL, 1-ethyl-3-methylimidazolium bis(trifluoromethylsulfonyl)imide.

Ionic liquids possess an exceptional combination of intrinsic properties such as negligible volatility [22], thermal stability [23], low flammability (with some rare exceptions) [24], and high ionic conductivity [25]. However, their most important feature bears on their tunability, which makes them unique and incomparable to other organic solvents. As an example, the melting point of ionic liquids can be regulated by modification of either the cation or the anion [26].

Furthermore, Ionic liquids (ILs) play an important role in both fundamental research and industrial usage because of their high potential for a broad range of applications such as organic synthesis [27-33], electronic devices [34], and extraction separations [35,36].

Compared to the amine-based solvent used for CO_2 (absorption) capture from flue gas, ILs provide many advantages such as a potentially lower energy demand for regeneration, and a negligible vapor pressure. However, large-scale application of conventional ILs in this process is mainly hindered by their low CO_2 absorption capacity under post-combustion industrial conditions. In fact, the solubility of CO_2 in conventional ILs is much lower compared to the amine solvent. As an example, in the best conventional IL, only 0.05 mole of CO_2 per mole of IL can be captured for a partial pressure ~0.15 bar [21]. To overcome the limitation of the conventional IL, active site-containing ILs able to react with the CO_2 through chemisorption have been developed (*i.e., amino-based ILs, amino acid-based ILs, azolate-based ILs, phenolate-based ILs, and pyridine-containing ILs*) [37]. Hence, more attention is now devoted in the literature to these task-specific ILs in order to obtain solvents with both higher energy efficiency and higher reaction stoichiometry, superior to those of MEA solvents.

Other approaches involving the use of ILs have been considered for CO_2 capture and separation applications. As an example, ILs/solid CO_2 adsorbents namely Supported Ionic Liquid Phase (SILP) have been developed [38-42]. Concerning the ILs-based membranes, various morphologies and configurations have been tested. There is now a huge interest in the development of IL-derived membranes such as : Polymerized Ionic Liquid (PIL) membranes [43], Poly(Ionic Liquid)/Ionic Liquid (PIL/IL) ion-gel membranes [20] and Supported Ionic Liquid Membranes (SILMs) [44-51].

I.3. Ionic liquid-based membranes for CO_2 capture/separation technologies

As reported in the General Introduction, we aimed to realize Grafted Ionic liquid Membranes (GILMs) for continuous acid gas separation. Investigation of the key parameters and mechanisms involved in the preparation and working conditions of IL-based membranes, and including the role of interfaces, will allow to define the most relevant synthesis strategy.

This section provides an overview of the Supported Ionic Liquid Membranes (SILMs), polymer/ionic liquid composite membranes, gelled ionic liquid membranes and poly(ionic liquid)-based membranes, including issues related to the preparation methods, transport mechanisms and gas transport properties and membrane performance stability. Because our objective is the preparation of GILMs, in which the IL will be nanoconfined, a special attention will be paid in this section to evidence such type of effect.

Before describing the ILs-based membranes, basic introduction about gas transport mechanisms through dense IL-based membranes will be provided.

I.3.1. General introduction on IL-based membranes

Gas transport through IL-based membranes is governed by the Solution-Diffusion mechanism typically encountered for dense polymeric film or liquid membranes. As shown in Figure I. 5, when the feed gas mixture contacts the membrane surface, the membrane works as **a semi-permeable barrier (permselective layer)** and the gas of interest dissolves in the membrane, diffuses through it and desorbs on the permeate side. The gas is then swept away from the membrane surface, and it leaves the separation module as a permeate stream.

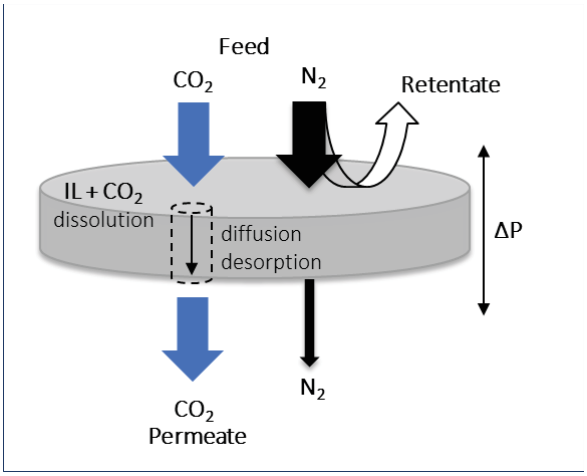

Figure I. 5. Shematic separation of CO_2 from N_2 with an IL-based membrane.

The equations and terminology presented below illustrate the general principles and basic concepts used both to describe gas transport through IL-based dense membranes, and to evaluate the membrane material performance.

- *Permeability, permeance and selectivity*

According to the solution-diffusion mass transfer mechanism, the permeability reflects the ability of a gas to transport through the active layer [52]. The permeability, P_i^*, of a given gas "i" reflects the ability of the material to dissolve this gas (solubility, S_i) and the ability of the gas to diffuse through this material (diffusivity, D_i).

Thus, the permeability P_i^* of a gas "i" through a given dense material, corresponds to the product of the diffusivity coefficient, D_i, and the solubility coefficient, S_i:

$$P_i^* = D_i . S_i \quad 1.1$$

The typical unit to express the permeability is the Barrer (1 Barrer = 10^{-10} cm^3 of gas i (STP).cm/(cm^2.s.cmHg)).

As described by Wijmans *et al.* [51], there are two basic assumptions behind this gas transport mechanism. Firstly, the gases on either side of the membrane are in equilibrium with the membrane material at the interface. Secondly, the concentration and pressure differences across the membrane are dependent only on the concentration gradient of dissolved permeating species within the membrane [51].

The permeability P_i^* of a gas "i" can also be defined as the steady-state gas flux, J_i, through a membrane under a transmembrane pressure drop ΔP and normalized to the membrane thickness, δ [53]. The transmembrane pressure drop is the partial pressure difference between permeate and retentate sides.

$$P_i^* = J . \frac{\delta}{\Delta P} \quad 1.2$$

For industrial applications and economical evaluation, the permeance is used instead of permeability to define gas transport through membranes. The following equation expressed the permeance, Π_i as the ratio of permeability to membrane thickness. Permeance is typically reported in "Gas Permeation Units (GPU)" (1 GPU = 1 x 10^{-6} cm^3 of gas i (STP).cm^{-1}.s^{-1}.$cmHg^{-1}$).

$$\Pi_i = \frac{P_i^*}{\delta} \quad 1.3$$

The ability of a membrane to separate different gases (in this case i and j) depends on the differences in permeability of the two gases, which depends on the membrane material properties. Selectivity is typically quantified as ideal membrane selectivity $\alpha_{i,j}$ which is the ratio of pure gas permeabilities values. The ideal membrane selectivity can also be expressed as the product of the diffusivity and solubility selectivity through the material for the considered single gases [54].

$$\alpha_{i,j} = \frac{P_i^*}{P_j^*} = \frac{D_i}{D_j} \times \frac{S_i}{S_j} \quad 1.4$$

The membrane performance is related to its permeability (or permeance) and selectivity for the gas of interest. The ideal membranes developed for CO_2 separation should thus provide both high CO_2 permeability (or permeance) and high separation selectivity [18]. To compare the performance of gas separation membranes, it is common to plot the selectivity α ($\alpha_{i,j}=P^*_i/P^*_j$) vs. CO_2 permeability; such representation corresponds to the so-called Robeson plot [10]. The IL-derived membranes performance is typically below or slightly above the critical line called the "upper bound". Most membranes, however, exhibit a trade-off between selectivity and permeability, that is, when permeability increases, selectivity decreases [54]. More permeable membranes usually permit both gases to pass through, and, their separation abilities decrease. Similarly, an increased selectivity causes a decrease in permeability [10]. When designing a membrane material for a specific application, it is thus important to consider whether permeability or selectivity is the main economical driver for the separation process [18]. In fact permeability often drives process costs [18] and IL materials have extremely high permeabilities due to the liquid-like transport of gases through them (*e.g. the commonly used IL [emim][Tf_2N] has a CO_2 permeability of 1000 Barrer with a CO_2/N_2 selectivity of 22 [20]*). However, the permeability of an IL-based membrane is related not only to the IL composition but also to the membrane thickness. Depending on the membrane morphology, the selective layer thickness can be drastically different.

Figure I. 6 presents three possible membrane designs including a dense selective layer [10]. Homogeneous dense membranes (Figure I. 6.A) usually exhibit low fluxes unless they can be very thin. For this reason, they are often cast as a "thin dense coating layer" on the surface of a porous support (Figure I. 6.B). This type of membrane is commonly called composite as the nature of the active layer usually differs from that of the porous support. The multilayer composite membrane shown in Figure I. 6.C contains several layers made from different materials. In this case, the selective layer is deposited on an intermediate layer (highly permeable "gutter layer") which limits the infiltration of the membrane material into the porous support. The porous support (usually macroporous) provides the necessary mechanical strength to the membrane. A protective top-coat can sometimes be used to protect or stabilize the selective dense layer in harsh working conditions [10].

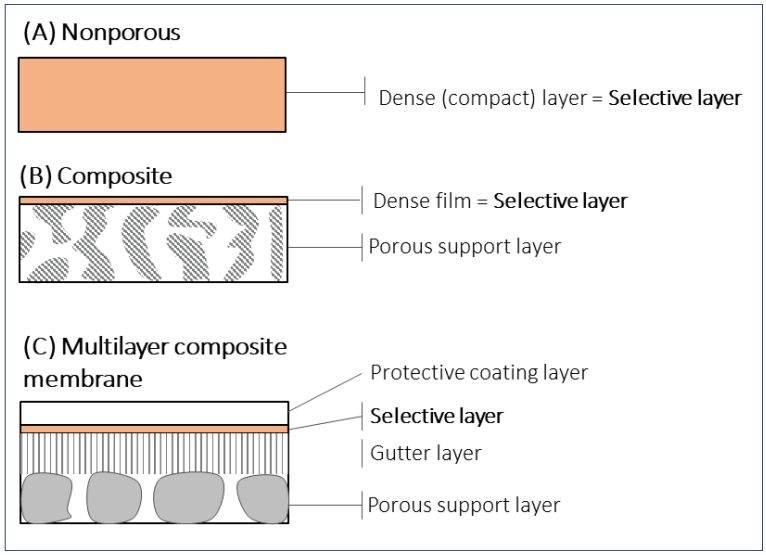

Figure I. 6. Schematic representation of possible membrane designs including a dense selective layer.

I.3.2. CO_2 separation performance of IL-based membranes

I.3.2.1. Supported Ionic Liquid Membranes (SILMs)

Supported Ionic Liquid Membranes (SILMs) are typically made of a porous solid support impregnated with an IL, which is maintained by capillary forces within the pores [51]. One of the main advantages of SILMs in comparison with common Supported Liquid Membranes (SLMs) [57] is that ILs are non-volatile, possess a large range of viscosity, high thermal stability and low flammability which make them ideal liquid phases [49]. SILMs have emerged during the 1990s [58], and since then, some research groups substantially contributed to the fundamental and systematical understanding of gas transport and separation properties of SILMs [50,51]. The porous support can be made of an organic polymer such as PES (polyethersulfone) [45-47], PVDF (polyvinylidene fluoride) [48,49] which are both commercial. Four methods for the preparation of SILMs are described in the literature, involving impregnation, immersion, vacuum or pressure-based processes. Each method can play an important role in tailoring the membrane performance [50]. To improve the thermomechanical stability of SILMs, some authors have considered replacing the polymeric support by a ceramic one due to its higher thermal and mechanical stabilities [59-65].

The considered porous ceramic supports are typically composed of oxide or non-oxide materials *(i.e. silica, alumina, titania, zirconia or silicon carbide)*, with either a symmetric or asymmetric architecture

(Figure I. 7.A.), various pore sizes/porous structures and different geometries, (*i.e. discs, single tubes or multichannel tubes as shown in Figure I. 7.B*).

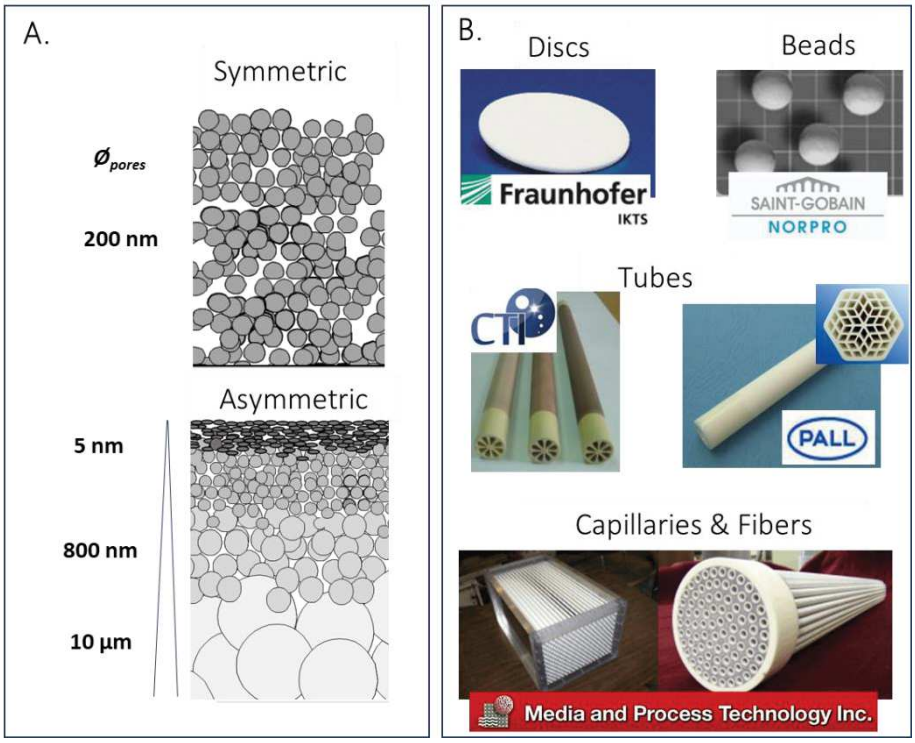

Figure I. 7. A. Schematic of symmetric and asymmetric membrane architectures, B. Examples of commercial porous ceramic supports.

In order to answer the question : "*which ILs are the most suitable for preparing CO_2-selective SILMs?*", a large number of different cation and anion structures have been combined in SILM systems. In fact, the separation performance of SILMs is essentially attributed to the characteristics of the impregnated IL, rather than to the porous membrane substrate. However, recent reports suggest that the physical nature of the IL confined inside the pores and its organization at the solid/liquid interface are key parameters that significantly influence the SILM separation performance [65]. In particular, Hayes *et al.* [66], suspected that transport properties could be modulated by modifying both the surface chemistry of the host material and the nature of the IL. As a consequence, it is difficult to compare the CO_2 separation performance of SILMs without considering the porous support composition. As an example, Figure I. 8 reports the CO_2/N_2 selectivity vs. CO_2 permeability value for various imidazolium-based SILMs composed of either polymeric or ceramic supports. The trend observed for the ceramic SILMs differs from the trend of polymer-based SILMs, demonstrating that a deep understanding of the effect of the support pore surface and its interactions with the ILs is crucial.

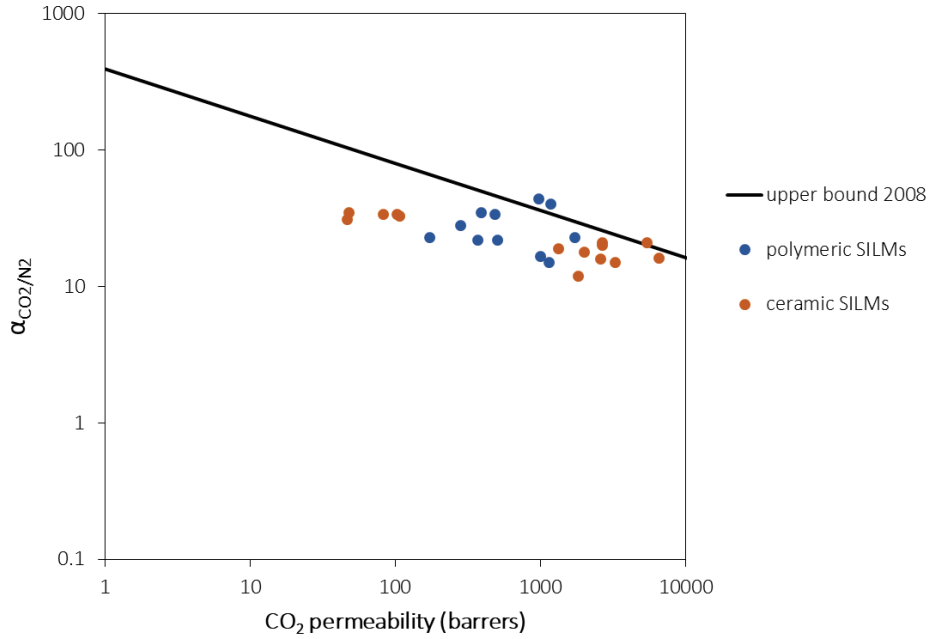

Figure I. 8. CO_2/N_2 permselectivity vs. CO_2 permeability of SILMs derived from either ceramic or polymeric porous supports. Data are plotted on a log-log scale, and the upper bound is adapted from Robeson [56]. (Note that all data points were obtained from the literature and are reported in Annex 3).

Neves *et al.* [49], were the first to prove the influence of pores surface chemistry on SILMs performance. By using PVDF porous supports, one hydrophobic and another hydrophilic, they observed that more stable SILMs were obtained with the hydrophobic support. Labropoulos *et al.* [65], studied the confinement of ILs in the pores of silica-based SILMs and showed that this strategy could considerably alter the gas diffusion properties of the gas in the liquid phase. Parameters such as ILs viscosity, porosity and support tortuosity were considered, but alone they were unable to explain the differences in permeability observed for the prepared SILMs. Therefore, the authors proposed that the the pore size and organizational effect of the silica layer on the IL molecules strongly impacts on CO_2 gas transport through the system. It was suggested that the negatively charged nanoporous silica material attracts the cations electrostatically towards the pore surface and thus facilitates the transport of CO_2.

In addition, Albo *et al.* [59,60], studied the impact of two types of ceramic supports on the CO_2 separation performances of [emim][Ac]-ceramic-based SILMs. They demonstrated that the affinity *(i.e., hydrogen bonding or electrostatic interactions*) between the IL and the different layers of the support are different in each SILMs and are influenced by the porous support characteristics: geometry, architecture and pore structure.

Investigation of the behavior and properties of IL immobilized in porous networks is not a new research area but it intensified in recent years [67,68]. Several studies revealed liquid properties similar to bulk-fluid ILs, while others evidenced the formation of organized IL structures at the vicinity of the solid surface as well as pore size dependent phase transitions. Thus, CO_2 solubility and diffusivity are enhanced compared to values observed in unconfined ILs. According to Banu *et al*. [69] a reorganization of the cations and anions at the pore/IL interface could increase the free volume available for CO_2 absorption. These confinement effects can also be evidenced for other types of IL-based membranes. Nevertheless, despite of their attractive CO_2 transport performance, the majority of the current state of the art polymer-based and ceramic-based SILMs suffer from easy or progressive disarrangement under continuous application of a transmembrane pressure.

I.3.2.2. Gelled IL membranes

The preparation of gelled IL-materials involves the physical gelation of a conventional IL with the help of an organic gelator (*i.e., the 12-hydroxystearic acid called LMOG*) able to solidify the IL at very low concentration by forming a fibrous network structure (Figure I. 9). The first supported IL gelled membrane was described by Voss *et al.* [70] and was composed of the [hmim][Tf_2N] IL with 1.5 wt% gelator (LMOG) impregnated and gelled by heating and cooling treatment, in a porous PES support. The supported gelled IL membranes (GSILMs) displayed a CO_2 permeability (P^*_{CO2} = 650 Barrer) and CO_2/N_2 selectivity ($\alpha^*_{CO2/N2}$ = 22) similar to a [hmim][Tf_2N] SILM made of PES (P^*_{CO2} = 1136 Barrer, $\alpha^*_{CO2/N2}$ = 15) [51,70]. The same authors developed gelled IL membranes from aspartame-based LMOG and [emim][Tf_2N] or [hmim][Tf_2N] ILs [71]. Compared to SILMs, the IL gelled membrane was coated on a PTFE porous support. An increase in the gelator content was found to generate stronger pressure-resistant gelled materials, but with lower CO_2 diffusion and permeability. As previously published [70], the CO_2 transport performance of the gelled-IL membranes was close to those of pure ILs or SILMs, but the gelled membranes offer improved mechanical strength and higher burst pressures compared to SILMs. The low CO_2 permeances were due to the relatively large membrane thicknesses, which are typically in the range 2-17 µm.

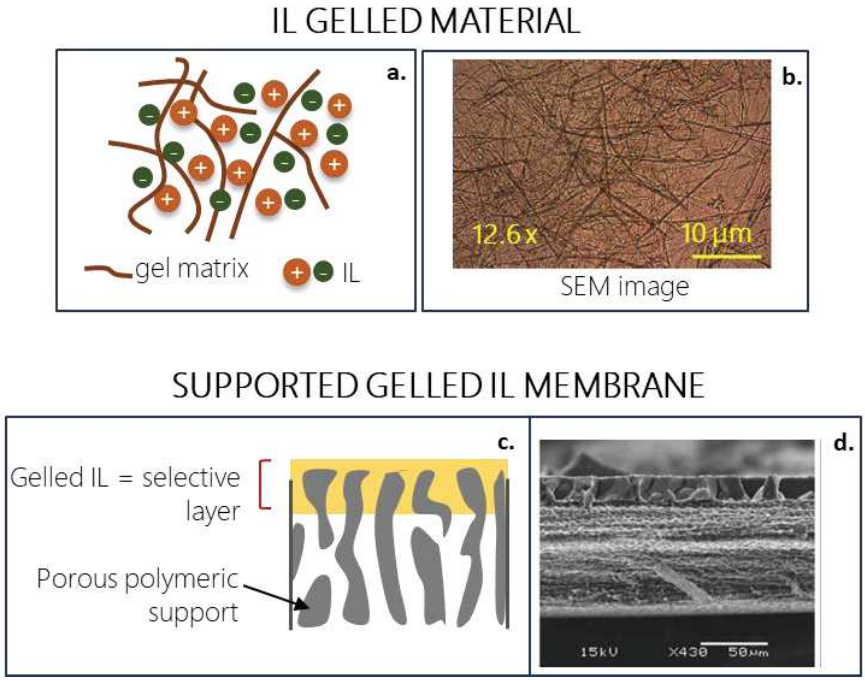

Figure I. 9. Gelled IL-based materials and membranes a. Schematic and **b**. SEM image [70] of a gelled IL material, **c.** Schematic and SEM image [71] of the cross-section of a supported gelled IL membrane.

I.3.2.3. Polymerized ionic liquid (PIL) membranes

Polymeric ionic liquids or poly(ionic liquid)s are composed of IL monomers (e.g., structures shown in Figure I. 10) able to polymerize and form a macromolecular framework [72]. From monomers to oligomers and further to high molecular weight polymers, certain special properties of ILs, such as negligible vapor pressure, thermal stability, non-flammability, high ionic conductivity and a wide electrochemical stability window, are transferred to polymer chains.

Also, IL monomers with two polymerizable units can be used for building more complex PIL networks. The most studied PILs contain $[Tf_2N]^-$ as the counter-anion. PILs can be used in many applications such as ionic conductors in electrochemical devices [73,74], dispersants and stabilizers [75,76], sensitive

materials [77], and gas separation [78]. A comprehensive overview of the PILs properties and applications has been recently published by Qian *et al.* [79].

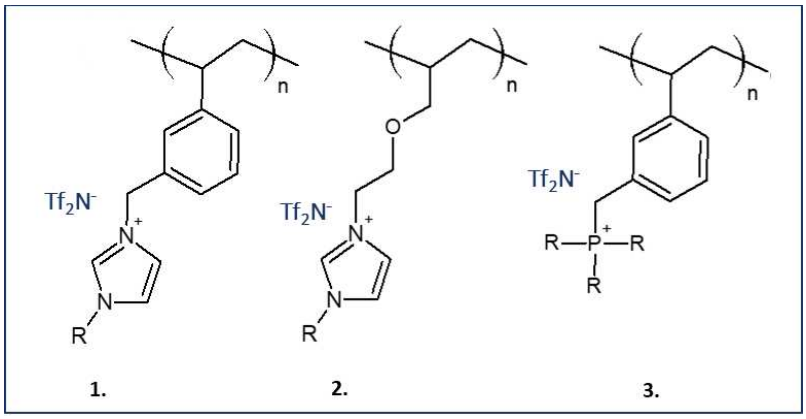

Figure I. 10. Chemical structures of 1. Imidazolium-based styrene PIL, 2. Imidazolium-based acrylate PIL and 3. Phosphonium-based styrene PIL with R representing an organic group such as alkyl, alkyl ethers, alkylnitrile, disiloxane.

Among the PILs developed, the poly[pvinylbenzyltrimethylammonium tetrafluoroborate] (P[VBTMA][BF_4]) and the poly[2-(methylacryloyloxy)ethyl-trimethylammoniumtetrafluoroborate] (P[MATMA][BF_4]) were found to exhibit the highest CO_2 sorption capacity, but they are too brittle to form mechanically stable membranes [80,81]. The first neat PIL membranes for CO_2 separation were presented by Noble's group [72]. As reported by Bara *et al.* [72], pure PIL-based membrane displays the gas transport properties expected for a polymeric material. Five PIL-based membranes were prepared by UV polymerization of the IL monomers solution directly on a porous polymeric support (*i.e., PES, PTFE or PVDF*). The IL monomers solution were composed of alkyl-imidazolium cations tethered to a polystyrene or polyacrylate backbone, 1 wt % of a photo-initiator and 5 mol % of a cross-linking agent (*i.e., divinylbenzene or 1,6-hexanediol diacrylate*). However, the best CO_2 separation performance achieved was an ideal CO_2 permeability of 32 Barrer with an ideal selectivity of 28 and 17 for CO_2/N_2 and CO_2/CH_4 gas pairs, respectively. With the intent of improving the CO_2 separation performance of PIL-based membranes, the same authors proposed the second generation of functionalized imidazolium-based PILs containing polar groups (*i.e., oligo(ethylene glycol*) or alkyl-terminated nitrile [82]. Nevertheless, the obtained CO_2 permeability was lower or in the same range as the PILs with alkyl analogs. Other modifications on the imidazolium cations like addition of cyclopentyl and isobutyl [83], or the incorporation of imidazolium ionene [84] were tested. Recently, phosphonium poly(ionic liquid)s (PILs) have been studied as alternatives to more common ammonium and imidazolium PILs [85]. The gas permeability was found to increase quasi-linearly with increasing alkyl chain length on the phosphonium group. The authors obtained a CO_2 permeability of 186 Barrer for the poly([P_{888VB}][Tf_2N]) which is the highest reported permeability value for neat PIL materials with ideal CO_2/N_2 and CO_2/CH_4 selectivities reaching 16 and 8, respectively.

To improve the mechanical stability and increase the CO_2 separation performance, recent advances of the PIL-based membranes have conducted to realize supported membranes made of **PIL/IL ion-gel materials**. PIL/IL ion-gel materials are composed of both PIL and "free IL". It is possible to obtain a thin selective layer of this material supported on/in a porous polymeric support [85]. Due to the relatively strong electrostatic charge-charge interactions between the PIL and the IL, the developed material presents a relatively good mechanical integrity. The presence of the IL also increases the CO_2 permeability compared to neat PILs. These initial linear PIL/IL ion-gels have been used to produce

100 nm thick active layers with a CO_2 permeance higher than 6000 GPU (2 x 10^{-6} mol.m^{-2}.s^{-1}.Pa^{-1}) and an ideal CO_2/N_2 selectivity of 22.

Based on this membrane, other PIL/IL-based membranes have been developed made of cross-linked PIL/IL materials, or epoxide/amine PIL/IL, or coPIL/IL whose CO_2 transport performance is similar or even higher than those of PIL/IL ion gel membranes. For a more complete description of these membrane materials, the reader is invited to consider several complete reviews recently published in this area [20,43].

I.3.3. Conclusion

The Figure I. 11. provides an overview of the CO_2 performance of IL-based membranes considered in this bibliographic study. It must be noted that it represents only a small part of the vast amount of data available in the open literature. The development of IL-based membrane is an emerging field that shows huge potential for CO_2 separation. It appears clearly from the Figure I. 11. that different IL-based membranes can exhibit very disparate behavior due to their intrinsic composition.

This chapter also shows that among the scarce number of research dealing with ceramic-based SILMs, the term "nanoconfinement" just started to emerge. Some authors suspect that the transport properties can be modulated by modifying the behavior of interfacial ILs, i.e., the surface chemistry of the host material and the nature of the IL. There is still a lack of understanding on the impact of the interactions between the IL and the other components of the membrane material. However, based on this literature survey, we can assume that the lowest CO_2 transport performance will be obtained for rigid IL structures. On the other hand the high CO_2 separation efficiency is expected to result from nanoconfined ILs where a reorganization of both the cations and anions at the support interface could increase the free volume available for CO_2 absorption and transport.

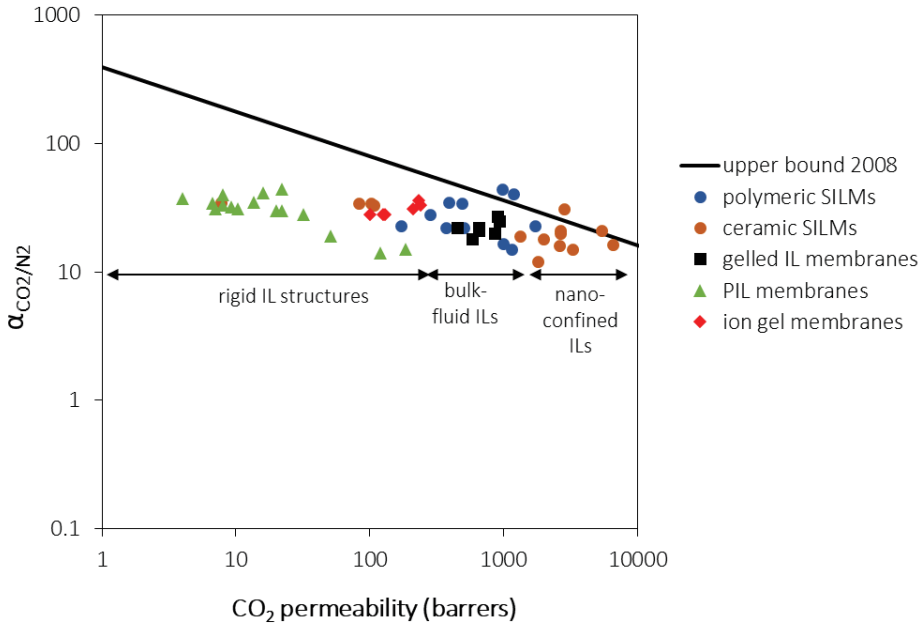

Figure I. 11. Robeson plot showing the performance of IL-based membrane materials discussed in this chapter and compared with the 2008 Robeson upper bound for the CO_2/N_2 gas pair (Note that all data points were obtained from the literature and are reported in Annex 3).

Taking into account all the above information, we decided to investigate in the PhD research work, the new generation of recently proposed SILMs, composed of ILs chemically grafted on the outer surface

and in the pores of mesoporous and microporous ceramic supports [86]. Our strategy is illustrated in Figure I. 12. By modulating the grafting reaction parameters and the ILs composition, we aimed to realize 3 types of grafted ILs ceramic membrane composed of: **i)** IL species grafted only on the top-layer surface of the porous support (case 1 in Figure I. 12), **ii)** monolayer of grafted IL species covering all the accessible surface area of the porous top-layers, **iii)** grafted IL species and "free IL" in the different layers of the ceramic support. This study aims to provide membranes in which the ILs will be stabilized by a tailored nanoconfinement through covalent bonds in the pores of a ceramic matrix. This approach targets to take an advantage of the ILs versatility for the development of a variety of original and sustainable separation systems with adjustable properties in terms of CO_2 solubility, permeability and separation efficiency.

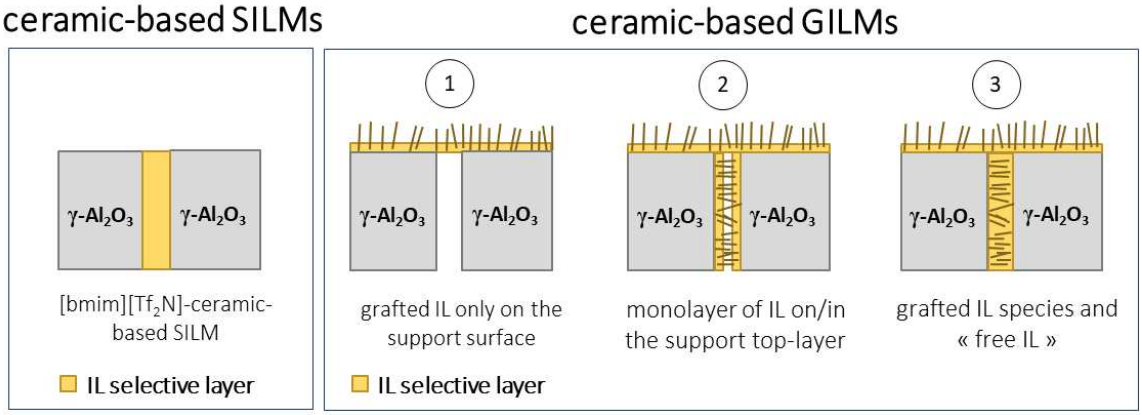

Figure I. 12. Schematic illustration of the possible architectures for the new generation of ceramic-based GILMs in comparison with SILMs.

References

1. "Carbon Capture and Storage". *International Energy Agency*. Web. 19 September 2017.
2. L.W. Hiselius, Â. Svensson, E-bike use in Sweden – CO_2 effects due to modal change and municipal promotion strategies, *J. Clean. Prod.,* 2017, *141*, 818-824.
3. W. Weldu, G. Assefa, The search for most cost-effective way of achieving environmental sustainability status in electricity generation: Environmental life cycle cost analysis of energy scenarios, *J. Clean. Prod.,* 2017, *142 (4),* 2296-2304.
4. 20 Years of Carbon Capture and Storage, OECD/IEA, 2016, 1-115.
5. B. Metz, O. Davidson, H.D. Coninck, M. Loos, L. Meyer, IPCC special report on carbon dioxide capture and storage, 2005.
6. R. Idem, T. Supap, H. Shi, D. Gelowitz, M. Ball, C. Campbell, P. Tontiwachwuthikul, Practical experience in post-combustion CO_2 capture using reactive solvents in large pilot and demonstration plants, *Int. J. Greenh. Gas Control*, 2015, *40*, 6-25.
7. IEA, Energy Technology Perspectives 2012.
8. Y. Le Moullec, Conceptual study of a high efficiency coal-fired power plant with CO_2 capture using a supercritical CO_2 Brayton cycle, *Energy*, 2013, *49,* 32-46.
9. A. Brunetti, F. Scura, G. Barbieri, E. Drioli, Membrane technologies for CO_2 separation, *J. Membrane. Sci.*, 2010, *359(1-2)*, 115-125.
10. R.W. Baker, B.T. Low, Gas Separation Membrane Materials: A Perspective, *Macromolecules*, 2014, *47*, 6999−7013.
11. G.T. Rochelle, Amine Scrubbing for CO_2 Capture, *Science*, 2009, *325(5948),* 1652-1654.
12. W. Conway, S. Bruggink, Y. Beyad, W. Luo, I. Melián-Cabrera, G. Puxty, P. Feron, CO_2 absorption into aqueous amine blended solutions containing monoethanolamine (MEA),N,N-dimethylethanolamine (DMEA), N,N-diethylethanolamine (DEEA) and 2-amino-2-methyl-1-propanol (AMP) for post-combustion capture processes, *Chem. Eng. Sci.*, 2015, *126*, 446–454.
13. W. Liang, R. Babarao, T.L. Churcha, D.M. D'Alessandro, Tuning the cavities of zirconium-based MIL-140 frameworks to modulate CO_2 adsorption, *Chem. Commun.,* 2015, *51*, 11286-11289.
14. W. Li, J.H. Drese, S. Choi, M. Hornbostel, G. Krishnan, P.J. Eisenberger, C. W. Jones, Steam-stripping for regeneration of supported amine-based CO_2 adsorbents, *ChemSusChem*, 2010, *3*, 899–903.
15. S. Choi, J.H. Drese, C.W. Jones, Adsorbent materials for carbon dioxide capture from large anthropogenic point sources, *ChemSusChem.*, 2009, *2*, 796-854.
16. C.A. Grande, R. Ribeiro, A.E. Rodrigues, Challenges of Electric Swing Adsorption for CO2 Capture *ChemSusChem.,* 2010, *3*, 892-898.
17. Baker, R. W., Membrane Technology and applications. 2nd ed.; John Wiley & Sons Ltd.: Chichester, 2004.
18. T.C. Merkel, H. Lin, X. Wei, R. Baker, Power plant postcombustion carbon dioxide capture: An opportunity for membranes, *J.Membr. Sci.*, 2010, *359(1-2)*, 126−139.
19. S.D. Hojniak, Ionic Liquids for Carbon Dioxide Separation on Membranes, Leuven, Science, Engineering & Technology, 2014
20. M.G. Cowan, D.L. Gin, R.D. Noble, Poly(ionic liquid)/Ionic Liquid Ion-Gels with high "free" ionic liquid content: platform membrane materials for CO_2/light gas separations, *Acc. Chem. Res.,* 2016, *49(4)*, 724−732.
21. M. Ramdin, T.W. De Loos, T.J.H. Vlugt, State-of-the-Art of CO_2 Capture with Ionic Liquids, *Ind. Eng. Chem. Res.,* 2012, *51(24)*, 8149-8177.

22. M.J. Earle, J.M.S.S. Esperanca, M.A. Gilea; J.N. Canongia Lopes, L.P.N. Rebelo, J.W. Magee, K.R. Seddon, J.A. Widegren, The distillation and volatility of ionic liquids, *Nature*, 2006, *439*, 831–834.
23. J.L. Anderson, R. Ding, A. Ellern, D.W. Armstrong, Structure and properties of high stability germinal dicationic ionic liquids, *J. Am. Chem. Soc*., 2004, *127(2)*, 593–604.
24. M. Smiglak, W.M. Reichert, J.D. Holbrey, J.S. Wilkes, L. Sun, J.S. Thrasher, K. Kirichenko, S. Singh, A.R. Katritzky, R.D. Rogers, Combustible ionic liquids by design: is laboratory safety another ionic liquid myth? *Chem. Commun*., 2006, 2554–2556.
25. H. Ohno, M. Yoshizawa, T. Mizumo, in electrochemical aspects of ionic liquids, ed. H. Ohno, John Wiley & Sons, Inc., New Jersey, 2005.
26. S. Zhang, N. Sun, X. He, X. Lu, X. Zhang, Physical properties of ionic liquids: database and evaluation, *J. Phys. Chem. Ref. Data.,* 2006, *35*, 1475-1517.
27. M.J. Earle, K.R. Seddon, Ionic liquids. Green solvents for the future, *Pure Appl. Chem*., 2000, *72(7)*, 1391–1398.
28. T. Ueki, M. Watanabe, Macromolecules in Ionic Liquids: Progress, Challenges, and Opportunities, *Macromolecules*, 2008, *41(11)*, 3739–3749.
29. V. I. Pârvulescu, C. Hardacre, Catalysis in Ionic Liquids, *Chem. Rev*., 2007, *107(6),* 2615–2665.
30. R. Sheldon, Catalytic reactions in ionic liquids *Chem. Commun.,* 2001, 23, 2399–2407.
31. D. Zhao, M. Wu, Y. Kou, E. Min, Ionic liquids: applications in catalysis, *Catal. Today*, 2002, *74(1-2),* 157–189.
32. S. Chowdhury, R.S. Mohan, J.L. Scott, Reactivity of ionic liquids, *Tetrahedron*, 2007, *63*, 2363–2389.
33. H. Olivier-Bourbigou, L. Magna, Ionic liquids: perspectives for organic and catalytic reactions *J. Mol. Catal. A: Chem*., 2002, *182–183*, 419–437.
34. E. Mourad, L. Coustan, P. Lannelongue, D. Zigah, A. Mehdi, A. Vioux, S.A. Freunberger, F. Favier, O.Fontaine, Biredox ionic liquids with solid-like redox density in the liquid state for high-energy supercapacitors, *Nat. Mater.,* 2016, *16*, 446-454.
35. J.G. Huddleston, R.D. Rogers, Room temperature ionic liquids as novel media for 'clean' liquid liquid extraction, *Chem. Commun.,* 1998, *0*, 1765–1766.
36. X. Sun, H. Luo, S. Dai, Ionic liquids-based extraction: a promising strategy for the advanced nuclear fuel cycle, *Chem. Rev.,* 2011, *112(4)*, 2100–2128.
37. G. Cui, J. Wang, S. Zhang, Active chemisorption sites in functionalized ionic liquids for carbon capture, *Chem. Soc. Rev.,* 2016, *45*, 4307-4339.
38. J. Zhang, S. Zhang, K. Dong, Y. Zhang, Y. Shen, X. Lv, Supported absorption of CO_2 by tetrabutylphosphonium amino acid ionic liquids, *Chem. Eur. J*., 2006, *12*, 4021 – 4026.
39. A.V. Perdikaki, O.C. Vangeli, G.N. Karanikolos, K.L. Stefanopoulos, K.G. Beltsios, P. Alexandridis, N.K. Kanellopoulos, G.Em. Romanos, Ionic liquid-modified porous materials for gas separation and heterogeneous catalysis, *J. Phys. Chem. C.,* 2012, *116(31)*, 16398−16411.
40. O.C. Vangeli, G.E. Romanos, K.G. Beltsios, D.Fokas, E.P. Kouvelos, K.L. Stefanopoulos, N.K. Kanellopoulos, Grafting of imidazolium based ionic liquid on the pore surface of nanoporous materials study of physicochemical and thermodynamic properties, *J. Phys. Chem. B.,* 2010, *114(19)*, 6480–6491.
41. J.M. Zhu, F. Xin, Y.C. Sunb, X.C. Dong, Phosphonium based ionic liquids grafted onto silica for CO_2 sorption, *Theor. Found. Chem. Eng*., 2014, *48(6),* 787–792.
42. K. Fujie, H. Kitagawab, Ionic liquid transported into metal–organic frameworks, *Coord. Chem. Rev*., 2016, *307(2)*, 382–390.
43. L.C. Tomé, I.M. Marrucho, Ionic liquid-based materials: a platform to design engineered CO_2 separation membranes, *Chem. Soc. Rev*., 2016, *45*, 2785-2824.
44. R. Fortunato, C.A.M. Afonso, M.A.M. Reis, J.G. Crespo, Supported liquid membranes using ionic liquids: study of stability and transport mechanisms, *J. Membrane. Sci*., 2004, *242(1-2),* 197–209.

45. P. Scovazzo, J. Kieft, D.A. Finan, C. Koval. D.Dubois, R.Noble, Gas separations using non-hexafluorophosphate $[PF_6]^-$ anion supported ionic liquid membranes, *J. Membrane. Sci*., 2004, *238*, 57–63.
46. J. Ilconich, C. Myers, H. Pennline, D. Luebke, Experimental investigation of the permeability and selectivity of supported ionic liquid membranes for CO_2/He separation at temperatures up to 125˚C *J. Membrane. Sci*., 2007, *298(1-2)*, 41–47.
47. S.M. Malhurin, J.S. Lee, G.A. Baker, H. Luo, S. Dai, Performance of nitrile-containing anions in task-specific ionic liquids for improved CO_2/N_2 separation, *J. Membrane. Sci.,* 2010, *353(1-2)*, 177–183.
48. P. Cserjési, N. Nemestóthy, K. Bélafi-Bakó, Gas separation properties of supported liquid membranes prepared with unconventional ionic liquids, *J.Membr. Sci.,* 2010, *349(1-2)*, 6–11.
49. L.A. Neves, J.G. Crespo, I.M. Coelhoso, Gas permeation studies in supported ionic liquid membranes, *J. Membrane. Sci*., 2010, *357(1-2)*, 160–170.
50. L.J. Lozano, C. Odínez, A.P de los Ríos, F.J.Hernández-Fernández, S.Sánchez-Segado, F.J.Alguacil, Recent advances in supported ionic liquid membrane technology, *J. Membrane. Sci*., 2011, *376(1-2)*, 1–14.
51. P. Scovazzo, Determination of the upper limits, benchmarks, and critical properties for gas separations using stabilized room temperature ionic liquid membranes (SILMs) for the purpose of guiding future research, *J. Membrane. Sci.*, 2009, *343*, 199–211.
52. M.G. Cowan, The application of membrane technology to post-combustion separation of carbon dioxide from coal-fired power plant flue gas, *Chem. New. Zealand*, 2015*, 79(2),* 79-83.
53. S. Matteucci, Y. Yampolskii, B. D. Freeman, I. Pinnau, in Materials Science of Membranes for Gas and Vapor Separation, John Wiley & Sons, Ltd, 2006, pp. 1-47.
54. J.G. Wijmans, R.W. Baker, The solution-diffusion model: a review, *J. Membrane. Sci.,* 1995, *107(1-2)*, 1–21.
55. B.D. Freeman, Basis of Permeability/Selectivity Tradeoff Relations in Polymeric Gas Separation Membranes, *Macromolecules*, 1999, *32(2)*, 375–380.
56. L.M. Robeson, The upper bound revisited, *J. Membrane. Sci*., 2008*, 320(1-2),* 390-400.
57. M. Teramoto, Y. Sakaida, S.S. Fu, N. Ohnishi, H. Matsuyama, T. Maki, T. Fukui, K. Arai, An attempt for the stabilization of supported liquid Membrane, *Sep. Purif. Technol.,* 2000, *21(1-2)*, 137–142.
58. R. Quinn, J.B. Appleby, G.P. Pez, New facilitated transport membranes for the separation of carbon dioxide from hydrogen and methane, *J. Membrane. Sci.,* 1995, *104(1-2*), 139–146.
59. J. Albo, T. Yoshioka, T. Tsuru, Porous Al_2O_3/TiO_2 tubes in combination with 1-ethyl-3-methylimidazolium acetate ionic liquid for CO_2/N_2 separation, *Sep. Purif. Technol.*, 2014, *122*, 440–448.
60. J. Albo, T. Tsuru, Thin Ionic Liquid Membranes Based on Inorganic Supports with Different Pore Sizes *Ind. Eng. Chem. Res*., 2014, *53*, 8045−8056.
61. J.J. Close, K. Farmer, S.S. Moganty, R.E. Baltus, CO_2/N_2 separations using nanoporous alumina-supported ionic liquid membranes: Effect of the support on separation performance, *J. Membrane. Sci.,* 2012, *390-391*, 201–210.
62. S.D. Hojniak, I.P. Silverwood, A.L. Khan, I.F.J. Vankelecom, W. Dehaen, S.G. Kazarian, K. Binnemans, Highly Selective Separation of Carbon Dioxide from Nitrogen and Methane by Nitrile/Glycol-Difunctionalized Ionic Liquids in Supported Ionic Liquid Membranes (SILMs), *J. Phys. Chem. B*., 2014, *118(26),* 7440–7749.
63. S.D. Hojniak, A.L. Khan, O. Hollo, B. Kirchner, I.F.J. Vankelecom, W. Dehaen, K. Binnemans, Separation of Carbon Dioxide from Nitrogen or Methane by Supported Ionic Liquid Membranes (SILMs): Influence of the Cation Charge of the Ionic Liquid, *J. Phys. Chem. B.,* 2013, *117(4)*, 15131−15140.
64. M. Adibi, S.H. Barghi, D. Rashtchian, Predictive models for permeability and diffusivity of CH_4 through imidazolium-based supported ionic liquid membranes, *J. Membr .Sci.,* 2011, *371(1-2)*, 127–133.

65. A.I. Labropoulos, G.Em. Romanos, E. Kouvelos, P. Falaras, V. Likodimos, M. Francisco, M.C. Kroon, B. Iliev, G. Adamova, T.J.S. Schubert, Alkyl-methylimidazolium Tricyanomethanide Ionic Liquids under Extreme Confinement onto Nanoporous Ceramic Membranes, *J. Phys. Chem. C.,* 2013, *117(19),* 10114−10127.
66. R. Hayes, G.G. Warrb, R. Atkin, Structure and Nanostructure in Ionic Liquids, *Phys. Chem. Chem. Phys.,* 2010, *12*, 1709–1723.
67. B. Coasne, L. Viau, A. Vioux, Loading-Controlled Stiffening in Nanoconfined Ionic Liquids, *J. Phys. Chem. Lett.,* 2011, *2*, 1150–1154.
68. J. Le Bideau, P. Gaveau, S. Bellayer, M. Néouze, A. Vioux, Effect of confinement on ionic liquids dynamics in monolithic silica ionogels: ^{1}H NMR study, *Phys. Chem. Chem. Phys.,* 2007, *9(40)*, 5419–22.
69. L.A. Banu, D. Wang, R.E. Baltus, Effect of Ionic Liquid Confinement on Gas Separation Characteristics, Energy Fuels., 2013, *27*, 4161−4166.
70. B.A. Voss, J.E. Bara, D.L. Gin, R.D. Noble, Physically gelled ionic liquids: solid membrane materials with liquid like CO_2 gas transport, *Chem. Mater.,* 2009, *21(14)*, 3027–3029.
71. P.T. Nguyen, B.A. Voss, E.F. Wiesenauer, D.L. Gin, R.D. Noble, Physically Gelled RTIL-based Thin-film Composite Membranes for CO_2/N_2 Separation: Effect of Composition and Thickness on Membrane Properties and Performance, *Ind. Eng. Chem. Res*., 2013, *52(26)*, 8812–8821.
72. J.E. Bara, S. Lessmann, C.J. Gabriel, E.S. Hatakeyama, R.D. Noble, D.L. Gin, Synthesis and Performance of Polymerizable Room-Temperature Ionic Liquids as Gas Separation Membranes, *Ind. Eng. Chem. Res.,* 2007, *46(4)*, 5397−5404.
73. R. Marcilla, F. Alcaide, H. Sardon, J. A. Pomposo, C. Pozo-Gonzalo, D. Mecerreyes, Tailor-made polymer electrolytes based upon ionic liquids and their application in all-plastic electrochromic devices, *Electrochem. Commun.*, 2006, *8(3)*, 482–488.
74. G.B. Appetecchi, G.T. Kim, M. Montanino, M. Carewska, R. Marcilla, D. Mecerreyes, I. De Meatza, Ternary polymer electrolytes containing pyrrolidinium-based polymeric ionic liquids for lithium batteries, *J. Power. Sources,* 2010, *195(11)*, 3668-3675.
75. M. Antonietti, Y. Shen, T. Nakanishi, M. Manuelian, R. Campbell, L. Gwee, Y. A. Elabd, N. Tambe, R. Crombez, J. Texter, Single-Wall Carbon Nanotube Latexes, *ACS Appl. Mater. Interfaces,* 2010, *2(3)*, 649–653.
76. T. Fukushima, A. Kosaka, Y. Yamamoto, T. Aimiya, S. Notazawa, T. Takigawa, T. Inabe, T. Aida, Dramatic Effect of Dispersed Carbon Nanotubes on theMechanical and Electroconductive Properties of Polymers Derived from Ionic Liquids, *Small.*, 2006, *2(4)*, 554–560.
77. Y.S. Vygodskii, A.S. Shaplov, E.I. Lozinskaya, P.S. Vlasov, I.A. Malyshkina, N.D. Gavrilova, P. Santhosh Kumar, M.R. Buchmeiser, Cyclopolymerization of N,N-Dipropargylamines and N,N-Dipropargyl Ammonium Salts, *Macromolecules*., 2008, *41*, 1919–1928.
78. L.C. Tomé, D. Mecerreyes, C.S.R. Freire, L.P.N. Rebelo, I.M. Marrucho, Polymeric ionic liquid membranes containing IL–Ag^{+} for ethylene/ethane separation via olefin-facilitated transport, *J. Mater. Chem. A.*, 2014*, 2,* 5631–5639.
79. W. Qian, J. Texter, F. Yan, Frontiers in poly(ionic liquid)s: syntheses and applications, *Chem. Soc. Rev*., 2017, *46(4)*, 1124-1159.
80. J. Tang, W. Sun, H. Tang, M. Radosz, Y. Shen, Enhanced CO_2 absorption of polyionic liquids, *Macromolecules,* 2005, *38(6)*, 2037–2039.
81. J. Tang, W. Sun, H. Tang, M. Radosz, Y. Shen, Polyionic liquids: novel materials for CO_2 absorption, *Chem. Commun.,* 2005, *26*, 3325–3327.
82. J.E. Bara, C.J. Gabriel, E.S. Hatakeyama, T.K. Carlisle, S. Lessmann, R.D. Noble, D.L. Gin, Improving CO_2 selectivity in polymerized room-temperature ionic liquid gas separation membranes through incorporation of polar substituents, *J. Membrane. Sci.*, 2008, *321(1-2)*, 3−7.

83. J. Horne, M.A. Andrews, M.S. Shannon, K.L. Terrill, J.D. Moon, S.S. Hayward, J.E. Bara, Effect of branched and cycloalkyl functionalities on CO_2 separation performance of poly(IL) membranes, *Separation and Purification Technology.,* 2015, *155,* 89–95.
84. T.K. Carlisle, J.E. Bara, A.L. Lafrate, D.L. Gin, R.D. Noble, Main-chain imidazolium polymer membranes for CO_2 separations: An initial study of a new ionic liquid-inspired platform, *J. Membrane. Sci.,* 2010, *359(1-2)*, 37–43.
85. M.G. Cowan, M. Masuda, W.M. McDanel, Y. Kohno, D.L. Gin, R.D. Noble, Phosphonium-based poly(Ionic liquid) membranes: The effect of cation alkyl chain length on light gas separation properties and Ionic conductivity, *J. Membrane. Sci.,* 2016, *498(1-2)*, 408–413.
86. O.C. Vangeli, G.E. Romanos, K.G. Beltsios, D. Fokas, E.P. Kouvelos, K.L. Stefanopoulos, N.K. Kanellopoulos, Grafting of imidazolium based ionic liquid on the pore surface of nanoporous materials - Study of physicochemical and thermodynamic properties, *J. Phys. Chem. B.,* 2010, *114(19)*, 6480–6491.

Chapter II. Designing phosphonate-based ILs for CO_2/light-gas separation applications.

In this chapter, the determination of the key parameters influencing the CO_2 separation performance of ILs were investigated to design and synthesize novel phosphonate-based ILs with different organic spacers. Solubilities and ideal solubility selectivities of CO_2, N_2, and CH_4 in these ILs were determined. Comparison to corresponding conventional IL analogues reveals a lower CO_2 solubility, and a same or higher ideal CO_2/N_2 solubility selectivity.

Chapter II. Designing phosphonate-based ILs for CO_2/light-gas separation applications

II.1. Introduction

Several strategies were proposed for moderating CO_2 emissions, such as improving the energy use efficiency, decreasing the carbon density, developing and promoting both renewable energies and new technologies to capture and store CO_2. The properties of ILs make them promising liquid absorbents for CO_2 separation, thus contributing to CO_2 capture.

In order to get an overall view of the different kinds of relevant solvents for CO_2 separation, the absorption-related properties of commercial solvents such as the Dimethyl Ether of Polyethylene Glycol (DMPEG), N-Methyl-Pyrrolidone (NMP), Propylene Carbonate (PC), MonoEthanolAmine (MEA) and a conventional IL (*i.e,. [emim][Tf_2N]*) were collected and listed in Table II. 1 (adapted from Ramdin *et al.* [1]). Among the listed solvents, some of them are physical absorbents (*i.e.,* DMPEG, PC, NMP), whereas others are chemical absorbents (MEA). Concerning the ionic liquids, two classes exist depending on the type of absorption: ***i)*** the conventional ILs (*e.g*., [emim][Tf_2N]) which are a physical absorbents, and ***ii)*** the task-specific ILs, mostly similar to conventional ILs but exhibiting relevant functional groups for CO_2 capture (*e.g,.* amine groups) [2].

Except for the ILs, all the physical or chemical CO_2 solvents presented in Table II. 1 are applied industrially in the natural gas sweetening processes [1,3,4]. As reported by Ramdin *et al.* [1], ILs are more expensive than conventional solvents, and to date, only a few of them are considered/synthesized at large scale. Thus, a cost comparison between ILs and common industrial solvents is hardly realistic. Also, commonly used ILs are often not easily biodegradable [5], which strongly restricts their large-scale industrial applications. ILs are known to be viscous solvents in comparison with the classical commercial solvents. For example, the viscosity of [emim][Tf_2N] is 17 times higher than the viscosity of NMP. Nevertheless, ILs are suitable in processes where a low vapour pressure is required, as far as their vapour pressure is very low [6], even in comparison with molecular solvents with low vapour pressure such as DMPEG (*i.e. 95°C at 78.8 Pa for DMPEG, and 120°C at 1.2 Pa for [bmim][Tf_2N]*). The CO_2 solubility and gas selectivity related to the CO_2 separation efficiency are also reported in Table II. 1. For physical absorbents such as DMPEG, PC, and NMP, the CO_2 solubility at high pressure is lower than the values measured in MEA and [emim][Tf_2N] at low pressure. Nevertheless, MEA offers higher CO_2 capture capacity and kinetics than [emim][Tf_2N]. On the other hand, some drawbacks are still associated with the use of MEA *(i.e. high volatility generating fugitive emissions and product loss; corrosive behavior; high water content yielding relatively high energy consumption)* [2]. As an alternative, ILs are highly tunable, and can thus capture CO_2 via a range of chemical or physical mechanisms. Park *et al.* [2], pointed out that conventional ILs have a low capture capacity but also a low energy requirement for their regeneration. This is why conventional ILs have been considered to design Supported Liquid Membranes (SILMs) for gas separation applications (see Chapter I., section I.3.2.1) [7-10].

Table II. 1. Comparison of the properties[a] and performance of commercially used solvents and [emim][Tf_2N] for CO_2 capture ([a]Properties at 25 °C and 1 bar, unless otherwise stated. [b]Ideal selectivity, Properties of pure MEA are reported unless otherwise stated. [c]Viscosity of 30 wt% aqueous MEA solution is 2.2 mPa·s^{-1} at 25 °C. [d]Solubility selectivity in a solution of 30wt% MEA).

Solvent	DMPEG	NMP	PC	MEA	[emim][Tf_2N]
Absorption type	Physical	Physical	Physical	Chemical	Physical
Viscosity (mPa.s^{-1})	5.8	1.65	3	18.98[c]	28 [11]
Vapor pressure (mmHg)	0.00073	0.4	0.085	0.36	0.75 (300°C)
Max. operating temp. (°C)	175	202	65	150	455 [11]
Operating pressure	High	High	High	Low	Low
$\Delta_{abs}H$ (kJ.mol^{-1} CO_2)	-14.3	-16.4	-15.9	-85	-13 [12]
$\Delta_{vap}H$ (kJ.mol^{-1})	76.16	54.5	60.2	49.8	120.6 [13]
CO_2 solubility (mol.m^{-3})	3.63	3.57	3.4	80-85[d]	110 [14]
CO_2/CH_4 selectivity[b]	15	14	26	n/a	15 [12]
CO_2/N_2 selectivity[b]	50	50	117	n/a	38 [12]

As reported in Chapter I, Section I.3.1, gas transport through Supported Ionic Liquid Membranes (SILMs) is governed by a solution-diffusion mechanism. The gas solubility plays a more important role than the diffusivity in determining the CO_2/N_2 or CO_2/CH_4 selectivity values in SILMs. We postulated that the same trend should be observed in the Grafted Ionic Liquid Membranes (GILMs). Thus, to design the most suitable ILs able to yield the highest performance for separating CO_2 from N_2 or CH_4, a literature review was conducted in this Chapter for evidencing the key parameters affecting the gas solubility coefficient. With the aim to graft the ILs to the γ-Al_2O_3 ceramic support, we selected the diethyl ester phosphonate as a coupling function to be tethered to the cation by an organic spacer (as sketched in Figure II. 1). In fact, the use of alkyl phosphonate esters coupling functions allowed a controlled surface grafting, while excluding the formation of bulk phases even under prolonged heating [15]. Gas permeability, solubility, and diffusivity of analogous ILs without any coupling function, such as [hmim][Tf_2N], have already been reported in the literature. These ILs were studied as bulk liquids [14,16,17], or as selective layers in SILM based on either polymer [18] or ceramic matrix [19]. However, there is no report about the gas performance of ILs bearing a diethyl phosphonate coupling function, neither as bulk liquids (*i.e. with a free coupling function*) nor in hybrid materials (*i.e. with the coupling function anchored to a solid surface*). Experimental values of the solubility and diffusivity coefficients of single gases in the bulk liquid allow valuable prediction of the membrane efficiency for gas mixture separations. Also, these values are useful to compare the behavior and performance of a free IL and its nanoconfined (grafted) counterpart.

Several types of ILs have been investigated in this chapter; their acronym, abbreviations, names, as well as the structures of both cations and anions are provided in the Figure I. 4 of Chapter I.

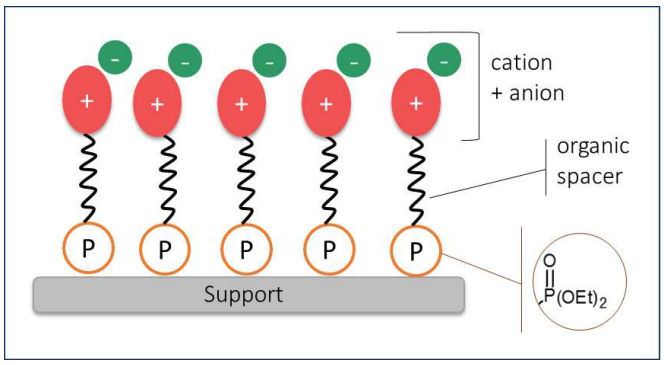

Figure II. 1. Schematic view of a Supported Ionic Liquid Phase composed of an IL covalently bond to a support surface by organophosphorus coupling functions.

II.2. Key factors influencing the CO_2 transport and separation

The solution-diffusion mechanism which governs gas transport through IL-based membranes is defined as the product of the diffusivity coefficient and the solubility coefficient. The former is related to the mobility of gas molecules in the membrane material and the latter reflects the concentration of gas molecules dissolved in the membrane. The following parts discuss the key factors influencing these two coefficients in order to select the most appropriate ILs to realize CO_2-selective SILMs in which the ILs will be chemically grafted to the ceramic support.

II.2.1. Key parameters influencing the diffusion coefficient of gas in ILs

According to Freeman [20], gas diffusivity plays a more important role than solubility in determining the upper bound selectivity values for polymeric membranes. At the opposite, the selectivity of SILMs is dominated by the solubility selectivity. However, as reported by Scovazzo [7], two parameters can influence the gas diffusion coefficient in SILMs: the IL viscosity and its molar volume. Scovazzo and coworkers [8-10] studied gas diffusivity in conventional ILs to develop a diffusivity model which could be used to predict the permeability of synthesized SILMs. This correlation, applicable for ammonium-, phosphonium- and imidazolium-ILs, is expressed as follows:

$$\boldsymbol{D_{1,IL} = A\frac{V_{IL}^{a}}{\mu_{IL}^{b}.V_{1}^{c}}} \quad 2.1$$

where A, a, b and c are IL-class specific parameters (*depending on the cation*), $D_{1,IL}$ is the diffusivity of solute #1 in the IL, V_{IL} is the IL molar volume and μ_{IL} the IL viscosity. The same author evidenced that gas diffusivity in IL is less dependent on viscosity, and more dependent on solute size. For example, the diffusivity of CO_2 is higher than that of CH_4 and similar to that of N_2 (*This fits the evolution of gases kinetic diameters: CO_2 (3.4 Å) < N_2 (3.6Å) < CH_4 (3.8Å))* [7]. In fact, the diffusion selectivity in an IL membrane can be expressed as follows:

$$\boldsymbol{\alpha_{1,2}\,(diffusivity)} \approx \left(\frac{V_2}{V_1}\right) \quad 2.2$$

where $\alpha_{1,2}$ (diffusivity) is the diffusion selectivity of solute 1 vs. solute #2, V_1 is the molar volume of solute #1, and V_2 the molar volume of solute #2. Therefore, the diffusivity selectivity is proportional to the ratio of the molar volumes of the considered gases. When considering CO_2/N_2 and even CO_2/CH_4 separations, the diffusivity selectivity is close to one [7]. Thus, it is clear that there is no sense to exploit the diffusion coefficients to enhance the separation performance of SILM. However, it is important to note that the diffusivity will have a large impact on the separation rates in ILs with larger viscosities, yielding SILMs with smaller permeability.

II.2.2. Key parameters influencing the solubility coefficient of a gas in ILs

ILs are known for their high CO_2 solubility and selectivity over other light gases. In the past decade, large amount of solubility data of CO_2 in ILs has been published leading to a number of predictive thermodynamic models (e.g., *UNIFAC, RST, COSMO-based models..*), experimental methods for measuring solubility (*e.g. gravimetric method, isochoric saturation method, synthetic (bubble point) method..*) and theories about the mechanisms governing CO_2 solubility. In 2014, Lei *et al.* [21], realized a database of gas solubility (*i.e., CO_2, SO_2, N_2, etc…)* in conventional ILs. The authors provided a complete and clear information on the subject, including links between the molecular structures of ILs (or gases) and the corresponding gas solubility values. A detailed description of both the predictive models and experimental methods is also given in their review [21]. The following paragraphs are just a short overview of the key parameters influencing the CO_2, N_2, and CH_4 solubility coefficients.

Before entering the core of our research work, it is important to define the absorption phenomenon which occurs when a gas contacts a liquid and solubilizes, and to provide description of the CO_2 solubility mechanisms.

II.2.2.1. Theory

As reported in Chapter I section I.1.2, the gas absorption mechanisms can involve physical or chemical absorption. The solubility of a gas in a liquid, at a given temperature and pressure, corresponds to the concentration of the dissolved gas at the equilibrium and can be expressed according to the Raoult's law as follows:

$$\boldsymbol{p_i = p_i^*.x_i} \quad 2.3$$

with p_i is the partial vapor pressure of gas " i "above the liquid, and p_i^* is the vapor pressure of the pure gas "i". From the experimental data, the mole fraction x_i of gas "i" in the liquid is expressed as (Eq. 2.4):

$$\boldsymbol{x_i = \frac{n_i}{n_i + n_L}} \quad 2.4$$

where n_L is the amount of liquid predetermined before the experiment, and n_i is the amount of gas dissolved into liquid and calculated from the ideal law gas relation. In the cases of a non-ideal solution, for large dilutions, and for low pressures, Henry's law can be applied (eq. 2.5). The equilibrium partial pressure corresponds to the product of Henry's constant by the mole fraction of the gas solubilized:

$$\boldsymbol{p_A^* = H_a.x_A} \quad 2.5$$

Thus, comparison of Henry's constants provides an effective method for comparing the solubility of different gases in a substance (*i.e., the ideal solubility selectivity*) and allows comparison of how effective a series of materials (*such as ionic liquids*) are at dissolving those gases. Note that the Henry's constant is inversely proportional to how much gas is dissolved, when the quantity of gas absorbed increases, the Henry's law constant decreases.

To be consistent with the literature, the partial pressure, vapor pressure and Henry's law constant have been expressed in units of atm.

II.2.2.2. CO_2 solubility

a) Mechanisms

A combination of four theories has been proposed to explain the CO_2 solubility in bulk ILs: *i) the anion effect* [22], *ii) the Lewis acid-base interaction* [23], *iii) the free volume effect* [24], *and iv) the chemical interaction theory* [25]. The three first theories refer to physical absorption applied to conventional ILs while the latter concerns chemical absorption.

The *anion effect theory* supposes that anions plays a primary role in determining the CO_2 solubility, whereas the contribution of cations is secondary [26]. This theory was supported by the experimental data of Cadena and coworkers [22]. The *Lewis acid-base interaction theory* permitted to provide by ATR-IR spectroscopy a first direct indication of the effect of anions (*e.g., $[PF_6]^-$ or $[BF_4]^-$*) in the weak Lewis acid–base interactions with CO_2 molecules [23].

In contrast, another paper examined the effect of cation size while keeping the anion constant, showing that the CO_2 solubility was highly dependent on the alkyl chain length (*i.e., cation size*) in imidazolium-based ionic liquids (Figure II. 2) [12,27-30].

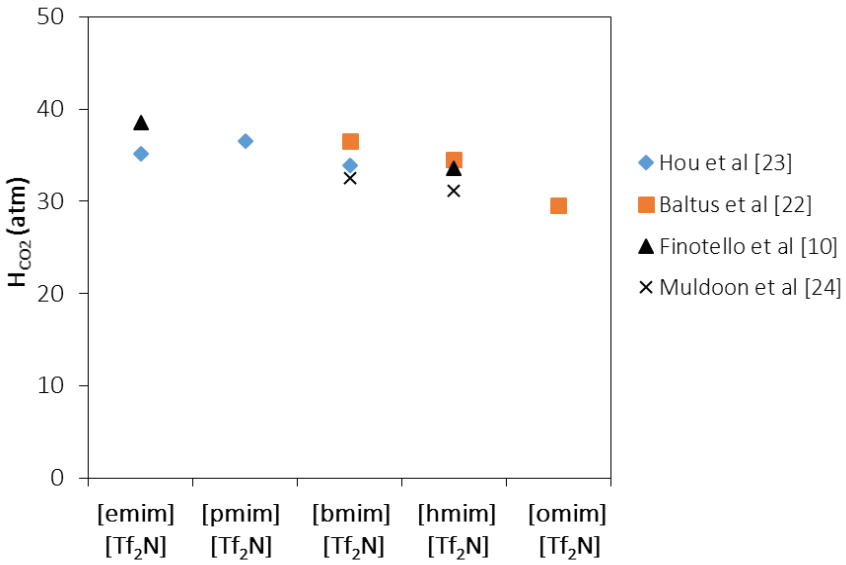

Figure II. 2. Evolution of Henry's law constant at 25°C for CO_2 solubilized in ILs with different alkyl chain lengths on the imidazolium cation.

To account for the effect of the cation, several studies have suggested that there is a free volume in the interionic space between cation and anion which could play a significant role in dissolving CO_2 [24]. In fact, according to *Hu et al.* [31], the bulk structure of ILs is nano-segregated, *i.e.,* that anions and charged imidazolium rings organize into polar domains to form a 3-dimensional ionic network, while the alkyl chains of the cations (more than three carbon atoms) tend to segregate into non polar domains. When a gas dissolves in the IL, it induces conformational rearrangements of the ions which lead to the formation of cavities in both types of domains. Thus, the fractional free volume (FFV) has been defined to express this theory by the ratio between the empty space and the occupied space in a material [32]. As shown in Eq. 2.6, the FFV is directly connected to the molar volume (V_m) and the van der Waals volume (V_{vdw}) of the IL:

$$FFV = \frac{V_m - 1.3V_{vdW}}{V_m} \quad 2.6$$

In order to explore the relationship between the CO_2 solubility and the FFV, Shannon *et al.* [24], have studied 165 actual and theoretical combinations of [$C_n$mim][X] ILs to identify a trend. They concluded that large and delocalized anions (*i.e., $[Tf_2N]^-$ or $[beti]^-$*) create a free volume which drives both CO_2 solubility and selectivity. At the opposite, free volume related to the pendant n-alkyl chains appears to reduce both CO_2 solubility and selectivity [24,25]. This theory explains the results observed when, for a given anion, the solubility changes with the alkyl chain length of the cation.

However, it also appears that the absolute values of CO_2 solubility and selectivity in ILs are highly dependent on both free volume and strength of the IL-gas interactions. More detailed simulations are still needed to characterize and quantify both the size distribution and nature of cavities comprising empty spaces [31].

Finally, with the aim to increase the CO_2 solubility of ILs, Bates *et al.* [25], realized the first example of CO_2 chemisorption by a ''task-specific'' IL (TSIL) based on the chemical reaction of CO_2 with an active sites-containing IL. This functionalized IL (1-propylamide-3-butyl imidazolium tetrafluoroborate) was composed of an amino group tethered to the imidazolium cation. This compound was able to capture 10 times more CO_2 per mole of IL under ambient pressure compared to conventional ILs (*e.g.,* as mentioned in Chapter I, the best conventional IL can reach only 0.05 mole of CO_2 per mole of IL for a partial pressure ~0.15 bar [1]). The amino group on the cation reacted with CO_2 through a carbamate

mechanism similar to the aqueous amine system, resulting in a stoichiometry of one CO_2 molecule for two amines, as shown in Figure II. 3.

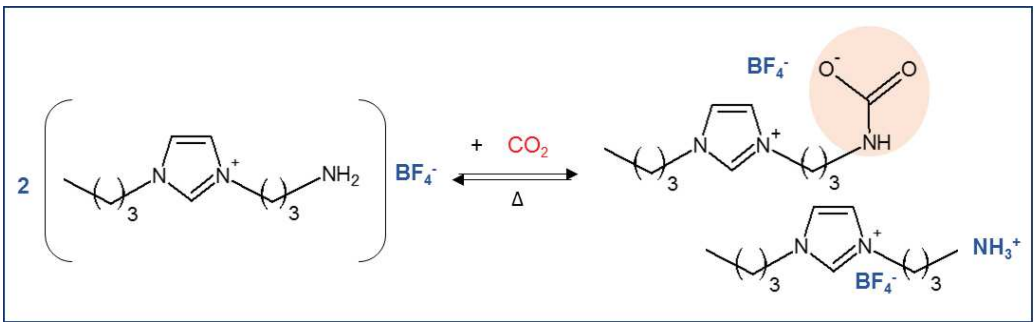

Figure II. 3. Proposed reaction scheme between an amino-functionalized IL and CO_2 (Bates *et al.* [25]).

Since the publication of this original article in 2002, many derived works were published, including strategies using other functionalized ILs such as the amino-based ILs, amino acid-based ILs, azolate-based ILs, phenolate-based ILs, and pyridine-containing ILs. A more in-depth look at the CO_2 capture by task-specific ILs is reported in the review of Cui *et al.* [33].

b) Influence of the ILs composition

In light of the research results described above, which show that the anion plays a key role in CO_2 solubility in ionic liquids, the question becomes: which anion is 'best'? The effect of the anion on CO_2 solubility has been studied experimentally by pairing the [bmim] cation with several anions as shown in Figure II. 4 [26]. The CO_2 solubility was found to increase in the following order: $[NO_3]^-$ < $[dca]^-$ < $[BF_4]^-$ ~ $[PF_6]^-$ < $[TfO]^-$ < $[Tf_2N]^-$ < $[methide]^-$.

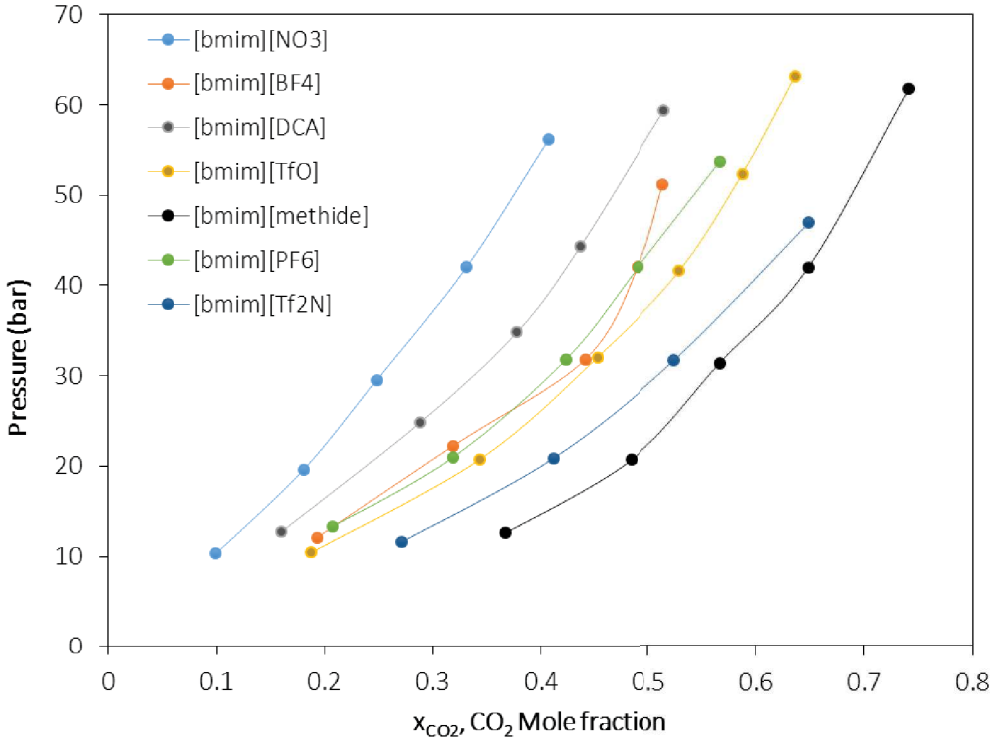

Figure II. 4. Effect of both the anion type and the pressure on the solubility of CO_2 in [bmim]-cation-based ILs at 25 °C (from Aki *et al.* [26]).

In fact, the $[Tf_2N]^-$ anion is known to yield a very high CO_2 solubility, and this anion is a common choice when designing ILs for CO_2 separation from N_2 or CH_4 [21,27,34,35]. Recently, the $[B(CN)_4]^-$ anion received particular attention because it can generate higher CO_2 solubility compared to classical ILs [36-40]. Mahurin *et al.* [36], studied the performance of SILMs containing [emim][Tf_2N] or [emim][$B(CN)_4$]. The CO_2 solubility in the latter is 30% higher than those measured in the fluorinated [emim][Tf_2N]. The same authors showed that increasing the cation alkyl chain (*e.g.,* [bmim][$B(CN)_4$]), or substituting the hydrogen in the position 2 of the imidazolium ring by a methyl (*e.g.,* [emmim][$B(CN)_4$]) yields CO_2 solubility values which are higher than those measured in [emim][$B(CN)_4$] IL [38].

It is also important to note that anions such as BF_4^- and PF_6^- are easily hydrolyzed by air moisture and generate highly toxic and corrosive HF gas [40]. Thus, such anions cannot be employed because the generated HF will promote the formation of lamellar compounds during the grafting reaction [41]. As an alternative to the toxic fluorinated anions, Wang *et al.* [43], recently proposed the use of dialkyl phosphate anions which offer higher CO_2 solubility capacity than $[BF_4]^-$, $[DCA]^-$, $[TfO]^-$, $[PF_6]^-$ anions, but does not exceed the values found for $[Tf_2N]^-$ anion as shown in Figure II. 5.

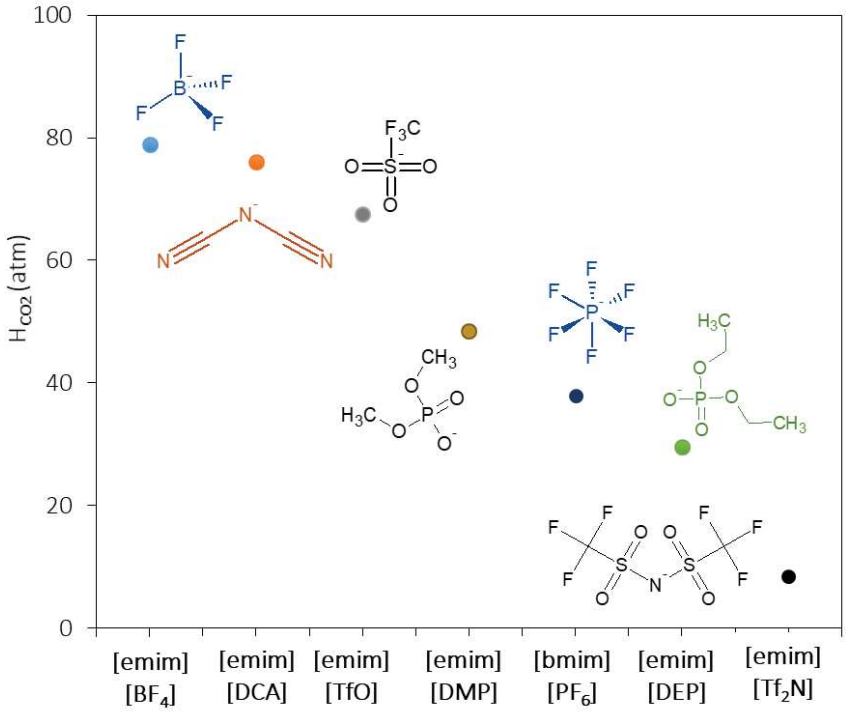

Figure II. 5. Comparison of Henry's law constant for CO_2 at 25°C (298.15 K) in different ILs with the same cation [emim], except for [bmim][PF6] (from Wang *et al.* [43]).

Many authors considered that the contribution of cations to CO_2 solubility is secondary, although the situation might change when the alkyl chain length of the cation increases (§ I.2.2.a). In the literature, most of the studies are realized on imidazolium-based ILs because imidazolium-based Ionic Liquids (RTILs) usually yield high CO_2 solubility values over a wide range of temperatures and applied pressures [27]. However, the hydrogen attached to the C_2 position (C_2-H) on the imidazolium ring is also known to be acidic. Therefore, some authors have investigated the effect of this acidity by replacing the proton at the C_2 position with a methyl group (C_2-methyl). As shown in Table II. 2, a decrease of the CO_2 solubility is observed when the proton in C_2 position is replaced: the solubility values in [bmim][PF_6] and [emim][Tf_2N] are higher than those in the corresponding substituted ILs.

One of the most common strategy used to increase the CO_2 solubility is a structural modification of ILs with various functional groups; examples are shown in Figure II. 6.

Table II. 2. Values of CO_2 Henry's law constant (H_{CO2} in atm at 25°C) for a series of imidazolium-based ILs ([a] from Cadena *et al.* [22], [b] from Hou *et al.* [29]).

Ionic liquid	H_{CO2} (atm) at 25°C
[emim][Tf_2N]	35.13[a]
[emmim][Tf_2N]	39.08[a]
[bmim][PF_6]	52.70[b]
[bmmim][PF_6]	60.99[b]

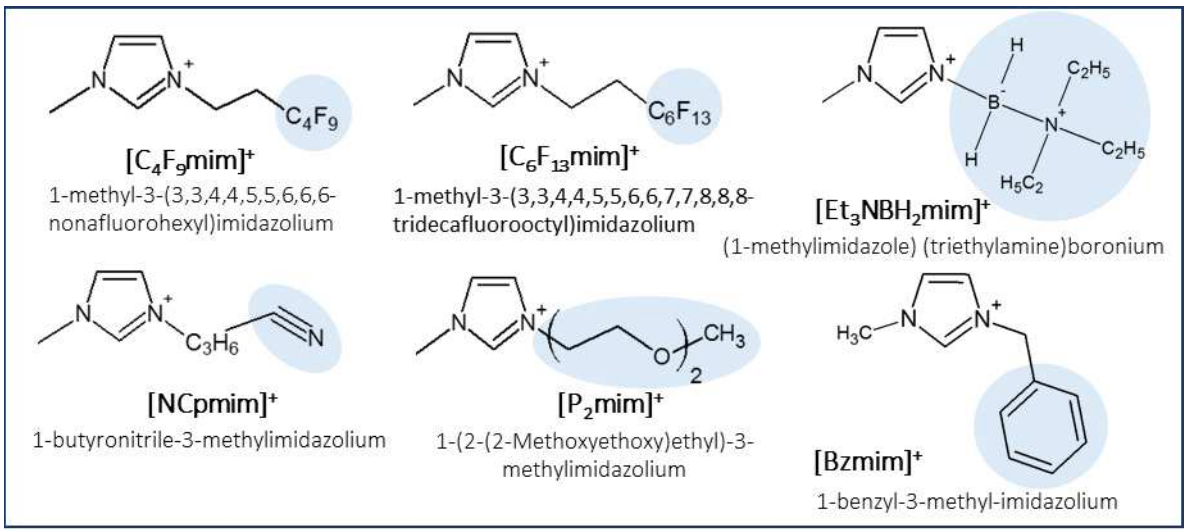

Figure II. 6. Examples of functional groups used to enhance the CO_2 solubility in ILs.

Values of CO_2 Henry's law constant at 25°C for series of functionalized imidazolium-based ILs having the same anion ([Tf_2N]) are compared in Table II. 3. The ILs with fluoroalkyl substituents [30, 44] show enhanced CO_2 solubility in comparison with their alkyl substituted analogues (*i.e.,* [$C_6H_4F_9$mim][Tf_2N]> [hmim][Tf_2N]). Bara *et al.* [16] demonstrated that ILs functionalized with an oligo(ethylene glycol) chain present CO_2/N_2 or CO_2/CH_4 selectivity values which are 30 to 75% higher than those measured for the same ILs without any functional group.

Table II. 3. Values of CO_2 Henry's law constant (H_{CO2} in atm, at 25°C) for a series of functionalized imidazolium-based ILs ([a] from Muldoon *et al.* [30], [b] from Finotello *et al.* [12], [c] from Baltus *et al.* [28], [d] from Mahurin *et al.* [36], [e] from Carlisle *et al.* [17]).

Ionic liquid	H_{CO2} (atm) at 25°C
[$C_6H_4F_9$mim][Tf_2N]	28.02[a]
[hmim][Tf_2N]	33.55[b]
[omim][Tf_2N]	29.60[c]
[Et_3NBH_2mim][Tf_2N]	32.60[a]
[Bzmim][Tf_2N]	39.37[d]
[NCpmim][Tf_2N]	47 ± 1[e]

II.2.2.3. N_2 solubility

Jacquemin *et al.* [34,35], observed that the N_2 solubility in [bmim][BF_4] and [bmim][PF_6] decreases when the temperature increases. Finotello *et al.* [12], found the opposite trend for [emim][Tf_2N], [hmim][Tf_2N], [mmim][$MeSO_4$] and [emim][BF_4] by using the semi-infinite volume method. Also, Bara *et al.*[27], reported that polar groups such as ethers, or nitriles are much more effective than hydrocarbons for the separation of CO_2 from N_2 and CH_4. The same authors showed that N_2 solubility was lower in oligo(ethylene glycol)-functionalized ILs than in the corresponding alkyl-imidazolium-based ILs [16].

II.2.2.4. CH_4 solubility

It is known that CH_4 has a higher solubility than H_2, CO, N_2, and O_2 in ILs, but much lower than CO_2. However, compared with other gaseous hydrocarbons such as ethane, propane, and butane, CH_4 is significantly less soluble in ILs [12,16]. The trend for CH_4 solubility follows the opposite trend observed for N_2. As an example, CH_4 solubility decreases when the IL is made with polar groups [12,16].

II.2.3. Conclusions

Aiming at the development of hybrid ILs-based membranes (*i.e.* GILMs) composed of functional ILs chemically grafted and nanoconfined in the pores of a ceramic support, the most suitable cations, anions, and organic spacers (functional groups) have been selected as shown in Figure II. 7. The bis(trifluoromethanesulfonimide) has been selected as an anion because it is known to be chemically stable and to solubilize the CO_2 easily. The commonly used 1-methylimidazolium was chosen as a cation and used as a reference for comparison with 1,3-dialkylimidazolium-based ILs that have already been reported for gas separation applications [7, 27]. Concerning the organic spacer between the imidazolium cation and the phosphonate coupling function, three different functional groups were chosen: a propyl chain, a dodecyl chain, and an oligo(ethylene glycol) chain.

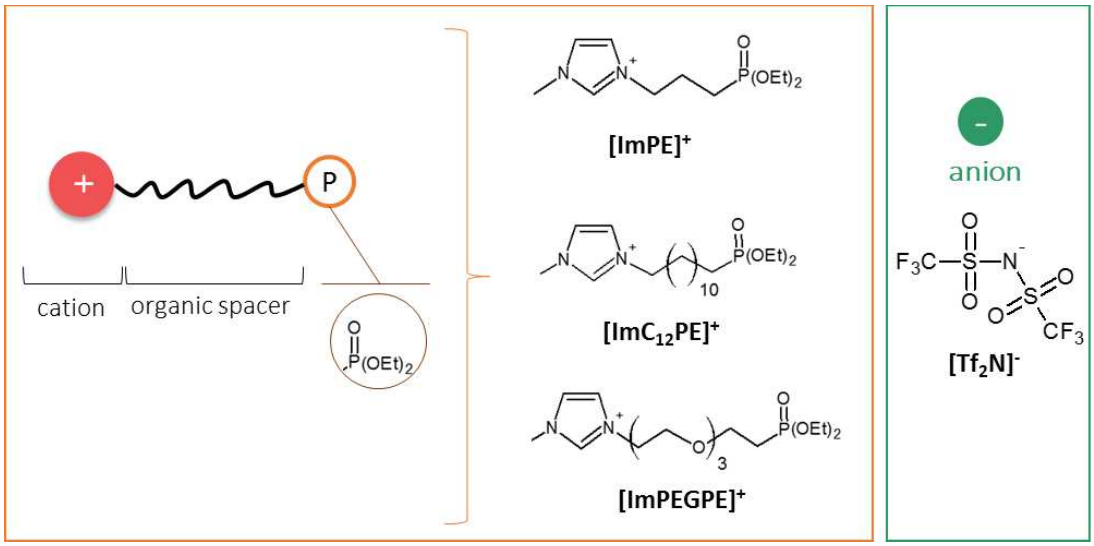

Figure II. 7. Structure of the selected cations ([ImPE]$^+$, [ImC_{12}PE]$^+$, [ImPEGPE]$^+$) and anion [Tf_2N]$^-$ for preparing the hybrid ILs-based membranes (i.e. GILMs).

II.3. Challenges in the synthesis of ILs with phosphonate coupling functions

To date, there is no report in the open literature describing the use of phosphonate-based ILs for CO_2 separation applications. Such ILs are rather employed for actinides and rare earth elements recovery processes [45,46], as solvents for U(VI) extraction [47] or as lubricants [48,49]. Several strategies can be used to introduce the phosphonic acid or ester function in the organic molecule skeleton.

Two main routes can be explored to obtain functional phosphonate-based ILs: **i)** the direct quaternization of the imidazole part using phosphonate functionalized reagents [route A] and **ii)** the coupling reactions between already prepared functionalized ILs and suitable phosphonate function precursors [route B]. Our work focused on the synthesis of [ImPE][Tf_2N] and [ImPEGPE][Tf_2N] by using respectively the 1,3-dibromopropane or the 1-Bromo-2-(2-(2-(2-bromoethoxy)ethoxy)ethoxy)ethane which are commercially available or easily synthesized. For the synthesis of [$ImC_{12}PE$][Tf_2N], a commercial diethyl (12-bromododecyl)phosphonate reagent was used.

II.3.1. Direct quaternization with phosphonate reagents [route A]

As shown in Figure II. 8, the direct quaternization reaction using phosphonate reagents can be divided into 3 steps: ***1)*** synthesis of the functional organophosphorus precursor, ***2)*** quaternization reaction yielding an imidazolium bromide IL and ***3)*** anion exchange reaction yielding the IL containing $[Tf_2N]^-$ as an anion.

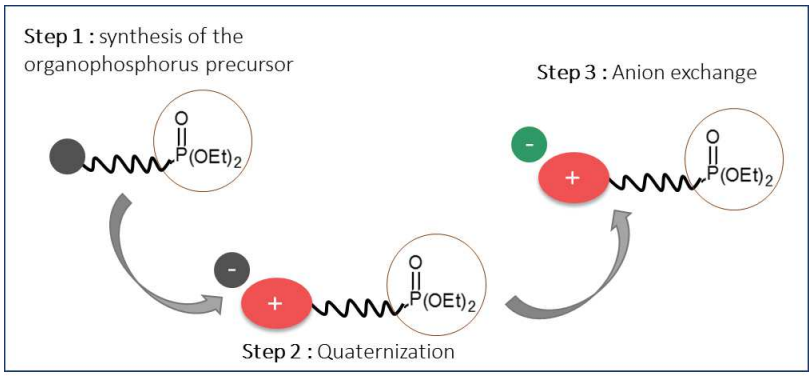

Figure II. 8. Scheme of the different steps involved in the synthesis of imidazolium-based ILs with phosphonate coupling agent using the quaternization route (route A).

Step 1: Synthesis of the organophosphorus precursor

In the case of both 1,3-dibromopropane and 1–Bromo–2–(2–(2–(2–bromoethoxy)ethoxy)ethoxy)-ethane, we used the Michaelis–Arbuzov reaction in which an alkylhalide reacts with trialkyl phosphite to form a stable P-C bond [53]. During such reaction, the phosphorus converts from trivalent to pentavalent species (Scheme II. 1).

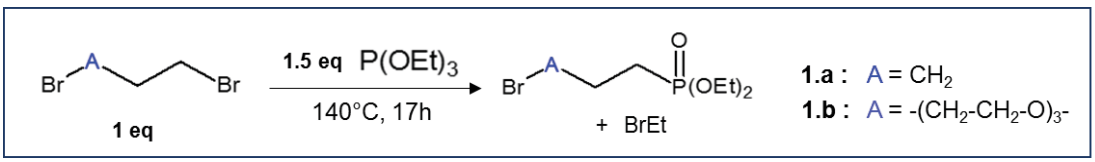

Scheme II. 1. Michaelis-Arbuzov reaction.

Using this strategy, we obtained the diethyl(3-bromopropyl)phosphonate and the diethyl 2–(2–(2–(2–bromoethoxy)ethoxy)ethoxy)ethyl phosphonate with 50% and 17% yields, respectively. The liquid state ^{31}P NMR spectra, indicate that these compounds present a singlet peak centered at 31.8 ppm and 28.6 ppm, respectively. The limited reaction yield for the diethyl(3-bromopropyl)phosphonate can be explained by the presence of 2 secondary reactions which occur in the Michaelis-Arbuzov reaction.

The first reaction is a rearrangement of the triethyl phosphite at elevated temperature, yielding the diethyl ethylphosphonate (Mechanism II. 1) [53].

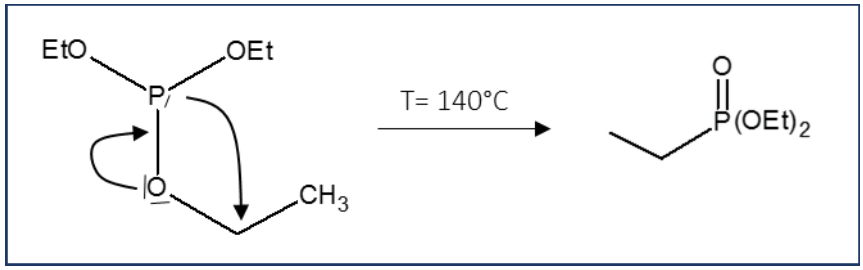

Mechanism II. 1. Mechanism of the triethyl phosphite rearrangement at elevated temperature.

The second one consist of a cyclization of the organophosphorus expected compound following the mechanism described below to afford the 1,2-oxaphospholane (see Mechanism II. 2.) [54].

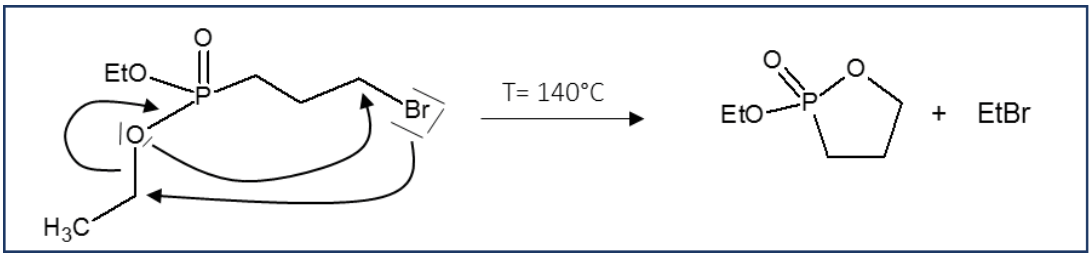

Mechanism II. 2. Cyclization of the diethyl(3-bromopropyl)phosphonate.

The 17% yield obtained for the diethyl 2–(2–(2–(2–bromoethoxy)ethoxy)ethoxy)ethylphosphonate is due to the product loss during the multiple purification steps, cumulating with the possible occurrence of the above mentioned secondary reactions.

Another option (not used) for the synthesis of those compounds is the Michaelis-Becker reaction, using a secondary phosphite as a reagent (Scheme II. 2). This synthesis protocol, used by Balczewski *et al.* [55], allows working in soft reaction conditions. In this reaction, sodium hydride reacts with diethylphosphite to form an intermediary diethylphosphite sodium salt which reacts with an alkyl halide precursor.

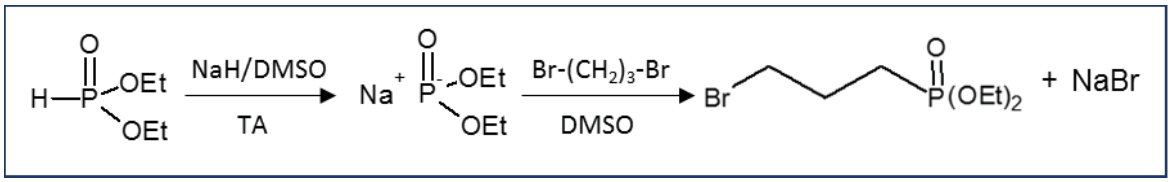

Scheme II. 2. Michaelis-Becker reaction.

Step 2: Quaternization reaction

The quaternization of 1-alkylimidazole with haloalkanes has already been largely discussed. In general, the reaction may be carried out by heating a mixture of chloroalkane, bromoalkane, or iodoalkane, with 1-alkylimidazole compounds [50]. The reaction parameters (temperature and time) are very dependent on the haloalkane type as expected for nucleophilic substitution reactions. As an example, the complete quaternization of 1-methylimidazole with 3-chlorobutane typically required 2 days at 80°C [51], 1 day at 70°C with 3-bromobutane [52].

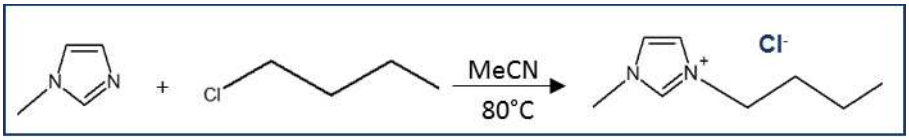

Figure II. 9: Synthesis of 1-methyl-3-butylimidazolium chloride.

The reaction can be achieved without any solvent because the reagents are usually miscible liquids, while the produced ILs are usually immiscible. Furthermore, ILs are mostly denser than solvents, so a decantation step can be realized to remove both the excess of solvent and reactants. A washing treatment or vacuum is useful to ensure that all the starting products residues are removed.

Mu *et al.* [48,56] and Rout *et al.* [46], separately reported the synthesis of phosphoryl-based ILs containing short side chains (C_2 to C_3) via nucleophilic substitution of 1-alkylimidazole with diethyl bromoalkylphosphonates between 80 and 100°C, in 24–40 h and without any solvent. For the synthesis of [ImPE][Br], we used soft reaction conditions. The quaternization was realized in THF at 70°C for 3 days. A washing treatment was necessary to remove the excess of reactants. By using this soft synthesis protocol, we obtained a 88% yield. Furthermore, the syntheses of both [ImC_{12}PE][Br] and [ImPEGPE][Br] were realized in the conditions described by Rout *et al.* [46] with slight modifications. The reaction kinetic was followed using ^{1}H liquid NMR and allowed to reduce the synthesis duration to only 1h at 100°C. In the case of [ImC_{12}PE][Br], a final distillation step under reduced pressure was necessary to remove any impurities and to obtain the IL with a 89% yield. At the opposite, [ImPEGPE][Br] was obtained without any purification step with a 99% yield.

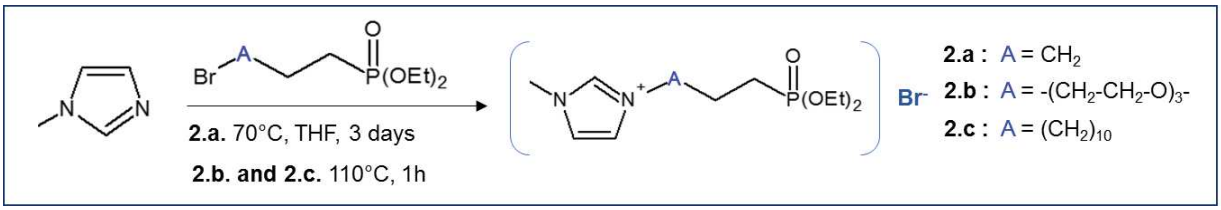

Scheme II. 3. Quaternization reactions leading to [ImPE][Br], [imC_{12}PE][Br] and [ImPEGPE][Br] compounds.

Step 3: Anionic exchange

The anion modification is commonly the last reaction step and consists of an anion exchange. This transformation can be carried out by direct treatment of the imidazolium salt with a Lewis acid (*e.g., $AlCl_3.6H_2O$*), leading to the formation of a metal counter ion (*e.g., $AlCl_4^-$*). In our work, we used the metathesis exchange reaction of anions (Figure II. 10) [12] which is adapted to commercial salts such as lithium bis(trifluoromethanesulfonimide). This reaction leads to the desired ILs with both high yield and high purity.

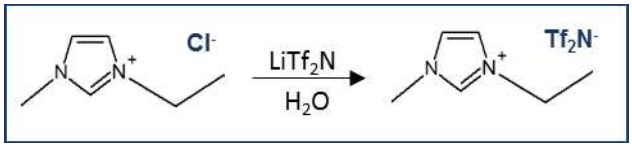

Figure II. 10: Synthesis of 1-methyl-3-ethylimidazolium bis(trifluoromethanesulfonimide).

Concerning the anionic exchange reaction, Rout *et al.* [46] added a pre-cooled aqueous solution of $LiNTf_2$ to an aqueous solution of [ImPE][Br] at 25°C. The mixture was stirred overnight and the bottom IL layer was separated then washed several times with water. When applying this protocol to different ILs issued from the quaternization, anion-exchanged ILs with an average yield of 70% were obtained.

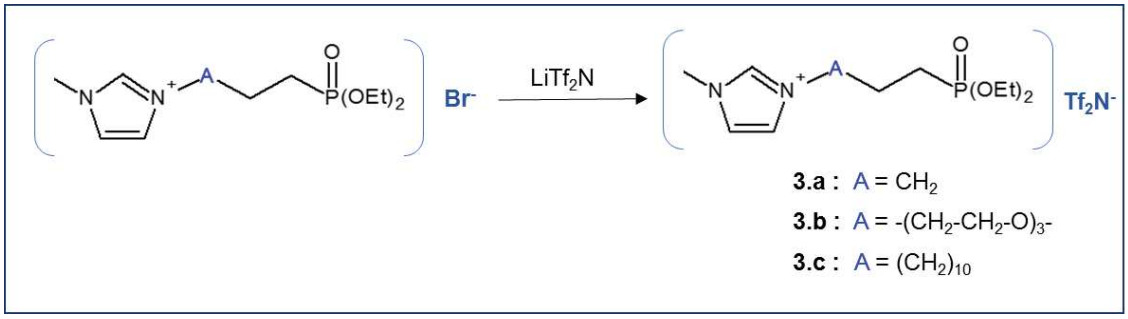

Scheme II. 4. Metathesis reaction leading to the formation of [ImPE][Tf_2N], [imC_{12}PE][Tf_2N] and [ImPEGPE][Tf_2N].

II.3.2. Coupling of reactions using suitable functionalized reagents with an already prepared IL [route B]

As for the first route, the process can be divided into 3 steps: ***1)*** quaternization reaction to obtain an -ene or -yne functionalized IL, ***2)*** anion exchange to obtain an $[Tf_2N]^-$ exchanged IL and ***3)*** a coupling reaction to introduce the phosphonate function.

For example, Braun *et al.* [57] reported the synthesis of a serie of novel phosphonyl containing ILs with Tf_2N^- anion. By using the Pudovic "click" reaction with $Mn(OAc)_2$ as a catalyst, the authors obtained the expected ILs in good yields without futher purification/work up procedure and solvent-free conditions. The produced ILs showed a great potential for use in the calcium separation/extract process (*e.g.* decalcification of crude oil) and also for the development of synthetic bone-seeking compounds with calcium anti-resorptive and mineralization properties. However, even if ILs bearing -ene or -yne function are commercially available, they are still highly expensive.

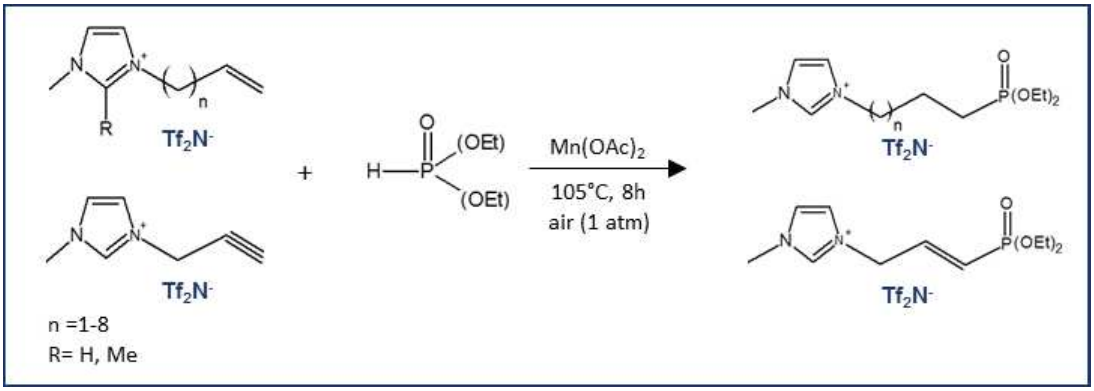

Figure II. 11: Aerobic hydrophosphonylation of various -ene and -yne bearing ILs catalyzed by $Mn(OAc)_2$ to form the phosphonyl functionalized ionic liquids (from Braun *et al.* [57]).

II.3.3. Conclusion

As a conclusion, the route B could be an interesting alternative to route A, but the overall synthesis yield of the reaction was not provided by the authors. A yield of 87% was reported for the last reaction step for [ImPE][Tf_2N] but no yield values were reported for the previous reaction steps [57]. As an indication, *Marcilla et al.*[58], reported a yield of 74 % for the synthesis of the 1-vinyl-3-ethylimidazolium bromide and Carlisle *et al.*[59], a yield of 38% for the synthesis of the 1-ethanenitrile-3-methylimidazolium bis(trifluoromethane) sulfonamide, showing that the yield is strongly affected by the functional groups or by anionic exchange. Thus, more information is required before considering this synthesis route.

By using the route A, we have been able to realize a series of imidazolium-based phosphonate ILs: [ImPE][Tf_2N], [ImPEGPE][Tf_2N] and [ImC_{12}PE][Tf_2N]. The yields reported in Table II. 4 were obtained. As mentioned in the section II.3.2, the low yield of step 1 is due to secondary reactions and/or product loss during the purification. Step 2 shows the best yield for the [ImPEGPE][Br] IL, certainly due to the complete reaction of the reactant and the absence of purification step. Finally, a yield of 70% is obtained at step 3 for all the ILs, certainly due to loss of products during the subsequent aqueous washing step and extraction. This observation can be rationalized by the fact that ILs bearing a phosphonate function are more readily water soluble than their imidazolium alkyl analogue due to the H-bond formation capability of phosphonate group. The overall reaction yield is low for both [ImPE][Tf_2N] and [ImPEGPE][Tf_2N] ILs.

Table II. 4. Reaction yields obtained at each step of the synthesis of [ImPE][Tf_2N], [ImPEGPE][Tf_2N] and [ImC_{12}PE][Tf_2N] ([a.] from [57]).

	ILs	Step 1	Step 2	Step 3	Overall yield
Route A	[ImPE][Tf_2N]	40%	88%	70%	25%
	[ImPEGPE][Tf_2N]	17%	99%	74%	12%
	[ImC_{12}PE][Tf_2N]	/	88.5%	70%	62%
Route B	[ImPE][Tf_2N]	/	/	87%[a]	/

II.4. Single-Gas Solubilities and derived Ideal Solubility Selectivities.

As mentioned in the introduction, it is possible to predict the efficiency of a given IL-derived membrane for the selective transport of CO_2 by using the experimental values of both the solubility and diffusivity coefficients of single gases in the bulk IL. In this section, an investigation of the gas sorption properties of phosphonate-based ILs has been realized because gas solubility plays a more important role than the diffusivity in determining the CO_2/N_2 or CO_2/CH_4 selectivity values in SILMs. The solubility of singles gases (CO_2, N_2 and CH_4) at 20, 30 and 40°C were measured and the solubility selectivity was estimated from these measurements. In order to compare with data for conventional-ILs, [bmim][Tf_2N], [P_3mim][Tf_2N] and [decmim][Tf_2N] were selected as analogues (see Figure II. 12). When no data were available, [emim][Tf_2N] and/or [hmim][Tf_2N] were used to allow comparison with the literature.

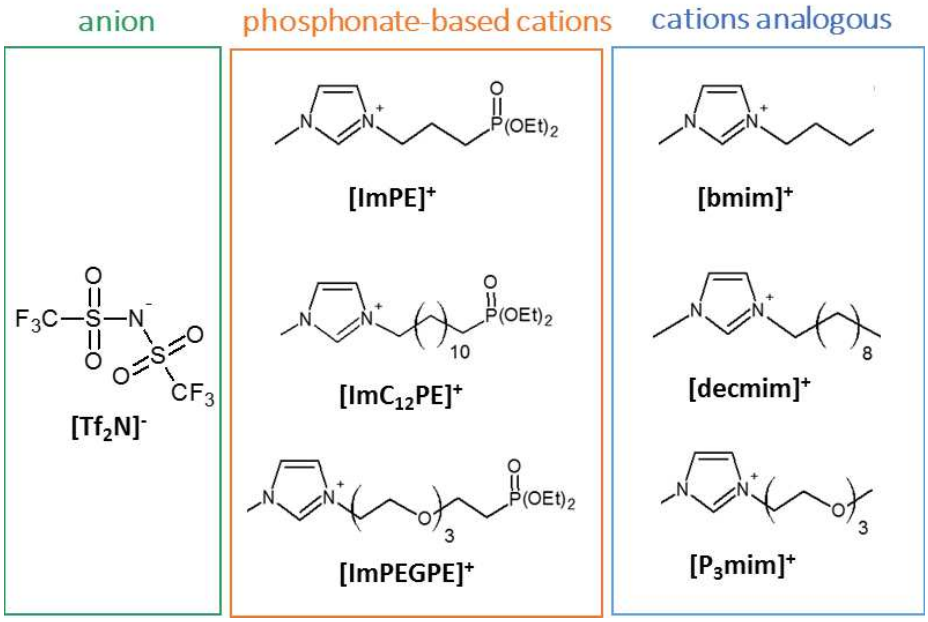

Figure II. 12. Structure of the phosphonate-based ILs and analogues ILs described in this section.

II.4.1. Principle of gas solubility measurements

Inspired by the experimental set-up developed by R. Noble and co-workers [16], we developed a system capable of measuring single-gas solubility using the isochoric saturation method. Details about the experimental system and protocols are given in the "Experimental & Modeling" section at the end of Chapter II. In brief, the measurement principle involves the contact between given amounts of gas with the outgazed liquid contained in a closed cell at a constant temperature. As time goes, the system pressure first decreases and then stabilizes. When the equilibrium is reached, the maximum quantity (*n*) of gas absorbed in the IL can thus be determined by the following equation:

$$\boldsymbol{n_{gas\ aborbed}} = \frac{\boldsymbol{\Delta P.V_{cell}}}{\boldsymbol{R.T}} \qquad 2.7$$

with ΔP (atm) the pressure difference in the cell between the beginning of the experiment and the equilibrium state, V_{cell}(L) the volume of the empty cell (IL volume subtracted), T(K) the temperature, and R (L.atm.mol^{-1}.K^{-1}) the ideal gas law constant. As reported by Lei *et al.* [19], we assumed that no volume expansion occurs, that is, the volume of the saturated solution is equal to that of the pure IL.

The mole fraction of solubilized gas (x_{gas}) can be then calculated by Eq. 2.8:

$$\boldsymbol{x_{gas}} = \frac{\boldsymbol{n_{gas\ absorbed}}}{\boldsymbol{n_{gas\ absorbed} + n_{IL}}} \quad 2.8$$

where n_{IL} is the amount of IL (predetermined before the experiment) and $n_{gas\ absorbed}$ is the amount of gas dissolved into the IL, calculated from the ideal gas law.

The mole fraction of gas dissolved in the IL (x_{gas}) and the final pressure P_{final} (in atm) recorded in the cell was used to calculate the Henry constant H (atm) using Eq. 2.9:

$$\boldsymbol{H} = \frac{\boldsymbol{P_{final}}}{\boldsymbol{x_{gas}}} \quad 2.9$$

However, the CO_2 solubility should not be evaluated only by the gas mole fraction because of the strong impact of the molecular weight (molar volume). When considering IL applications, it is often recommended to analyze the solubility either per volume of solvent (molarity) or on a molality basis [17]. Thus, the gas solubility S_{gas} (mol.L^{-1}.atm^{-1}) was determined by using the amount of gas dissolved ($n_{gas\ absorbed}$), the IL volume used (V_{IL}), and the final pressure (P_{final}):

$$\boldsymbol{S_{gas}} = \frac{\boldsymbol{n_{gas\ absorbed}}}{\boldsymbol{V_{IL}.\ P_{final}}} \quad 2.10$$

The volume of IL used is determined by using the volumetric mass density of the compound. The relative volumetric mass densities of the phosphonate-based ILs were measured with a pycnometer at controlled temperature and humidity level. The observed volumetric mass density (ρ) and molecular weight for all ILs are provided in Table II. 5. As observed, each phosphonate-based IL has a density value which is in the same range than the analogous imidazolium-based IL.

Table II. 5. Physical properties of the ionic liquids used in this study (data at 22°C) (* Bara *et al.*[16]).

Ionic liquid	ρ (g.cm^{-3})	MM (g.mol^{-1})
[ImPE][Tf_2N]	1.48	541.43
[ImPEGPE][Tf_2N]	1.40	645.29
[ImC_{12}PE][Tf_2N]	1.47	667.30
[bmim][Tf_2N]	1.43*	419.37
[P_3mim][Tf_2N]	1.43*	509.44
[decmim][Tf_2N]	1.27*	503.53

II.4.2. Results and Discussion

Table II. 6 summarizes the measured ideal gas solubilities, the Henry constants (*H(atm)*), and the molar gas fraction, for CO_2, and N_2, at 20, 30, and 40°C for the phosphonate-based ILs developed (*i.e. respectively [ImPE][Tf_2N], [ImPEGPE][Tf_2N], [ImC_{12}PE][Tf_2N]*). The CH_4 solubility was measured only for [ImPE][Tf_2N] and [ImC_{12}PE][Tf_2N] at 30 °C for the first IL and 30°C then 40°C for the second.

Table II. 6. Henry constants, gas solubility and molar gas fraction for [ImPE][Tf_2N], [ImPEGPE][Tf_2N] and [ImC_{12}PE][Tf_2N]([a] from reference [14], [b] from reference [16]).

Ionic liquid	gas	T(°C)	H (atm)	S_{gas} (mol.L^{-1}.atm^{-1})	x_{gas} (10^{-2})
[ImPE][Tf_2N]	CO_2	20	24.3 ± 0.4	0.12 ± 0.002	4.52 ± 0.08
		30	37.5 ± 2.4	0.08 ± 0.05	3.49 ± 0.56
		40	41.2 ± 0.8	0.066 ± 0.002	2.73 ± 0.07
	N_2	20	528 ± 17	0.0052 ± 0.0002	0.22 ± 0.02
		30	520 ± 26	0.006 ± 0.001	0.25 ± 0.01
		40	857 ± 106	0.004 ± 0.001	0.26 ± 0.01
	CH_4	30	233 ± 57	0.012 ± 0.003	0.59 ± 0.13
[ImPEGPE][Tf_2N]	CO_2	20	32.2 ± 0.6	0.120 ± 0.002	4.16 ± 0.01
		30	45. ± 10.3	0.083 ± 0.016	2.76 ± 0.37
		40	56.2 ± 1.4	0.066 ± 0.002	2.19 ± 0.6
	N_2	20	258 ± 87	0.015 ± 0.005	0.35 ± 0.24
		30	239 ± 9	0.015 ± 0.001	0.60 ± 0.10
		40	880± 74	0.004 ± 0.0003	0.15 ± 0.02
[ImC_{12}PE][Tf_2N]	CO_2	20	23.2 ± 1.5	0.095 ± 0.003	5.0 ± 0.15
		30	31.9 ± 1.8	0.072 ± 0.004	3.68 ± 0.19
		40	37.2 ± 0.8	0.061 ± 0.001	3.61 ± 0.15
	N_2	20	1230 ± 88	0.0017 ± 0.0001	0.10 ± 0.01
		30	1101 ± 59	0.0020 ± 0.0001	0.150 ± 0.004
		40	655 ± 102	0.003 ± 0.001	0.27 ± 0.03
	CH_4	30	167 ± 18	0.013 ± 0.001	0.83 ± 0.09
		40	231 ± 28	0.009 ± 0.001	0.61 ± 0.07
[emim][Tf_2N][a]	CO_2	25	35.9 ± 0.5	0.110	-
		40	47.6 ± 0.7	0.082	-
	N_2	40	1160 ± 83	-	-
[decmim][Tf_2N][a]	CO_2	25	29.0 ± 0.5	0.090	-
		40	37.0 ± 0.6	0.073	-
[P_3mim][Tf_2N][b]	CO_2	40	37.3 ± 1.0	0.076	-
	N_2	40	1240 ± 40	-	-

As expected the absorption process is exothermic, i.e., the relative amount of CO_2 absorbed per amount and per volume of phosphonate-based ILs decreases as the temperature increases. As shown in Figure II. 13. A., these results follow similar trends to those observed for [emim][Tf_2N], [decmim][Tf_2N] and [P_3mim]. Specifically, [ImC_{12}PE][Tf_2N] and [ImPEGPE][Tf_2N] present a diminution of 16.5% and 13% in CO_2 solubility (mol.L^{-1}.atm^{-1}) at 40°C compared to their corresponding analogues [decmim][Tf_2N] and [P_3mim][Tf_2N]. However, the situation is different at 20°C. For example, the CO_2 solubility of [ImC_{12}PE][Tf_2N] is 5% (mol.L^{-1}.atm^{-1}) higher than the CO_2 solubility of [decmim][Tf_2N] at 25°C. Thus, these first results suggest that the CO_2 solubility properties of the phosphonate-based ILs are more attractive at low temperature.

Concerning the N_2 solubility, the amount of gas dissolved is significantly higher in [ImPEGPE][Tf_2N] compared to [ImPE][Tf_2N] and [$ImC_{12}PE$][Tf_2N]. The N_2 Henry constants measured for the phosphonate-based ILs are low in comparison with those of [emim][Tf_2N] and [P_3mim][Tf_2N] ILs, indicating that significantly higher number of N_2 moles are dissolved in the studied phosphonyl ILs. Nevertheless, the N_2 solubility is still low compared to the CO_2 solubility and remains nearly constant when the temperature increases.

Regarding the CH_4 solubility, the same value was obtained at 30°C for both [ImPE][Tf_2N] and [$ImC_{12}PE$][Tf_2N]. The values reveal relatively high absorption of CH_4 compared to conventional ILs, suggesting that the phosphonate-based ILs are not good candidates for the CO_2/CH_4 separation (*e.g., H_{CH4} of [hmim][Tf_2N] is 350 atm at 25°C, and 233 atm for [ImPE][Tf_2N]*). In the case of [ImPEGPE][Tf_2N], no reproducible results were obtained.

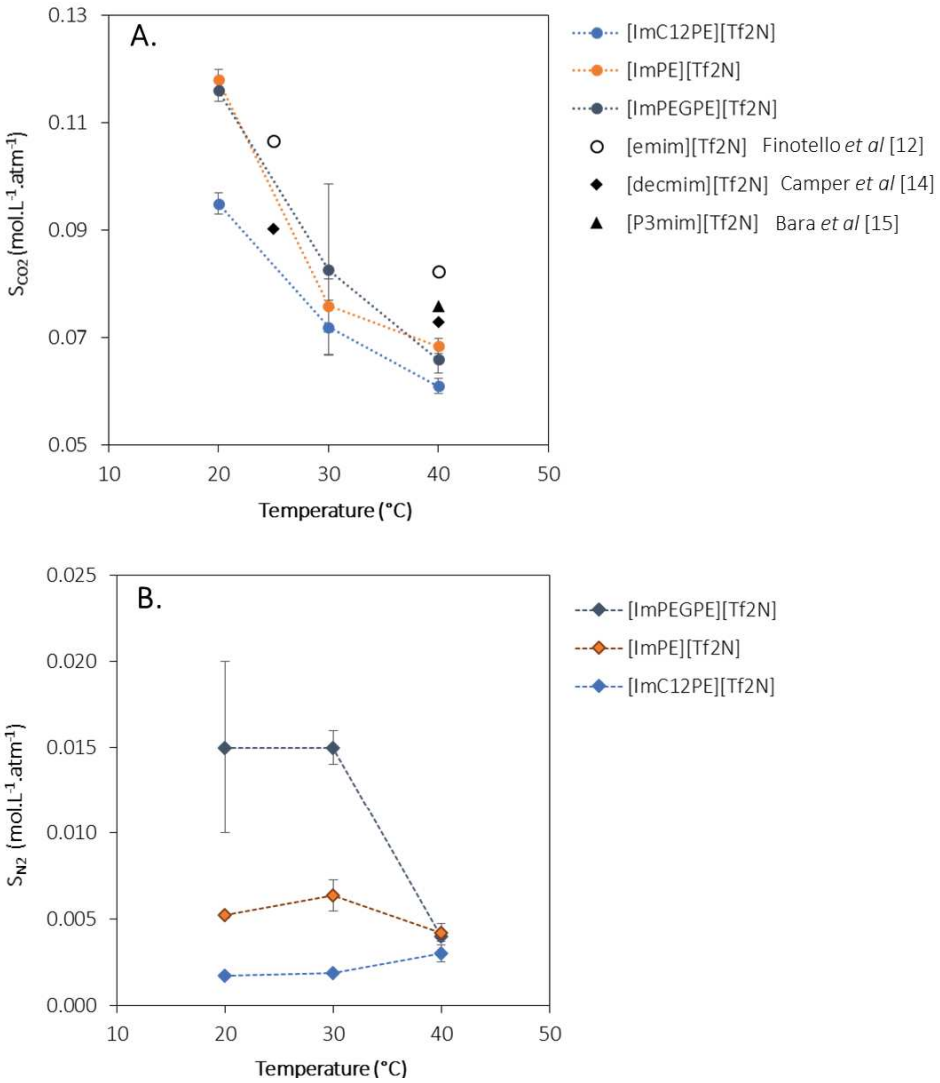

Figure II. 13. Evolution of **A.** CO_2 solubility, and **B.** N_2 solubility, vs. temperature.

Solubility measurements were used to estimate the ideal solubility selectivities (Table II. 7) of the phosphonate-based IL, by calculating the ratio of S_{CO2}, (i.e., solubility of CO_2) and S_j, (i.e., solubility of either N_2 or CH_4). Table II. 7 and Figure II. 14 makes it obvious that, at high temperatures, the ideal S_{CO2}/S_{N2} selectivity of all the ionic liquids converge to a value in the range 16-23 (*except [P_3mim][Tf_2N] which is out of the trend with a higher value at ~33*). At the opposite, at 20°C [$ImC_{12}PE$][Tf_2N] displays a

S_{CO2}/S_{N2} selectivity of 55 ± 5, which is the highest value observed among all the tested samples. This result is in contrast to the [$C_x$mim][Tf_2N] family of ILs, where the cation with the shortest chain length, [emim][Tf_2N] has the lowest CO_2 solubility and the highest CO_2/N_2 selectivity [14]. In the phosphonate family studied here, it is the longest chain analogue ([$ImC_{12}PE$][Tf_2N]) that provides the highest CO_2/N_2 solubility selectivity. At the opposite, the CO_2/CH_4 solubility selectivity is very close to the value reported for [hmim]|Tf_2N] in the literature (S_{CO2}/S_{CH4} =10 at 25°C) [12]. Therefore, these results of ideal solubility selectivities shows that a CO_2/N_2 gas separation processes using the [ImPE][Tf_2N] and [$ImC_{12}PE$][Tf_2N] ILs will be most effective at ambient or lower temperatures. As suspected, the phosphonate-based ILs are not efficient to separate CO_2 from CH_4.

Table II. 7. Evolution of the CO_2/N_2 and CO_2/CH_4 ideal solubility selectivity vs. temperature for a series of ILs ([a] from reference [14], [b] from reference [15]).

S_{CO2}/S_X	S_{CO2}/S_{N2}			S_{CO2}/S_{CH4}	
Temperature (°C)	**20**	**30**	**40**	**30**	**40**
[ImPE][Tf_2N]	23 ± 1.1	12 ± 2	16 ± 2	6 ± 1	6 ± 1
[$ImC_{12}PE$][Tf_2N]	55 ± 5	38 ± 4	20 ± 2	6 ± 0.2	-
[ImPEGPE][Tf_2N]	8 ± 2.7	6 ± 1.4	17 ± 1.9	-	-
Temperature (°C)	**25**		**40**	**25**	**40**
[emim][Tf_2N][a]	36		22	15	12
[bmim][Tf_2N][b]	-		23	-	11
[decmim][Tf_2N][b]	-		18	-	8
[P_3mim][Tf_2N][b]	-		33	-	12

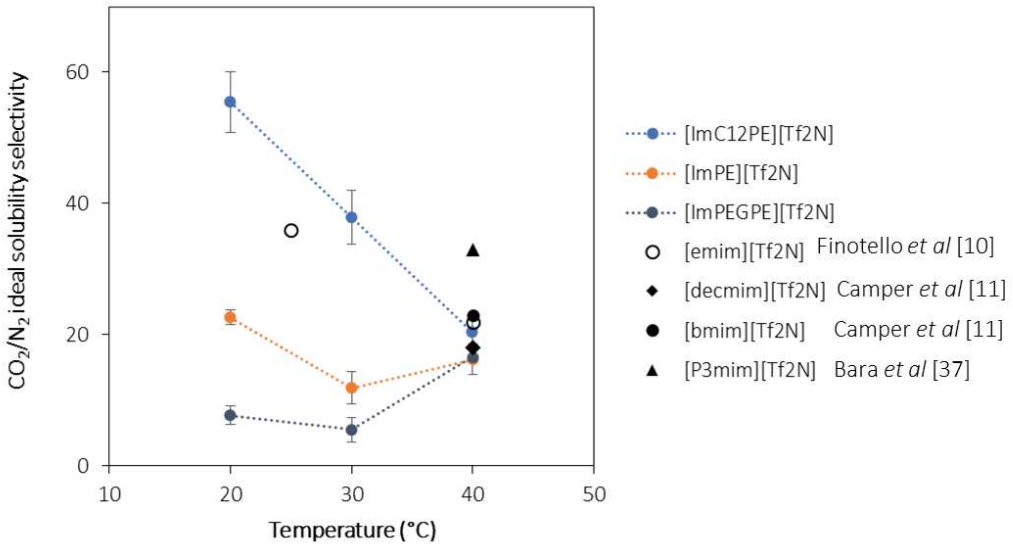

Figure II. 14. Evolution of CO_2/N_2 ideal solubility selectivity vs. temperature for a series of ILs.

To understand the evolution of CO_2 solubility results at 20°C and 40°C, we have sought to estimate the free volume within the ILs, which is often considered as the underlying property driving both gas solubility and selectivity (see section I.2.2) [24,27,32]. From the study published by Shannon *et al.* [24], we were able to calculate the free volumes V_f ($cm^3.mol^{-1}$) of the phosphonate-based ILs with the aim to compare with their conventional ILs counterpart. Calculation details are reported in the *Experimental and modeling part* of this chapter. The phosphonate-based ILs offer ~40% higher free volume in comparison with their non phoshonated analogues. As an increase of the free volume is connected with a decrease of CO_2 solubility [32], these results fit with the observed behavior of the phosphonate-based

ILs at 40°C, but not at 20°C. Thus, the sole free volume consideration cannot explain the results obtained for the solubility selectivity.

Table II. 8. Physical properties of the ionic liquids used in this study (at 22°C).

Ionic liquid	ρ (g.cm^{-3})	MM (g.mol^{-1})	V_m (cm^3.mol^{-1})/100	V_f (cm^3.mol^{-1})/100
[ImPE][Tf_2N]	1.48	541.43	3.66	0.54
[ImPEGPE][Tf_2N]	1.40	645.29	4.61	0.67
[ImC_{12}PE][Tf_2N]	1.47	667.30	4.54	0.73
[bmim][Tf_2N]	1.43	419.37	2.93	0.38
[P_3mim][Tf_2N]	1.43	509.44	3.56	0.47
[decmim][Tf_2N]	1.27	503.53	3.96	0.60

Some authors suggested that the CO_2 solubility and associated selectivity could also depend on the strength of IL-gas interactions, on the size of the cavities produced upon gas dissolution and on the conformational equilibria of the ions [31]. As mentioned in section II.1, the bulk structure of ILs is considered as nano-segregated, i.e. that anions and charged imidazolium rings organize into polar domains to form a 3-dimensional ionic network, while the alkyl chains of the cations (more than three carbon atoms) tend to segregate into non polar domains. When a gas dissolves in the IL, it induces conformational rearrangements of the ions which lead to the formation of cavities in both types of domains. In order to visualize the different domains of the ILs, Bara and co-workers [24,32], used the COSMOTherm software to generate the σ-surface of the ILs. This software generates a visual representation of the conformational equilibria for [bmim][Tf_2N], [decmim][Tf_2N] and [P_3mim][Tf_2N] ILs as shown in Figure II. 15. The individual charges and charge distribution in the molecules are optimized to minimize the system energy. Knowing the polarity distribution of the [$C_x$mim][Tf_2N] ILs family, Horne *et al.*[32], were able to link the free volumes to the conformational equlibria of the ions and to the CO_2 solubility in the corresponding ILs.

To obtain the conformation equilibria of the phosphonate-based ILs developed in the present study and visualized the polar/non polar domains, we employed the quantum chemical DFT method which offers a good compromise between the required computational effort and results reliability. The structure of the phosphonate-based ILs was calculated at B3LYP level on the basis of the work of Buijs *et al.*[62]. After calculations of the optimum molecule geometry and energy, we were able to generate for each molecule, the electrostatic potential (ESP) maps shown in Figure II. 16. For each molecule, the ESP map reveals the negative charges in red, the positive charges in blue, and the non-polar areas in green.

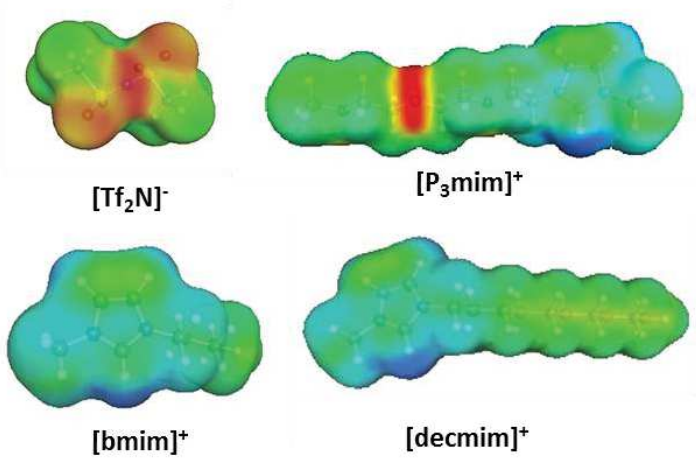

Figure II. 15. COSMOTherm σ-surfaces of the anion $[Tf_2N]^-$ and the cations $[bmim]^+$, $[P_3mim]^+$ and $[decmim]^+$. Negative charges are in red, positive charges in blue, and non-polar areas in green ($[bmim][Tf_2N]$, $[decmim][Tf_2N]$ from Ref [24] and $[P_3mim][Tf_2N]$ from Ref [32]).

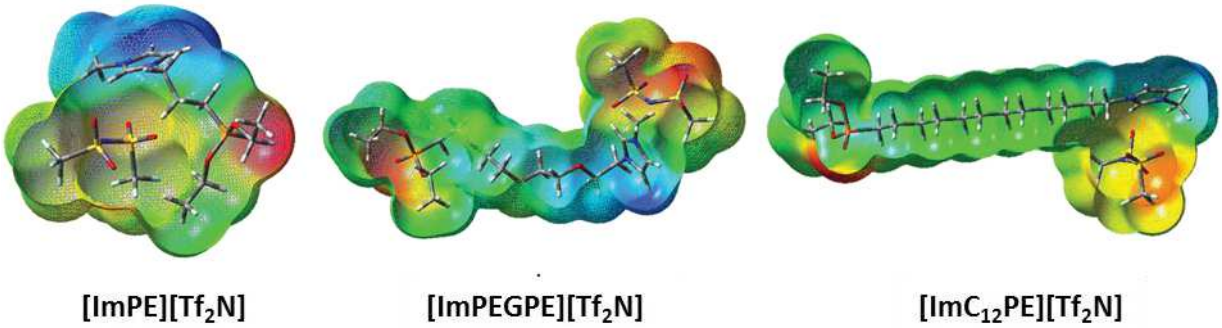

Figure II. 16 : Structure of $[ImC_3PE][Tf_2N]$, $[ImP_3PE][Tf_2N]$ and $[ImC_{12}PE][Tf_2N]$ IL molecules synthesized in the present work. The calculated electrostatic potential are projected on the van der Waals surface (negative charges in red, positive charges in blue, and non-polar areas in green). .

A comparison of the ESP maps for the three phosphonate-based IL reveals three different conformation equilibria related to the three selected organic spacers *(i.e. propyl, dodecyl and glycol chain)*. The ESP maps reveal several differences and similarity between the phosphonate-based ILs and their analogues. For example, the C_{10} chain of $[decmim][Tf_2N]$ IL and the C_{12} chain of $[ImC_{12}PE][Tf_2N]$ are fully extended but the composition of the ionic domains are different. In fact, $[ImC_{12}PE][Tf_2N]$ is composed of two ionic domains, one attributed to the cation/anion and another one corresponding to the phosphonate coupling function. The examination of the $[ImC_{12}PE][TF_2N]$ ESP map reveals also that these domains are strictly organized (ionic-nonpolar-ionic). We suppose that this special arrangement contributes to decrease the energy required for cavity formation upon gas dissolution, thus enhancing the CO_2/N_2 ideal solubility selectivity. The $[ImPE][Tf_2N]$ and $[ImPEGPE][Tf_2N]$ molecules present also an additional ionic domain linked to the coupling function. Also, like for $[P_3mim][Tf_2N]$, the $[ImPEGPE][Tf_2N]$ phosphonate-based IL is composed of ethylene glycol groups which creates additional ionic domains in the final equilibria conformation. We suppose that the arrangement of these domains in both $[ImPEGPE][Tf_2N]$ and $[ImPE][Tf_2N]$ favors the presence of cavities which increase the N_2 solubilisation.

Even if more detailed simulations are needed to characterize and quantify both the size distribution and the nature of cavities, these first results reveal the impact of the organic spacer on the IL molecule conformation and the location of the apolar and ionic domains. In addition, studies on the IL-gas interactions should be required to confirm the absence of any chemisorption phenomena between CO_2

and the phosphonate-based ILs. Finally, it should be strongly relevant, although highly tricky, to investigate how the grafting reactions of these ILs on a ceramic support (cf. Chapters 3 and 4) will modify the charge distribution and conformation of the molecules.

II.5. Diffusion coefficient

Viscosities measurements were also performed on all the phosphonate-based ILs in order to confirm that the diffusivity coefficient was low for all of them.

Another important question when considering gas transport through ILs and solubility-driven separation processes in general, is how fast the gas can diffuse through the ionic liquid. As observed in the literature, the CO_2 diffusivity could have a large impact on the permeability through SILMs composed of ILs with an important viscosity. According to Morgan *et al.*[8], the CO_2 diffusivity, $D_{CO2,bulk}$ ($cm^2.s^{-1}$), in bulk ILs can be estimated by using the following equation:

$$D_{i,bulk} = 2.66 \times 10^{-3}.\frac{1}{\mu_{IL}^{0.66}.V_{CO_2}^{1.04}} \quad 2.11$$

with μ_{IL} *(mPa.s),* the IL viscosity and V_{O2} *($cm^3.mol^{-1}$)*, the molar volume of CO_2.

The viscocity of phosphonate-based ILs were measured using a Stabinger viscosimeter at 10, 20, 30, and 40°C (Table II. 9, Figure II. 17). In Figure II. 17.A., the viscosity values of [$ImC_{12}PE$][Tf_2N] and [ImPE][Tf_2N] are compared with those of conventional IL analogues (*e.g., [emim][Tf_2N], [bmim][Tf_2N] and [decmim][Tf_2N]*). It must be noted that the viscosity of [ImPEGPE][Tf_2N] was too low to be measured. At 30°C, the viscosity of [decmim][Tf_2N] is 9 times lower than the viscosity measured for [$ImC_{12}PE$][Tf_2N]. The same trend is observed for [ImPE][Tf_2N] which is largely more viscous than [bmim][Tf_2N]. However, the CO_2 diffusion coefficient follows the opposite trend of the viscosity as shown for [emim][Tf_2N] in Figure II. 17.B. Thus, as estimated from equation **2.11,** the diffusion coefficient of CO_2 in the phosphonate-based ILs is very low.

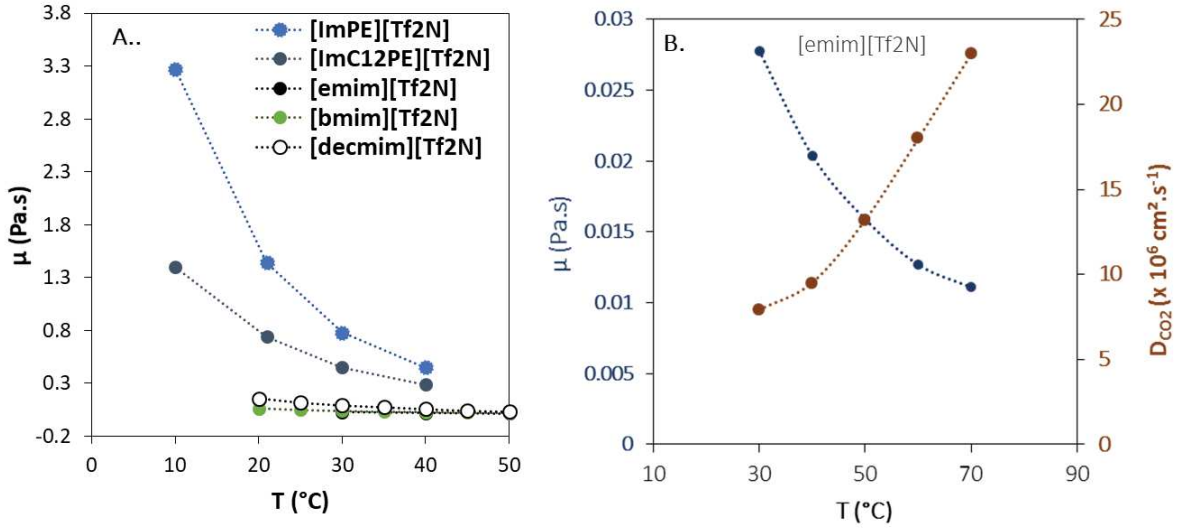

Figure II. 17. A. Evolution of the viscosity of [$ImC_{12}PE$][Tf_2N], [ImPE][Tf_2N] and a conventional IL vs. temperature. B. Comparative evolution vs. temperature of the viscosity of [emim][Tf_2N] and associated CO_2 diffusion coefficient (from [14]).

Table II. 9. Viscosity of the phosphonate-based ILs [ImPE][Tf_2N] and [$ImC_{12}PE$][Tf_2N] at different temperatures in the range 10-40°C. Diffusion coefficient of CO_2 through these ILs at 30°C (*calculated from the equation 2.11, [a] from reference [14], [b] from reference [64], [c] from reference [8]).

.	μ (Pa.s)				D_{CO2} x 10^6 ($cm^2.s^{-1}$)*
Temperature (°C)	10	20	30	40	30
[ImPE][Tf_2N]	3.27	1.44	0.78	0.45	1.3
[$ImC_{12}PE$][Tf_2N]	1.40	0.74	0.45	0.29	1.9
[emim][Tf_2N][a]	-	-	0.03[a]	0.02[a]	6.6[c]
[bmim][Tf_2N][b]	-	0.06	0.04	0.03	9.0
[decmim][Tf_2N][b]	-	0.16	0.09	0.06	5.2

II.6. Conclusions

This chapter describes the synthesis and basic characterization of a series of phosponate-based ILs with various organic spacer lengths, that will be relevant to carry out the key challenge of this PhD research work, i.e. investigate the influence of tethering and confining ionic liquids on/in porous ceramics for selective and sustainable CO_2 transport.

Basic characterization of the solubility of CO_2, N_2, and CH_4 in $[ImC_{12}PE][Tf_2N]$, $[ImPE][Tf_2N]$ was performed. The CO_2 solubility values in phosponate-based ILs were found to be lower than those of conventional IL analogues. However, these low solubility values does not impact on the CO_2/N_2 ideal solubility selectivity of $[ImC_{12}PE][Tf_2N]$ which is higher at 20°C than the values reported for most of the conventional ILs such as $[emim][Tf_2N]$.

The computational study revealed the influence of the coupling function design on the ILs polarity. We made the assumption that the well-organized equilibria conformation of $[ImC_{12}PE][Tf_2N]$ contributes to lower the energy required for cavity formation and as a result contributes to increase the CO_2/N_2 solubility selectivity for this particular IL. However, further detailed simulations and experimental studies are still needed in particular to exclude the presence of any potential chemisorption interaction between the CO_2 and the IL bulk.

Finally, the grafting reactions of these ILs on a ceramic supports will be investigated in both Chapters 3 and 4 which will certainly modify the charge distribution and conformation of the IL molecules. Modeling experiments in this area should be strongly relevant (although highly tricky) to complete this work.

References

1. M. Ramdin, T.W. De Loos, T.J.H. Vlugt, State-of-the-Art of CO_2 Capture with Ionic Liquids, *Ind. Eng. Chem. Res*., 2012, *51(24)*, 8149-8177.
2. Y. Park, K.Y.A. Lin, A.H.A. Park, C. Petit, Recent advances in anhydrous solvents for CO_2 capture: ionic liquids, switchable solvents, and nanoparticle organic hybrid materials, *Front. Energy Res.,* 2015, *3(42)*, 1-14.
3. 20 Years of Carbon Capture and Storage, OECD/IEA, 2016, 1-115.
4. B. Metz, O. Davidson, H.D. Coninck, M. Loos, L. Meyer, IPCC special report on carbon dioxide capture and storage, 2005.
5. Y. Yu, X. Lu, Q. Zhou, K. Dong, H. Yao, S. Zhang, Biodegradable Naphthenic Acid Ionic Liquids: Synthesis, Characterization, and Quantitative Structure–Biodegradation Relationship, *Chem. Eur. J*., 2008, *14(35)*, 11174-11182.
6. O. Aschenbrenner, S. Supasitmongkol, M. Taylor, P. Styring, Measurement of vapour pressures of ionic liquids and other low vapour pressure solvents, *Green Chem*., 2009, *11(8)*, 1217-1221.
7. P. Scovazzo, Determination of the upper limits, benchmarks, and critical properties for gas separations using stabilized room temperature ionic liquid membranes (SILMs) for the purpose of guiding future research, *J. Membrane. Sci.,* 2009, *343(1-2)*, 199-211.
8. D. Morgan, L. Ferguson, P. Scovazzo, Diffusivity of gases in room temperature ionic liquids: data and correlation obtained using a lag-time technique, *Ind. Eng. Chem. Res.,* 2005, *44(13),* 4815-4823.
9. L. Ferguson, P. Scovazzo, Solubility, diffusivity, and permeability of gases in phosphonium-based room temperature ionic liquids: data and correlations, *Ind. Eng. Chem. Res.,* 2007, *46(4)*, 1369-1374.
10. R. Condemarin, P. Scovazzo, Gas permeabilities, solubilities, diffusivities, and diffusivity correlations for ammonium-based room temperature ionic liquids with comparison to imidazolium and phosphonium RTIL data, *Chem. Eng. J.,* 2009, *147(1)*, 51-57.
11. J.G. Huddleston, A.E. Visser, W.M. Reichert, H.D. Willauer, G.A. Broker, R.D. Rogers, Characterization and comparison of hydrophilic and hydrophobic room-temperature ionic liquids incorporating the imidazolium cation, *Green Chem.,* 2001, *3(4),* 156-164.
12. A. Finotello, J.E. Bara, D. Camper, R.D. Noble, Room-Temperature Ionic Liquids: temperature dependence of gas solubility selectivity, *Ind. Eng. Chem. Res.,* 2008, *47(10),* 3453-3459.
13. H. Luo, G.A. Baker, S. Dai, Isothermogravimetric determination of the enthalpies of vaporization of 1-alkyl-3-methylimidazolium ionic liquids, *J. Phys. Chem. B.*, 2008, *112(33)*, 10077-10081.
14. D. Camper, J. Bara, C. Koval, R. Noble, Bulk-fluid solubility and membrane feasibility of rmim-based room-temperature ionic liquids, *Ind. Eng. Chem. Res.,* 2006, *45(18)*, 6279-6283.
15. G. Guerrero, P.H. Mutin, A. Vioux, Organically modified alumina by grafting and sol–gel processes involving phosphonate derivatives, *J. Mater. Chem.,* 2001, *11(12)*, 3161-3165.
16. J.E. Bara, C.J. Gabriel, S. Lessmann, T.K. Carlisle, A. Finotello, D.L. Gin, R.D. Noble, Enhanced CO_2 separation selectivity in oligo(ethylene glycol) functionalized room-temperature ionic liquids, *Ind. Eng. Chem. Res.,* 2007*, 46(16)*, 5380-5386.
17. T.K. Carlisle, J.E. Bara, C.J. Gabriel, R.D. Noble, D.L. Gin, Interpretation of CO_2 solubility and selectivity in nitrile-functionalized Room-Temperature Ionic Liquids using a group contribution approach, *Ind. Eng. Chem. Res.,* 2008, *47(18)*, 7005-7012.
18. P. Scovazzo, D. Havard, M. McShea, S. Mixon, D. Morgan, Long-term, continuous mixed-gas dry fed CO_2/CH_4 and CO_2/N_2 separation performance and selectivities for room temperature ionic liquid membranes, *J. Membrane. Sci*., 2009, *327(1-2)*, 41-48.

19. J.J. Close, K. Farmer, S.S. Moganty, R.E. Baltus, CO_2/N_2 separations using nanoporous alumina-supported ionic liquid membranes: Effect of the support on separation performance, *J. Membrane. Sci.,* 2012, *390-391*, 201-210.
20. B.D. Freeman, Basis of permeability/selectivity trade-off relations in polymeric gas separation membranes, *Macromolecules*, 1999, *32(2)*, 375-380.
21. Z. Lei, C. Dai, B. Chen, Gas Solubility in Ionic Liquids, *Chem. Rev*., 2014, *114(2)*, 1289-1326.
22. C. Cadena, J.L. Anthony, J.K. Shah, T.I. Morrow, J.F. Brennecke, E.J. Maginn, Why is CO_2 so soluble in imidazolium-based ionic liquids? *J. Am. Chem. Soc*., 2004, *126(16)*, 5300-5308.
23. S.G. Kazarian, B.J. Briscoe, T. Welton, Combining ionic liquids and supercritical fluids: in situ ATR-IR study of CO_2 dissolved in two ionic liquids at high pressures, *Chem. Commun.,* 2000, 2047.
24. M.S. Shannon, J.M. Tedstone, S.P.O. Danielsen, M. Michelle, S. Hindman, A.C. Irvin, J.E. Bara, Free volume as the basis of gas solubility and selectivity in imidazolium-Based Ionic Liquids, *Ind. Eng. Chem. Res*., 2012, *51(15)*, 5565-5576.
25. E.D. Bates, R.D. Mayton, I. Ntai, J.H. Davis, CO_2 capture by a Task-Specific Ionic Liquid, *J. Am. Chem. Soc*., 2002, *124(6),* 926-927.
26. N.V.K.S. Aki, B.R. Mellein, E.M. Saurer, J.F. Brennecke, High-pressure phase behavior of carbon dioxide with Imidazolium-based Ionic Liquids, *J. Phys. Chem. B.,* 2004, *108(52)*, 20355-20365.
27. J.E. Bara, T.K. Carlisle, C.J. Gabriel, D. Camper, A. Finotello, D.L. Gin, R.D. Noble, Guide to CO_2 Separations in imidazolium-based Room-temperature Ionic Liquids, *Ind. Eng. Chem. Res.,* 2009, *48(6)*, 2739-2751.
28. R.E. Baltus, B.H. Culbertson, S. Dai, H. Luo, D.W. De Paoli, Low-pressure solubility of carbon dioxide in Room-Temperature Ionic Liquids measured with a quartz crystal microbalance, *J. Phys. Chem. B.,* 2004, *108(2)*, 721-727.
29. Y. Hou, R.E. Baltus. Experimental Measurement of the Solubility and Diffusivity of CO_2 in Room-Temperature Ionic Liquids Using a Transient Thin-Liquid-Film Method, *Ind. Eng. Chem. Res.*, 2007, *46(24)*, 8166-8175.
30. M.J. Muldoon, S.N.V.K. Aki, J.L. Anderson, J.K Dixon, J.F. Brennecke, Improving carbon dioxide solubility in ionic liquids, *J. Phys. Chem. B.*, 2007, *111(30)*, 185-92.
31. Y.F. Hu, Z.C. Liu C.M. Xu, X.M. Zhang, The molecular characteristics dominating the solubility of gases in ionic liquids, *Chem. Soc. Rev*., 2011, *40*, 3802-3823.
32. W.J. Horne, M.S. Shannon, J.E. Bara, Correlating fractional free volume to CO_2 selectivity in [Rmim][Tf_2N] ionic liquids, *J. Chem. Thermodynamics.*, 2014, *77*, 190-196.
33. G. Cui, J. Wang, S. Zhang, Active chemisorption sites in functionalized ionic liquids for carbon capture, *Chem. Soc. Rev*., 2016, *45(15)*, 4307-4339.
34. J. Jacquemin, M.F. Costa Gomes, P. Husson, V.J. Majer, Solubility of carbon dioxide, ethane, methane, oxygen, nitrogen, hydrogen, argon, and carbon monoxide in 1-butyl-3-methylimidazolium tetrafluoroborate between temperatures 283 K and 343 K and at pressures close to atmospheric, *Chem. Thermodyn*., 2006, *38(4)*, 490-502.
35.J. Jacquemin, P. Husson, V. Majer, M.F.C. Gomes, Low-pressure solubilities and thermodynamics of solvation of eight gases in 1-butyl-3-methylimidazolium hexafluorophosphate, *Fluid Phase Equilib.,* 2006, *240(1)*, 87-95.
36. S.M. Mahurin, J.S. Lee, G.A. Baker, H. Luo, S. Dai, Performance of nitrile-containing anions in task-specific ionic liquids for improved CO_2/N_2 separation, *J. Membrane. Sci.,* 2010, *353(1-2)*, 177-183.
37. M.T. Mota-Martinez, M. Althuluth, M.C. Kroon, C.J. Peters, Solubility of carbon dioxide in the low-viscosity ionic liquid 1-hexyl-3-methylimidazolium tetracyanoborate, *Fluid Phase Equilibr.,* 2012, *332*, 35-39.

38. S.M. Mahurin, P.C. Hillesheim, J.S. Yeary, D.-e. Jiang, S. Dai, High CO_2 solubility, permeability and selectivity in ionic liquids with the tetracyanoborate anion, *RSC Adv*., 2012, *2*, 11813-11819.
39. R. Babarao, S. Dai, D.E. Jiang, Understanding the high solubility of CO_2 in an ionic liquid with the tetracyanoborate anion, *J. Phys. Chem. B.,* 2011, *115(32)*, 9789-9794.
40. A. Blahut, V. Dohnal, P. Vrbka, Interactions of volatile organic compounds with the ionic liquid 1-ethyl-3-methylimidazolium tetracyanoborate, *J. Chem. Thermodyn*., 2012, *47*, 100-108.
41. M.G. Freire, C.M.S.S. Neves, I.M. Marrucho, J.A.P. Coutinho, A.M. Fernandes, Hydrolysis of tetrafluoroborate and hexafluorophosphate counter ions in imidazolium-based ionic liquids, *J. Phys. Chem. A.,* 2010, *114(11)*, 3744-3749.
42. D. Medoukali, P. H. Mutin, A. Vioux, Synthesis and characterization of microporous pillared α-zirconium Phosphate-biphenylenebis(phosphonate), *J. Mater. Chem.,* 1999, *9*, 2553-2557.
43. J. Wang, C. Petit, X. Zhang, AH. A. Park, Simultaneous measurement of CO_2 sorption and swelling of phosphate-based ionic liquid, *Green Energy & Environment*., 2016, *1(3)*, 258-265.
44. D. Almantariotis, T. Gefflaut, A.A.H. Padua, J.-Y. Coxam, M.F. Costa Gomes, Effect of fluorination and size of the alkyl side-chain on the solubility of carbon dioxide in 1-alkyl-3-methylimidazolium bis(trifluoromethylsulfonyl)amide ionic liquids, *J. Phys. Chem. B*., 2010, *114(10)*, 3608-3617.
45. I.L. Odinets, E.V. Sharova, O.I. Artyshin, K.A. Lyssenko, Y.V. Nelyubina, G.V. Myasoedova, N.P. Molochnikova, E.A. Zakharchenro, Novel class of functionalized ionic liquids with grafted CMPO-moieties for actinides and rare-earth elements recovery, *Dalton Trans*., 2010, *39(17)*, 4170-4178.
46. A. Rout, K.A. Venkatesan, T.G. Srinivasan, P.R. Vasudeva Rao, Unusual extraction of plutonium(IV) from uranium(VI) and americium(III) using phosphonate based task specific ionic liquid, *Radiochim. Acta,* 2010, *98(8)*, 459-466.
47. A. Ouadi, O. Klimchuk, C. Gaillard, I. Billard, Solvent extraction of U(VI) by task-specific ionic liquids bearing phosphoryl groups, *Green Chem*., 2007, *9*, 1160-1162.
48. ZG. Mu, F. Zhou, SX. Zhang, YM. Liang, WM. Liu, Effect of the functional groups in ionic liquid molecules on the friction and wear behavior of aluminum alloy in lubricated aluminum-on-steel contact, *Tribology International.,* 2005, *38*, 725-731.
49. G. Yu, S. Yan, F. Zhou, X. Liu, W. Liu, Y. Liang, Synthesis of dicationic symmetrical and asymmetrical ionic liquids and their tribological properties as ultrathin films, *Tribology Letters*., 2007, *25(3)*, 197-205.
50. Ionic Liquids in Synthesis. Edited by Peter Wasserscheid, Thomas Welton Copyright © 2002 Wiley-VCH Verlag GmbH & Co. KGaA, Weinheirn, Germany.
51. J. Dupont, C.S. Consorti, P.A.Z. Suarez, R.F. de Souza, preparation of 1-butyl-3-methyl imidazolium-based room temperature ionic liquids, *Organic Syntheses*., 2004, *10*, 184.
52. Y-N. Li, J-Q. Wang, L-N. He, Z-Z. Yang, A-H. Liu, B.Yu, C-R. Luan, Experimental and Theoretical Studies on Imidazolium Ionic Liquids-Promoted Conversion of Fructose to 5-Hydroxymethylfurfural, *Green Chem.,* 2012, *14*, 2752-2758.
53. A. Bhattacharya, G. Thyagarajan, The Michaelis-Arbuzov rearrangement, *Chem. Rev.,* 1981, *81*, 415-430.
54. L.F. Rozko, V.V. Ragulin, E.N. Tsvetkov, *Russ. J. Gen. Chem.,* 1996, *66*, 1065-1067.
55. P. Balczewski, W.M. Pietrzykowski, A free radical approach to functionalization of phosphonates utilizing novel 2- and 3-phosphonyl radicals, *Tetrahedron*., 1996, *52(43)*, 13681-13694.
56. Z.-G. Mu, F. Zhou, S.-X. Zhang, Y.-M. Liang, W.-M. Liu, Preparation and Characterization of New Phosphonyl-Substituted Imidazolium Ionic Liquids, *Helvetica chimica acta*, 2004, *87(10)*, 2549-2555.
57. R.A. Braun, J.L. Bradfield, C.B. Henderson, N. Mobarrez, Y.Sheng, R.A. O'Brien, A. C. Stenson, J.H. Davis Jr., A. Mirjafari, Click chemistry mediated synthesis of bioinspired phosphonyl-functionalized ionic liquids, *Green Chem*., 2015, *17*, 1259-1268.

58. R. Marcilla, J. Alberto Blazquez, J. Rodriguez, J.A. Pomposo, D. Mecerreyes, Tuning the solubility of polymerized ionic liquids by simple anion-exchange reactions, *J. Polym. Sci. A Polym. Chem*., 2004, *42*, 208-212.
59. T.K. Carlisle, J.E. Bara, C.J. Gabriel, R.D. Noble, D.L. Gin, Interpretation of CO_2 solubility and selectivity in nitrile-functionalized room-temperature ionic liquids using a group contribution approach, *Ind. Eng. Chem. Res.,* 2008, *47*, 7005.
60. A.B. Butrow, J.H. Buchanan, D.E. Tevault, Vapor Pressure of Organophosphorus Nerve Agent Simulant Compounds, *J. Chem. Eng. Data*., 2009, *54(6)*, 1876-1883.
61. M.J. Earle, J. M.S.S. Esperanca, M.A. Gilea, J.N. Canongia Lopes, L.P.N. Rebelo, J.W. Magee, K.R. Seddon, J.A. Widegren, The distillation and volatility of ionic liquids, *Nature*., 2006, *439(16)*, 831-834.
62. W. Buijs, GJ. Witkamp, M. C. Kroon, Correlation between Quantumchemically Calculated LUMO Energies and the ElectrochemicalWindow of Ionic Liquids with Reduction-Resistant Anions, *International Journal of Electrochemistry*, 2012, *2012*, 1-6.
63. D. Camper, C. Becker, C. Koval, R. Noble, Diffusion and solubility measurements in room temperature ionic liquids, *Ind. Eng. Chem. Res*., 2006, *45*, 445-450.
64. M. Tariq, P.J. Carvalho, J.A.P. Coutinho, I.M. Marrucho, J.N. Canongi Lopes, L.P.N. Rebelo, Viscosity of (C_2–C_{14}) 1-alkyl-3-methylimidazolium bis(trifluoromethylsulfonyl)amide ionic liquids in an extended temperature range, *Fluid Phase Equilibria*., 2011, 22-32.

Experimental section

Organic synthesis

Starting materials

The synthesis reactions were realized under an inert atmosphere using standard schlenk line methods.

Solvents

High quality grade dichloromethane (CH_2Cl_2), pentane, methanol, acetone, ethanol and tetrahydrofuran (THF) were purchased from Sigma-Aldrich. The solvents were used as received, except for THF which was dried on a silica-alumina drying column (PureSolv- InnovativeTechnology).

Chemicals

Triethyl phosphite (98%), 1-methylimidazole (≥99%) and 2-bromoethane (≥99%) were purchased from Sigma-Aldrich and were used as received. 1,3-dibromopropane (98%) was provided by Acros Organics. The diethyl(3-bromododecyl)phosphonate (99%) was purchased from Sikemia. Lithium trifluoromethanesulfonimide (99%) was purchased from Solvionic.

Characterizations

Liquid state NMR experiments: ^{1}H, ^{13}C, ^{31}P, and ^{19}F NMR spectra were recorded using a Bruker 300 MHz NMR spectrometer at respective frequencies of 300.13, 75.42, 121.49 and 282.4 MHz, equipped with a 5 mm QNP probe. Chemical shift data were given in δ ppm and were calibrated to TMS on the basis of the relative chemical shift of the solvent as an internal standard.

Mass Spectra were measured on a Synapt G2-S mass spectrometer (Waters) by using the electrospray ionization (ESI) mode.

Elemental analyses were performed using an Elementar Vario Micro Cube instrument.

Synthesis protocols

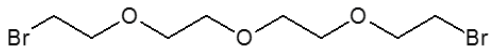

1–Bromo–2–(2–(2–(2–bromoethoxy)ethoxy)ethoxy)ethane

In a 10 L bottom flask, 857 g (4.41 mol) of tetraethylene glycol was suspended in 6 L of dichloromethane and placed in an ice bath. Then, 2.699 kg (9.70 mol) of triphenylphosphine was added under stirring. The N-bromosuccinimide addition (1.726 kg, 9.70 mol) was realized by fractions of 50 g in order to maintain the temperature below 10°C. At the end, the reaction was allowed to warm up to room temperature and stir for 2 days. The dichloromethane was removed under reduced pressure (10 mbar). The product was extracted from the by crystallization with pentane. The resulting salts were disaggregated (grind), mixed in pentane and the mixture was filtered. The desired product was obtained by evaporation of the pentane was purified from the remaining impurities over a chromatography column with 7 L of dichloromethane. After removal of the solvent under vacuum, the product was isolated as a yellow oil with a 62 % yield (850 g) and dried under vacuum overnight.

^{1}H NMR (300 MHz, $CDCl_3$, δ (ppm)) 3.84 (4H, t); 3.70 (8H, s); 3.50 (4H, t).

^{13}C NMR (75.432 MHz, $CDCl_3$, δ (ppm)): 71.64; 70.97-71.09; 30.77.

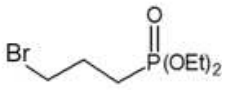

diethyl(3-bromopropyl)phosphonate

The diethyl(3-bromopropyl)phosphonate was synthesized via an Arbuzov reaction from triethyl phosphite and 1,3-dibromopropane, as described in [3]; its physicochemical constants was in good agreement with the literature data.

^{1}H NMR (300 MHz, $CDCl_3$, δ(ppm)): 4,05 (m, 4H, –PO(C*H*$_2$CH$_3$)$_2$); 3.41 (t, 2H, Br–C*H*$_2$–CH$_2$); 2.07 (m, 2H, –C*H*$_2$–CH$_2$–P); 1.80 (m, 2H, –CH$_2$–C*H*$_2$–P); 1.27 (t, 6H, –PO(CH$_2$C*H*$_3$)$_2$).

^{31}P NMR (121.442 MHz, $CDCl_3$): δ(ppm) 30.8.

Elemental analysis calculated for $H_{16}C_7O_3PBr$ (%): C (32.5); H (6.2); found: C (32.5); H (6.7).

Exact mass calculated for ESI(+), (m/z): 259.0099; found: 259.0101.

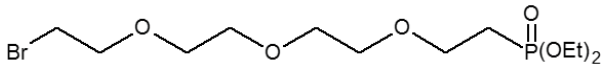

diethyl 2–(2–(2–(2–bromoethoxy)ethoxy)ethoxy)ethylphosphonate

In a 1 L three necked bottom flask, 238 g (743 mmol) of 1-Bromo-2-(2-(2-(2-bromoethoxy)ethoxy)ethoxy)-ethane was heated to 140°C. With an addition funnel, 97 g (584 mmol) of triethyl phosphite was added in 3 portions under argon. The diethyl(ethyl)phosphonate and the bromoethane generated by the reaction was evacuated by a recovery still head during all the addition of triethyl phosphite. At the end, the mixture was stirred and heated to 140°C overnight. The desired product was purified on a 3.8 L silica chromatography column, eluting first with dichloromethane then increasing the solvent polarity with methanol (Rf = 0.13, methanol 5%, $KMnNO_4$ stain used for TLC). Leftover the 1-bromo-2-(2-(2-(2-bromoethoxy)ethoxy)ethoxy)ethane (Rf = 0.80, methanol 5%, $KMnO_4$ stain used for TLC) but not the side product such as the diethyl ethylphosphonate or the bis(diethyl 2–(2–(2–(2–bromoethoxy)ethoxy)ethoxy)ethylphosphonate). A second purification process was performed on an 800 mL (1.2 m length) silica chromatography column eluting first with dichloromethane containing v/v 1% then 3% of methanol, in order to obtain the desired product as a clear liquid (Rf=0.13, methanol 5%, $KMnO_4$ stain used for TLC) (36.47 g, 16.56% yield).

^{1}H NMR (500 MHz, $CDCl_3$, δ (ppm)): 4.16 (q, $^{3}J_{H\text{-}H}$ = 7.11 Hz, 4H, OC*H*$_2$CH$_3$); 3.868 (t, 2H, BrCH$_2$C*H*$_2$); 3.79 (m, 2H, PCH$_2$C*H*$_2$); 3.74 – 3.66 (m, 8H, OCH$_2$CH$_2$O-); 3.532 (t, 2H, BrC*H*$_2$CH$_2$); 2.19 (m, 2H, PC*H*$_2$CH$_2$); 1.254 (t, 6H, OCH$_2$C*H*$_3$).

^{13}C NMR (125.721 MHz, $CDCl_3$, δ (ppm)): 71.23; 70.63 - 70.2; 65.16; 61.66, 61.61; 30.29; 26.46; 27.56; 16.42; 16.45.

^{31}P (202.404 MHz, $CDCl_3$, δ (ppm)): 28.61.

Elemental analysis calculated for $H_{26}C_{12}O_6PBr$ (%): C (38.2); H (6.90); found: C (37); H (7.1).

Exact mass calculated for ESI(+), (m/z): 377.0729; found: 377.0728.

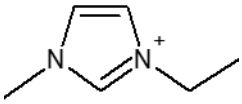

Br^-

1-methyl-3-ethyl-imidazolium bromide

The 1-methyl-3-ethyl-imidazolium bromide was obtained as a white solid in high yield by nucleophilic substitution of 1-methylimidazole with 2-bromoethane adapted from the procedure published by Finotello *et al.* [12]. The 1-bromoethane precursor (15.45 g, 142 mmol) was dissolved in 50 mL of dry THF. Then, 1-methylimidazole (10.9 g, 133 mmol) was added dropwise and the mixture was heated to reflux at 70°C during 1 day under argon. After cooling to room temperature and decanting, two phases could be distinguished as a yellow oil phase and a liquid phase. The two phases were separated and the yellow oil was washed twice with 50 mL of anhydrous diethylether leading to the precipitation of a white solid. The mixture was filtered and the precipitate washed again with 50 mL of anhydrous Et_2O. The colorless crystals produced were collected, dried under vacuum to afford **[emim][Br]** as a colorless hydroscopic solid (20.4 g, 81%)

^{1}H NMR data were consistent with published values [12].

^{1}H NMR (300 MHz, $CDCl_3$, δ(ppm)): 10.49 (s, 1H, N–C*H*–N); 7.49 (t, 2H, N–C*H*); 4.42 (q, 2H, CH_2–N); 4.13 (s, 3H,CH_3–N); 1.62 (t, 3H,–CH_2–CH_3).

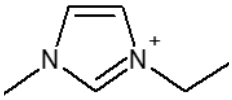

Tf_2N^-

1-methyl-3-ethyl-imidazolium bis(trifluoromethanesulfonimide)

19.2 g (100 mmol) of 1-methyl-3-ethyl-imidazolium bromide [emim][Br] were dissolved in 120 mL of distilled water. Lithium bis(trifluoromethanesulfonimide) (28.7 g, 100 mmol) was then added, and immediately a biphasic mixture is formed. The reaction mixture was stirred for 30 min, after which time the product present in the organic phase was extracted into 120 mL of CH_2Cl_2. The CH_2Cl_2 phase was washed three times with distilled water (3 x 50 mL) and extracted. CH_2Cl_2 was removed under reduced pressure (0.1 bar) at 60°C for 2h to afford 31g (80 mmol, 80%) of **[emim][Tf_2N]** as a yellow liquid.

^{1}H NMR (300 MHz, DMSO, δ(ppm)): 9.04 (s, 1H, N–C*H*–N); 7.74 (s, 1H, N–C*H*); 7.66 (s, 1H, N–C*H*); 4.19 (q, 2H, CH_2–N); 3.85 (s, 3H,CH_3–N); 1.42 (t, 3H,–CH_2–CH_3).

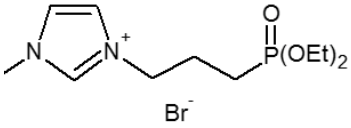

1-methyl-3-(3-(diethylphosphinyl)propyl)-imidazolium bromide

The 1-methyl-3-(3-(diethylphosphinyl)propyl)-imidazolium bromide was obtained as a yellow oil in high yield from the coupling reaction of 1-methylimidazole with diethyl(3-bromopropyl)phosphonate adapted from the procedure published by Mu *et al.* [4]. The diethyl(3-bromopropyl)phosphonate precursor (27.00 g, 107 mmol) was dissolved in 50 mL of dry THF. Then, 1-methylimidazole (8.80 g, 107 mmol) was added dropwise and the mixture was heated to reflux at 70°C during 3 days under argon. After cooling to room temperature and decanting, two phases could be distinguished as a yellow oil phase and a liquid phase. The two phases were separated and the yellow oil was washed twice with 50 mL of THF, then separated by liquid-liquid extraction with CH_2Cl_2 and H_2O. The aqueous fractions were concentrated under vacuum to afford **[ImPE][Br]** as a yellow oil with an 88% yield (32 g).

^{1}H NMR (300 MHz, $CDCl_3$, δ(ppm)): 10.53 (s, 1H, N–C*H*–N); 7.54 (s, 1H, N–C*H*); 7.36 (s, 1H, N–C*H*); 4.57 (t, 2H, CH_2–N); 4.06 (m, 4H, O–CH_2–CH_3); 4.06 (s, 3H,CH_3–N); 2.17-1.77 (m, 4H, CH_2–CH_2–P); 1.34 (t, 6H,O–CH_2–CH_3).
^{13}C NMR (75.432 MHz, $CDCl_3$, δ(ppm)): 137.5; 123.7; 122.5; 62.0; 49.3; 36.7; 23.9; 22.8; 20.9; 16.5.
^{31}P NMR (121.442 MHz, $CDCl_3$, δ(ppm)): 29.8.
Exact mass calculated for ESI(+), (m/z): 261.1368; found: 261.1367.
Exact mass calculated for ESI(-), (m/z): 78.9183; found: 78.9186.

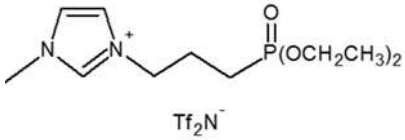

1-methyl-3-(3-(diethylphosphinyl)propyl)-imidazolium bis(trifluoromethanesulfonimide)

18.8 g (55.13 mmol) of 1-methyl-3-(3-(diethylphosphinyl)propyl)-imidazolium bromide were dissolved in 50 mL of absolute ethanol. Lithium bis(trifluoromethanesulfonimide) (23 g, 80 mmol) was then added and rapidly a white precipitate appeared. The reaction was stirred for 24 h, after which time the mixture was concentrated via rotary evaporation. 30 mL of distilled water was added under stirring to the remaining suspension to solubilize the solid part and the product was extracted with 30 mL of CH_2Cl_2. The CH_2Cl_2 phase was washed three times with distilled water (3 x 30 mL) and the organic phase extracted. CH_2Cl_2 was removed under reduced pressure (0.1 bar) at 60°C for 2h to afford 20.82 g (38.5 mmol, 70%) of **[ImPE][Tf_2N]** as a light yellow viscous oil.

^{1}H NMR (300 MHz, DMSO, δ(ppm)): 9.07 (s, 1H, N–C*H*–N); 7.76 (s, 1H, N–C*H*); 7.69 (s, 1H, N–C*H*); 4.20 (t, 2H, CH_2–N); 3.98 (m, 4H, O–CH_2–CH_3); 3.831 (s, 3H,CH_3–N); 2.1-1.68 (m, 4H, CH_2–CH_2–P); 1.22 (t, 6H,O–CH_2–CH_3).
^{13}C NMR (75.432 MHz, DMSO, δ(ppm)): 136.87; 126; 123.78; 122.23; 121.73; 117.47; 113.2; 61.29; 61.2; 49.07; 48.81; 35.78; 23.27; 23.22; 22.36; 20.5; 16.23; 16.15.
^{31}P RMN (121.442 MHz, DMSO, δ(ppm)): 30.39.
^{19}F NMR (170.385 MHz, DMSO, δ(ppm)): -78.71.
Elemental analysis calculated (%): C (38.7); H (6.5); N (8.0); S (12.2); found: C (26.29); H (3.54); N (9.16); S (13.35).
Exact mass calculated for ESI(+), (m/z): 261.1368; found: 261.1368.
Exact mass calculated for ESI(-), (m/z): 279.9173; found: 279.9178.

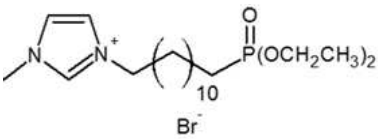

1-methyl-3-(3-(diethylphosphinyl)dodecyl)-imidazolium bromide

The diethyl(3-bromododecyl)phosphonate precursor (93.1 g, 242 mmol) was dissolved in 300 mL of dry THF. Then 1-methylimidazole (20.6 g, 251 mmol) was added rapidly and the mixture was heated at 70°C during 17h under argon. After cooling to room temperature, the THF was evaporated to afford an orange oil. The mixture was purified using distillation under reduced pressure (0.05 mbar) at 120°C to remove 1-methylimidazole introduced in excess and to afford **[ImC$_{12}$PE][Br]** as an orange oil with a 88.5% yield (100 g, 214 mmol).

^{1}H NMR (300 MHz, MeOD, δ(ppm)): 8.96 (s, 1H, N–C*H*–N); 7.65 (s, 1H, N–C*H*); 7.58 (s, 1H, N–C*H*); 4.22 (t, 2H, CH_2–N); 4.08 (m, 4H, O–CH_2–CH$_3$); 3.94 (s, 3H,CH_3–N); 1.9 – 1.73 (m, 4H, CH_2–CH_2–P); 1.56 – 1.22 (m, 24H).
^{13}C NMR (75.432 MHz, CDCl$_3$, δ(ppm)): 137.5; 123.7; 122.5; 62.0; 49.3; 36.7; 23.9; 22.8; 20.9; 16.5.
^{31}P NMR (121.442 MHz, DMSO, δ(ppm)): 32.07.
Elemental analysis calculated (%): C (51.4); H (8.6); N (6.0); found: C (48.60); H (8.78); N (7.95).
Exact mass calculated for ESI(+), (m/z): 387.2777; found: 387.2780.
Exact mass calculated for ESI(-), (m/z): 78.9183; found: 78.9184.

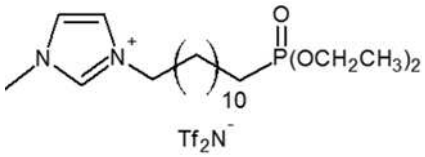

1-methyl-3-(3-(diethylphosphinyl)dodecyl)-imidazolium bis(trifluoromethanesulfonimide)

10.35 g (22.14 mmol) of 1-methyl-3-(3-(diethylphosphinyl)dodecyl)-imidazolium bromide were dissolved in 30 mL of distilled water. 6.9 g (24 mmol) of Lithium bis(trifluoromethanesulfonimide) was then added, and rapidly a white oil appeared. The reaction was stirred for 1h at room temperature. After decanting, two phases could be distinguished as an orange white oil phase and a white aqueous phase. The two phases were separated and the orange oil was dissolved in dichloromethane (15 mL). The purification was realized by adding 15 mL of water and by centrifugation of the mixture at 8500 rpm during 5 min. The resulting two phases were separated. The CH_2Cl_2 phase was evaporated inder reduced pressure (0.1 bar, at 60°C for 2h) to afford 11.15 g (16.7 mmol, 70%) of **[ImC$_{12}$PE][Tf$_2$N]** as a yellow liquid.

^{1}H NMR (300 MHz, DMSO, δ(ppm)): 9.08 (s, 1H, N–C*H*–N); 7.75 (s, 1H, N–C*H*); 7.69 (s, 1H, N–C*H*); 4.13 (t, 2H, CH_2–N); 3.95 (m, 4H, O–CH_2–CH$_3$); 3.83 (s, 3H,CH_3–N); 1.76 – 1.6 (m, 4H, CH_2–CH_2–P); 1.45 – 1.18 (m, 24H).
^{13}C NMR (75.432 MHz, CDCl$_3$, δ(ppm)): 136.7; 124; 122.7; 122.7; 122; 117.8; 113.2; 61.2; 61.1; 49.2; 36.2, 30.2; 30.; 29.8; 29.4; 29.3; 28.9; 28.8; 25.9; 25.8; 24; 22.5; 22.4; 16.8; 16.7.
^{31}P NMR (121.442 MHz, DMSO, δ(ppm)): 32.07.
^{19}F NMR (270.385 MHz, DMSO, δ(ppm)): -78.71.
Elemental analysis calculated (%): C (39.6); H (6.0); N (6.3); S (9.6); found: C (39.2); H (5.87); N (8.15); S (10.34).
Exact mass calculated for ESI(+), (m/z): 387.2777; found: 387.2779.
Exact mass calculated for ESI(-), (m/z): 279.9173; found: 279.9175.

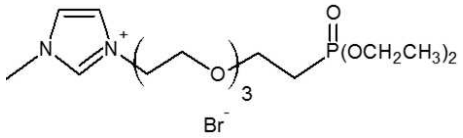

1-methyl-3-(3-(diethylphosphinyl) 2–(2–(2–(2–ethoxy)ethoxy)ethoxy)ethyl)-imidazolium bromide

The diethyl-(2-{2-[2-(2-bromo-ethoxy)-ethoxy]-ethoxy}-ethyl)phosphonate precursor (6.12 g, 16.2 mmol) was mixed with 1-methylimidazole (1.25 g, 15.2 mmol) without any solvent. The mixture was heated and stirred at 110°C for 40 minutes under argon to afford the **[ImPEGPE][Br]** ionic liquid as a yellow liquid with a 99% yield (15.2 mmol, 6.96g).

^{1}H NMR (300 MHz, $CDCl_3$, δ (ppm)): 10.4 (s, 1H, N^+-C*H*-N); 7.69 (s, 1H, =C*H*); 7.4 (s, 1H, =C*H*); 4.63 (t, 2H, N^+-CH_2); 4.12 (q, $^{3}J_{H-H}$ = 9.81 Hz, 4H, O$CH_2$$CH_3$); 4.07 (s, 3H, CH_3-N^+); 3.90 (m, 2H, $N^+CH_2CH_2$); 3.75 – 3.63 (massif, 12H, CH_2-O); 2.11 (m, 2H, P$CH_2$$CH_2$); 1.35 (t, 6H, OCH_2CH_3).

^{13}C NMR (75.432 MHz, $CDCl_3$, δ (ppm)): 137.917; 123.601; 122.605; 70.35; 70.284; 70.245; 70.148; 69.031; 65.105; 61.75; 49.75; 36.586; 27.844; 25.996; 16.476; 16.397.

^{31}P NMR (121.442 MHz, $CDCl_3$, δ(ppm)): 28.54.

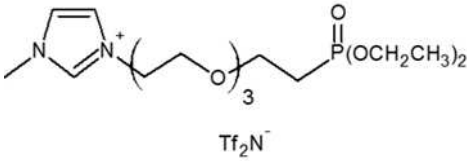

1-methyl-3-(3-(diethylphosphinyl) 2–(2–(2–(2–ethoxy)ethoxy)ethoxy)ethyl)-imidazolium bis(trifluoromethanesulfonimide)

9.77 g (21.25 mmol) of 11-methyl-3-(3-(diethylphosphinyl) 2–(2–(2–(2–ethoxy)ethoxy)ethoxy)ethyl)-imidazolium bromide were dissolved in 30 mL of distilled water. Lithium bis(trifluoromethanesulfonimide) (6.6 g, 22.93 mmol)) was then added, and rapidly a white precipitate appeared. The reaction mixture was stirred for 1 h. After decantation, two phases could be distinguished: a yellow oil phase and a white aqueous phase. The two phases were separated and the yellow oil was washed three times with distilled water (3 x 20 mL). Traces of water were removed under reduced pressure (0.1 bar) at 80°C for 3h to afford 10.45 g (15.8 mmol, 74%) of **[ImPEGPE][Tf_2N]** as a light yellow viscous oil.

^{1}H NMR (300 MHz, DMSO, δ(ppm)): 9.04 (s, 1H, N^+-C*H*-N); 7.71 (s, 1H, =C*H*); 7.69 (s, 1H, =C*H*); 4.33 (t, 2H, N^+-CH_2); 3.98 (q, $^{3}J_{H-H}$ = 9.81 Hz, 4H, O$CH_2$$CH_3$); 3.86 (s, 3H, CH_3-N^+); 3.76 (t, 2H, $N^+CH_2CH_2$); 3.61 – 3.48 (massif, 12H, CH_2-O); 2.11 (m, 2H, P$CH_2$$CH_2$); 1.21 (t, 6H, OCH_2CH_3).

^{13}C NMR (75.432 MHz, $CDCl_3$, δ(ppm)): 135.95; 124.98; 122.52; 121.83; 120.76; 116.49; 112.27; 69.81; 69.70; 69.53; 67.28; 63.56; 60.15; 60.07; 47.91; 34.87; 26.04; 24.23; 15.42; 15.34

^{31}P NMR (121.442 MHz, DMSO, δ(ppm)): 28.66.

^{19}F NMR (270.385 MHz, DMSO, δ(ppm)): -78.73.

Elemental analysis calculated (%): C (33.5); H (5.0); N (4.0); S (9.9); found: C (30.97); H (4.29); N (8.65); S (10.61).

Exact mass calculated for ESI(+), (m/z): 379.1998; found: 379.1995.

Exact mass calculated for ESI(-), (m/z): 279.9173; found: 279.9177.

Characterization methods and protocols

Gas solubility measurements

The home-made system (Figure II. 18) used for measuring the solubility of gases in ILs was specifically designed to fit into a temperature controlled chamber (Sartorius Certomat HK). Two experiments can be run at the same time by using 2 stainless steel cells with volumes of 105 and 57 cm^3 respectively. Each cell top is sealed via a copper gasket (Neyco- CF CU 39) and connected to a reference cell of 15 cm^3 (Swagelok) used for gas injection. The instrument is composed of VCR connections with aluminum gasket (Swagelok). Pressure gauges (one PA33X/0-10 bars and two PA33X/0-3 bars, Keller) are interfaced with a home-made software for automated data collection. The upper chamber is made of stainless steel with a 1000 cm^3 volume capacity. The temperature of the installation is continuously adjusted and controlled (+/- 2% for the heating circuit). Before any measurement, both the system and the ILs were strongly outgassed overnight under vacuum (5.0×10^{-5} mbar) using a turbomolecular pump (Leybold, Turbovac 50). To verify the system integrity (connections, valves), the apparatus was progressively filled with He in order to measure possible leaks (Alcatel ASM series Leak detectors). Prior to measurements, the volume of each part of the apparatus were carefully determined with He, using the ideal gas law.

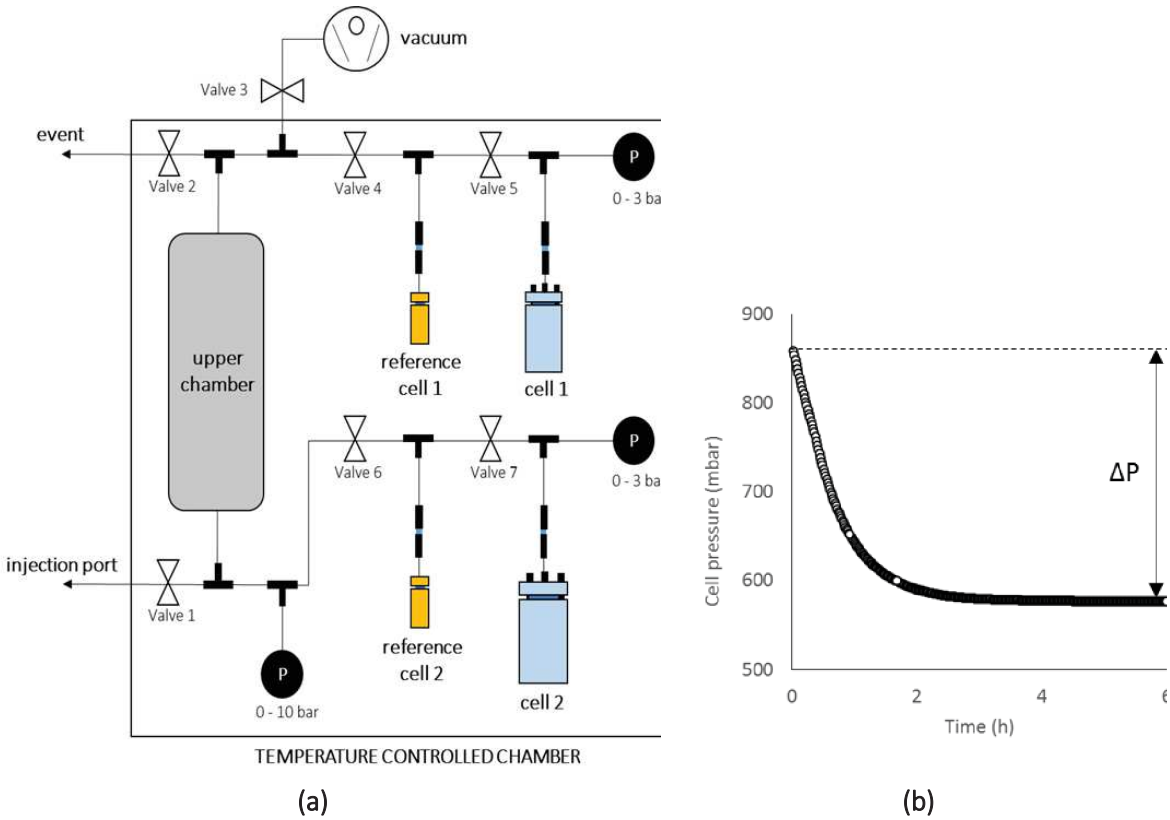

Figure II. 18: (a) Schematic of the system for gas solubility measurements, (b) Typical experimental curve showing the evolution of the pressure in the cell vs. time.

Gas solubility values were measured as follows: the considered IL (≈10-20 mL) was introduced in the reference cell n°1 with a stir bar (of known volume), and the system was sealed. Then, the IL was degassed for at least 10h (vacuum pressure of $5x10^{-5}$ mbar) by opening the valves 3, 4 and 5. Then, the

valves 3 and 5 were closed. The valve 1 was opened gradually to fill both the upper chamber and the reference cell n°1 with the desired gas at a pressure between 7.5 and 8.5 bars. Before starting the experiment, the gas was allowed to expend in the apparatus for 30 minutes. Then, the valve 4 was closed and the automated data collection started once the valve 5 was opened. The pressure decrease (resulting from gas absorption into the IL) is monitored over time (Figure II. 18.b). Depending of the quantity and the ILs, the equilibrium was reached after 1 or 3h. Solubility data obtained for [emim][Tf_2N] on the apparatus gave value for CO_2 in line with the literature (i.e. H_{CO2} at 42 atm) [12].

The CO_2/N_2 selectivity value reported in Table II. 7 is significantly under-estimated. This is due to the limited precision of the pressure gauges used for the experiment. Therefore, we are unable to correct the portion of N_2 gas adsorbed in the blank cell (i.e. $N_{2(total)} = N_{2(IL)} + N_{2(Cell)}$), which is low but certainly corresponds to a considerable portion of the total measured N_2 sorption "in the ionic liquids".

ILs volumetric mass density measurements

The volumetric mass density of the [ImC_3PE][Tf_2N], [ImP_3PE][Tf_2N] and [$ImC_{12}PE$][Tf_2N] ILs were measured at 22°C with volumetric flasks of either 2 or 5 mL and weight measurements were realized on a custom-made installation. An analytical balance (Gravimetric AG, Precisa LX320A -readability and repeatability 1 mg) and a controlled humidity/temperature instrument (OMEGA, UWRH-2-(+/- 1°C and +/- 2.5 RH) were placed in a hermetic box with dry silica gel containers. The balance and sensors were interfaced with a home-made software for automated data collection. Before staring the experiments, each flask was calibrated with cyclohexane in order to check the volume uncertainty. The flask was filled with cyclohexane and the weight variation was registered during 100 min. The graphics representing the variation with time of the weight, temperature, and relative humidity are presented in Figure II. 19. The average mass and temperature, measured at constant humidity value of 22%, gave the following values: mass=19.183 ± 0.009 g and temperature= 21.74 ± 0.05 °C. Thus, we were able to check the volume of the empty flask by the following equation:

$$V_f = \frac{m_c - m_v}{\rho_c} \qquad 2.12$$

where V_f, is the flask volume filled with cyclohexane (mL), ρ_c the cyclohexane volumetric mass density (0.779 g/cm^3), m_v the mass of the empty flask (g) and m_c the mass of the flask filled with cyclohexane (g). As an example with the flask of 2 mL, the volume of the empty flask was 1.9 mL and thus it was in the range of the uncertainty defined by the constructor (0.1 mL).

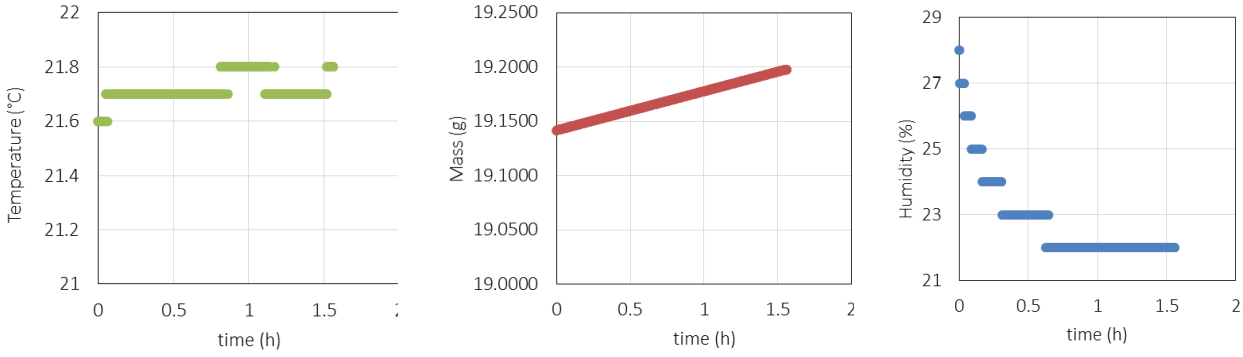

(a) (b) (c)

Figure II. 19. Evolution of the temperature (a), mass (b) and humidity (c) during the measurements of the empty flask volume.

The same protocol was repeated with the ILs and all the average values were measured at a constant humidity of ~ 22%. The IL volumetric mass density ρ_{IL} (g/cm^3) was calculated using the equation below:

$$\boldsymbol{\rho_{IL}} = \frac{\boldsymbol{m_{IL} - m_v}}{\boldsymbol{V_f}} \quad 2.13$$

with V_f the volume of the empty flask previously measured (mL), m_v the mass of the empty flask (g) and m_{IL} the mass of the flask filled with IL (g).

Molecular modeling

The molecular modeling was performed using [ImPE][BF_4] as the model [62]. Calculations were performed with the help of Density Functional Theory (DFT) with B3LYP levels, using 6-311G(2d,p) as basis set on Gaussian 09 program package. Geometry optimization and harmonic vibrational frequencies were calculated at the same DFT level. The ESP mapping illustrates the polarization of the cation with the imidazolium ring corresponding to the blue region and phosphonyl group as the least positively charge region (in red).

The free volume can be evaluated by using the following equation:

$$\boldsymbol{V_f = Q.V_m + Z} \quad 2.14$$

with $\boldsymbol{Q}$ = 0.2177 (case of the Tf_2N^- anion, constant expressed without units) which represents the asymptotic value of the free volume fraction (FFV_{IL}) in the IL; $\boldsymbol{Z}$ equals to -26.07 $cm^3.mol^{-1}$, which is the contribution of the cation-anion pair to FFV_{IL}[3] and $\boldsymbol{V_m}$ the IL molar volume ($cm^3.mol^{-1}$).

[3] The values of Z and Q are different for ether functionalized cations [$P_x$mim][Tf_2N] (*i.e., respectively, 0.1844 and -18.21*) [32].

Chapter III. Grafting of phosphonate-based ionic liquids on γ-alumina for CO_2 sorption

In this chapter, phosphonate-based ILs composed of different coupling functions, organic spacers and anions were grafted on γ-alumina (γ-Al_2O_3) powders. These powders were prepared as companion samples of conventional mesoporous γ-alumina membranes, in order to favor a possible transfer of the results to supported membrane materials which could be used for continuous CO_2 separation. Effective grafting and influence of the IL composition were demonstrated by using a set of characterization techniques, such as Energy Dispersive X-ray Spectroscopy (EDX), N_2 physisorption measurements, Fourrier transform infrared spectroscopy (FTIR) and a special attention was paid to solid-state Nuclear Magnetic Resonance (NMR) spectroscopy through the study of the ^{1}H, ^{13}C, ^{31}P, ^{27}Al and ^{19}F nuclei.

Chapter III. Grafting of phosphonate-based ionic liquids on γ-alumina for CO_2 sorption

III.1. Introduction

Organic-inorganic hybrid materials based on metal oxide materials functionalized with ILs species are emerging as an important class of materials for the adsorptive separation of acid gases (*i.e., CO_2, SO_2*) from dilute gas streams [1-4]. In competition with amines [5], ILs are known to interact strongly and reversibly with CO_2 [1]. The remarkable properties of ILs have led to the realization of Supported Ionic Liquid Phase (SILP) materials for use in adsorptive or membrane for CO_2 separation applications [2-6]. These systems are composed of two parts, the support material and the IL [2,3] which are linked either by weak interactions (Class I) (*i.e., van der Waals forces, hydrogen bond*), or by strong interactions (Class II) (*i.e., covalent bond, coordination bond*) onto a high surface area support (Figure III. 1).

The first class can be prepared by using impregnation techniques (*e.g., support immersion in IL solution and solvent evaporation*), by coating and/or by vacuum/pressure assisted infiltration. In this type of system, the properties of the ILs remain unchanged. However, these preparation techniques lead to low stability materials due to weak interactions of the physisorbed species with the support surface. The class II can be synthesized by direct grafting on the support surface using an IL solution and drove to the formation of a chemisorbed organic monolayer. This method leads to hybrid materials with higher chemical and thermo-mechanical stabilities.

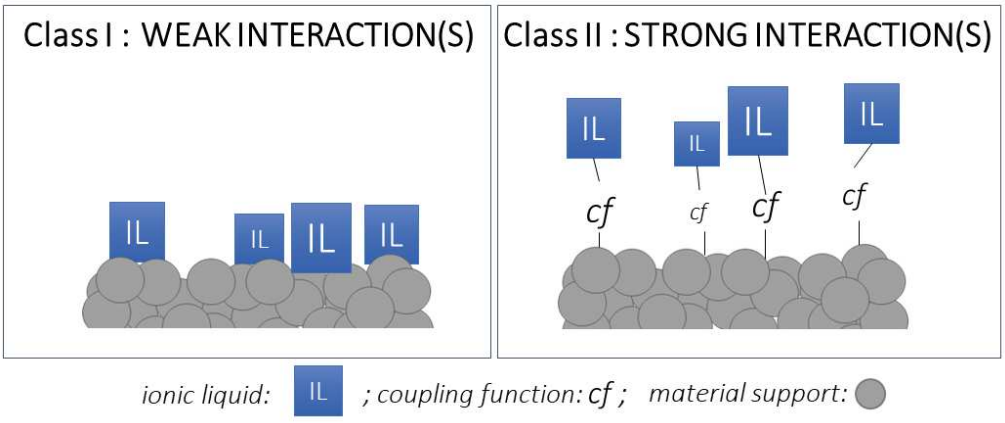

Figure III. 1. The two classes of supported ionic liquid systems: class I (physisorbed ILs with weak interactions with the support) and class II (grafted IL with strong interactions with the support).

As reported by Ferhman *et al.* [6], tailoring the chemical nature of the support, as well as its microstructure (*e.g., pore size, size distribution, specific surface area…*), govern both IL grafting efficiency and distribution on the support surface. However, the grafting strategy is much more challenging than a simple impregnation method. Obviously, the chemical reaction at the support surface requires an optimization of the reaction conditions to avoid secondary reactions and to control the formation of an IL monolayer. Many efficient Supported Ionic Liquid Phase (SILP) systems based on physisorbed ILs have been developed such as Supported Ionic Liquid Catalysts (SILC), Supported Ionic Liquid Nanoparticles (SILnPs) and Supported Ionic Liquid Membranes (SILMs).

As reported in chapter I, section I.3.1, the Supported Ionic Liquid Membranes (SILMs) (Class I) are composed of ILs physisorbed either on top or inside a porous support [7-13]. Whatever the support material (polymer or ceramic porous support), Class I SILMs suffer from both easy disarrangement (*e.g., under continuous pressure*) and partial homogeneity.

As an alternative to increase membrane thermomechanical stability, we proposed in this work to chemically graft functionalized ILs on the pore walls of ceramic supports using a phosphonate coupling function. γ-alumina is a commonly used mesoporous ceramic material, and its hydroxylated surface is attractive for grafting active species for either gas sorption or heterogeneous catalysis [14]. Also, this material can be cast easily as a continuous (membrane) film on various supports and was thus selected in this work as a relevant ceramic material for grafting phosphonate-based ILs. Surface modification of oxide materials using phosphonate coupling molecules has already been widely reported in the literature [15,16]. In this study, the phosphonate coupling function has been tethered to the cation part of the ILs by an organic spacer (Figure III. 2). Because the characterization of supported membranes (very thin top-layer on thick commercial ceramic supports) is often tricky, unsupported membranes, *i.e.,* γ-Al_2O_3 powders prepared by the sol-gel method, were used as model materials to optimize the grafting reaction conditions. The protocols optimized on these companion samples of conventional mesoporous γ-alumina membranes will be easily transfered to the supported γ-alumina membranes (in chapter IV).

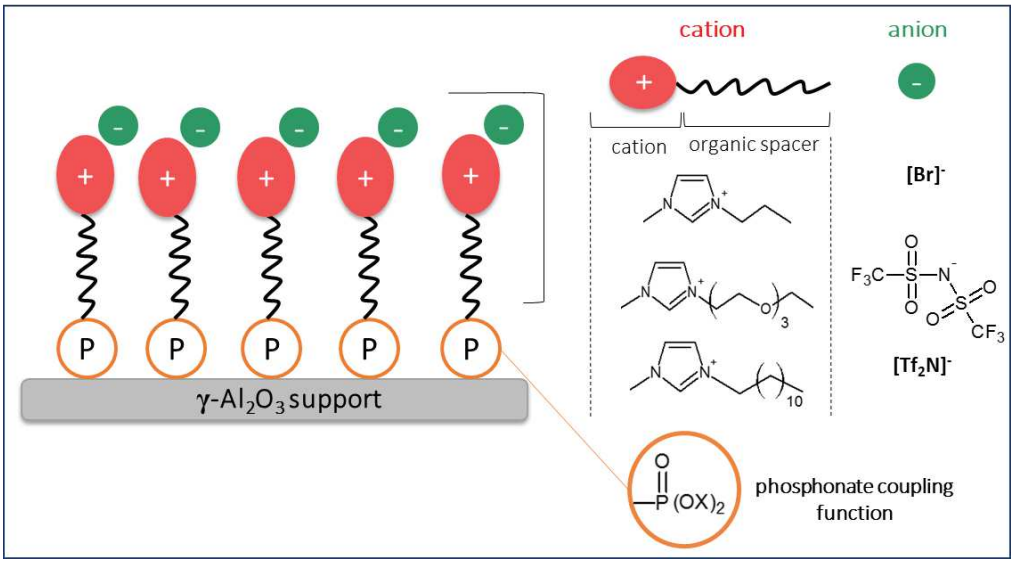

Figure III. 2. γ-alumina support with grafted phosphonate-based IL.

In order to generate highly stable systems with a maximum quantity of grafted ILs on the γ-Al_2O_3 pore surface, a literature review was first required. This review evidenced the key parameters affecting the grafting of phosphonate molecules on γ-Al_2O_3 material and allowed to select the most appropriate characterizations techniques.

To date, the phosphonate-based ILs are employed in the recovery of actinides and rare earth elements or as solvents for the extraction of U(VI) [17,18]. Also, their tribological behavior as lubricants for aluminum-on-steel sliding system has been evaluated [19]. Only very few reports concern the grafting of phosphonate-based ILs on γ-Al_2O_3. As an example, Guerrero and co-workers patented a process for modifying an inorganic substrate with imidazolium-based ILs with phosphonate coupling agents, which have been used for their intrinsic antimicrobial properties in relevant antibacterial applications [20].

In Chapter II, we designed three phosphonate-based ILs *(i.e., [ImPE][Tf_2N], [$ImC_{12}PE$][Tf_2N] and [ImPEGPE][Tf_2N])* potentially attractive for separating CO_2 from N_2. This chapter III focusses on the development of relevant protocols for grafting these ILs on the pore walls of a mesoporous γ-Al_2O_3 powder.

The experimental grafting methods together with the associated characterization of the supported γ-Al_2O_3 phosphonate-based ILs will be reported. Special techniques were used to evidence the grafting degree and mechanisms. Several types of ILs have been investigated in this chapter III, their names, acronyms and structure are described in the Figure I. 4 of Chapter I.

III.2. Grafting of phosphonate-based molecules: key parameters and characterization techniques

As previously shown in the **General Introduction**, phosphonic acids and esters are increasingly being used for controlling surface and interface properties in hybrid or composite materials [15]. In this section, a concise survey of phosphonate coupling molecules is first presented, including details on the grafting mechanism(s) at the surface of metal oxide materials.

III.2.1. The phosphonate-based coupling agents

III.2.1.1. General description

As shown in Figure III. 3, phosphonic acids contain a tetravalent phosphorus atom in the +V oxidation state, bound to two acidic hydroxyl groups and a double–bonded oxygen atom (*i.e., known as a phosphoryl group*). The phosphonic esters are similar except that the two acidic protons are replaced by alkyl, aryl and even trimethylsilyl groups (X = $Si(CH_3)_3$). The fourth component is an organic carbonated moiety linked to phosphorus with a P-C bond assuming a good chemical stability.

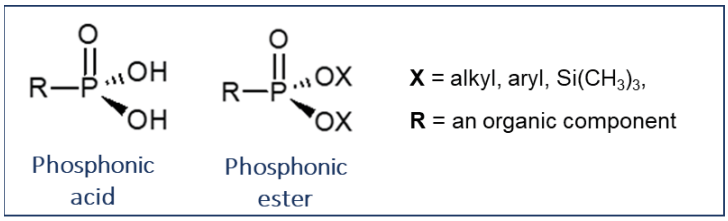

Figure III. 3. The structure of phosphonate coupling agents.

The acidity constants related to the acid dissociation in aqueous solutions have been measured for the alkylphosphonic acid and substituted aliphatic phosphonic acids compounds [21]. As an example, the propylphosphonic acid has a pKa_1 at ~2.5 and a pKa_2 at ~8. These pKa values increase with the length of the alkyl chain [21]. For the substituted aliphatic phosphonic acids, the pKa depends on the substituted group (Figure III. 4) (*Note: ester phosphonate are pH neutral such as common esters*). The resulting pH of the aqueous solution depends on the phosphonic acid concentration, and such parameter should be taken into account during the grafting reaction on metal oxide materials to avoid any phenomenon.

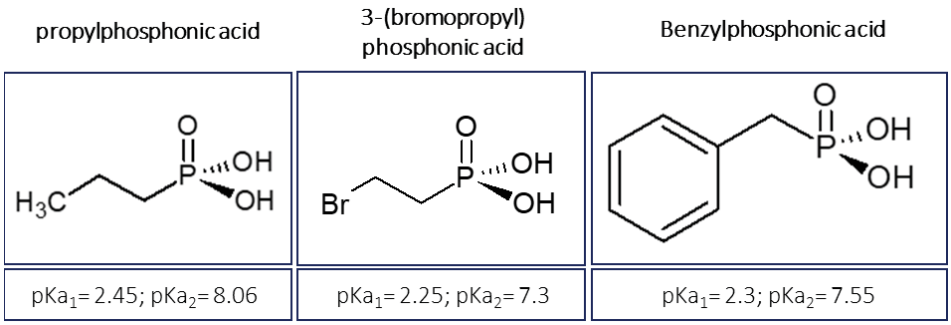

Figure III. 4. Values of pKa and structures of the propylphosphonic acid, the 3-(bromopropyl)phosphonic acid, and the benzylphosphonic acid.

Phosphonate ligands are famous for their versatile coordination chemistry, allowing them to bind to different metal ions via P-O-metal ionocovalent bonds. Furthermore, unlike other coupling agents such as organosilanes, phosphonate coupling agents are not subjected to homocondensation reactions between the coupling functions. This allows the controlled formation of organic monolayers of grafted phosphonate molecules on the surface of inorganic supports.

III.2.1.2. Applications

Initially, phosphonic acids were employed to react with a large variety of metal ions (*i.e., salt and oxides*), to prepare metal-phosphonate compounds [22] and hybrid materials [22,23] (*i.e., 1D to 3D, with a wide variety of compositions and structures*). Phosphonate coupling functions are also used for grafting organic monolayers and self-assembled monolayers (SAMs) on various substrates [24]. Randon *et al.* [25], have linked phosphoric acid and alkyl phosphonic acid to the surface of both titania and zirconia membranes to improve their performance for the ultrafiltration of BSA (Bovine Serum Albumin) proteins. The same author also realized the chemical modification of mesoporous alumina membrane with n-butane phosphonic acid and n-dodecylphosphate for the separation of gaseous hydrocarbons [26]. The influence of the grafted organic layer on the gas transport mechanisms was evidenced and was found to improve both the membrane permeability and selectivity for propane/nitrogen separation [26]. Caro *et al.* [27], modified a γ-Al_2O_3 membrane top-layer with alkyl or aryl phosphonic acids for obtaining membranes with both narrow pore sizes and organophobic behavior. Grafting of phosphonate coupling molecules have thus received increasing attention during the last decades and appears as an attractive alternative to the commonly used thiols, silanes, and carboxylic acid coupling functions.

III.2.2. Grafting of phosphonate-based molecules on γ-Al_2O_3

The reaction of organophosphorus derivatives on γ-Al_2O_3 surface is supposed to involve: *i) the coordination of the oxygen atom from the phosphoryl group (P=O) to Lewis acid sites, and ii) the condensation reactions of P-OH or P-OX functions (X could be -CH_3, -CH_2CH_3 or -$Si(CH_3)_3$) with Al-OH surface groups* (Scheme III. 1) [15,31].

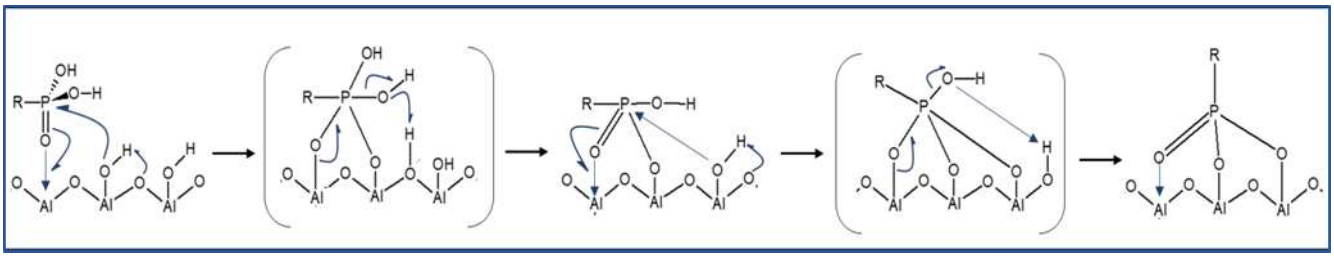

Scheme III. 1. Proposed mechanims for the grafting of phosphonic acid on γ-Al_2O_3 leading to a tridentate bonding mode [31].

Up to three P-O-Al bonds for each phosphonate unit can be formed during the grafting reaction and conduct to different bonding modes. The tridentate bonding mode involves three P-O-Al bonds and the monodentate or bidentate bonding modes involve respectively one P-O-Al bond and two P-O-Al bonds. Furthermore, these bonds can be either bridging (each oxygen atom binds to a different metal atom) or chelating (two or three oxygen atoms bind to the same metal atom) [28]. Hydrogen bonds can also exist between residual P-OH or P=O groups and hydroxyl surface groups of the γ-Al_2O_3. All of these possibilities give a large variety of possible bonding modes which are all represented in Scheme III. 2.

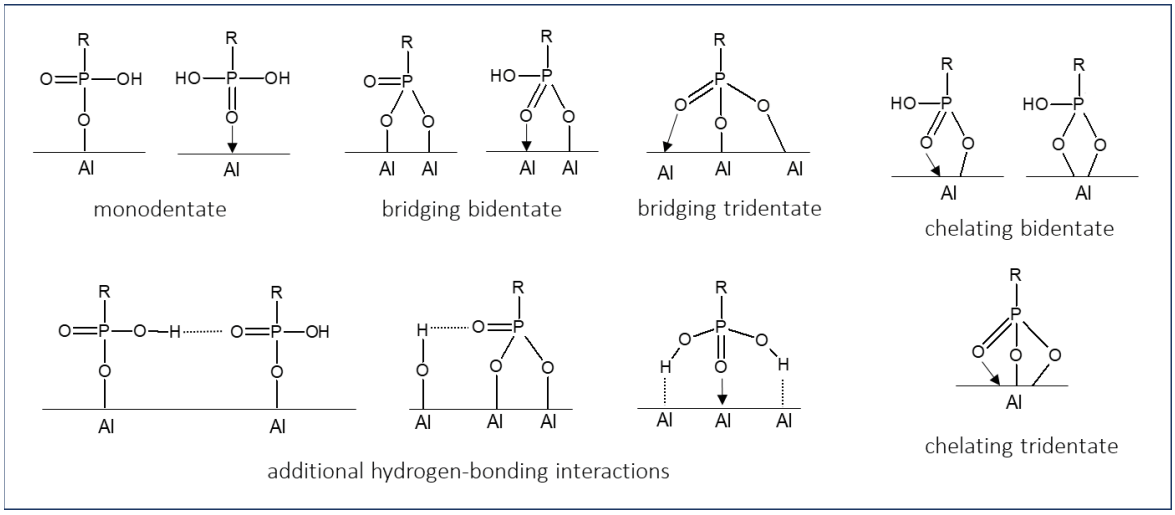

Scheme III. 2. Schematic representation of bonding modes of phosphonate-based molecules on hydroxylated alumina surface. Adapted from reference [31].

It must also be noted that depending on both the chemical stability of the substrate and the reaction conditions (*i.e., solvent, concentration, pH, reaction time and temperature*), the formation of metal phosphonate bulk phases by a dissolution-precipitation process can occur [29,30]. This competition between surface modification and dissolution–precipitation process has been evidenced when grafting phenylphosphonic acid on TiO_2 or γ-Al_2O_3 powders [29,30]. The dissolution-precipitation phenomenon can be avoided in most cases by carefully choosing the reaction conditions, or by using alkylester derivatives (*e.g., RPO(OCH₂CH₃)₂*) instead of the parent acids [29]. In fact, it has been evidenced that grafting with a diethyl phenylphosphonate coupling molecule resulted in a maximum 50% surface coverage [29]. It was also pointed out that the use of the dialkyl ester derivatives in organic media allowed controling the grafting while excluding the formation of metal phosphonate phases even under prolonged heating [29,30].

III.3. Grafting of phosphonate-based ionic liquids on γ-alumina

III.3.1. Preparation and characterization of γ-alumina substrate

Different methods based on the sol-gel process can be used to prepare γ-alumina powders. It was important in this work to select a sol formulation typically well adapted for casting top-layers (membranes) on porous supports. Sols derived from the controlled hydrolysis of aluminum alkoxides can be used to coat porous supports with unifom gel layers, which can be dried and thermally treated to generate continuous γ-alumina supported membranes [32].

In the present work, the colloidal sol-gel method described by Leenaars *et al.* [33], was used. An aluminum oxy-hydroxide precursor called boehmite (AlOOH) was dispersed in deionized water and an acidic solution (HNO_3, 2M) was used as a peptizing agent. The dehydration of the colloidal γ-AlOOH sol leads to a gel, then to cracked and crumbled films. The films were manually crushed and calcined in air at 600°C for 3h. The resulting γ-Al_2O_3 material was finally dried for 3h at 400°C under N_2 flow to remove any physisorbed species and the powders were stored under Ar atmosphere. As reported by Shayesteh *et al.* [34], the dehydration and calcination steps involve a short-range rearrangement of the atoms in the crystal structure. A schematic representation of the synthesis steps is shown in Figure III. 5.

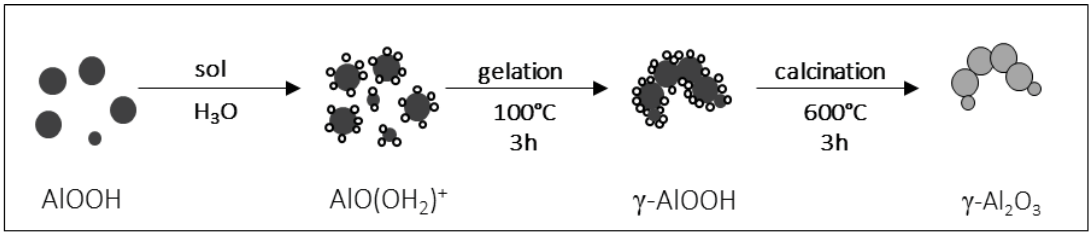

Figure III. 5. Schematic representation of the synthesis steps of γ-alumina powder by the sol-gel process starting from boehmite precursor.

Depending on the final thermal treatment conditions, five metastable phases can be formed either as a single phase or mixed phases. These metastable phases have been studied for many years and are listed in Figure III. 6. The γ-Al_2O_3 phase is reported to occur between 475 and 775°C [35].

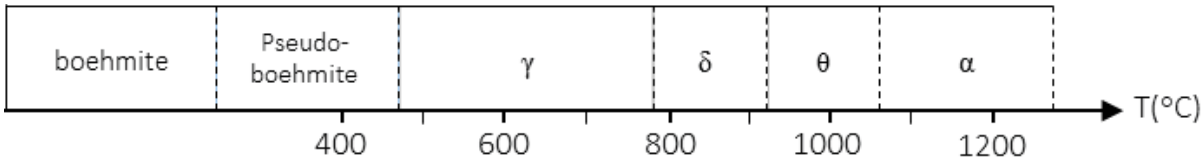

Figure III. 6. The different alumina phases depending on the calcination temperature.

When the sol-gel method is employed to produce continuous γ-Al_2O_3 top-layers on a porous ceramic support, a polymeric binder (*e.g.,* polyvinyl alcohol, PVA[4]) is added before the gelation step to the boehmite sol [36]. By this way, it is possible to control the sol viscosity and help the formation of crack-free layers. It has been checked that this additive did not modify the characteristics of the final γ-alumina powders obtained at 600°C, after its degradation.

According to the literature, the sol-gel method allows to obtain γ-alumina particles with a specific surface area in the range 70- 500 $m^2.g^{-1}$ [37]. In our case, γ-Al_2O_3 particles with platelet morphology and sizes ~20 nm (see TEM imaging, Annex 2, Figure A2. 4) were synthesized. Their specific surface area was ~200 $m^2.g^{-1}$ (N_2 physisorption-BET method) and the C_{BET} constant was ~91 (C_{BET} is a characteristic parameter for adsorbate/material surface interactions, as reported by Galarneau *et al.* [38]). The crystalline structure of γ-Al_2O_3 is traditionally considered as a cubic defect spinel type, built on tetrahedral (Al_{IV}) and octahedral (Al_{VI}) aluminum centers [35], this can be evidenced by both XRD analysis and ^{27}Al solid-state NMR.

Both the nature and concentration of surface acid and basic sites on the γ-alumina surface depend on the thermal treatment conditions. The acidic character is attributed to surface hydroxyl groups linked to water protons and to aluminum ions presenting a saturated coordination. The basic character is due to the oxygen anion [35]. It must also be noted that the surface sorption behavior of γ-Al_2O_3 has been widely studied and the point of zero charge (PZC) for this oxide is reported to vary between 6 and 9 [35]. Concerning the surface topology of γ-Al_2O_3, some models have been suggested to help understanding [39,40]. These models were correlated to the IR spectrum of γ-Al_2O_3, and more specifically to the signals in the region of hydroxyl groups (several elongation vibration (ν_{OH}) bands between 3798 and 3630 cm^{-1}). Recently, Taoufik and co-workers [41] used advanced solid-state NMR to evidence experimentally the characteristics and topology of hydroxyl groups on the surface of a partially dehydroxylated γ-Al_2O_3.

[4] Polyvinyl alcohol: polymer with vinyl acetate, 25/140 RHODOVIOL®

III.3.2. Choice of the phosphonate coupling functions

Our initial investigations focused on the choice of the ester phosphonate coupling functions. Two ILs composed of the same cation, anion and organic spacer were used, the only difference was related to the coupling function which was a diethyl ([ImPE][Br]) or a bis(trimethoxysilyl) ([ImTMSP][Br]) ester phosphonate function (Figure III. 7). Different grafting reaction conditions were tested with the two coupling agents and the resulting samples were characterized using Energy Dispersive X-ray Spectroscopy (EDX), Fourrier transform infrared spectroscopy (FTIR), solid-state Nuclear Magnetic Resonance (NMR) and X-Ray Diffraction (XRD) to evidence the effects of both the reaction conditions and the type of ester phosphonate on the efficiency of the grafting process.

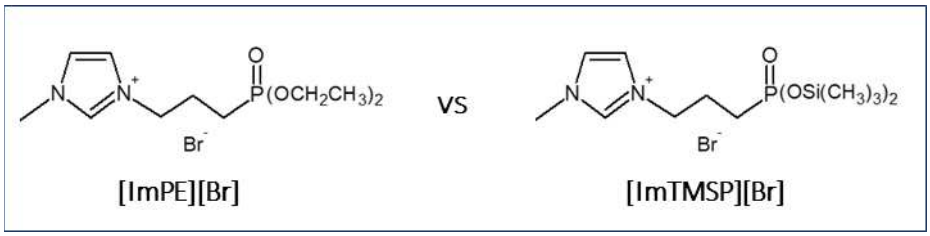

Figure III. 7. Structure of the phosphonate-based ILs: *1-methyl-3-(3-(diethylphosphinyl)propyl)- imidazolium bromide ([ImPE][Br]), and 1-methyl-3-(3-((trimethoxysilyl)phosphinyl)propyl)- imidazolium bromide ([ImTMSP][Br]).*

III.3.2.1. General protocol for the preparation of grafted samples

The γ-alumina powders surface was modified by treatment with an organic or aqueous grafting solution containing a 6-fold excess (3.6 mmol) of either [ImPE][Br] or [ImTMSP][Br] ILs. The quantity of IL used corresponds to 6 times the amount needed for a full surface coverage of the γ-Al_2O_3 specific surface area (*i.e. 0.6 mmol, assuming an area of 25 Å² per IL molecule*). Depending on the IL used, different reaction conditions were applied (Table III. 1).

To evidence the spectroscopic characteristics of physisorbed phases or unreacted species on the γ-alumina surface, grafting experiments were first performed with [ImPE][Br] in standard reaction conditions during several days in alcoholic solvents (*3 days in the Ethanol; 3 and 12 days in 2-butanol*), while grafting with [ImTMSP][Br] were realized during either 17h or 3 days in dry methylene chloride.

Also, as reported for the grafting of diethylphenylphosphonate coupling agent on γ-Al_2O_3, the use of forcing reaction conditions (*i.e., excess of coupling agent relative to full surface coverage, and high temperature*) did not lead to dissolution-precipitation mechanism (*no formation of bulk aluminum phosphonate phases*), and was found to improve the surface grafting density [29,30].

So secondly, forcing reaction conditions were also tested with [ImPE][Br] in aqueous media for 3 days by increasing the reaction temperature up to 110°C then to 130°C. After the grafting treatment, samples were centrifuged, washed with an ethanol-water solution to remove unreacted and physisorbed species, and dried at 70°C before analysis (cf. Experimental and Modeling part).

Table III. 1. Physisorption, standard and forcing conditions for the grafting of [ImPE][Br] and [imTMSP][Br] ILs on γ-alumina powders.

Grafting Conditions	IL	Solvent (mL)	T (°C)	Reaction time (h)	Sample reference
Standard Conditions	[ImPE][Br]	Ethanol (5)	70	72 (3 days)	ImPE-Br (1)
		2-butanol (5)	90	72 (3 days)	ImPE-Br (2)
		2-butanol (5)	90	288 (12 days)	ImPE-Br (3)
	[ImTMSP][Br]	CH_2Cl_2 (14)	25	17	ImTMSP-Br (1)
		CH_2Cl_2 (14)	25	72 (3 days)	ImTMSP-Br (2)
Forcing conditions	[ImPE][Br]	water (10)	110	72 (3 days)	ImPE-Br (4)
		water (10)	130	72 (3 days)	ImPE-Br (5)

III.3.2.2. Characterizations

All the grafted samples were characterized by EDX analysis, X-Ray diffraction, FTIR, and solid-state NMR.

- *EDX*

The characteristics of pristine and grafted γ-alumina powders are compared in Table III. 2. The average phosphorus concentrations (P wt%) estimated by EDX demonstrate the presence of phosphorus in all the grafted samples. The concentrations never exceed a full surface coverage (*i.e., 3.2 P wt%*) in agreement with the expected surface reactions of the ILs coupling agents on γ-alumina.

Table III. 2. Characteristics of the γ-alumina powders before and after IL grafting ([a]From EDX analysis, [b]Average number of coupling molecules per nm^2).

Sample	P wt%[a]	P nm^{-2} [b]
γ-Al_2O_3	0	/
ImPE-Br (1)	0.36 ± 0.03	0.5
ImPE-Br (2)	0.73 ± 0.10	0.9
ImPE-Br (3)	0.90 ± 0.05	1.2
ImPE-Br (4)	1.14 ± 0.03	1.4
ImPE-Br (5)	1.42 ± 0.05	1.8
ImTMSP-Br (1)	1.16 ± 0.10	1.5
ImTMSP-Br (2)	1.00 ± 0.10	1.3

As shown in Figure III. 8, the sample obtained after 72h reaction with [ImPE][Br] in forcing conditions (*i.e., 110°C-ImPE-Br (4), 130°C-ImPE-Br (5)*) exhibit an increase of phosphorus content by comparison with the samples reacted in standard conditions for 72h (*i.e., ImPE-Br (1), ImPE-Br (2))* or 288h (*i.e., ImPE-Br (3))*. This result suggests that a higher temperature tends to increase the rate of surface reaction. In the case of ImTMSP-Br samples, P contents are in the range of values obtained for [ImPE][Br] derived samples. Nevertheless, no heat activation was required for [ImTMSP][Br], suggesting differences in IL reactivity [29]. Also, the efficiency of grafting reactions with [ImTMSP][Br] did not seem to depend on reaction times because similar P concentrations were mearsured in both samples.

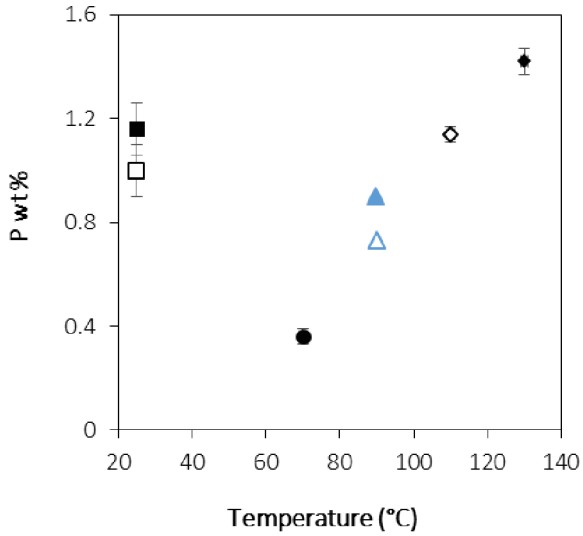

Figure III. 8. Evolution of the phosphorus concentration (wt % P) in grafted samples vs. reaction temperature with various ILs: ImPE-Br (1) (●); ImPE-Br (2) (Δ); ImPE-Br (3) (▲); ImTMSP-Br (1) (□); ImTMSP-Br (2) (■); ImPE-Br (4) (◇); ImPE-Br (5) (◆).

The grafting density (P nm^{-2}) on the surface of the γ-alumina powders was estimated from both the phosphorus concentration and specific surface area of the grafted samples, assuming a 25 Å² area per phosphonate unit (Table III. 2). A full surface coverage of the alumina particles should never exceed 4 P atoms by nm^2. The grafting density values estimated for the prepared sample series were in the range 0.5-1.8, suggesting that surface coverage never exceeded ~45% of a full monolayer. In the case of the diethyl ester derivative, this result fits with the ~50% surface coverage announced in the literature for diethyl phenylphosphonate coupling molecule on Degussa γ-alumina in organic medium [29]. The authors also evidenced that grafting with the bis-trimethylsilylester phenylphosphonate coupling agent could also lead to higher concentration of phosphorus atoms on the surface but attributed to a bulk aluminum phosphonate phase. We already pointed out that dialkyl ester derivatives in organic media allowed to control the grafting and excluded the formation of metal phosphonate phases even after prolonged heating. Thus, the partial surface coverage obtained in this study with diethyl imidazoliumphosphonate coupling molecule could result from possible steric hindrance effect on the γ-alumina surface (due to both alkyl chain and imidazolium ring) and also from the low reactivity of the coupling function.

- *XRD and ^{27}Al NMR*

Powder X-ray diffraction patterns (XRD) and ^{27}Al MAS NMR spectra of both selected grafted samples and pristine γ-Al_2O_3 are presented respectively in Figure III. 9 and Figure III. 10.

The γ-alumina ^{27}Al NMR spectrum is composed of two large peaks, at 10.6 and 69.2 ppm corresponding respectively to aluminum atoms in octahedral (Al_{VI}) and tetrahedral (Al_{IV}) coordination modes [42]. In some cases, pentahedral coordination mode (Al_V) at 35 ppm, attributed to hydration phenomena, can be observed with variable amount, depending on the pristime powder storage conditions. A comparison of the ^{27}Al NMR spectra for the different pristine γ-alumina batches used in this work is shown in ANNEX 2 (Figure A2. 1).

The ^{27}Al MAS NMR spectra of the grafted samples only reveal the presence of the signals observed for pristine γ-Al_2O_3 and we did not detect any additional upfield sharp resonance which could result from the formation of bulk aluminum phosphonate phases by a dissolution/precipitation phenomenon. This observation was confirmed by the XRD patterns which were similar for both the grafted samples and the pristine γ-Al_2O_3.

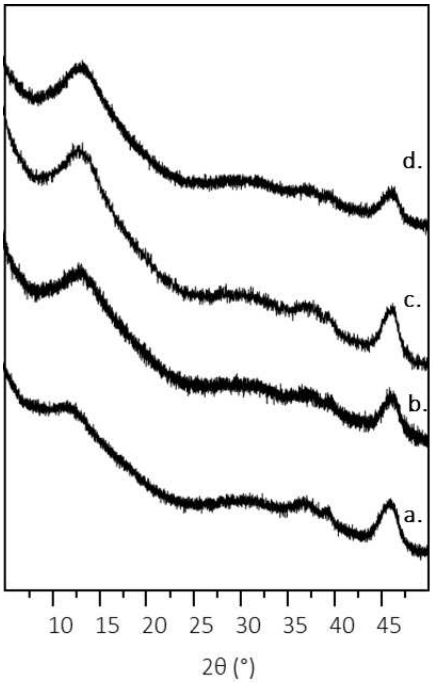

Figure III. 9. XRD patterns for a) pristine γ-Al_2O_3 powder and for grafted samples with various ILs b) ImPE-Br(3), c) ImPE-Br(5), and d) ImTMSP-Br(2).

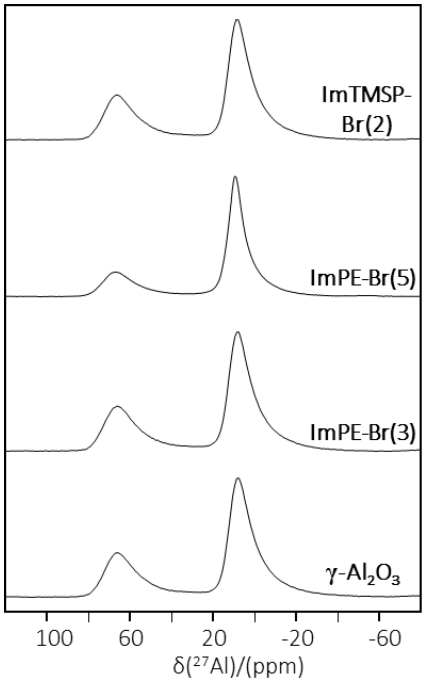

Figure III. 10. ^{27}Al MAS NMR spectra for the pristine γ-Al_2O_3 powder and for grafted samples with various ILs (ImPE-Br(3), ImPE-Br(5) and ImTMSP-Br(2)).

Chemical and thermal characterizations methods (*e.g.,* EDX, elemental analysis, TGA[5]…) can provide information on the surface coverage for the different samples. X-ray diffraction and ^{27}Al solid-state NMR confirmed the integrity of the alumina material after grafting. However, these techniques cannot be used to evidence the grafting of ILs on metal-oxide surface. IR spectroscopy, and ^{31}P solid-state NMR were selected as relevant techniques for this purpose and for studying the different bonding modes

- *FTIR spectroscopy*

The identification of the characteristic frequencies for the various phosphonate vibrational modes is useful for both characterizing the compounds and determining whether they bound to a metal oxide surface, by checking the occurence of stretching vibrations associated to free phosphonic acids and to P-O-M bonds. Several disagreements can be found in the literature about the exact assignment of the frequencies corresponding to the different P-O vibrational modes. Table III. 11 summarizes the most commonly accepted values for the phosphonate coupling functions [30, 43].

The P=O stretching frequency of ester phosphonate is in the range 1200-1300 cm^{-1} (*e.g., $(C_2H_5O)_2CH_3PO$:(P=O)=1250 cm^{-1}; $(C_2H_5O)_2C_4H_9PO$: ν(P=O)=1243 cm^{-1}*) [44]. The P–O–M bands are usually broad (indicative of electrons delocalization) and fall within the 900-1200 cm^{-1} range. In the grafted samples, the formation of P–O–M bonds might be associated to the disappearance of P=O and the symmetric/asymmetric P–O–X bands (*i.e., X = CH_2-, CH_3 or Si-*), depending on the bonding modes (mono-, bi-, or tridentate).

[5] TGA : Thermogravimetric Analysis

A combination of these indicators can thus provide a clear picture of the nature and type of bonding modes. As an example, Guerrero *et al.* [30], reported the grafting of diethylphenylphosphonate on TiO_2 Degussa particles with a majority of tridentate bonding mode. This assumption was based on the detection of a broad IR absorption band in the range 900-1200 cm^{-1} related to P-O-Ti bonds, a strong band at ~1140 cm^{-1} characteristic of P-C_6H_5 groups and the total disappearance of the normal P=O and P-O-C bands [30].

Table III. 3. List of the main IR band assignments and frequencies for the functional groups in phosphonates.

Vibrational Modes	Frequency (cm^{-1})
P=O (acid)	1150-1220[43]
P=O (ester)	1200-1320[43]
P-O-H	1600-1740[43]
P-O-(H)	917-950[43]
P-O-(H)	972-1030[43]
P-O-C_2H_5	1008-1042[43]
P-O-Si	820-860[30]
P-C	680-785[43]

The FTIR spectra of the [ImPE][Br] and [ImTMSP][Br] ILs between 1400 and 800 cm^{-1} are shown in Figure III. 11. The P=O stretching vibration is observed at 1230 cm^{-1} for [ImPE][Br] and 1251 cm^{-1} for [ImTMSP][Br]. The C–H deformation vibration is detected at 1014 cm^{-1} for [ImPE][Br] and 1035 cm^{-1} for [ImTMSP][Br]. Asymmetric and symmetric P–O–C stretching vibrations are only present for [ImPE][Br] at 1042 and 958 cm^{-1} [21,30]. The spectra of [ImTMSP][Br] shows a P-O-Si deformation vibration at 833 cm^{-1}. Starting from the IL structure, DFT calculations were used to estimate the different vibration modes of the coupling agents (ANNEX 1, Figure S10) and to identify several specific deformation bands such as the =C-H imidazolium band and the -CH_2- band present at ~1165 cm^{-1} for both ILs.

In all the grafted samples, we can notice the disappearance of the phosphoryl (P=O) stretching bands at 1233 and 1253 cm^{-1}, suggesting that the phosphoryl oxygen is strongly bonded to the alumina Lewis acid surface sites by coordination (Figure III. 11., part II. a, b and c). Moreover, whatever the IL and grafting reaction conditions are, an absorption band is observed at 1171 cm^{-1}, typical of =C-H and -CH_2- deformation in the imidazolium ring and the alkyl chain spacer, respectively. The location of the "PO" region for the grafted samples (in the range between 950 and 1250 cm^{-1}) differ depending on both the considered IL and the applied reaction parameters. The IR spectra of samples treated in forcing reaction conditions with [ImPE][Br] (Figure III. 11. part II.b) present a strong absorption band at 1065 cm^{-1}, tentatively ascribed to the P-O-Al stretching vibration [45]. It can be noted that the intensity of this band gradually increases with the amount of grafted species. Also, the presence of weak absorption bands at about 1040 and 950 cm^{-1} (region of P-O-C stretching bands) does not exclude the existence of some P-OEt residual groups.

The FTIR spectrum of ImPE-Br (3) (standard reaction conditions) (Figure III. 11., part II.a) shows a broad absorption band ~1080 cm^{-1} corresponding to P-O stretching mode. This band could be attributed to P-O surface species in organophosphonate/metal oxide materials according to Quiñones *et al.* [46]. Also, the presence of a strong residual P-O-C stretching band at ~1040 cm^{-1} cannot be excluded. The IR spectra of samples grafted with [ImTMSP][Br] (Figure III. 11.II.c) in standard conditions are quite similar to the spectrum of the ImPE-Br (3) sample. The main difference is the detection of residual P-O-Si deformation vibration in the range 1000-800 cm^{-1}, suggesting that all the coupling functions did not react with the γ-alumina surface [29].

To conclude, IR spectroscopy of samples grafted in standard reaction conditions reveals the presence of either residual P-O-C or P-O-Si vibrations, stating that phosphonate units are preferentially linked to the alumina surface through bidentate (or monodentate) bonding modes. In the case of samples prepared in

forcing conditions, the detection of weak residual P-O-C stretching modes in the infrared IR spectra, indicate that the dominating bonding mode of the phosphonate groups seems to involve tridentate PO_3 units.

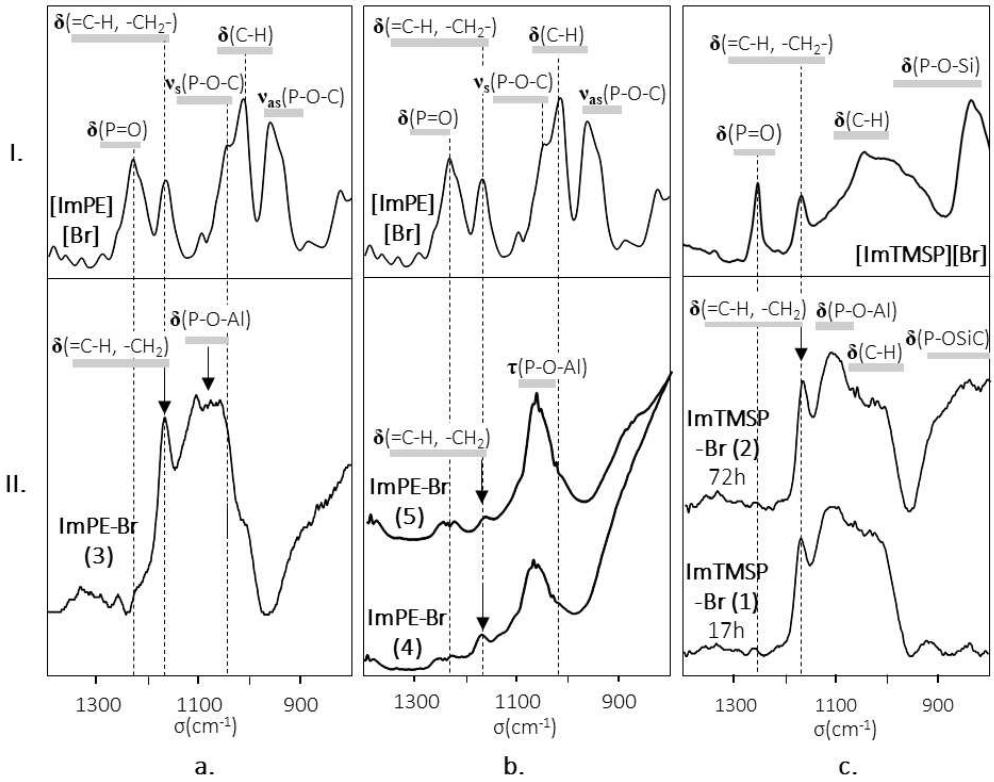

Figure III. 11. Experimental FTIR spectra of [ImPE][Br] IL (I.a, b) and [ImTMSP][Br] IL (I.c) and corresponding grafted γ-Al_2O_3 samples prepared with different reaction conditions: (II.a) with [ImPE][Br] in standard conditions (ImPE-Br (3)), (II.b) with [ImPE][Br] in forcing conditions (ImPE-Br (4) at 110°C; ImPE-Br (5) at 130°C), and (II.c) with [ImTMSP][Br] in standard conditions (ImTMSP-Br (1), ImTMSP-Br (2) at 25°C).

- *^{31}P solid-state NMR*

Solid-sate Nuclear Magnetic Resonance (ssNMR) is one of the most powerful techniques which can be used to distinguish chemisorbed from physisorbed species thanks to the NMR-active nuclei present in the system (*i.e.,* ^{13}C, ^{31}P, ^{17}O).

^{31}P NMR is often used to determine the possible bonding modes of phosphonic acids on metal oxide surfaces [29,30,47]. Guerrero *et al.* [29,30], combined the results of ^{31}P MAS NMR, DRIFT and TGA analysis to assign the bonding modes with the ^{31}P chemical shift obtained for phosphonate/metal-oxide grafted samples. The protonation rate of the phosphonic acid coupling function (monoprotonated or deprotonated) can also be determined by measuring the ^{31}P chemical shift anisotropy parameters [48], by recording fast Magic Angle Spinning (fast MAS) ^{1}H NMR spectra at high field [24], and/or by performing ^{31}P-^{1}H cross-polarization (CP) MAS experiments [49]. High-field ^{17}O solid state NMR can directly prove the formation of P-O-Ti bonds between phosphonates and TiO_2 particles, and helps to estimate the number of residual P=O and P-OH bonds [28]. However, given the poor abundance of ^{17}O (0.04%) such experiments requires the utiliszation of expensive ^{17}O-enriched samples.

As a reference sample in this work, the identification of the ^{31}P NMR signal corresponding to simply physisorbed IL species has been done with a sample treated under physisorption reaction conditions with ImPE-Br (cf. ANNEX 1, SI). The NMR spectra of this sample present a sharp resonance at 32.1 ppm (ANNEX

1, Figure S11), very close to the spectra obtained for the pure ImPE-Br IL, characteristic of phosphonate species in weak interactions with the alumina support.

The ^{31}P MAS NMR spectra of the grafted γ-alumina treated with [ImPE][Br] and [ImTMSP][Br] ILs are shown in Figure III. 12. The peak related to physisorbed species was not present in the samples. Also, in good agreement with both XRD and ^{27}Al ssNMR analysis, we did not observe any additional upfield sharp resonance peak in the ^{31}P ssNMR spectra, *i.e.,* no formation of aluminum phosphonate bulk phases.

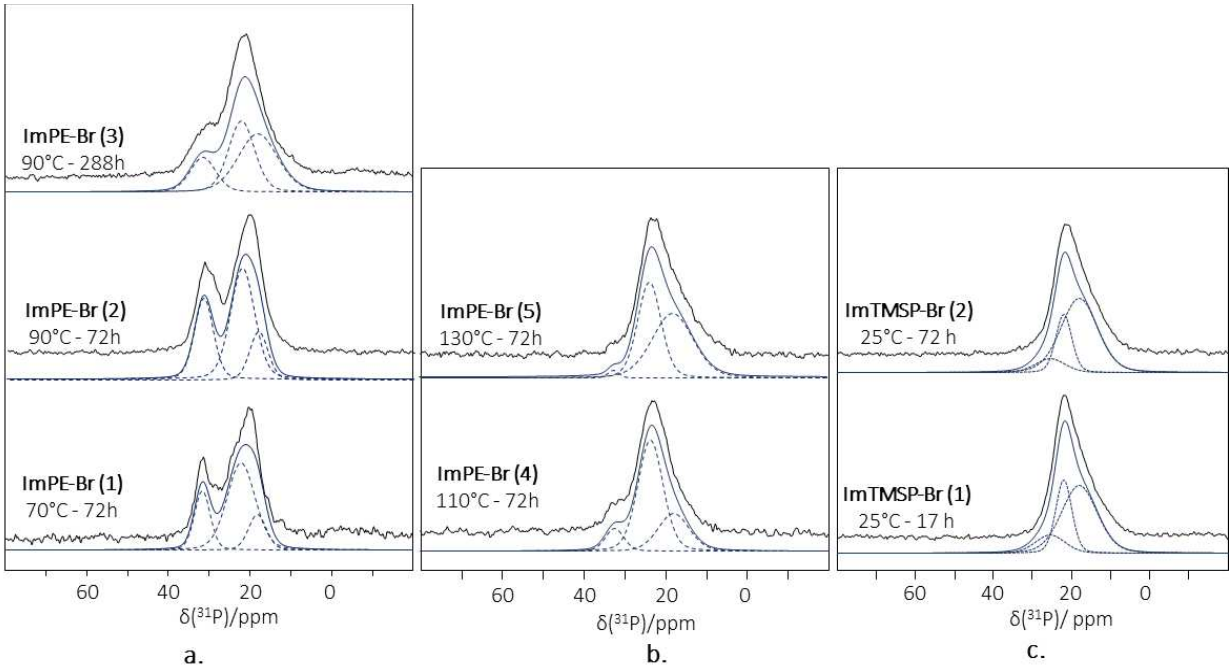

Figure III. 12. (a) ^{31}P MAS NMR spectra of γ-Al_2O_3 grafted samples prepared under standard reaction conditions with [ImPE][Br] IL (70°C-72h for ImPE-Br (1); 90°C-72h for, ImPE-Br (2); 90°C-288h for ImPE-Br (3)); (b) ^{31}P CP-MAS NMR spectra of γ-Al_2O_3 grafted samples prepared under forcing conditions with [ImPE][Br] (72h) at different temperature (ImPE-Br (4) at 110°C ; ImPE-Br (5) at 130°C); (c) ^{31}P MAS NMR spectra of γ-Al_2O_3 grafted samples prepared under standard conditions with [ImTMSP][Br] (25°C) at various reaction times: ImTMSP -Br (1) (17h); ImTMSP-Br (2) (72h).

The ^{31}P MAS NMR spectra of γ-alumina grafted powder with [ImPE][Br] under standard reaction conditions are displayed in Figure III. 12.a (*i.e., ImPE-Br (1), ImPE-Br (2), ImPE-Br (3)*). The spectra of ImPE-Br (1) and ImPE-Br (2) are very similar, with two broad resonances centered at about 31.4 and 20.2 ppm. This result suggests that the grafting reaction temperature (70 or 90°C) and the type of alcoholic solvent (Ethanol or 2-butanol) poorly impact on the IL bonding modes. On the contrary, the spectrum of the ImPE-Br (3) sample (2-butanol, 288h) with a broad resonance at 21.6 ppm and an important downfield asymmetrical shape, strongly differs from the two previous ones, obtained after 72h reaction. The simulation of the ImPE-Br (1), ImPE-Br (2) and ImPE-Br (3) spectra assuming a minimum number of signals with Gaussian-Lorentzian shape reveals the presence of at least 3 sites (Figure III. 12.a, Table III. 4) at 31.6, 22.1 and 18.1 ppm, evidencing the presence of multiple main bonding modes (Scheme III. 2). As reported by Brodard-Severac *et al.* [28], the interaction of the P=O groups with Lewis or Bronsted acidic surface sites should lead to a downfield shift. Starting from both this consideration and the IR results showing the presence of residual P-OEt functions, the signal at 31.6 ppm integrating from 18 to 30% could be tentatively ascribed to the monodentate bonding mode involving the phosphoryl function (Scheme III. 2). As far as proportion of this bonding mode decreases when the grafting duration increases (*i.e., ImPE-Br (2) to (3): 30 to 18%),* thus the bidentate or tridentate bonding modes are favored for longer reaction times.

Table III. 4. Parameters used for the simulation of ^{31}P MAS NMR spectra of γ-Al_2O_3 grafted with [ImPE][Br] under standard reaction conditions.

Grafted IL/ γ-Al_2O_3 sample	ImPE-Br (1) 70°C-72h			ImPE-Br (2) 90°C-72h			ImPE-Br (3) 90°C-288h		
δ (ppm)	31.6	22.1	18.1	31.6	22.1	18.1	31.6	22.1	18.1
Width (ppm)	61.1	90.2	36.5	40.8	56.0	23.9	7.5	7.6	11.5
Integration (%)	23	62	15	30	53	17	18	37	45

The ^{31}P CP-MAS NMR spectra of γ-alumina grafted powder with [ImPE][Br] under forcing reaction conditions are displayed in Figure III. 12.b (ImPE-Br (4), ImPE-Br (5)). All the spectra present a broad resonance band centered at about 23.6 ppm. As for standard conditions, spectra simulations reveal the presence of at least three sites (signals at 32.4, 23.6 and 17.9 ppm (Figure III. 12.b, Table III. 5) revealing the presence of multiple bonding modes (Scheme III. 2). Through the IR spectra, we showed the presence of low residual P-O-C species, suggesting a dominating bonding mode of phosphonate groups involving tridentate PO_3 units. Therefore, we propose to ascribe the main signal at 23.6 ppm, integrating from 45 to 64%, to tridentate phosphonate PO_3 units grafted on the γ-alumina surface. The third resonance at 17.9 ppm, integrating from 27 to 53%, was attributed to grafted phosphonate functions in a bidentate mode. For both ImPE-Br (4) and ImPE-Br (5) samples, we noticed that the increase in the proportion of this bidentate bonding mode correlates well with the increasing intensity of the P-O-Al absorption band in IR spectra. Consequently, by increasing the temperature from 110°C to 130°C in the forcing reaction conditions, the bidentate bonding mode of phosphonate units is favored while the monodentate bonding mode becomes negligible.

Table III. 5. Parameters used for the simulation of ^{31}P MAS NMR spectra of γ-Al_2O_3 grafted with [ImPE][Br] under forcing reaction conditions.

Grafted IL/ γ-Al_2O_3 sample	ImPE-Br (4) 110°C- 72h			ImPE-Br (5) 130°C- 72h		
δ (ppm)	32.4	23.6	17.9	32.4	23.6	17.9
Width (ppm)	14.3	69.9	23.6	4.3	59.4	39.6
Integration (%)	9	64	27	2	45	53

Figure III. 12.c displays the ^{31}P MAS NMR spectra of γ-Al_2O_3 grafted under standard conditions (25°C) with [ImTMSP][Br] using different reaction times (17h and 72h). The spectra of ImTMSP-Br (1) and (2) samples are qualitatively similar to those of γ-alumina grafted with [ImPE][Br] in forcing reaction conditions. In all cases, the NMR signals present an asymmetric shape and are centered at 22.1 ppm. According to the simulated spectra, three chemical shifts at 25.6, 22.1, and 18.1 ppm were identified with a major resonance for the latter (Table III. 6). As for the ImPE-Br samples in standard condition, the IR spectra of ImTMSP-Br (1) and (2) revealed important residual P-$OSiMe_3$ functions, implying an increasing proportion of monodentate and/or bidentate bonding modes for the phosphonate units. The liquid state ^{31}P NMR spectrum of [ImTMSP][Br] (ANNEX 1, Figure S9) revealed an upfield chemical shift at 24.7 ppm (to be compared with 29.8 ppm for pure [ImPE][Br]) (ANNEX 1, Figure S5), in good agreement with the P-OEt to P-$OSiMe_3$ conversion [30]. On this basis, the signal at 25.6 ppm, integrating from 10 to 13%, could be tentatively ascribed to the monodentate bonding mode with two P-$OSiMe_3$ functions available (Scheme III. 2). As for ImPE-Br (4) and (5) samples, the main resonances, attributed to phosphonate units with bidentate bonding mode, correspond to the upfield chemical shift located at 18.2 ppm and integrating from 58 to 67%. The last signal at 22.1 ppm could be ascribed to tridentate phosphonate units. By using [ImTMSP][Br]

as a coupling agent, we cannot correlate unambiguously the reaction time with the proportion of the different bonding modes.

Table III. 6. Parameters used for the simulation of ^{31}P MAS NMR spectra of γ-Al_2O_3 grafted with [ImTMSP][Br].

Grafted IL/ γ-Al_2O_3 sample	ImTMSP-Br (1) 25°C-17h			ImTMSP-Br (2) 25°C- 72h		
δ (ppm)	25.6	22.1	18.2	25.6	22.1	18.2
Width (ppm)	9	4.9	11.2	9	4.9	10.8
Integration (%)	10	23	67	13	29	58

The above results suggest that the reaction of γ-alumina with either [ImPE][Br] or [ImTMSP][Br] IL in standard conditions promote the grafting of phosphonate units with mainly bidentate configuration. An increase of the grafting reaction temperature with [ImPE][Br] favors both the tridentate and bidentate bonding modes for the phosphonate units on the γ-alumina surface.

III.3.2.3. Conclusion

One important outcome of this study bears on the possibility to effectively graft [ImPE][Br] or [ImTMSP][Br] IL on γ-alumina surfaces, either in aqueous medium or organic solvents (alcohol, dry methylene chloride) respectively. By comparison with previous studies published in the literature describing the grafting of phenylphosphonic acid or its bis(trimethylsilyl) ester derivatives, no bulk aluminum phosphonate phase was evidenced in the present work. Moreover, this study confirms that the use of diethyl imidazoliumphosphonate coupling molecule allows good control of the grafting reaction by using either prolonged heating or higher temperature. FTIR and solid state NMR spectroscopy (^{31}P) were relevant techniques to demonstrate that γ-alumina surface modification with diethylphosphonate coupling agent strongly depends on the grafting conditions.

Soft standard reaction conditions mainly promote bidentate and monodentate bonding modes of the phosphonated-IL on the surface, with a minority of tridentate phosphonate units. Conversely, the forcing reaction conditions mainly favor the formation of tridentate and bidentate bonding modes on the alumina surface, with a minority of monodentate ones.

The grafting of [ImTMSP][Br] in standard conditions also promotes alumina surface modification by phosphonate units, mostly in bidentate configuration. Despite the fact that 35% of the full monolayer was reached for samples grafted with the bis(trimethylsilyl)ester IL, the reaction time did not impact on the density of grafted species.

The grafting reaction with [ImTMSP][Br] IL present major disadvantages. The IL is a sticky brown paste which is difficult to handle and which is steam sensitive (hydrolysis). Fresh dry solvents are thus required for the grafting reaction. Conversely, [ImPE][Br] is a yellow oil and the grafting process in forcing condition at 130°C lead to high grafting density (~45%) in aqueous solutions.

We can thus conclude that the best grafting reaction conditions, using [ImPE][Br] IL, correspond to those used for sample ImPE-Br (5). This sample, prepared with the reaction parameters summarized in Table III. 7, provides the highest grafting density.

Table III. 7. Optimized grafting reaction conditions yielding high grafting density with [ImPE][Br] IL.

Grafted sample	IL	Solvent (mL)	Reaction T (°C)	n-fold excess	Reaction time (h)	P wt %	^{31}P NMR spectra

ImPE-Br (5)	[ImPE][Br]	water (10)	130	6	72 (3 days)	1.42 ± 0.05	3 signals (32.4, 23.6, 17.9 ppm)

III.3.3. Influence of the anion type on the grafting kinetic of phosphonate based ILs

We previously demonstrated that γ-alumina can be grafted with [ImPE][Br] and [ImTMSP][Br] IL under different reaction conditions. The forcing reaction conditions with [ImPE][Br] revealed to be the most promising for modifying the γ-alumina surface. The grafting process was found to be time-dependent and does not favor the formation of bulk aluminum phosphonate phases even in aqueous media. The next step of the work, will focuss on the optimization of the reaction kinetics using the forcing conditions reaction parameters.

Two ILs were used: [ImPE][Br] (*i.e.,* the 1-methyl-3-(3-(diethylphosphinyl)propyl)-imidazolium bromide) and [ImPE][Tf_2N] (*i.e.,* the 1-methyl-3-(3-(diethyl-phosphinyl)propyl) imidazolium bis(trifluoro methanesulfonimide) which are composed of the same cation and two different anions, Br^- and Tf_2N^-. The [ImPE][Br] IL used in the section III.3.2. will serve as a reference for direct comparison with the [ImPE][Tf_2N] IL which is CO_2-philic (cf. Chapter II). The synthesis of both [ImPE][Br] and [ImPE][Tf_2N] is described in Chapter II.

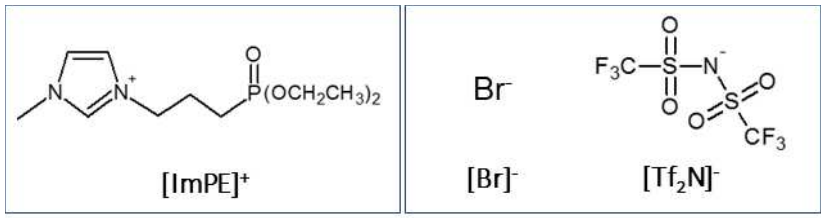

Figure III. 13. Structure of ImPE phosphonate-based ILs with two different anions: [ImPE][Br] and [ImPE][Tf_2N].

III.3.3.1. Procedure for the preparation of grafted powders

The quantity of grafted species and the formation of bulk aluminum phosphonate phases are related to both the nature of the starting materials (γ-alumina and ILs) and the grafting reaction conditions. To increase the quantity of grafted species, several several reaction times were tested at 130°C with IL solutions containing a 12-fold excess (7.2 mmol) of the IL in either ethanol-water co-solvent (*for [ImPE][Tf_2N]*) or in aqueous medium (*for [ImPE][Br]*). Details on the reaction times used for each sample are reported in Table III. 8. As reported in ANNEX 1, an increase of IL solution concentration compared to our preliminary tests (III.2) should increase the proportion of grafted species.

After the grafting process, the samples were centrifuged and washed with an ethanol-water solution to remove unreacted and physisorbed species. A washing treatment by the Soxhlet method (dry ethanol, 110°C, 24h) was used for the sample grafted with [ImPE][Tf_2N]. All the samples were then dried at 70°C before analysis (cf. Experimental and Modeling part of this chapter). A specific sample prepared by grafting [ImPE][Tf_2N] in "physisorption conditions" (cf. ANNEX 2, Figure A2. 3) was used to evidence the spectroscopic characteristics of physisorbed or unreacted [ImPE][Tf_2N] species on the surface of γ-Al_2O_3.

Table III. 8. Reaction times used for the grafting of [ImPE][Br] and [ImPE][Tf_2N] on γ-Al_2O_3 in forcing conditions.

Sample	ImPE-Br (6)	ImPE-Br (7)	ImPE-Br (8)	ImPE-Br (9)	ImPE-Br (10)	ImPE-Br (11)	ImPE-Br (12)
Reaction time (h)	17	27	40	45	48	64	92

Sample	ImPE-Tf_2N (1)	ImPE-Tf_2N (2)	ImPE-Tf_2N (3)	ImPE-Tf_2N (4)	ImPE-Tf_2N (5)	ImPE-Tf_2N (6)
Reaction time (h)	20	30	40	48	64	92

III.3.3.2. Characterizations

All the grafted samples were characterized by EDX analysis, X-Ray diffraction, IR spectroscopy, ssNMR.

- *EDX*

The characteristics of the grafted γ-alumina samples are summarized in Table III. 9 and Figure III. 14. EDX analysis reveals the presence of phosphorus in all the samples. By comparison with the optimized grafted sample prepared in the section III.2 (cf. Table III. 7), equal or higher weight % of phosphorus were measured for the new ImPE-Br samples series corresponding to longer grafting reaction times for more concentrated IL solutions (*i.e., P wt% $\geq$ 1.42 ± 0.05 when the reaction is $\geq$ 17h*). As an example, the sample reacted for 17h in 12-fold excess of [ImPE][Br] (*i.e., ImPE-Br (7)*) exhibit the same P content as the sample modified in 6-fold excess during 72h in forcing conditions (*i.e., ImPE-Br (5)*). The quantity of grafted species increases continuously with the reaction time up to 48h, *i.e.,* when the P content exceeds the value corresponding to full surface coverage (*i.e., 3.2 P wt%*). This result suggests that higher concentration of the grafting solution can increase the quantity of grafted species for shorter reaction times. However, the high phosphorus content observed for both samples *ImPE-Br (12) and ImPE-Br (13)* suggests the formation of bulk aluminum phosphonate phases [29]. Concerning the ImPE-Tf_2N samples series, EDX analysis of sulfur and fluorine concentration confirmed the conservation of the S/F molar ratio (results not shown) and thus preservation of the anion integrity in all the grafted samples. During this grafting kinetic study, the P concentration in the grafted samples never exceeds the value corresponding to full surface coverage (*i.e., 2.5 P wt% for ImPE-Tf_2N samples*) and reaches its maximum value after a 64h reaction time.

Table III. 9. Characteristics of the γ-alumina powders grafted with [ImPE][Br] and [ImPE][Tf_2N] in forcing reaction conditions.

Sample	ImPE-Br (6)	ImPE-Br (7)	ImPE-Br (8)	ImPE-Br (9)	ImPE-Br (10)	ImPE-Br (11)	ImPE-Br (12)
Time (h)	17	27	40	45	48	64	92
P wt%	1.42 ± 0.03	1.42 ± 0.17	1.73 ± 0.08	2.00 ± 0.03	2.41 ± 0.25	5.16 ± 0.65	4.17 ± 1.15
P nm^{-2}	1.8	1.8	2.2	2.6	3.1	6.7	5.4
Sample	**ImPE-Tf_2N (1)**	**ImPE-Tf_2N (2)**	**ImPE-Tf_2N (3)**	**ImPE-Tf_2N (4)**	**ImPE-Tf_2N (5)**	**ImPE-Tf_2N (6)**	
Time (h)	20	30	40	48	64	92	
P wt%	0.92 ± 0.01	0.98 ± 0.13	1.34 ± 0.08	1.29 ± X	1.60 ± 0.04	0.94 ± 0.10	
P nm^{-2}	1.6	1.6	2.2	2.2	2.6	2.0	

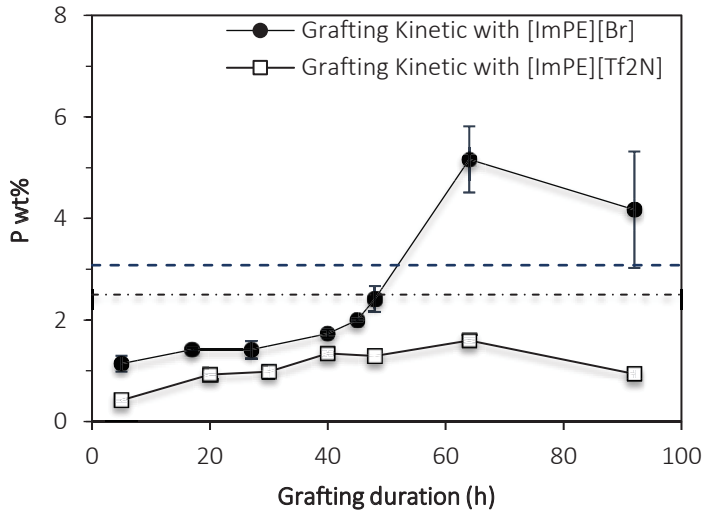

Figure III. 14. Evolution of the weight percentage of phosphorus in the grafted samples series vs. grafting reaction time. The limit value of P wt% for full surface coverage corresponds to the line (--) for ImPE-Br samples (●) and to the line (·-·) for ImPE-Tf_2N samples (□).

From the weight percentage of phosphorus, we can estimate the grafting density (P nm^{-2}) on the γ-alumina surface (Table III. 9). In both grafted samples serie, the grafting density values vary in the range 1.5-6.7 for ImPE-Br samples series and in the range 0.7-2.6 for ImPE-Tf_2N series The maximum P concentration measured for the ImPE-Br series suggests that ~170% of the full monolayer was reached (*e.g.,* 6.7 P nm^{-2} for ImPE-Br (12)). This aberrant value indicates that a bulk aluminum phosphonate phase is certainly formed. In the case of ImPE-Tf_2N series, ~65% of the full monolayer was achieved after 64h reaction time. Thus, the nature of the anion seems to play a key role on the formation of bulk aluminum phosphonate phases. However, it is difficult to clearly conclude because the solvent (H_2O:EtOH mixture instead of H_2O) might also influence the reaction media and pathways.

- *FTIR spectroscopy*

The FTIR spectra between 1400 and 800 cm^{-1} of the [ImPE][Br] and [ImPE][Tf_2N] ILs are presented in Figure III. 15.I.d and II.d. The spectra of [ImPE][Br] was previously described in the section III.3.2.2 (Figure III. 11).

The FTIR spectrum of the sample grafted with [ImPE][Br] during 40h under forcing reaction conditions (Figure III. 15.I.a.) is similar to the spectrum of ImPE-Br (5) observed previously (cf. Figure III. 11.c). Thus, the concentration of the grafting solution or the grafting reaction time does not seem to impact on the phosphonate bonding modes (*i.e., with dominanting bidentate and tridentate bonding modes*) but only on the concentration of grafted species. However, when the grafting reaction increases from 48h to 64h (Figure III. 15.I.b and c), the absorption bands become broad suggesting the presence of different P-O-Al bonds producing multiple vibration bands.

The spectrum of [ImPE][Tf_2N] is dominated by vibrations related to the Tf_2N^- anion, *asymmetric and symmetric -SO_2 stretching vibrations at respectively 1327-1346 and 1132 cm^{-1},–CF_3 stretching vibration at 1224 cm^{-1} and –SNS stretching vibrations at 1061 cm^{-1} [50].* When comparing the [ImPE][Br] spectrum and DFT calculated spectrum of [ImPE][Tf_2N], we were able to estimate the different vibration modes and associated wavenumbers of the coupling agents (ANNEX 2, Figure A2. 2). It was possible to identify several vibrations related to the cation such as *the P=O stretching vibration at 1266 cm^{-1}, the asymmetric and symmetric P–O-C stretching vibrations at 960 and 1050 cm^{-1} [21,30], and the C-H and -CH_2 stretching vibration at 1017 cm^{-1} and 1195 cm^{-1}, respectively [50].*

In the FTIR spectra of ImPE-Tf_2N grafted samples, the main absorption bands were associated to the Tf_2N^- anions at 1346, 1327, 1224, 1195, 1132 and 1061 cm^{-1} and confirmed the conservation of the anion integrity as expected from EDX measurements. Concerning the cation, we noticed the disappearance of the phosphoryl (P=O) stretching band at ~1266 cm^{-1} (Figure III. 15., part II. a,b and c) and a strong absorption band at ~1058 cm^{-1} close to the position of the P-O-Al stretching vibrations previously observed (cf. Figure III. 11). Despite the presence of strong absorption bands corresponding to the anion, the P-O-Al band becomes gradually more intense when the quantity of grafted species increases. Furthermore, the presence of weak absorption bands at ~1050 and 960 cm^{-1} (region of P-O-C stretching bands) can be also noticed, suggesting the existence of P-OEt residual groups.

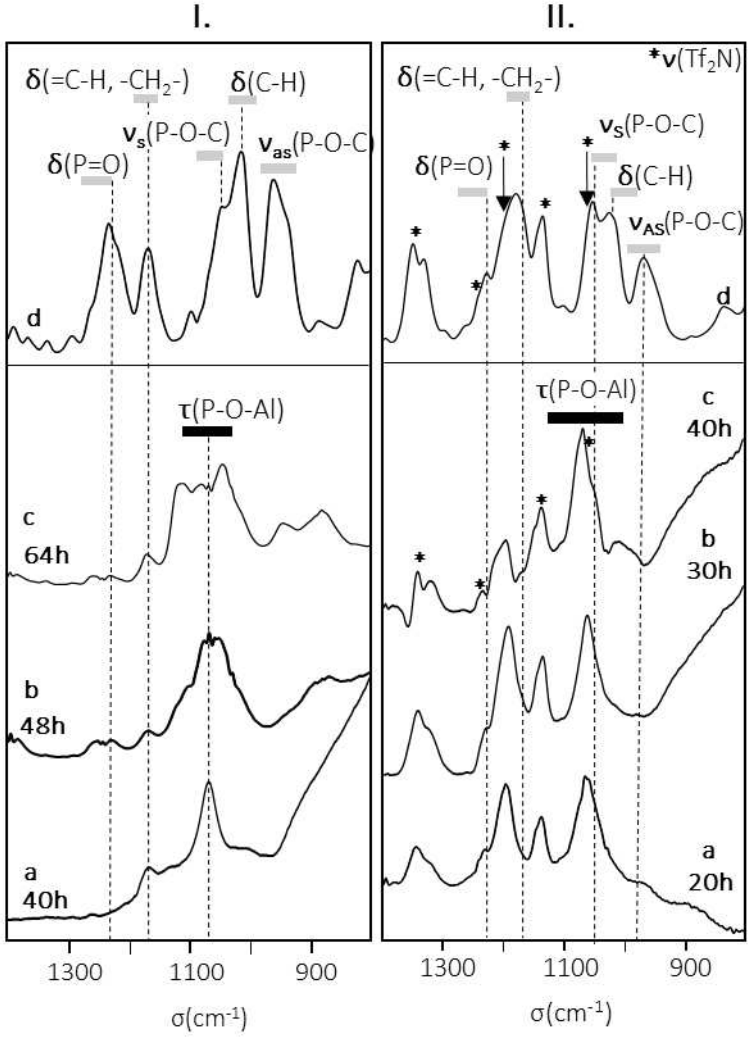

Figure III. 15. Experimental FTIR spectra of [ImPE][Br] IL (I.d), [ImPE][Tf_2N] IL (II.d) and respective grafted samples under forcing conditions at different reaction times (I.a) ImPE-Br (8)-40h, (I.b) ImPE-Br (10)-48h, (I.c) ImPE-Br (11)-64h, (II.a) ImPE-Tf_2N (1)-20h, (II.b) ImPE-Tf_2N (2)-30h, (II.c) ImPE-Tf_2N (3)-40h. The symbol (*) is used to indicate the positions of the Tf_2N- vibration bands.

- *^{19}F NMR*

The solid-state ^{19}F NMR was used both to highlight the presence the Tf_2N^- anion in the grafted samples and to confirm the preservation of their integrity. In comparison with the ^{19}F NMR liquid spectrum of [ImPE][Tf_2N] which displays a thin peak corresponding to the $-CF_3$ functions at -78.7 ppm (Figure III. 16.I) , the ^{19}F MAS solid state NMR spectra of the grafted sample ImPE-Tf_2N (3) (Figure III. 16.II) shows a broad

signal centered at -80.6 ppm, corresponding to $–CF_3$ functions. The sharpening line in the ^{19}F liquid spectra of the IL is due to "motional narrowing", while the broad signal in the grafted samples can be explained by the cation immobilisation on the γ-Al_2O_3 surface, thus reflecting the difference between immobilized/grafted IL and pure liquid phase IL. No other signal was present thus confirming that Tf_2N^- anions were preserved during the grafting process as suggest by FTIR spectroscopy.

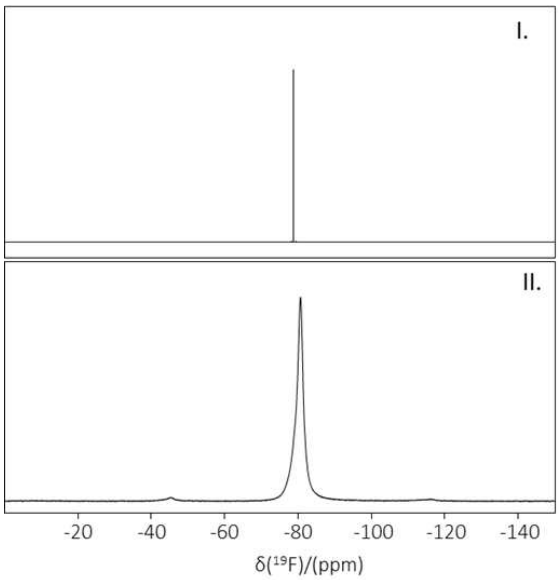

Figure III. 16. ^{19}F NMR spectra of I. pure liquid phase IL [ImPE][Tf_2N] (liquid NMR), II. grafted ImPE-Tf_2N (3) powder sample (MAS ssNMR).

- *^{31}P NMR*

^{31}P CP-MAS NMR was a useful tool to highlight the presence of the phosphorus atoms in the hybrid materials and to distinguish the grafted species from the bulk aluminum phosphonate phases. These latter have been largely described in the literature and are characterized by individual or multiple thin peaks in ^{31}P ssNMR [29, 30]. The ^{31}P CP-MAS NMR spectra of the samples grafted with either [ImPE][Br] or [ImPE][Tf_2N] unsing reaction times in the range 17h-92h, are shown in Figure III. 17.

For long grafting reaction times, the measured weight percentage of phosphorus (EDX analysis) was found to overpass the value expected for the sole surface modification. The high values recorded after 64h and 92h could be attributed to the presence of a supplementary dissolution-precipitation process leading to the formation of bulk aluminum phosphonate phases. The ^{31}P CP-MAS NMR spectra of the corresponding samples (*i.e. ImPE-Br (11) for 64h grafting and ImPE-Br (12) for 92h grafting*) (Figure III. 17.I), contain a unique thin symmetric peak at 12.6 ppm, characteristic of the ordered environment in bulk aluminum phosphonate phases [29]. Surprisingly, the same signal was observed for ImPE-Br (10) (*i.e., 48h of grafting*) and ImPE-Br (9) (*i.e., 45h of grafting*) in addition to the signal related to grafted species (cf. part III.2.).

The simulation of the ImPE-Br (9) and ImPE-Br (10) spectra (Figure III. 17, Table III. 10) reveals the presence of at least 3 sites for each samples (*i.e., at 23.6, 16.4 and 12.7 ppm for ImPE-Br (9), and 23.6, 17.9, 14.4 ppm for ImPE-Br (10)*). These two samples present equal proportions of grafted species (*i.e., characterized by the 23.6 and 17.9 ppm signals*) and bulk aluminum phosphonate phases (*i.e., characterized by the 12.7 and 14.4 ppm signals*). The sample obtained after 40h grafting (*i.e., ImPE-Br (8)*) presents the same spectrum than ImPE-Br (5) obtained previously (Figure III. 12). For both samples, the relative proportions of the three signals (32.4, 23.6 and 17.9 ppm) are really close and the same bonding modes can be attributed. As in the part III.3.2, the effect of the grafting reaction conditions on the bonding modes

can be evidenced. As an example, between 17h and 45h reaction (*i.e.,* from ImPE-Br (6) to ImPE-Br (9)) a constant increase in the proportion of the bidentate bonding mode (*i.e., indicated by the 18.1 and 17.9 ppm signals)* is noted, until 45h when the bulk aluminum phosphonate phase starts to appear.

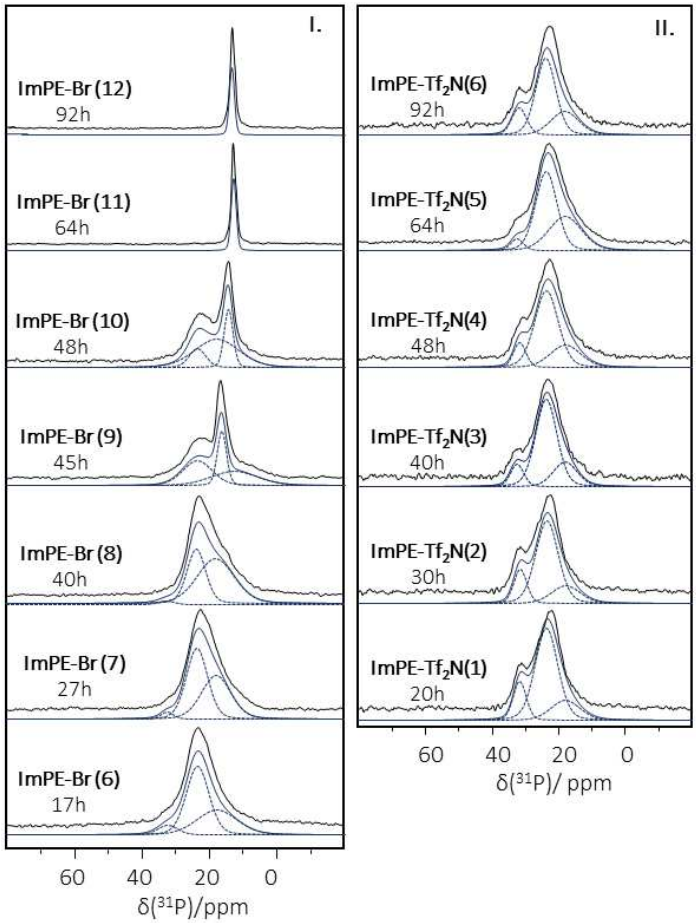

Figure III. 17. ^{31}P solid-state CP-MAS NMR spectra of grafted samples series: I) kinetic grafting study with [ImPE][Br], II) kinetic grafting study with [ImPE][Tf_2N].

^{31}P CP-MAS NMR spectra of the sample series grafted with [ImPE][Tf_2N], reveal a broad signal centered at 23.6 ppm and a spectrum shape similar to those observed for ImPE-Br samples series. The absence of the thin peaks characteristic of bulk aluminum phosphonate phase, even after long grafting times, highlights the strong impact of the anion nature on the grafting reaction mechanism. The [ImPE][Tf_2N] IL allows to limit the reaction to a grafting process. Difference could come from the lower solubility of [ImPE][Tf_2N] in aqueous solutions that imposed the use of organic co-solvent (H_2O:EtOH) potentially limiting the dissolution-precipitation process. The simulation of the different spectra reveals the presence of at least three sites in all the ImPE-Tf_2N samples (Figure III. 17, Table III. 11) at the same positions than those of the ImPE-Br series. On the basis of the results obtained for the optimized sample (ImPE-Br (5)) and the IR analysis which presents only residual P-O-C bands, we can tentatively ascribe the different signals and bonding modes as follows:

i) signals at 32.4 and 31.6 ppm : monodentate bonding mode,
ii) signal at 17.9 ppm : bidentate bonding mode,
iii) signal at 23.6 ppm : tridentate bonding mode.

In addition, the integration of the different resonances indicates that the tridentate bonding mode seems to be the dominating one for the grafted species.

Table III. 10. Parameters used for the ^{31}P CP-MAS NMR spectra simulation of samples grafted with [ImPE][Br] using different reaction times (kinetic study).

Sample	ImPE-Br (6) 17h			ImPE-Br (7) 27h			ImPE-Br (8) 40h			ImPE-Br (9) 45h		
δ (ppm)	32.4	23.6	17.9	32.4	23.6	17.9	32.4	23.6	17.9	23.6	16.4	12.7
Width (ppm)	8.4	62.9	22.7	3.7	41.5	25.5	3.2	41.5	25.5	22.6	49.8	12.5
Integration (%)	7	57	37	3	52	45	2	37	61	39	27	34

Sample	ImPE-Br (10) 48h			ImPE-Br (11) 64h	ImPE-Br (12) 92h
δ (ppm)	23.6	17.9	14.4	12.8	12.4
Width (ppm)	13.5	20.1	41.9	73.1	69.2
Integration (%)	15	61	24	100	100

Table III. 11. Parameters used for the ^{31}P CP-MAS NMR spectra simulation of samples grafted with [ImPE][Tf_2N] using different reaction times (kinetic study).

Sample	ImPE-Tf2N (1) 20h			ImPE-Tf2N (2) 30h			ImPE-Tf2N (3) 40h			ImPE-Tf2N (4) 48h		
δ (ppm)	31.6	23.6	17.9	31.6	23.6	17.9	32.4	23.6	17.9	31.6	23.6	17.9
Width (ppm)	30.2	67.7	14.5	28.8	67.9	14.8	13.1	51	14.1	24.6	74.6	22.7
Integration (%)	21	62	17	16	66	18	11	68	21	11	64	25

Sample	ImPE-Tf2N (5) 64h			ImPE-Tf2N (6) 92h		
δ (ppm)	32.4	23.6	17.9	31.6	23.6	17.9
Width (ppm)	9	59.5	25.4	19.8	54.9	17.1
Integration (%)	5	57	38	16	58	26

- *^{27}Al MAS NMR*

^{27}Al MAS NMR spectra of the grafted samples ImPE-Tf_2N and ImPE-Br series are respectively presented in Figure III. 18 and Figure III. 19.

^{27}Al MAS NMR spectra of ImPE-Tf_2N samples were very similar to the γ-alumina spectrum. The two signals at 10.6 and 69.2 ppm, corresponding respectively to aluminum atoms in octahedral (Al_{VI}) and tetrahedral (Al_{IV}) coordination modes, were still present and confirmed that the γ-alumina structure is maintained in all samples (Figure III. 18). The pristine γ-alumina contains five-coordinated aluminum atoms with an additional weak signal around 35 ppm (Figure III. 18). The variable amounts of Al_V, certainly due to short exposure to atmospheric water, are mainly located at the surface of the oxide [35]. After the grafting treatments, Al_V resonances were no more detected as expected after the drying treatment and/or possible reaction with the phosphonate coupling agents. As expected, no additional resonance was detected, thus confirming the absence of bulk aluminum phosphonate phases already highlighted using EDX and ^{31}P ssNMR.

^{27}Al MAS NMR spectra of ImPE-Br grafted samples series (Figure III. 19), reveal the progressive formation of bulk aluminum phosphonate phases through the appearance after 45h grating (*i.e.,*

ImPE-Br (9) of a new resonance at ~-5 ppm whose intensity increases with the grafting time from 45h to 92h. In parallel, when the grating time increases, the progressive disappearance of the Al_{IV} atoms coordination mode is highlighted to the benefit of the formation of the thin resonance attributed to Al_{VI} atoms in aluminum imidazolium-based phosphonate phase [54]. The occurrence of this signal fits the conclusions derived from ^{31}P MAS NMR, XRD and EDX analysis: after ~40h grafting time, a dissolution-precipitation phonomena occurs, leading to the formation of an aluminum phosphonate lamellar phase.

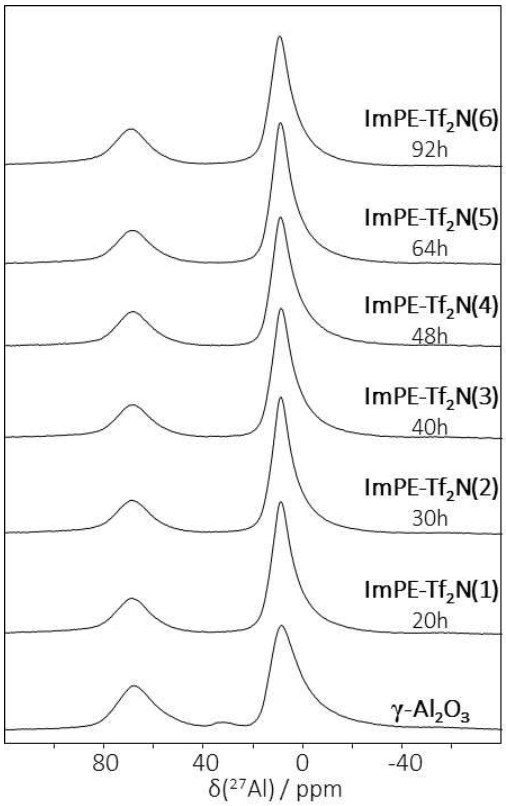

Figure III. 18. ^{27}Al MAS NMR spectra for pristine γ-alumina and for selected samples of the ImPE-Tf_2N series.

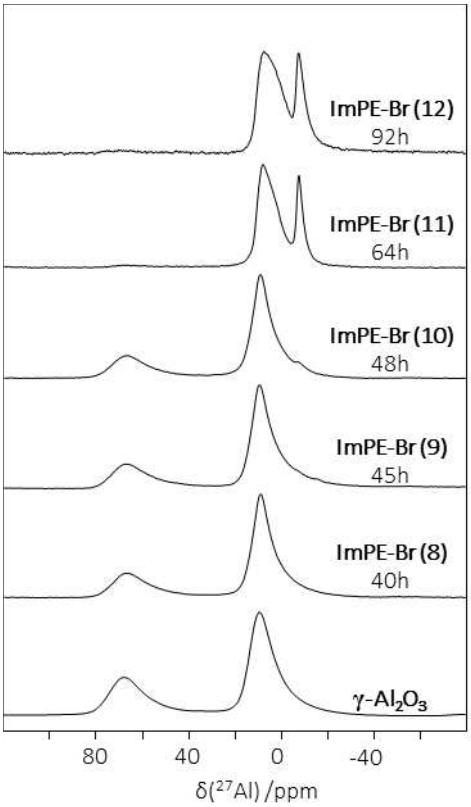

Figure III. 19. ^{27}Al MAS NMR spectra for pristine γ-alumina and for selected samples of the ImPE-Br series.

- *XRD*

The XRD patterns of ImPE-Tf_2N and ImPE-Br grafted samples are presented respectively in Figure III. 20 and Figure III. 21. The γ-alumina structure is maintained in all the ImPE-Tf_2N sample series and until 40h reaction time for the ImPE-Br samples (Figure III. 20).

In the ImPE-Tf_2N sample series, additional boehmite diffraction peaks can be detected after ~30h reaction. The intensity of these peaks does not clearly increase for longer reaction times, but they reaveal a partial hydrolysis of the support (surface or bulk) during the grafting treatment (*A such reaction might help or compete with the grafting reaction. It should be interesting to clarify this point and the role of boehmite formation in the grafting process*.).

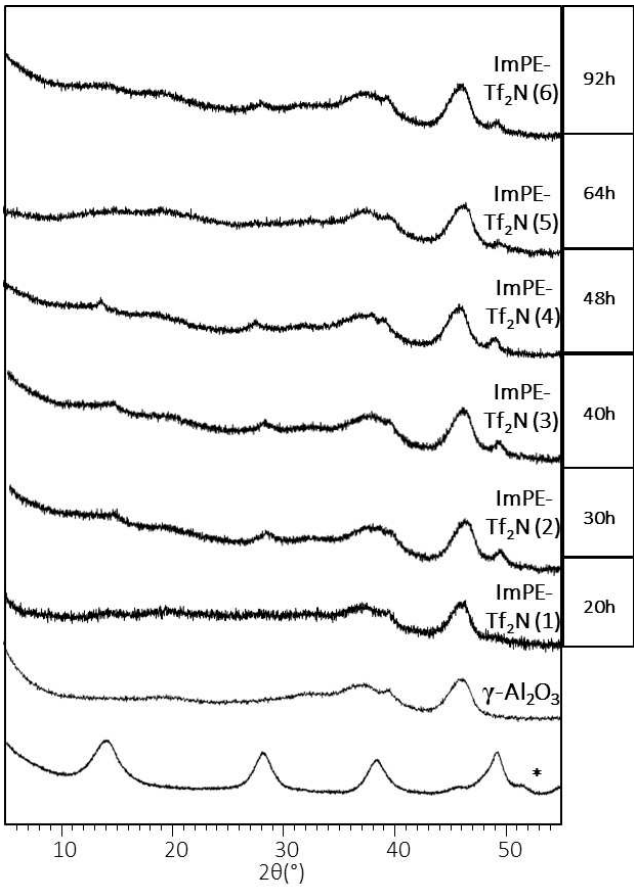

Figure III. 20. XRD diffraction patterns for pristine γ-alumina, for selected samples of the ImPE-Tf_2N series and for boehmite (*).

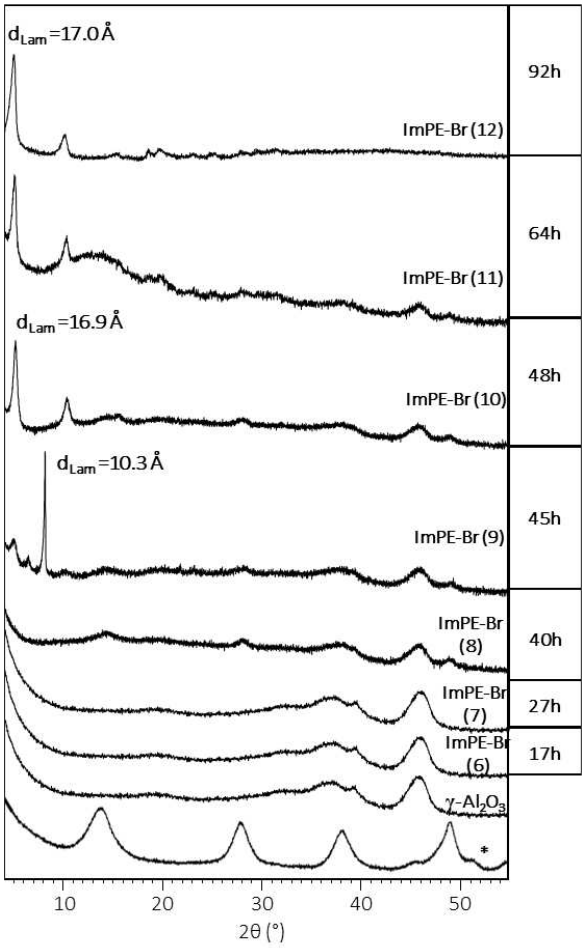

Figure III. 21. XRD diffraction patterns for pristine γ-alumina, for selected samples of the ImPE-Br series and for boehmite (*).

Boehmite was also detected in the ImPE-Br sample series, after ~40h grafting (*i.e., ImPE-Br (8)*) (Figure III. 20). The XRD patterns of ImPE-Br (9) to ImPE-Br (12) are presented in Figure III. 21. In each case, we can distinguish a low angle diffraction peak characteristic of lamellar structures, with an interlamellar spacing d_{001} (related to inter-sheets distance) from 10.3 to 17.0 Å. As an example, the interlamellar spacing for aluminium phenylphosphonate phases is classically in the range 14-15 Å; the proposed structure is shown in Figure III. 22 [51], with phenyl groups in adjacent positions. However, this structural organization could vary depending on the reaction conditions; the interlamellar spacing can increase for less well-packed arrangements [52].

These results suggest in both case a dissolution mechanism resulting from an hydrolysis of the γ-alumina support leading to: *i) the formation of boehmite for [ImPE][Tf_2N] and [ImPE][Br] and ii) the formation of bulk aluminium phosphonate phases for [ImPE][Br]*.

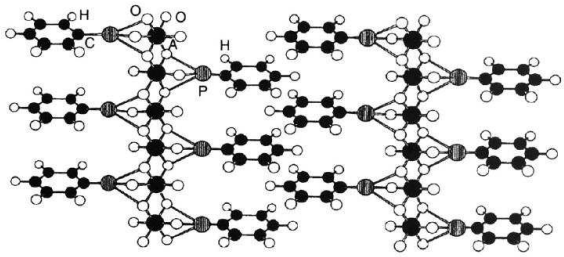

Figure III. 22. Structure of an aluminium phenylphosphonate phase proposed by Raki *et al.* [51].

III.3.3.3. Conclusion

The kinetic investigation of the grafting reaction revealed that surface coverage can be improved using forcing reaction conditions with selected reaction times for controling the grafting density on the γ-alumina surface. Boehmite was detected by XRD after 30-40h reaction for both [ImPE][Tf_2N] and [ImPE][Br] samples. Bulk aluminum phosphonate phases were only detected for [ImPE][Br] after 45h reaction. The hydrolysis of [ImPE][Br] and [ImPE][Tf_2N] in forcing aqueous conditions leads, in solution, to the formation of parent phosphonic acids or monoester species in different proportions. However, the hydrolysis kinetics of [ImPE][Br] and [ImPE][Tf_2N] strongly differ under the same experimental conditions. [ImPE][Tf_2N] IL seems to be more stable than [ImPE][Br] in aqueous media; this is in favor of a sole grafting reaction pathway for [ImPE][Tf_2N] while bulk aluminum phosphonate phases are form more easily with [ImPE][Br]. Thus, the chemical nature of the anion and the reaction time must be carefully chosen to control γ-alumina dissolution and/or avoid or minimize the formation of bulk aluminum phosphonate phases.

The best reaction conditions for each IL are summarized in Table III. 12. In the ImPE-Br sample series, we selected the longer possible reaction time (40 h) without any detection of bulk aluminum phosphonate phase. In the ImPE-Tf_2N series, we selected the sample prepared after a 40h grafting, in order to limit the γ-alumina dissolution.

Table III. 12. Optimized grafting reaction conditions yielding high grafting density with [ImPE][Br] and [ImPE][Tf_2N] IL.

Grafted sample	IL	Solvent (mL)	Reaction T (°C)	n-fold excess	Reaction time (h)	P wt%	^{31}P NMR spectra
ImPE-Br (8)	[ImPE][Br]	H_2O (10)	130	12	40	1.73 ± 0.08	3 signals (32.4, 23.6, 17.9 ppm)
ImPE-Tf_2N (3)	[ImPE][Tf_2N]	H_2O:EtOH (10)	130	12	40	1.34 ± 0.08	3 signals (31.6, 23.6, 17.9 ppm)

III.3.4. Influence of the IL organic spacer on the grafting

The important role of the anion on the stability of dialkylphosphonate esters during grafting under aqueous forcing conditions was previously demonstrated, as well as the predominance of the grafting process towards the dissolution-precipitation phenomenon. In chapter II, we also evidenced the influence of the organic spacer on both CO_2 solubility and CO_2/N_2 solubility selectivity. On the basis of these previous results, we aimed to determine the best-operating conditions for grafting either [ImC_{12}PE][Tf_2N] (*i.e., the 1-methyl-3-(3-(diethyl-phosphinyl)dodecyl)-imidazolium bis(trifluoromethanesulfonimide)* or [ImPEGPE][Tf_2N] (*i.e., the 1-methyl-3-(3-(diethylphosphinyl)2–(2–(2–(2–ethoxy)ethoxy)ethoxy)ethyl)-imidazolium bis(trifluoromethane-sulfonimide)* in forcing reaction conditions. As previously observed during the kinetic studies, a hydrolysis phenomenon occurs between 40 and 50h reaction. Thus, we decided to

limit the grafting reaction times to 48h. The synthesis of [ImC_{12}PE][Tf_2N] and [ImPEGPE][Tf_2N] ILs were described in Chapter II. More details about the hydrolysis reactions of these ILs is provided in ANNEX 4.

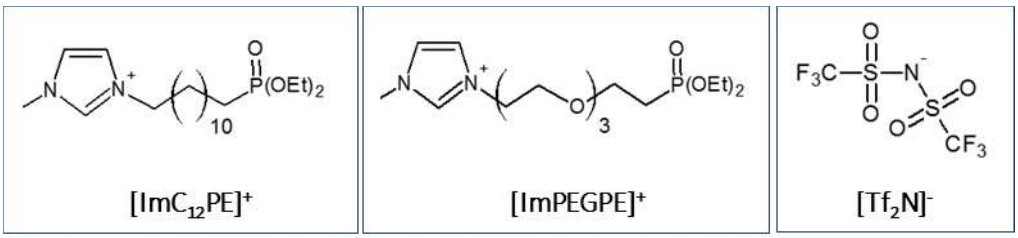

Figure III. 23. Structure of the phosphonate-based ILs with two different organic spacers.

III.3.4.1. Protocol for the preparation of the grafted powder

The preparation protocol is identical to the protocol used for [ImPE][Tf_2N] (III. 3.3). The only difference comes from the concentration of the IL solution which was fixed to a 6-fold excess because of the poor IL solubility at high concentration. The reaction times used for grafting [ImC_{12}PE][Tf_2N] and [ImPEGPE][Tf_2N] on γ-alumina in forcing conditions are reported in Table III. 13.

Table III. 13. Reaction time used for the grafting of [ImC_{12}PE][Tf_2N] and [ImPEGPE][Tf_2N] in Forcing conditions.

Sample	ImC_{12}PE-Tf_2N (1)	ImC_{12}PE-Tf_2N (2)	ImPEGPE-Tf_2N (1)	ImPEGPE-Tf_2N (2)
Time (h)	20	40	20	40

III.3.4.2. Characterizations

All the grafted samples were characterized by EDX analysis, X-Ray diffraction, IR spectroscopy, ^{31}P and ^{27}Al ssNMR.

- *EDX*

The Table III. 14 summarizes the average phosphorus weight percentage for each samples. The results are consitent with sole surface grafting reactions of the IL coupling agents on γ-Al_2O_3 and do not exceed the values for full surface coverage *(i.e., 2.2 P wt% for [ImC_{12}PE][Tf_2N] and 2.3 wt % for [ImPEGPE][Tf_2N]).* For both ILs, we note a constant increase in the quantity of grafted species when grafting time increases. A maximum grafting density is achieved for 40h reaction with a maximum value of 2.5 P nm^{-2} for ImC_{12}PE-Tf_2N and of 2.6 P nm^{-2} for ImPEGPE-Tf_2N representing respectively 62.5 and 65% of the full monolayer. Thus, in comparison with previous results (Table III. 9), the nature of the organic spacer does not seem to be a key factor to optimize the grafting density.

Table III. 14. Characteristics of the γ-alumina powders grafted with [ImC_{12}PE][Tf_2N] and [ImPEGPE][Tf_2N] in forcing reactions conditions.

Sample	ImC_{12}PE-Tf_2N (1)	ImC_{12}PE-Tf_2N (2)	ImPEGPE-Tf_2N (1)	ImPEGPE-Tf_2N (2)
Time (h)	20	40	20	40
P wt%	1.24 ± 0.15	1.43 ± 0.39	0.91 ± 0.04	1.47 ± 0.06
P nm^{-2}	2.2	2.5	1.6	2.6

- *FTIR spectroscopy*

The Figure III. 24. shows the infrared spectra for pure [ImC$_{12}$PE][Tf$_2$N] and [ImPEGPE][Tf$_2$N] IL, with a focus at the 1400-800 cm^{-1} region. As already observed for [ImPE][f$_2$N] (cf. Figure III. 15), the two spectra are dominated by the vibrations of the Tf$_2$N$^-$ anion at 1346, 1327, 1124, 1127, 1132 and 1061 cm^{-1}. The P=O stretching vibrations were associated to the bands at 1250 cm^{-1} for [ImPEGPE][Tf$_2$N] and 1236 cm^{-1} for [ImC$_{12}$PE][Tf$_2$N] respectively. The asymmetric and symmetric P–O-C stretching vibrations were located respectively at 960 and 1050 cm^{-1} [21,30] in the same range than for [ImPE][Tf$_2$N] derived samples.

Concerning the grafted samples, the IR spectra were also dominated by absorption bands related to the Tf$_2$N$^-$ anions at 1346, 1327, 1224, 1195, 1132 and 1061 cm^{-1}, and confirmed again the presence and the conservation of the anion integrity as detected by EDX analysis (results not shown). Concerning the cationic part, we can notice a decrease of the intensity of the phosphoryl (P=O) stretching bands for both samples. As already observed in sections III.3.2 and III.3.3, a strong absorption band was observed at 1058 cm^{-1}, which is attributed to the P-O-Al stretching vibration.

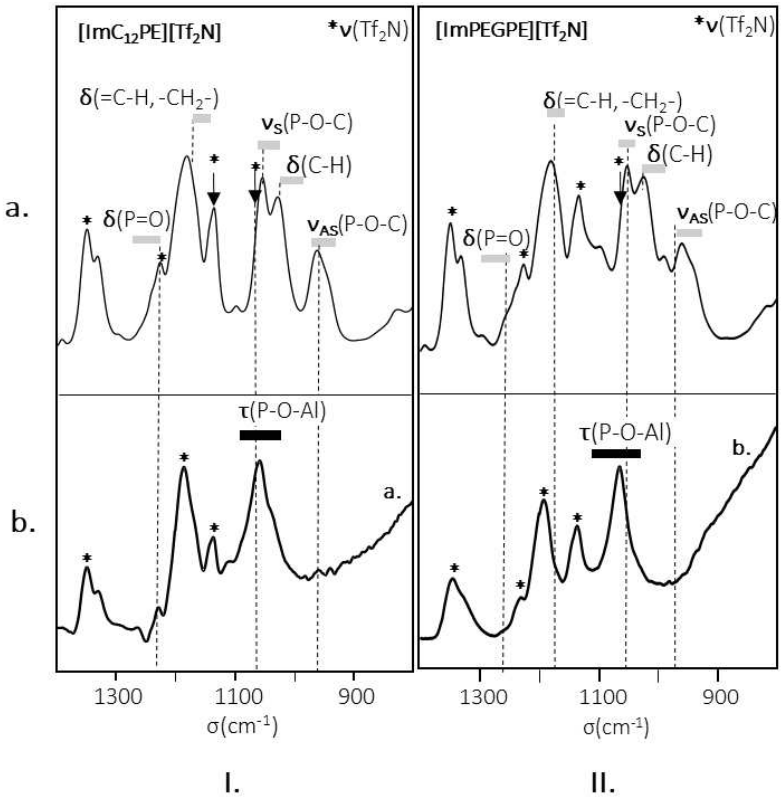

Figure III. 24. Experimental FTIR spectra of: a) pure ILs: [ImC$_{12}$PE][Tf$_2$N] (I.a.) and [ImPEGPE][Tf$_2$N] (II.a), b) γ-Al$_2$O$_3$ samples grafted with: ImC$_{12}$PE-Tf$_2$N (2) (I.b) and ImPEGPE-Tf$_2$N (2) (II.b).

- *^{31}P NMR*

The ^{31}P CP-MAS NMR spectra of the ImC$_{12}$PE-Tf$_2$N and ImPEGPE-Tf$_2$N samples are presented in Figure III. 25.

The ^{31}P spectra ImC$_{12}$PE-Tf$_2$N (1) and (2) show two dominant signals, the first one is centered at 25 ppm while the second is at 33 ppm for ImC$_{12}$PE-Tf$_2$N (1) and 31.7 ppm for ImC$_{12}$PE-Tf$_2$N (2). The simulation of the different spectra using a minimum number of resonance lines with a Gaussian-Lorentzian shape reveals the presence of at least two equivalent in the ImC$_{12}$PE-Tf$_2$N (1) sample and, a high fiel additional resonance

for $ImC_{12}PE\text{-}Tf_2N$ (2) (Figure III. 25, Table III. 15). The broad signal centered at ~0 ppm on the spectra of $ImC_{12}PE\text{-}Tf_2N$ samples is attributed to impurities in the solid-state NMR rotor.

Two signals are also observed for $ImPEGPE\text{-}Tf_2N$ samples at ~21 and 30 ppm and are similar to those observed for $ImC_{12}PE\text{-}Tf_2N$ samples. The spectra simulation reveals the presence of at least three sites for $ImPEGPE\text{-}Tf_2N$ (2) and four sites for $ImPEGPE\text{-}Tf_2N$ (1) (Figure III. 25, Table III. 15). In the case of $ImPEGPE\text{-}Tf_2N$ (2), we can note the disappearance of the signal at 30.8 ppm attributed to residual physisorbed species. The evolution of the peaks integration with the grafting reaction time suggests that the grafted species continues to rearrange on the surface.

By comparison with ^{31}P ssNMR spectra of $ImPE\text{-}Tf_2N$ samples presented previously (cf. Figure III. 17), the chemical shifts of the different resonances were quiet similar for $ImPEGPE\text{-}Tf_2N$ and $ImC_{12}PE\text{-}Tf_2N$ samples. Nevertheless, the major bonding mode was the tridentate in $ImPE\text{-}Tf_2N$ samples. The overall shape of the ^{31}P NMR signals allowed us to tentatively conclude to the presence of a mixture of phosphonate units in a monodentate (~33 ppm), a tridentate (~21 and ~25ppm) and a bidentate (~18 ppm) bonding modes in different proportions according to reaction parameters. In the case of $ImC_{12}PE\text{-}Tf_2N$, well-packed arrangements were expected on the alumina surface as already described for long hydrocarbon chained phosphonic acids in self-assembled monolayer (SAMs) which lead to ^{31}P NMR spectra with thin resonances characterizing the well-packed arrangement of the grafted species [53]. The multiple broad resonances present in $ImC_{12}PE\text{-}Tf_2N$ samples indicated that this kind of self-assembled organization was not present in our samples as a result of steric hindrance or disorder.

To finish, it must be noted that in the case of the $ImC_{12}PE\text{-}Tf_2N$ and $ImPEGPE\text{-}Tf_2N$ samples, the correlation between IR and ssNMR spectroscopy is more difficult than in the case of $ImPE\text{-}Tf_2N$ samples to make assumptions on the different bonding modes due to the preponderance of the Tf_2N^- adsorption bands.

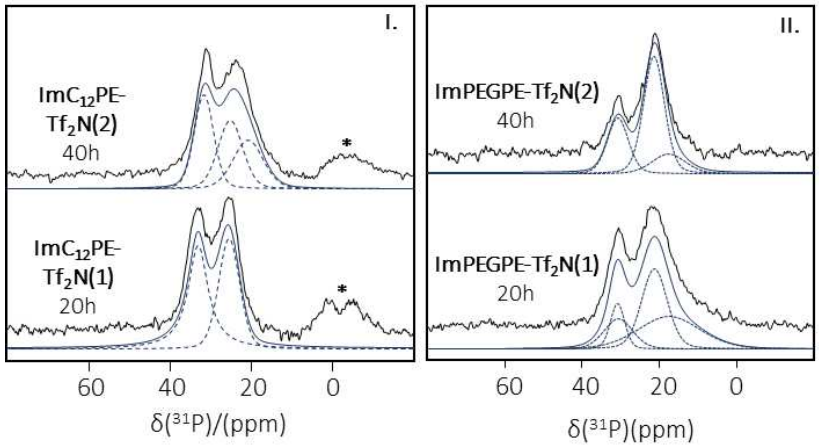

Figure III. 25. ^{31}P solid-state CP-MAS NMR spectra of $\gamma\text{-}Al_2O_3$ grafted with: I) $ImC_{12}PE\text{-}Tf_2N$, and II) $ImPEGEPE\text{-}Tf_2N$. (*) signal attributed to impurities in the rotor.

Table III. 15. Parameters used for the ^{31}P CP-MAS NMR spectra simulation of samples grafted with $[ImC_{12}PE][Tf_2N]$ and $[ImPEGPE][Tf_2N]$.

Grafted Sample	$ImC_{12}PE\text{-}Tf_2N$ (1) 20h		$ImC_{12}PE\text{-}Tf_2N$ (2) 40h			$ImPEGPE\text{-}Tf_2N$ (1) 20h				$ImPEGPE\text{-}Tf_2N$ (2) 40h		
δ (ppm)	33.08	25.4	31.7	25.2	20.8	30.8	30.6	21.3	17.5	30.6	21.3	17.5
Width (ppm)	6	6.1	65.7	48.1	34.4	4.4	8.8	7.9	18.9	6.5	6.4	10.3
Integration (%)	42	58	34	36	30	12	16	37	36	28	57	15

- *XRD*

The XRD patterns of $ImC_{12}PE\text{-}Tf_2N$ and $ImPEGPE\text{-}Tf_2N$ samples confirmed that the γ-alumina structure is maintained in all cases (Figure III. 26 and Figure III. 27). The formation of boehmite was slightly detected in the grafted samples indicating the slight hydrolysis of the alumina support in some samples. Nevertheless, as suggested by ^{31}P CP-MAS ssNMR, no resonances corresponding to the formation of bulk aluminum phosphonate phases were found. This was confirmed using XRD spectroscopy with the absence of thin peaks at low angles.

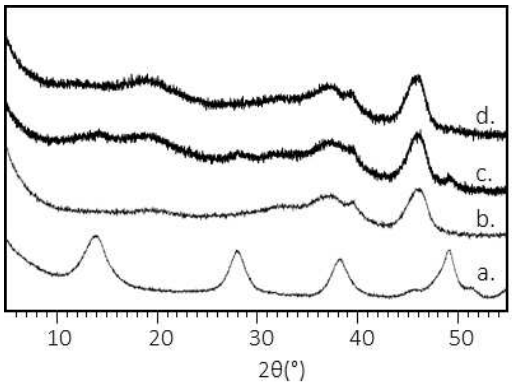

Figure III. 26. XRD patterns of a) Boehmite, b) pristine γ-alumina powder, c) $ImC_{12}PE\text{-}Tf_2N$ (1), and d) $ImC_{12}PE\text{-}Tf_2N$ (2) grafted samples.

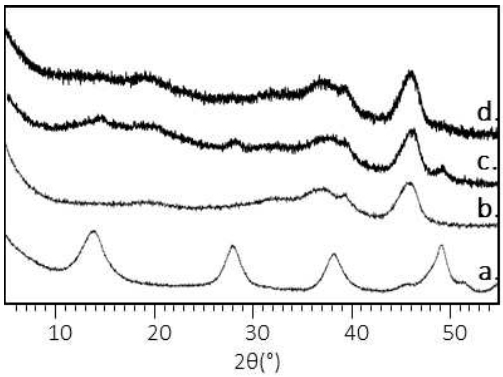

Figure III. 27. XRD patterns of: a) Boehmite, b) pristine γ-alumina powder, c) $ImPEGPE\text{-}Tf_2N$ (1), and d) $ImPEGPE\text{-}Tf_2N$ (3) grafted samples

- *^{27}Al NMR*

^{27}Al MAS NMR spectra of the $ImC_{12}PE\text{-}Tf_2N$ and $ImPEGPE\text{-}Tf_2N$ samples (Figure III. 28 and Figure III. 29) were very similar to the spectra of $ImPE\text{-}Tf_2N$ samples and γ-alumina. The two signals at 9.3 and 69.2 ppm corresponding respectively to aluminum atoms in octahedral (Al_{VI}) and tetrahedral (Al_{IV}) coordination modes were also present and confirmed that the γ-alumina structure is maintained in all the samples (Figure III. 28 and Figure III. 29). After grafting treatments with $ImC_{12}PE\text{-}Tf_2N$ and $ImPEGPE\text{-}Tf_2N$, no Al_V resonances were detected probably due to the drying treatment and/or their reactivity with the phosphonate coupling agents as in the case of $ImPE\text{-}Tf_2N$ samples. No additional high-field resonance were detected in good agreement with the absence of bulk aluminum phosphonate phases already highlighted using EDX and ^{31}P ssNMR.

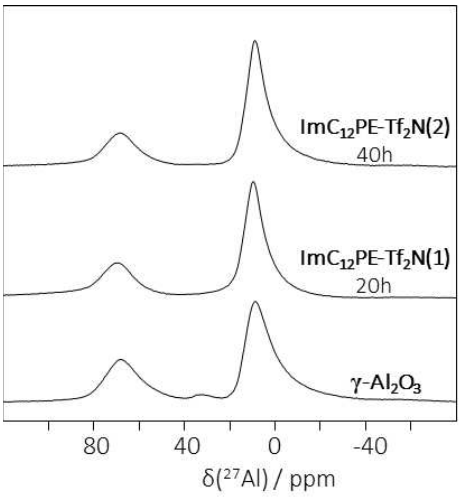

Figure III. 28. ^{27}Al MAS NMR spectra of pristine γ-alumina and $ImC_{12}PE\text{-}Tf_2N$ samples.

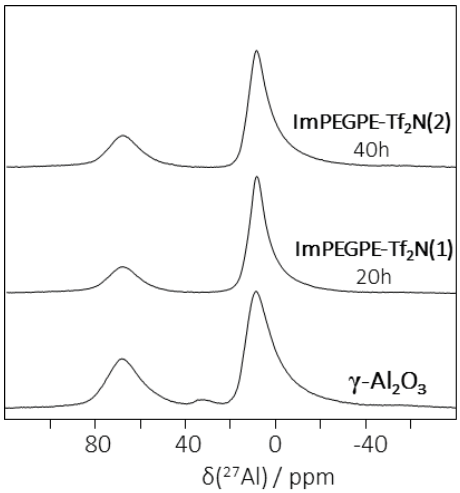

Figure III. 29. ^{27}Al MAS NMR spectra of pristine γ-alumina and $ImPEGPE\text{-}Tf_2N$ samples.

III.3.4.3. Conclusion

This last part of the work was focused on the determination of the best operating conditions for grafting either [ImC_{12}PE][Tf_2N] (*i.e., the 1-methyl-3-(3-(diethyl-phosphinyl)dodecyl)-imidazolium bis(trifluoromethanesulfonimide)* or [ImPEGPE][Tf_2N] (*i.e., the 1-methyl-3-(3-(diethylphosphinyl)2–(2–(2–(2–ethoxy)ethoxy)ethoxy)ethyl)-imidazolium bis(trifluoromethane-sulfonimide)* on γ-alumina in forcing reaction conditions. By controlling the grafting reaction time, we can avoid/limit the formation of boehmite (detected on XRD patterns). Despite the strong intensity of the adsorption bands of the Tf_2N^- anions in FTIR spectroscopy, we tentatively tried to ascribe the different bonding modes through the use of the ^{31}P ssNMR spectroscopy. We showed that in opposite to ImPE-Tf_2N grafted samples which present a major tridentate bonding mode, the grafting reactions with ImC_{12}PE-Tf_2N and ImPEGPE-Tf_2N led to samples with phosphonate units presenting different bonding modes in various proportions. However, other solid-state NMR techniques could be considered to obtain more information on the surface characteristic of these grafted samples.

The best grafting reaction conditions for each ILs are resumed in Table III. 16. A grafting reaction time of 40h was selected to yield a maximum surface coverage (~60%).

Table III. 16. Best grafting reaction conditions yielding maximum surface coverage with [imC_{12}PE][Tf_2N] and [ImPEGPE][Tf_2N].

sample	IL	Solvent (mL)	T (°C)	n-fold excess	time (h)	Wt (P) %	^{31}P NMR
ImC_{12}PE-Tf_2N	[ImC_{12}PE][Tf_2N]	H_2O:EtOH (10)	130	6	40	1.43 ± 0.39	3 signals (31.7, 25.2, 20.8 ppm)
ImPEGPE-Tf_2N	[ImPEGPE][Tf_2N]	H_2O:EtOH (10)	130	6	40	1.47 ± 0.06	3 signals (30.6, 21.3, 17.5 ppm)

III.4. Using NMR techniques for the study of grafted samples

In the previous part, we showed how FTIR and ^{31}P ssNMR can be used to study the influence of grafting reaction conditions on the bonding modes of phosphonate-based ILs grafted on γ-Al_2O_3 surface. Optimized reaction conditions were defined to maximize the quantity of grafted IL species on the surface, and these protocols can be now transferred to porous γ-Al_2O_3 membrane supports (cf. chapter IV). A relevant characterization protocol has been proposed to differentiate the spectroscopic signature of physisorbed species, grafted species and bulk aluminum phosphonate phases. Assumptions were made about the possible bonding modes of the phosphonate groups grafted on the γ-Al_2O_3 surface, but their definitive surface assignments cannot be confirmed.

To obtain this information, high-field ^{17}O MAS NMR can be used as shown in the study of Brodard-Severac *et al.* [28], investigating the binding of self-assembled monolayers of ^{17}O enriched phosphonic acids on titania anatase surface. Such experiments require ^{17}O enrichment of the samples (the coupling agents) and are thus expensive. As an alternative, the spatial proximity between the ^{31}P nuclei of phosphonate-based ILs and the ^{27}Al nuclei of γ-Al_2O_3 surface could be attractively investigated by using double resonance NMR methods. Indeed, in most cases the demonstration of the spatial proximity is selective enough to be representative of the chemical connectivity [55]. Only few of the possible available methods can be applied to our systems. As an example, the basic CP (cross-polarisation) experiment is difficult when the system contains quadrupolar nucleus such as the ^{27}Al, due to quadrupolar interactions. Trébosc and co-workers [56] proposed the 2D *D*-HMQC method to demonstrate the spatial proximity between phosphorus and quadrupolar nuclei in mixed phosphate network materials. This technique is significantly more robust for the correlation between spin ½ and quadrupolar nuclei. Even if the concentration of phosphorus in their systems is higher compare to our samples, the *D*-HMQC method seems adaptable to our study. Another possible way to identify IL/oxide surface interactions is HR-MAS (High-Resolution Magic Angle Spinning) NMR spectroscopy.

Recently, ^{1}H HR-MAS NMR was used to investigate macroporous alumina membranes (pore size ~200 nm) containing [MBPyrr][Tf_2N][6] IL physisorbed into the porous network [57]. The authors were able to identify the ^{1}H nuclei affected by IL/oxide surface interactions. By using the 2D ^{1}H HR-MAS NOESY NMR experiments, the authors also showed that correlation experiments could demonstrate the decrease of local motions, the presence of different conformations, and the appearance of new chemical environments for the adsorbed IL.

In this section, both D-HMQC and HR-MAS solid-state NMR techniques will be explored in order to further investigate the surface configuration of the phosphonate-based grafted samples. New experimental ssNMR techniques, specifically relevant for studying the grafted samples series, have been developed. D-HMQC experiments were conducted with **Prof G. Silly** from the ICGM-Montpellier. HR-MAS analysis was also carried out by **Dr. P. Gaveau** from ICGM and **C. Totee** from the ENSC-Montpellier under the guidance of **Prof. G. Silly**. All experiments were made on the *ssNMR Platform of Analysis and Characterization* hosted at the University of Montpellier-France.

[6] [MBPyrr][Tf_2N]: *N*-methyl-*N*-(n-butyl) pyrrolidinium bis(trifluoromethanesufonyl) imide

III.4.1. D-HMQC NMR experiments

As mentioned in section III.2.2, hydroxyl surface groups can be involved in the grafting mechanisms through the condensation of P-OCH_2CH_3 functions with Al-OH surface groups. Thus, ^{1}H-^{27}Al D-HMQC experiments can be used to evidence the different types of OH-groups on the alumina surface. Both ^{1}H-^{27}Al and ^{31}P-^{27}Al D-HMQC experiments will be then applied to study several samples grafted with [ImPE][Br] IL in forcing reaction conditions (model sample). Finally, D-HMQC experiments will be used to understand the structural transformation leading to the formation of bulk aluminum phosphonate phase in the [ImPE][Br] grafted samples series.

III.4.1.1. General

The D-HMQC NMR pulse sequence derives from the J-HMQC sequence and allows here to study both the ^{31}P-^{27}Al and ^{1}H-^{27}Al spacial proximity. During the experiment (Figure III. 30.a), the dipolar coupling interaction between the ^{27}Al and ^{31}P (or ^{1}H) nuclei are restored under MAS by applying a dipolar recoupling scheme named "SR_4^{21}" which was rotor-synchronized during τ (excitation and reconversion periods). During the first τ delay, the dephasing of the ^{27}Al nuclei allows the creation of heteronuclear multiple-quantum coherences through the first π/2 pulse on the ^{31}P channel. During t_1, the multiple-quantum coherences evolve and are converted back into observable central transition transverse magnetization of ^{27}Al nuclei by the second π/2 pulse on ^{31}P nuclei (t_1=n.τ). With this experiment, one or two-dimensional correlation NMR spectra can be obtained. A 1D NMR spectra allows observing the ^{27}Al or the ^{31}P NMR spectra issued from the projection of correlation experiment. Compared to the basic ^{27}Al spin-echo NMR spectra, ^{31}P-^{27}Al 1D-HMQC shows only the ^{27}Al nuclei which are close to ^{31}P (or ^{1}H) nuclei (Figure III. 30.b). If there is no spatial proximity between the nuclei, no signal is observed (Figure III. 30.b). At the opposite, a 2D correlation map allows visualizing the direct spatial proximity between ^{1}H (or ^{31}P) and ^{27}Al nuclei.

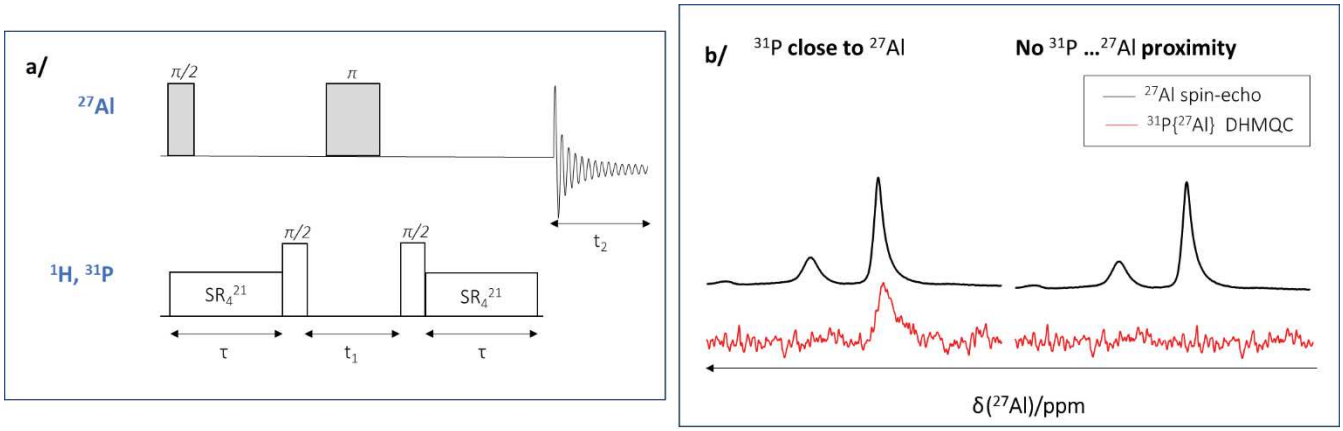

Figure III. 30. **a/** Schematic representation of the ^{1}H or ^{31}P-^{27}Al D-HMQC NMR sequence used, **b/** comparison of spectra acquired with recoupling and ^{31}P π/2 pulses allows for ^{27}Al-(^{31}P) proximities.

III.4.1.2. ^{1}H-^{27}Al D-HMQC

Thanks to ^{1}H-^{27}Al D-HMQC experiments, Taoufik *et al.* [41], established the first coordination map of surface hydroxyl groups on a commercial γ-Al_2O_3 powder (Degussa) dehydroxylated at 500°C. The authors demonstrated the robustness and highlighted the variety and high concentration of OH-groups on the surface (Table III. 17). It must be noted that the chemical shift for Al_{IV} (tetra-coordinate), Al_V

(pentacoordinate) and Al_{VI} (hexacoordinate) are attributed to signals around 60, 40, and 0 ppm, respectively.

In our case, the γ-Al_2O_3 powder was prepared by a sol-gel process adapted to cast a thin γ-Al_2O_3 layer on ceramic membrane supports. The final thermal treatment was realized under N_2 at 400°C, and the powder was stored under argon. As the nature of surface OH-groups strongly depends on the *starting material, synthesis method, thermal treatment and storage conditions* [35], we can expect that the surface hydroxyl groups of the sol-gel γ-Al_2O_3 powders will differ from those found in the Degussa γ-Al_2O_3 powder. Samples to be analysed were prepared in an argon glove-box to avoid any pollution with air moisture. We also used nitride boron drive caps to reduce the potential ^1H signal from the rotor.

Table III. 17. Hydroxyl surface groups on a Degussa γ-Al_2O_3 powder dehydroxylated at 500°C, according to Taoufik *et al.* [41].

Structure		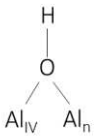	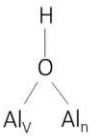	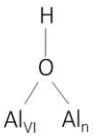	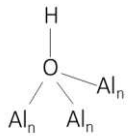
	μ_1	μ_2	μ_2	μ_2	μ_3
^1H [ppm]	-0.2	2.3-0.8	2.2 - 1.5	2.5 - 1.9	4.0 - 2.5
^{27}Al [ppm]	70	16	39	76	not determined

The 2D map spectrum derived from ^1H-^{27}Al D-HMQC experiments with the pristine γ-Al_2O_3 is shown in Figure III. 31.a. We distinguish two localized signals at **i)** 1.75 ppm on the ^1H projection spectra, **ii)** 9 and 35 ppm on the ^{27}Al projection spectra. The 2D ^1H-^{27}Al D-HMQC map reveals two types of ^{27}Al nuclei which are close to ^1H nuclei but in different coordination environments. In comparison, Taoufik and co-workers have observed HO-μ_2 types of OH-groups characterized by a broad correlation involving Al_{IV}, Al_V and Al_{VI} nuclei (Table III. 17). In our case, we suppose that the two independent signals could refer to either terminal or bridging hydroxyl groups, *i.e.,* μ_1 Al_{VI}-OH type at 9 ppm on the ^{27}Al chemical shift and μ_1 Al_V-OH type at 35 ppm or μ_2 Al_{VI}-Al_V-OH type.

^1H-^{27}Al D-HMQC experiment was also performed on the ImPE-Br (8) grafted sample with high grafting density. The sample to be analysed was also prepared in an argon glovebox. The 2D ^1H-^{27}Al D-HMQC spectra of ImPE-Br (8) (Figure III. 31.b.) shows that only Al_{VI} nuclei correlate with ^1H nuclei. The broad signal allows only to conclude that the ^1H nuclei involved in the correlation are in the range of chemical shift observed for the ^1H nuclei of the cation. Nevertheless, this experiment evidences the ^1H-^{27}Al spatial proximity *i.e.,* potential interaction between the IL nuclei and the γ-Al_2O_3 surface.

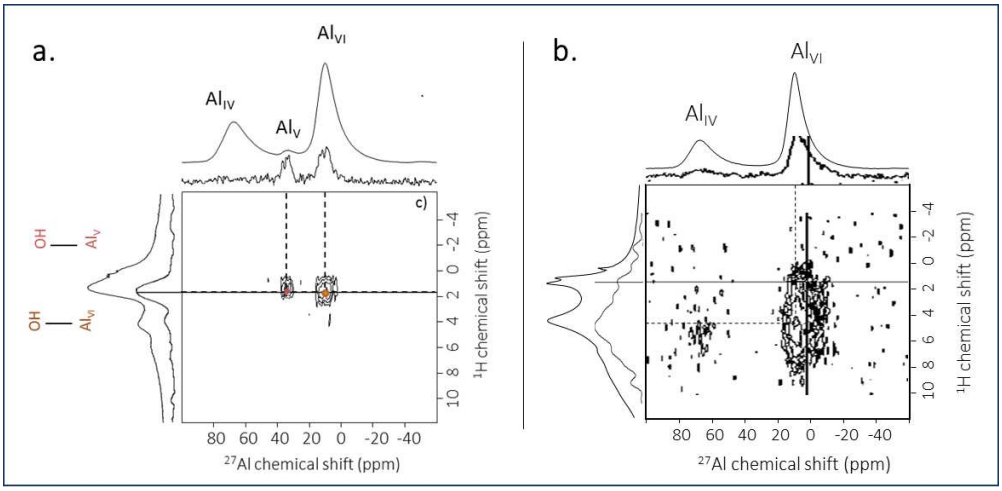

Figure III. 31. 2D ^{27}Al{^{1}H} D-HMQC MAS NMR spectra with the ^{27}Al and ^{1}H calculated projections, the ^{27}Al OP MAS NMR spectra, and ^{1}H OP MAS NMR spectra for: a) Pristine γ-Al_2O_3 and b) grafted ImPE-Br (8) sample.

III.4.1.3. ^{31}P-^{27}Al D-HMQC

^{31}P-^{27}Al D-HMQC experiments were used both to get more information on the bonding configurations of phosphonate groups and to understand the structural transformations occurring during the grafting reaction with [ImPE][Br] in forced conditions. We selected three samples containting different quantities of grafted and lamellar species:

i) ImPE-Br (8) with only grafted species and maximum grafting density;
ii) ImPE-Br (9) with both grafted and lamellar species
iii) ImPE-Br (12) with only the bulk aluminum phosphonate phase.

Unfortunately, the quantity of phosphorus in both ImPE-Br (8) and ImPE-Br (9) samples was too low for 2D experiments in a correct period, thus, only 1D experiments were realized for these samples. We were not able to access the projections related the ^{31}P nuclei.

The 2D-^{31}P-^{27}Al D-HMQC of ImPE-Br (12) sample is shown in Figure III. 32. The ^{27}Al One-pulse MAS NMR spectra and the 1D ^{27}Al NMR projection spectra from the ^{31}P-^{27}Al D-HMQC experiment are shown in Figure III. 33. for all the samples.

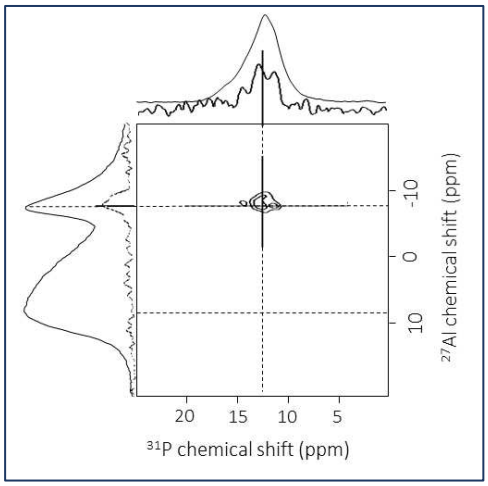

Figure III. 32. 2D and projections of the ^{31}P-^{27}Al D-HMQC experiment for ImPE-Br (12) sample.

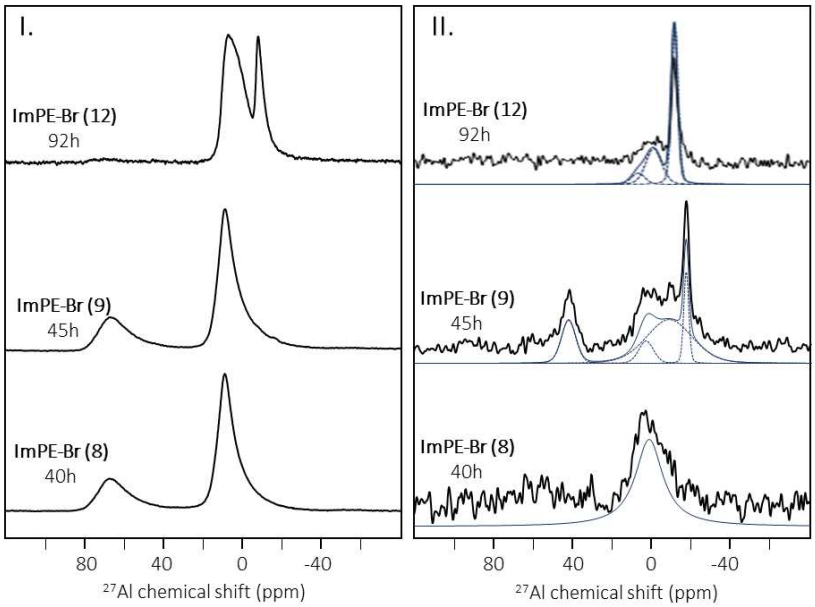

Figure III. 33. I. ^{27}Al MAS NMR spectra of ImPE-Br (8), ImPE-Br (9), and ImPE-Br (12) samples, II. 1D ^{27}Al NMR spectra issued from ^{31}P-^{27}Al D-HMQC experiment for ImPE-Br (8), ImPE-Br (9), and ImPE-Br (12).

The ^{31}P-^{27}Al D-HMQC experiments evidenced the proximity between the ILs and the aluminum, demonstrating that [ImPE]$^{+}$ cations are located at the oxide surface. True structural information can be obtained from ^{31}P-^{27}Al dipolar HMQC, as already exemplified by Tricot and co-workers [55]. In fact, the ^{27}Al chemical shift in oxides strongly depends on its coordination environment. A comparison between the ^{27}Al spectra from one-pulse experiment and ^{31}P-^{27}Al D-HMQC immediately shows that the nature of the ^{27}Al nuclei in ImPE-Br samples differs from those on bulk or surface γ-Al_2O_3.

Simulation of the 1D ^{27}Al NMR projection spectra using a minimum number of signals with Gaussian-Lorentzian shape reveals the presence of multiple sites listed in Table III. 18. It is now possible to distinguish between the different types of ^{27}Al nuclei involved in the grafting from those present in bulk lamellar aluminum phosphonate or alumina phases:

1) $Al_{VI\text{-}lam\text{-}1}$: in the 2D ^{31}P-^{27}Al D-HMQC spectra of ImPE-Br (12) the ^{27}Al nuclei corresponding to the bulk aluminum phosphonate phase appears as a sharp signal on the ^{27}Al projection correlating with ^{31}P nuclei at 13.5 ppm on the ^{31}P chemical shift. On the ^{27}Al chemical shift, the signal is attributed at -7.86 ppm and assigned to hexacoordinated ^{27}Al nuclei in the crystalline phase.

2) $Al_{VI\ graf}$: in the 1D ^{31}P-^{27}Al D-HMQC spectra of ImPE-Br samples, we distinguished a broad signal centered at 3.33 ppm. This signal is present in all samples and predominant in ImPE-Br (8). As fars as ImPE-Br (8) does not contain any bulk aluminum phosphonate phase, the signal at 3.33 ppm is attributed to hexacoordinated ^{27}Al nuclei involved in the grafting.

3) $Al_{V\text{-}inter}$: the 1D ^{31}P-^{27}Al D-HMQC spectra of ImPE-Br (9) sample reveals the presence of pentacoordinated aluminum centers at ~43 ppm. However, the ^{27}Al one-pulse spectra of all samples never reveal any significant signal related to Al_V. The nature of this Al_V is thus quite unclear, and we assume that this nucleus is characteristic of a phase transition.

4) $Al_{VI\ lam\text{-}2}$: for ImPE-Br (9) sample, the hexacoordinated aluminum in bulk aluminum phosphonate phase appears as a sharp signal centered at -16 ppm. The difference observed in the chemical shift compared to $Al_{VI\text{-}lam\text{-}1}$ confirmed that ImPE-Br (9) sample corresponds to an intermediate step between a fully grafted sample and the formation of a lamellar phase.

5) $Al_{VI\ inter*}$: Spectra simulation allows to identify two signals at -8.46 ppm for ImPE-Br (9) and -0.51 ppm for ImPE-Br (12). The signals were too broad to be attributed to well-ordered lamellar phases and were not in the range of expected chemical shifts for grafted species. Thus, we classified these nuclei as characteristics of the transitions/rearrangements occuring upon time.

6) $Al_{IV\ Al2O3}$ and $Al_{VI\ Al2O3}$: The ^{27}Al nuclei from bulk γ-Al_2O_3, such as $Al_{IV\ Al2O3}$ and $Al_{VI\ Al2O3}$ were located around 68.8 and 9.8 ppm, respectively (for both ImPE-Br (8) and ImPE-Br (9)). As expected, they do not correlate with the ^{31}P nuclei from the phosphonate-based IL. This result is consistent with a surface coverage of ~55% without any degradation of the γ-Al_2O_3 support. When a support degradation occurs, only the $Al_{VI\ Al2O3}$ species are detected (cf. section III.3).

Table III. 18. Results derived from the simulation of 1D {^{31}P}–^{27}Al D-HMQC spectra for the grafted samples ImPE-Br (8), ImPE-Br (9) and ImPE-Br (12).

Grafted samples	Grafting reaction duration (h)	P (wt%)	Al_X type	^{27}Al [ppm]	Signal width (ppm)	Integration (%)
ImPE-Br (8)	40	1.73 ± 0.08	$Al_{VI\ graft}$	3.33	19.02	100
ImPE-Br (9)	45	2.00 ± 0.03	$Al_{V\ -inter}$	42.4	8.53	18
			$Al_{VI\ graft}$	3.33	8.83	10
			$Al_{VI\ inter*}$	-8.46	27.36	59
			$Al_{VI\ lam2}$	-16.9	2.99	14
ImPE-Br (12)	92	4.17 ± 1.15	$Al_{VI\ graft}$	3.33	3.94	8
			$Al_{VI\ inter*}$	-0.51	4.62	32
			$Al_{VI\ lam1}$	-7.89	1.9	60

III.4.1.4. Conclusion

D-HMQC techniques provided experimental evidence for the characterization and topology of hydroxyl groups at the surface of sol-gel derived γ-Al_2O_3. Two types of OH-groups were identified Al_{VI}-OH and Al_{IV}-OH. We also distinguished the ^{27}Al nuclei involved in the grafting from those involved in structural transformations and those present in lamellar phases. We demonstrated for the first time that all the relevant aluminum nuclei involved in the grafting of phosphonate-based molecules were hexacoordinated. These results coupled to those of section III.3 about the possible phosphonate bonding modes (tridentate, monodentate, and bidentate) in the ImPE-Br (8) sample, provide more complete information about the possible bonding configurations in the ILs/alumina system. An illustration is shown in Figure III. 34.

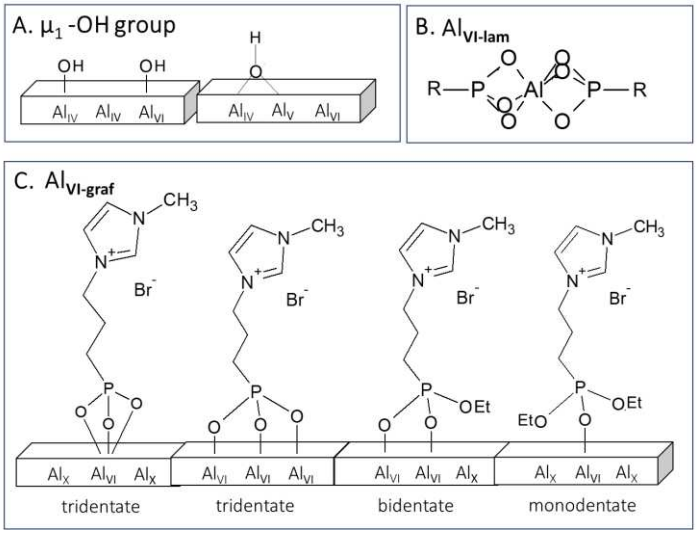

Figure III. 34. Schematic reprensentation of A. terminal OH-groups on the γ-Al_2O_3 surface, B. possible configuration of $Al_{VI\text{-}lam}$ in lamellar compounds, and C. possible bonding modes proposed for ImPE-Br (8) sample.

III.4.2. HRMAS

HR-MAS NMR experiments are known to provide significant spectra resolution improvements even at moderate spinning rates, in comparison with basic ssNMR experiments. The HR-MAS method is a perfect tool for samples which are in the liquid/solid classification [57]. Standard MAS (Magic Angle Spinning) ssNMR spectroscopy and HR-MAS NMR spectroscopy present multiple differences mainly related to the probe characteritics. Both experiments involve sample rotation at the so-called magic angle of 54.7° to suppress interactions causing signal broadening (*i.e.,* dipolar interactions, chemical shift anisotropy, etc..). Compared to basic MAS NMR methods, HR-MAS NMR is equipped with a magic angle gradient coil which produces a gradient along the rotor spinning axis and increases the resolution. Thus, the solid NMR spectra obtained by HR-MAS spectroscopy are often similar to those obtained in liquid phase NMR. As in liquid NMR, shimming and locking are the most tricky parts of the experiment. HR-MAS spectroscopy is classically used to study tissues or cells [58], to follow chemical reactions on solid supports [59] and more recently to study the grafting of peptide/PEG on the surface of iron oxide nanoparticles [60].

HR-MAS spectroscopy was used to enhance the resolution of both ^{1}H and ^{31}P NMR spectra of the ImPE-Br (8) sample. The sample was dried for 3h at 100°C under vacuum (70 mmHg), dispersed in a minimum of D_2O and inserted in HR-MAS rotor. Under standard MAS condition, the ^{1}H MAS NMR spectra of the sample presents a broad signal with no resolution, typical for a solid-state ^{1}H NMR spectra (Figure III. 35.B.). As expected the ^{1}H HR-MAS spectra of the same sample provides much high resolution (Figure III. 35.C). By comparison with the ^{1}H liquid NMR spectra of the neat IL, we can see that the protons from the imidazolium ring (H_2, H_3, and H_1) present very small changes in their chemical shift ($\Delta\delta < 0.1$ ppm) but have asymmetric line shape. Two additional ^{1}H signals are observed (compared to the neat IL) at 3.9 and 4.05 ppm, which are attributed to water species adsorbed on the γ-Al_2O_3 surface. Concerning the assignments of the ^{1}H nuclei representing the coupling functions (H_8 and H_9) and the organic spacer (H_5, H_6, and H_7) the resolution is very poor. We can suppose that steric hindrance or IL anchoring on the γ-Al_2O_3 surface could significantly decrease the mobility of the closest nuclei on the surface. Multiple bonding modes could cause also broaden signals.

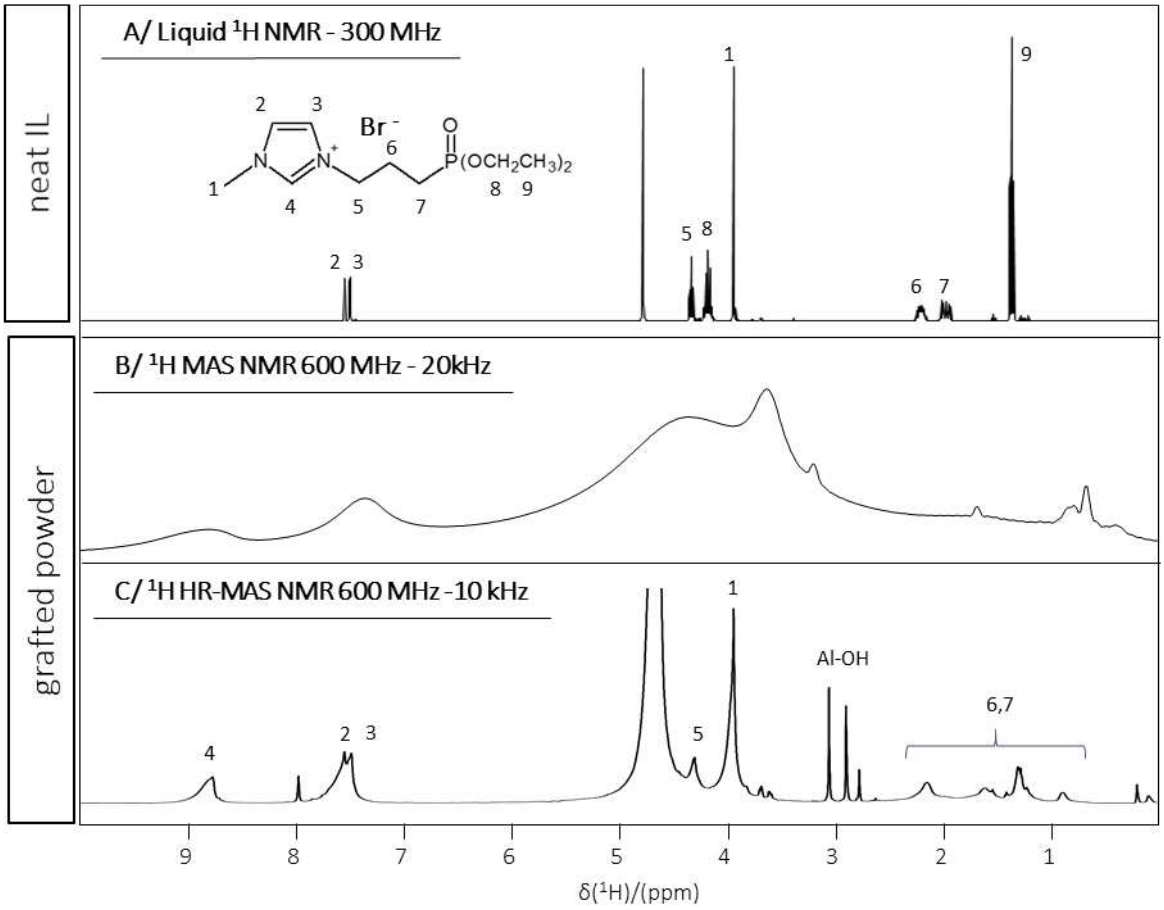

Figure III. 35. A/ ^{1}H liquid NMR spectra of the pure IL [ImPE][Br] in D_2O à 1 kHz, B/ 1H MAS NMR spectra of ImPE-Br (8) at 20 kHz, C/ ^{1}H HR-MAS spectra of ImPE-Br (8) in D_2O at 10 kHz.

In order to evidence a covalent grafting of the phophonate, ^{13}C HR-MAS spectra of the ImPE-Br (8) sample was also recorder (Figure III. 36). The good resolution of this spectra allows to evidence a decrease in the chemical shift ($\Delta\delta$ < 4 ppm) for all the ^{13}C nuclei in the grafted sample. Compare to the ^{1}H HR-MAS spectra, the ^{13}C nuclei of the organic spacer could be identified, at 46 and 20 ppm corresponding respectively to C_5 and C_6 /C_7. Again, a lower resolution is observed when the nuclei are the closest to the γ-Al_2O_3 surface, du to a decrease in their mobility.

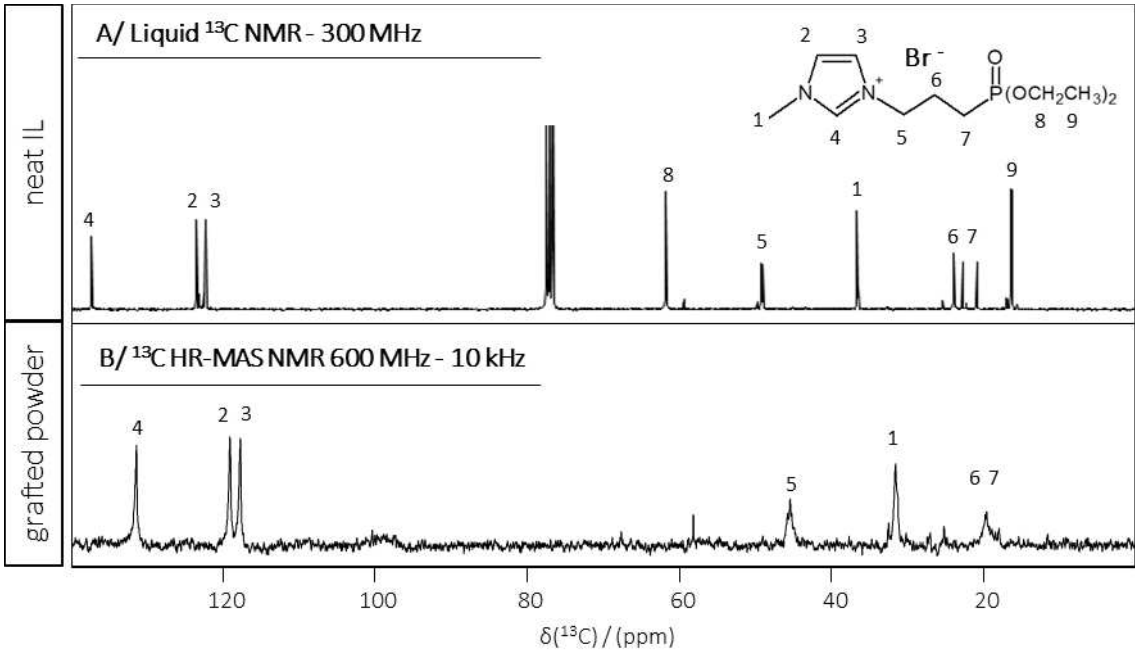

Figure III. 36. A/ ^{13}C liquid NMR spectra of the pure IL [ImPE][Br] in D_2O à 1 kHz, B/ ^{13}C HR-MAS spectra of ImPE-Br (8) grafted sample in D_2O at 10 kHz.

The ^{31}P HR-MAS NMR spectra of the samples were also recorded. Compare to the ^{31}P CP-MAS spectra of ImPE-Br (8), the HR-MAS allowed surprisingly to observe four sharp peaks at 28.5, 21.4, 20.9, and 18.8 ppm (1, 3, 4, and 5) and a broad signal centered at 26.2 ppm (2). This chemical shift is in the same range (18-32 ppm) than the sites 1', 2', and 3' resulting from the simulation of the ^{31}P CP-MAS NMR spectra with a minimum number of signals and Gaussian-Lorentzian shapes. The sites 1', 2' and 3' were tentatively ascribed to, respectively, the monodentate, tridentate and bidentate bonding modes. Thus, on the HR-MAS NMR spectra, the broad signal number 2 could be assigned to the tridentate bonding mode due to the loss of mobility in this configuration. The peaks 3, 4 and 5 could correspond to various bidentate bonding modes and the peak 1 to the monodentate mode. Although additional investigation is required to confirm this assessment, HR-MAS spectroscopy can be considered as a relevant and powerful technique to investigate the grafted IL samples.

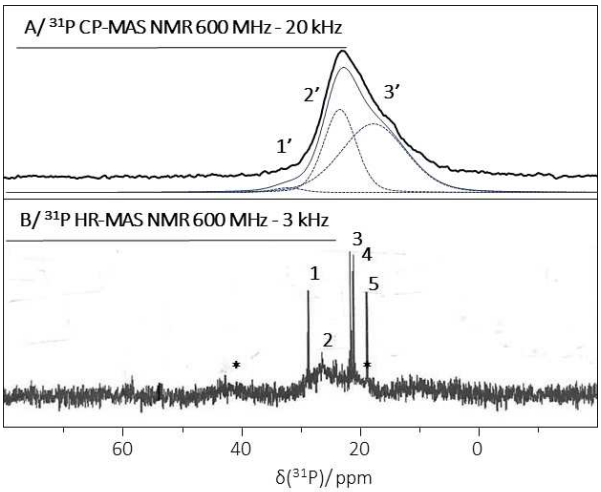

Figure III. 37. A/ ^{31}P CP-MAS NMR spectra of ImPE-Br (8), B/ ^{31}P HRMAS spectra of ImPE-Br (8) in D_2O at 3 kHz.

To briefly summarize, the grafted sample ImPE-Br (8) was analyzed by ^{1}H, ^{13}C, and ^{31}P HR-MAS NMR spectroscopy. Good resolution spectra, comparable to liquid NMR, were obtained for each nucleus. The ^{1}H and ^{13}C nuclei which were the closest to the coupling agent have less resolved signals possibly due to the anchoring effect decreasing the IL mobility. Finally, the ^{31}P NMR spectra present a surprisingly high resolution which opens the way to further experiments for understanding the correlation between the ^{1}H and ^{13}C nuclei. HR-MAS can thus be considered as a relevant complementary experiment to solid-state analysis which is required to investigate the ^{27}Al nuclei.

III.5. Gas sorption studies

Gas sorption experiments were conducted on the pristine γ-Al_2O_3 powder and on selected grafted samples (*i.e.,* ImPE-Br and ImPE-Tf_2N used for studying the grafting kinetics, ImC_{12}PE-Tf_2N (2) and ImPEGPE-Tf_2N (2)). The pristine γ-Al_2O_3 powder has been exposed to the conditions of the hydrothermal grafting without any phosphonate-based IL during 17h in water, and thus can be considered as a reference sample.

First, N_2 sorption experiments were conducted at -196 °C (77 K) to investigate the samples porous structure. The characteristics of the adsorption-desorption isotherms and the derived pore size distributions were used to study the influence of the grafted phosphonate-based ILs on ceramic surface interaction with N_2.

In a second part of the work, CO_2 sorption experiments have been carried out at IRCELyon (Drs. Cécile DANIEL and David FARRUSSENG) to investigate the CO_2/ILs interactions at 298 K. Before any gas sorption experiments, powders were outgassed during 17h under primary vacuum and during 3h under secondary vacuum at 100°C. The outgassing temperature was sufficiently low to avoid any degradation of the organic moieties but cannot permit guarantee the elimination of adsorbed impurities on the sample surface.

III.5.1. N_2 sorption experiment

Figure III. 38 shows the N_2 adsorption-desorption isotherms (1) and derived pore size distribution curves (2) of the grafted samples in comparison with those of the pristine γ-Al_2O_3. Information on samples preparation conditions and characteristics (grafting duration, grafting density, Brunauer Emmett Teller specific surface area S_{BET}, BET constants C_{BET}, and pore sizes derived from Barrett-Joyner-Halenda method) are listed in Table III. 19. The isotherms and pore size distribution curves are shown in Figure III. 38, in A1 and A2 for ImPE-Br samples, in B1 and B2 for ImPE-Tf_2N samples, and in C1 and C2 for ImPEGPE-Tf_2N (2) and ImC_{12}PE-Tf_2N (2) samples. The N_2 adsorption-desorption isotherms with a scale adapted to each sample are also presented in annex 2 (Figure A2.4 to A2.12).

The N_2 adsorption-desorption isotherm of the pristine γ-Al_2O_3 powder is a typical type IV isotherm with the hysteresis loop indicating the presence of mesopores (Figure III. 38, A1. A2). The hysteresis loop is a composite of H2(a) and H3 types, suggesting pore connectivity with channel-like or ink-bottle pores [61]. As shown in Figure III. 38, A1., the N_2 sorption isotherms for ImPE-Br (8) and ImPE-Br (10) are also type IV with a similar hysteresis loop but shifted to lower P/Po values but with slightly lower volume of N_2 adsorbed. However, the situation is different for ImPE-Br (12) which contains a bulk aluminum phosphonate phase covering the surface and consequently adsorb extremely low quantity of N_2 (apparatus detection limit). The shape of the isotherm is abnormal: it does not close perfectly at P/P_0=0.4 and the quantity of N_2 adsorbed tends to decrease when P/P_0 increases in the range 0.1-0.8. This result seems to confirm the loss of γ-Al_2O_3 structure integrity already evidenced in §III.3.3. Figure B1 shows the N_2 adsorption-desorption isotherms for the ImPE-Tf_2N samples. All the N_2 isotherms look similar to those of the ImPE-Br sample series, with mainly H2(a) type isotherms. Figure C1 compares the N_2 sorption isotherms for both ImC_{12}PE-Tf_2N (2) and ImPEGPE-Tf_2N (2) samples. We note a significant decrease of the amount of N_2 adsorbed by these samples in comparison with the values measured for ImPE-Br and ImPE-Tf_2N samples. In addition, in the case of ImPEGPE-Tf_2N (2), the desorption branch is associated with an increase in the amount of N_2 adsorbed.

The general shape of the N_2 adsorption-desorption isotherms clearly reveals the presence of mesopores in all the grafted samples, except when the aluminum phosphonate phase was formed (cf. §III.3.3). Secondly, the preservation of the isotherm type and the amount of N_2 adsorbed by the grafted samples in comparison with the pristine γ-Al_2O_3 sample, tend to show that only the material surface was modified, but not the whole pore volume. Also, the overall differences between the hysteresis loops of different grafted samples suggest an important impact of the composition of phosphonate-based ILs (i.e., anion and organic spacer).

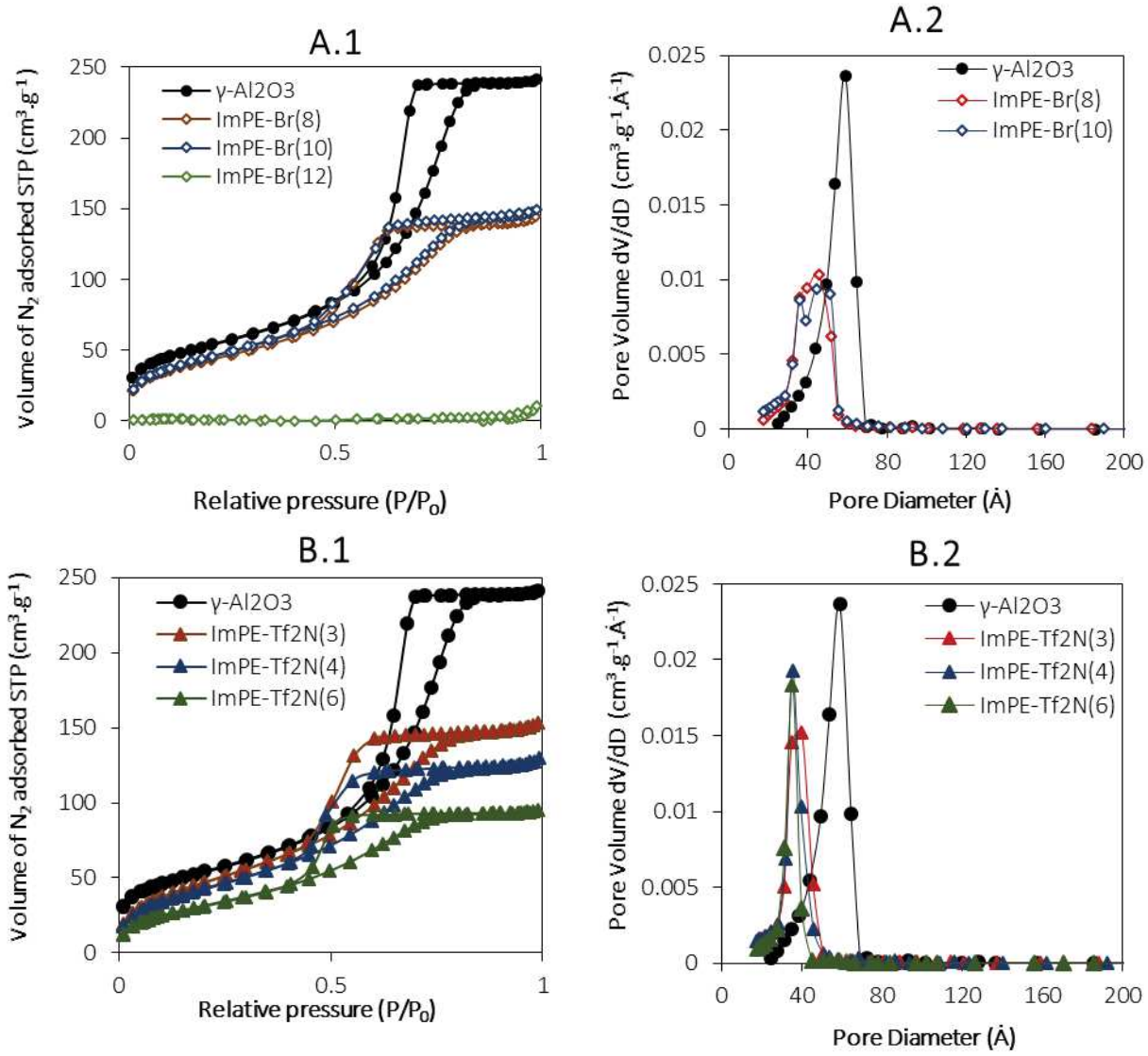

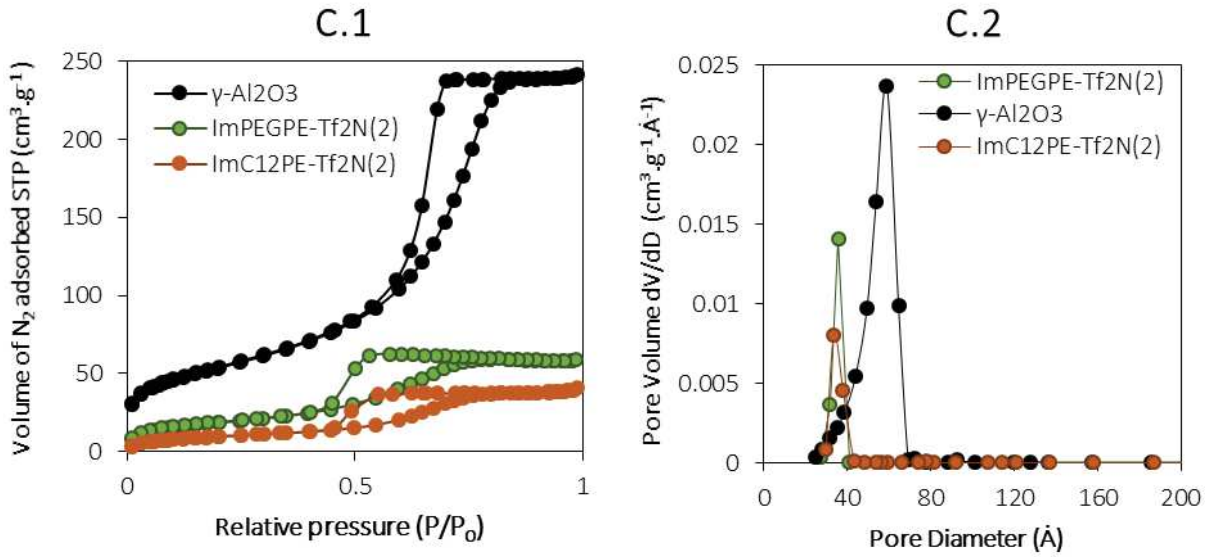

Figure III. 38. N_2 adsorption-desorption isotherms and derived pore-size distributions for the pristine γ-Al_2O_3 and for a series of grafted samples. The pore size distributions derive from the desorption branch of the isotherms, using the BJH equation.

The N_2 sorption experiments also yield the BET specific surface area values for both the pristine γ-Al_2O_3 and the grafted samples as listed in Table III. 19. The comparison of S_{BET} values for the pristine γ-Al_2O_3 powder and the grafted ImPE-Br or ImPE-Tf_2N sample series is consistent with surface modification. The important differences observed between the S_{BET} values for ImC_{12}PE-Tf_2N (2) and ImPEGPE-Tf_2N (2) samples (36 and 68 m^2/g, respectively), could result from either steric hindrance and/or disorder effects as suggested in section III.4.3.

Table III. 19. Specific surface area, BET constant (C_{BET}), pore size (#BJH maximum pore diameter from the desorption branch) determined from N_2 physisorption isotherms at -196°C (77 K), for a series of selected grafted samples (with various grafting duration and various weight % of phosphorus as measured by EDX) in comparison with the pristine γ-Al_2O_3. *For the sample ImPE-Br (12), an abnormal isotherm was obtained.

Sample	Grafting duration (h)	Grafting density P nm^{-2}	% mono-layer reached	S_{BET} ($m^2.g^{-1}$)	C_{BET}	Pore diameter#(nm)	Pore volume ($cm^3.g^{-1}$)
γ-Al_2O_3	-	-	-	192	135	5.3	0.38
ImPE-Br (8)	40	2.2	55	160	68	4.1	0.23
ImPE-Br (10)	45	2.6	65	163	60	4.1	0.24
ImPE-Br (12)	92	5.4	135	(*)	(*)	(*)	(*)
ImPE-Tf_2N (3)	40	2.2	55	179	40	3.7	0.24
ImPE-Tf_2N (4)	48	2.2	55	162	41	3.6	0.21
ImPE-Tf_2N (6)	92	2.0	50	120	40	3.4	0.15
ImC_{12}PE-Tf_2N (2)	40	2.5	63	36	51	3.7	0.06
ImPEGPE-Tf_2N (2)	40	2.6	65	68	86	3.6	0.09

The BET constant (C_{BET}) translates the affinity of the solid material with N_2 molecules, and can thus be considered as a characteristic value for the evaluation of adsorbate/material surface interactions [38]. The decrease of C_{BET} value reflects a reduction of the N_2 sorption enthalpy on the surface and thus gives qualitative information about surface modification. The C_{BET} values measured for all the grafted samples are lower than the value measured for the pristine γ-Al_2O_3 powder (Table III. 19). The highest C_{BET} value (C_{BET}= 86) is obtained for ImPEGPE-Tf_2N (2), although lower values are obtained for all the other samples

(C_{BET}~60-70 for ImPE-Br samples, C_{BET}~50 for $ImC_{12}PE\text{-}Tf_2N$ and C_{BET}~40 for $ImPE\text{-}Tf_2N$). In other words, N_2 sorption is favored for $ImPEGPE\text{-}Tf_2N$ (2) which is composed predominantly of polar domains (see Chapter II section II.3). The difference observed between C_{BET} values for ImPE-Br and $ImPE\text{-}Tf_2N$ derived samples suggests an effect of the anion. In fact, Tf_2N^- is known to be more hydrophobic than Br^- and could thus affects the N_2/surface interactions [62]. We have to note that this hydrophobicity has been demonstrated by contact angle measurements on titanium metal plates grafted with either ImPE-Br or $ImPE\text{-}Tf_2N$ (results not shown). The intermediate values of C_{BET} for $ImC_{12}PE\text{-}Tf_2N$ (2) samples could be due to the alkyl chain which was found in chapter II (§II.4.2) to have specific interactions with N_2.

Considering the complexity of sample characteristics and the diversity of N_2 sorption data, complementary experiments (*e.g.,* argon sorption isotherms and calorimetric studies) would be useful to better understand the gas sorption mechanisms on the grafted samples.

The characteristics of the N_2 adsorption-desorption isotherms, together with the S_{BET} and C_{BET} values reveal the influence of the ILs composition on the N_2 sorption behavior of the samples. In addition, information about pore-size distribution and pore surface coverage will be required for studying gas transport phenomena through the grafted IL-derived membranes.

In order to estimate the pore-size distribution, the conventional BJH model was applied to the desorption branch, as recommended [63]. The pore size distributions are shown in Figure III. 38, and the values at the maximum of the distributions are reported in Table III. 19. The pore size of $\gamma\text{-}Al_2O_3$ is centered at ~5 nm, and the size distribution is relatively narrow (peak width ~1.5 nm). This result is consistent with the uniform size, tightly stacked platelets observed by TEM (ANNEX 2, figure A2.3). Concerning the pore size of ImPE-Br (8) and ImPE-Br (10) derived samples, a decrease of ~1.2 nm is observed compared to the pristine $\gamma\text{-}Al_2O_3$ and the size distribution is larger (peak width ~1.9 nm) (Figure III. 38.A2). The $ImPE\text{-}Tf_2N$ derived samples ($ImC_{12}PE\text{-}Tf_2N$ (2) and $ImPEGPE\text{-}Tf_2N$ (2)) present a remarkable pore size decrease (~1.7 to 1.9 nm) in comparison with $\gamma\text{-}Al_2O_3$. For the ImPE-Br derived samples, the pore size distribution curves are fairly narrow (peak width ~0.7 nm) (Figure B2 and C2).

The isotherms and derived pore size distribution curves obtained for the grafted samples show that, except for ImPE-Br (12) sample, the pores remains accessible to the N_2 and are not blocked by accumulation of the phoshonate-based IL at the pore entrance. This result is also consistent with the estimated grafting density values (P nm^{-2}, Table III. 20), showing that the pore surface is not fully covered by the IL.

Surprisingly, for a given grafting density, similar pore volumes but different pore diameters can be obtained. As an example, the pore volume for ImPE-Br (8) and $ImPE\text{-}Tf_2N$ (3) samples is ~0.23 $cm^3.g^{-1}$ for a surface coverage reaching ~55% of the full monolayer. Pore sizes of ImPE-Br (8) sample decrease by ~1.2 nm in comparison with pristine $\gamma\text{-}Al_2O_3$ and those of $ImPE\text{-}Tf_2N$ (3) sample decrease by 1.6 nm. ^{31}P NMR spectroscopy investigation previously confirmed identical cations bonding modes for both sample series and DFT calculations in Chapter II (section II.4.) showed that the maximum cation length in its conformational equilibrium is ~1.1 nm. In addition, we evidenced the anion effect on the C_{BET} value which is lower for the Tf_2N^- sample than for the Br^- one, suggesting a stronger hydrophobic behavior for the former. Thus, the difference in pore diameters between ImPE-Br (8) and $ImPE\text{-}Tf_2N$ (3) derived samples should only result from the anion position on the $\gamma\text{-}Al_2O_3$ pore surface. This assumption will be investigated by computational study.

In conclusion, N_2 sorption experiments yield valuable information regarding the porous structure characteristics of the grafted samples. We demonstrate the retention of accessible mesopores in the

grafted samples and the effect of the phosphonate-based ILs composition on the N_2/surface interactions. In addition, we showed that the grafting did not yield full pore surface. All this information will be useful to investigate gas transport properties through the hybrid IL/ceramic systems.

III.5.2. CO_2 sorption experiment

CO_2 sorption experiments (preliminary work at IRCELyon, to be completed) were conducted on the pristine γ-Al_2O_3, and on the grafted samples ImPE-Br (8) and ImPE-Tf_2N (3).

The CO_2 adsorption isotherm obtained for the γ-Al_2O_3 powder (Figure III. 39) is similar to the isotherm obtained at 315 K by Cabrejas Manchado *et al.* [64]. With the help of both IR spectroscopy and previously published results, the authors identified the formation of three energetically different species as shown in Figure III. 40. The first species is a monodentate surface carbonate held by a chemical bond. This species formed by the nucleophilic attack of CO_2 on the hydroxyl surface groups of the γ-Al_2O_3 with the involvement of neighboring Lewis acidic centers. The surface bicarbonate are the second species considered in the reaction. These species can slowly convert to monodentate carbonate or uncoordinated ionic carbonate. The amount of carbonate and bicarbonate considered as chemisorbed species strictly depends on the pretreatment conditions, while the species nature is primarily determined by the coordination of surface cations [65]. The chemisorbed species react onto high adsorption energy sites, adsorbed at negligible equilibrium pressure such as the initial uptake at ~130 µmol.g^{-1} observed on the γ-Al_2O_3 adsorption isotherm. The last species correspond to physisorbed CO_2 species, the adsorption is energetically weak and therefore requires a higher gas phase pressure to take place.

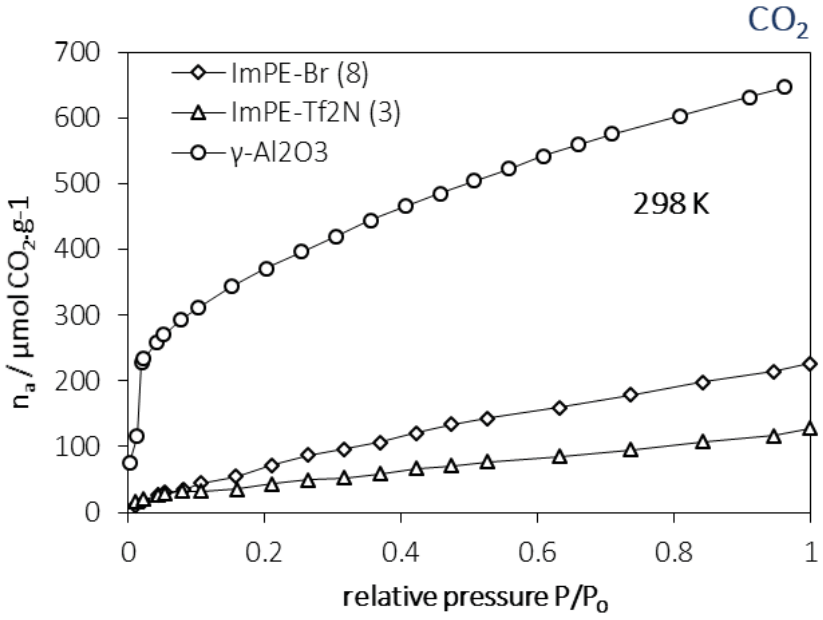

Figure III. 39. Adsorption isotherms of CO_2 on the pristine γ-Al_2O_3, and on ImPE-Br (8) and ImPE-Tf_2N (3) – grafted samples at 298 K.

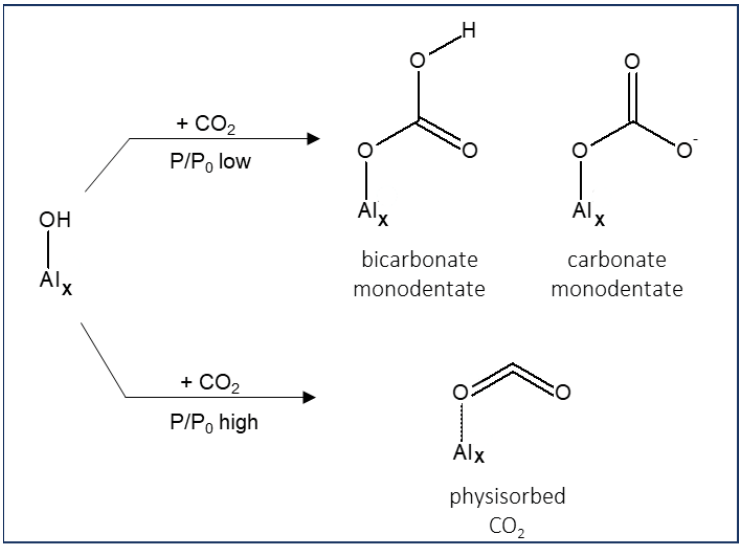

Figure III. 40. Possible configurations of species resulting from the reaction of CO_2 with the pristine γ-Al_2O_3, depending on the equilibrium pressure.

In the case of ImPE-Br (8) and ImPE-Tf_2N (3) derived samples, the initial CO_2 uptake is ~20 and 30 µmol.g^{-1} respectively and correspond to chemisorption interactions (acid-base type). As the majority of the γ-Al_2O_3 hydroxyl surface groups are involved in the grafting with the phosphonate-based ILs, the possible formation of carbonate or bicarbonate species is weak. Thus, the small CO_2 uptake at the beginning of the experiment could be due to the anion/CO_2 interaction described in Chapter II. Also, the amount of CO_2 adsorbed increases almost linearly with the pressure, thus revealing the dominating interactions of physisorbed CO_2 with the ILs.

III.6. Conclusions

In this chapter, phosphonate-based ILs composed of different coupling functions, organic spacers and anions were grafted on a γ-alumina (γ-Al_2O_3) powder.

The first part of the work allowed to demonstrate the influence of the coupling functions. We performed the grafting with either [ImPE][Br] or [ImTMSP][Br], in either aqueous or alcoholic solvents, or in dry methylene chloride solvent, respectively. Both FTIR and solid state NMR spectroscopy (^{31}P) were used to confirm that the diethyl phosphonate ester coupling function allowed to control the grafting reaction by using either prolonged heating or high reaction temperature. We thus selected this coupling function for preparing optimized grafted samples using optimized and controlled reaction conditions.

In the second part of this work, grafting kinetics study were investigated with both [ImPE][Br] and [ImPE][Tf_2N] ILs. We demonstrated that the surface coverage obtained in the first part of the work could be improved by using forcing reaction conditions with selected reaction times to control the grafting density on the γ-alumina surface. Surprisingly, we evidenced the formation of boehmite in both study and then to the formation of bulk aluminum phosphonate phases for the [ImPE][Br] IL. Our investigations led to the discovery of an hydrolysis reaction for both [ImPE][Br] and [ImPE][Tf_2N] ILs in forcing reaction condition producing the parent phosphonic acids or monoester species of the coupling function. However, the hydrolysis kinetics of [ImPE][Br] and [ImPE][Tf_2N] strongly differ under the same experimental conditions. Thus, we concluded that the choice of both the anion and the reaction time must be carefully chosen to avoid or minimize the formation of bulk aluminum phosphonate and/or the dissolution of the γ-alumina support.

The last part of this chapter focused on the determination of the best-operating conditions for grafting [$ImC_{12}PE$][Tf_2N] and [ImPEGPE][Tf_2N] in forcing reaction conditions. Knowing the hydrolysis phenomenon, the grafting reaction duration was selected to control the formation of boehmite. We obtained a grafting density in the same range than the grafting with [ImPE][Tf_2N] IL. However, compared to the study of [ImPE][Tf_2N] grafted samples, the determination/hypothesis of the bonding modes was more difficult due to the broadening of both IR and solid-state NMR signals, undoubtedly due to the critical length of the organic spacers.

Then, with the aim to propose new experimental ssNMR techniques adapted to the fine investigation of the phosphonate-grafted samples, both D-HMQC and HR-MAS solid-state NMR techniques were used. D-HMQC experiments were useful to reveal the nature of the aluminum nuclei involved in the grafting as well as the different types of hydroxyl surface groups on the pristine γ-alumina. The HR-MAS technique was useful to increase the resolution of the NMR spectra, thus leading to a resolution close to those of liquid NMR. Further experiments still need to be achieved but the first results confirmed the grafting and brought large detailed information about the configuration of grafted species.

Finally, N_2 sorption experiments were conducted and yield valuable information regarding the porous structure characteristics of the grafted samples. We demonstrate the retention of accessible mesopores in the grafted samples and the effect of the phosphonate-based ILs composition on the N_2/surface interactions. In addition, we showed that the grafting did not yield full pore surface. All this information will be useful to investigate gas transport properties through the hybrid IL/ceramic systems. In addition, sorption experiments revealed the dominating interactions by physisorption between CO_2 and grafted ILs.

The best grafting conditions evidenced along this Chapter III will be used to prepare hybrid membranes with the IL grafted within the pores of a γ-Al_2O_3 membrane (thin mesoporous top-layer) supported on a macroporous ceramic support, applicable for the selective transport of CO_2 and for continuous gas separation applications.

References

1. M. Ramdin, T.W. De Loos, T.J.H. Vlugt, State-of-the-Art of CO_2 Capture with Ionic Liquids, *Ind. Eng. Chem. Res.,* 2012*, 51(24)*, 8149-8177.
2. A.V. Perdikaki, O.C. Vangeli, G.N. Karanikolos, K.L. Stefanopoulos, K.G. Beltsios, P. Alexandridis, N.K. Kanellopoulos, G.E. Romanos, Ionic Liquid-Modified Porous Materials for Gas Separation and Heterogeneous Catalysis, *J. Phys. Chem. C.,* 2012, *116(31)*, 16398-16411.
3. O.C. Vangeli, G.E. Romanos, K.G. Beltsios, D. Fokas, E.P. Kouvelos, K.L. Stefanopoulos, N.K. Kanellopoulos, Grafting of imidazolium based ionic liquid on the pore surface of nanoporous materials - Study of physicochemical and thermodynamic properties, *J. Phys. Chem. B.,* 2010, *114(19)*, 6480-6491.
4. B. Xin, J. Hao, Imidazolium-based ionic liquids grafted on solid surfaces, *Chem.Soc.Rev*., 2014, *43(20)*, 7171-7187.
5. P. Bollini, S. A. Didas, C. W. Jones, Amine-oxide hybrid materials for acid gas separations, *J. Mater. Chem.,* 2011, *21*, 15100-15120.
6. Fehrmann, R.; Haumann, M. & Riisager, A. Introduction. In Supported Ionic Liquids: Fundamentals and Applications, 1st ed.; Fehrmann, R.; Riisager, A. & Haumann, M.; Wiley-VCH Verlag GmbH & Co. KGaA, Publisher: Weinheim, Germany, 2014, pp. 1-9.
7. L.J. Lozano, C. Godinez, A.P. de los Rios, F.J. Hernandez-Fernandez, S. Sanchez-Segado, F.J. Alguacil, Recent advances in supported ionic liquid membrane technology, *J. Membrane. Sci.,* 2011, *376(1-2)*, 1-14.
8. J. Albo, T. Yoshioka, T. Tsuru, Porous Al_2O_3/TiO_2 tubes in combination with 1-ethyl-3-methylimidazolium acetate ionic liquid for CO_2/N_2 separation, *Sep. Purif. Technol.*, 2014, *122*, 440-448.
9. J.J. Close, K. Farmer, S.S. Moganty, R.E. Baltus, CO_2/N_2 separations using nanoporous alumina-supported ionic liquid membranes: Effect of the support on separation performance, *J. Membrane. Sci.,* 2012, *390-391*, 201-210.
10. S.D. Hojniak, I.P. Silverwood, A.L. Khan, I.F.J. Vankelecom, W. Dehaen, S.G. Kazarian, K. Binnemans, Highly Selective Separation of Carbon Dioxide from Nitrogen and Methane by Nitrile/Glycol-Difunctionalized Ionic Liquids in Supported Ionic Liquid Membranes (SILMs), *J. Phys. Chem. B*., 2014, *118(26)*, 7440-7749.
11. S.D. Hojniak, A.L. Khan, O. Hollo, B. Kirchner, I.F.J. Vankelecom, W. Dehaen, K. Binnemans, Separation of Carbon Dioxide from Nitrogen or Methane by Supported Ionic Liquid Membranes (SILMs): Influence of the Cation Charge of the Ionic Liquid, *J. Phys. Chem. B.,* 2013, *117(48)*, 15131-15140.
12. M. Adibi, S.H. Barghi, D. Rashtchian, Predictive models for permeability and diffusivity of CH_4 through imidazolium-based supported ionic liquid membranes, *J. Membrane. Sci.,* 2011, *371(1-2)*, 127-133.
13. A.I. Labropoulos, G.E. Romanos, E. Kouvelos, P. Falaras, V. Likodimos, M. Francisco, M.C. Kroon, B. Iliev, G. Adamova, T.J.S. Schubert, Alkyl-methylimidazolium Tricyanomethanide Ionic Liquids under Extreme Confinement onto Nanoporous Ceramic Membranes, *J. Phys. Chem. C.,* 2013, *117(19)*, 10114-10127.
14. A. Julbe, D. Farrusseng, C. Guizard, Porous ceramic membranes for catalytic and reactors and overview and new ideas, *J. Membrane. Sci.,* 2001, *181(1)*, 3-20.
15. A. Cattani-Scholz, Functional Organophosphonate Interfaces for Nanotechnology: A Review, *ACS Appl. Mater. Interfaces*., 2017, *9(31),* 25643-25655.
16. G. Guerrero, J.G. Alauzun, M. Granier, D. Laurencin, P.H. Mutin, Phosphonate coupling molecules for the control of surface/interface properties and the synthesis of nanomaterials, *Dalton Trans*., 2013, *42(35)*, 12569-12585.
17. I.L. Odinets, E.V. Sharova, O.I. Artyshin, K.A. Lyssenko, Y.V. Nelyubina, G.V. Myasoedova, N.P. Molochnikova, E.A. Zakharchenro, Novel class of functionalized ionic liquids with grafted CMPO-moieties for actinides and rare-earth elements recovery, *Dalton Trans*., 2010, *39(17)*, 4170-4178.

18. A. Rout, K.A. Venkatesan, T.G. Srinivasan, P.R. Vasudeva Rao, Unusual extraction of plutonium(IV) from uranium(VI) and americium(III) using phosphonate based task specific ionic liquid, *Radiochim. Acta.,* 2010, *98(8)*, 459-466.
19. ZG. Mu, F. Zhou, SX. Zhang, YM. Liang, WM. Liu, Effect of the functional groups in ionic liquid molecules on the friction and wear behavior of aluminum alloy in lubricated aluminum-on-steel contact, *Tribology International.,* 2005, *38*, 725-731.
20. Mutin, P.H. Guerrero, G.; Almaric.J. (issued Nov 19, 2013) *Patent n° US 8586758 B2.* Preparation of an inorganic substrate having antimicrobial properties. Assignees: Centre National de la Recherche Scientifique, Paris (FR); Université Montpellier II Sciences et Techniques du Languedoc, Montpellier (FR).
21. L.D. Freedman, G.O. Doak, The preparation and properties of phosphonic acids, *Chemical Reviews*., 1957, *57(3)*, 479-523.
22. A. Clearfield, Unconventional metal organic frameworks: porous cross-linked phosphonates, Dalton Trans., 2008, *0(44)*, 6089-6102.
23. SF. Tang, JJ. Cai, LJ. Li, XX. Lv, C.Wang, XB. Zhao, A highly porous three-dimensional aluminum phosphonate with hexagonal channels: synthesis, structure and adsorption properties, *Dalton Trans*., 2014, *43(16)*, 5970-5973.
24. I.S. Pawsey, M. McCormick, P.S. De, R. Graf, Y.S. Lee, L. Reven, H.W. Spiess, ^{1}H Fast MAS NMR Studies of Hydrogen-Bonding Interactions in Self-Assembled Monolayers, *J. Am. Chem. Soc.,* 2003, *125(14)*, 4174-4184.
25. J. Randon, P. Blanc, R. Paterson, Modification of ceramic membrane surfaces using phosphoric acid and alkyl phosphonic acids and its effects on ultrafiltration of BSA protein, *J. Membrane. Sci.,* 1995, 98(1-2), 119-129.
26. J. Random, R. Paterson, Preliminary studies on the potential for gas separation by mesoporous ceramic oxide membranes surface modified by alkyl phosphonic acids, *J. Membrane. Sci.,*1997, *134(1-2)*, 219-223.
27. J. Caro, M. Noack, P. Kölsch, Chemically modified ceramic membranes. *Microporous and Mesoporous Mater.,* 1998, *22*, 321-332.
28. F. Brodard-Severac, G. Guerrero, J. Maquet, P. Florian, C. Gervais, P. H. Mutin, High-Field ^{17}O MAS NMR Investigation of Phosphonic Acid Monolayers on Titania, *Chem. Mater.,* 2008, *20(16)*, 5191-5196.
29. G. Guerrero, P.H. Mutin, A. Vioux, Organically modified alumina by grafting and sol–gel processes involving phosphonate derivatives, *J.Mater.Chem.,* 2001, *11(12)*, 3161-3165.
30. G. Guerrero, P.H. Mutin, A. Vioux, Anchoring of Phosphonate and Phosphinate Coupling Molecules on Titania Particles. *Chem. Mater.,* 2001, *13(11),* 4367-4373.
31. G. Guerrero, 2000, Utilisation d'agents de couplage organophosphorés pour la préparation d'hybrides organique-inorganique à base d'oxyde métallique (Thèse de doctorat Chimie organique, minérale et industrielle Montpellier, Université de Montpellier (France)).
32. A. Larbot, S. Alami-Younssi, M. Persin, J. Sarrazin, L. Cot, Preparation of a y-alumina nanofiltration membrane, *J. Membrane. Sci.*, 1994, *97*, 167-173.
33. A.F.M. Leenaars, K. Keizer, A.J. Bruggraaf, The preparation and characterization of alumina membrane with ultra-fine pores, *J. Mater. Sci*., 1984, *19(4)*, 1077-1088.
34. M. Shayesteh, M. Shafiee Afarani, A. Samimi, M. Khorram, Preparation of γ-Al_2O_3 and Prioritization of Affecting Factors on the Crystallite Size Using Taguchi Method, *TPNMS*, 2013, *1*, 45-52.
35. M. Trueba, S.P. Trasatti, γ-Alumina as a Support for Catalysts: A Review of Fundamental Aspects, *Eur. J. Inorg. Chem.*, 2005, *2005(17)*, 3393–3403.
36. A. Larbot, S. Alami-Younssi, M. Persin, J. Sarrazin, L. Cot, Preparation of a y-alumina nanofiltration membrane, *J. Membrane. Sci.*, 1994, *97*, 167-173.
37. K. Wefers, C.Misra, Oxides and Hydroxides of Aluminum, *Alcoa Technical Paper No. 19*, Alcoa Laboratories, 1987.

38. A. Galarneau, Z. Abid, B. Said, Y. Didi, K. Szymanska, A. Jarzębski, F. Tancret, H. Hamaizi, A. Bengueddach, F. Di Renzo, F. Fajula, Synthesis and Textural Characterization of Mesoporous and Meso-/Macroporous Silica Monoliths Obtained by Spinodal Decomposition. *Inorganics.,* 2016, *4*, 10.

39. H. Knözinger, P. Ratnasamy, Catalytic Aluminas: Surface Models and Characterization of Surface Sites, *Catal. Rev. Sci. Eng*., 1978, *17(1)*, 31.

40. C. Morterra, G. Ghiotti, F. Boccuzi, S. Coluccia, An infrared spectroscopic investigation of the surface properties of magnesium aluminate spinel, *J. Catal.,* 1978, 51(3), 299.

41. M. Taoufik, K. C. Szeto, N. Merle, I. Del Rosal, L. Maron, J. Trébosc, G. Tricot, R. M. Gauvin, L. Delevoye, Heteronuclear NMR Spectroscopy as a Surface-Selective Technique: A Unique Look at the Hydroxyl Groups of g-Alumina, *Chem. Eur. J.,* 2014, *20(14)*, 4038 – 4046.

42. L.A. O'Dell, S.L.P. Savin, A.V. Chadwick, M.E. Smith, A ^{27}Al MAS NMR study of a sol–gel produced alumina: Identification of the NMR parameters of the y-Al_2O_3 transition alumina phase, *j. ssnmr.,* 2007, *31(4),* 169-173.

43. P. J. Hotchkiss, 2008, The design, synthesis, and use of phosphonic acids for the surface modification of metal oxides (Doctoral dissertation, Georgia Institute of Technology, USA) Retrieved from https://smartech.gatech.edu/bitstream/handle/.../Hotchkiss_Peter_J_200812_phd.pdf

44. E.M.Popov, M.I. Kabachnik, L.S. Mayants, Vibrational spectra of organo-phosphorus compounds, *Russian chemical reviews.*, 1961, *30(7)*, 362-377.

45. A.Vega, P. Thissen, T. Peixoto, J.Y. Chabal, Environment-Controlled Tethering by Aggregation and Growth of Phosphonic Acid Monolayers on Silicon Oxide. *Langmuir.*, 2012, *28(21)*, 8046-8051.

46. R. Quiñones, E. S. Gawalt, Study of the Formation of Self-Assembled Monolayers on Nitinol. *Langmuir.,* 2007, *23(20)*, 10123-10130.

47. A. Roevens, J.G. Van Dijck, M. Tassi, J. D'Haen, R. Carleer, P. Adriaensens, F. Blockhuys, V. Meynen, Revealing the influence of the solvent in combination with temperature, concentration and pH on the modification of TiO_2 with 3PA, *j.materchemphys.*, 2016, *184(1)*, 324-334.

48. M.S. Ironside, M.J. Duer, D.G. Reid, S. Byard, Bisphosphonate protonation states, conformations, and dynamics on bone mineral probed by solid-state NMR without isotope enrichment, *Eur. J. Pharm. Biopharm.,* 2010, *76*, 120-126.

49. W. El Malti, D. Laurencin, G. Guerrero, M.E. Smith, P.H. Mutin, Surface modification of calcium carbonate with phosphonic acids, *J. Mater. Chem.,* 2012, *22(3)*, 1212-1218.

50. O. Höfft, S. Bahr, V. Kempter, Investigations with Infrared Spectroscopy on Films of the Ionic Liquid [emim][Tf_2N], *Langmuir.,* 2008, *24(20)*, 11562-11566.

51. L. Raki, C. Detellier, Lamellar organominerals: intercalation of phenylphosphonate into the layers of bayerite, *Chem. Commun.,* 1996, *(21)*, 2475-2476.

52. G. Alberti, M. Casciola, U. Costantino, R. Vivani, Layered and Pillared Metal(IV) Phosphates and Phosphonates, *Adv. Mater.,* 1996, *8(4)*, 291-303.

53. W. Gao, L. Reven, Solid-state NMR Studies of Self-Assembled Monolayers, *Langmuir*., 1995, *11*, 1860-1863.

54. G. Chaplais, J. Le Bideau, D. Leclercq, H. Mutin, A. Vioux, Novel aluminium phenyl, benzyl, and bromobenzylphosphonates: structural characterisation and hydration-dehydration reactions, *J. Mater. Chem.,* 2000, *10*, 1593-1601.

55. G. Tricot, O. Lafon, J. Trébosc, L. Delevoye, F. Méar, L. Montagne, J-P. Amoureux, Structural characterisation of phosphate materials: new insights into the spatial proximities between phosphorus and quadrupolar nuclei using the D-HMQC MAS NMR technique, *Phys. Chem. Chem. Phys.,* 2011, *13*, 16786–16794.

56. J. Trébosc, B. Hu, J. P. Amoureux, Z. Gan, Through-space R^3-HETCOR experiments between spin-1/2 and half-integer quadrupolar nuclei in solid-state NMR, *J. Magn. Reson*., 2007, *186*, 220-227.

57. T.M. Alam, J.E. Jenkins, Chapter 10: HR-MAS NMR Spectroscopy in Material Science. In Advanced Aspects of Spectroscopy, Ed., M.A. Farrukh, 2012, pp. 279-306.
58. M.C. Martinez-Bisbal, L. Marti-Bonmati, J. Piquer, A. Revert, P. Ferrer, J.L. Llacer, M. Piotto, O. Assemat, B. Celda, ^{1}H and ^{13}C HR-MAS spectroscopy of intact biopsy samples ex vivo and in vivo ^{1}H MRS study of human high grade gliomas, *NMR Biomed.,* 2004, *17*, 191-205.
59. L.R. Carvalho, M.C. Corvo, R. Enugala, M.M. Marques, E.J. Cabrita, Application of HR-MAS NMR in the solid-phase synthesis of a glycopeptide using Sieber amide resin, *Magn. Reson. Chem.,* 2010, *48(4)*, 323-330.
60. C. Henoumont, S. Laurent, R.N. Muller, L. Vander Elst, HR-MAS NMR Spectroscopy: An Innovative Tool for the Characterization of Iron Oxide Nanoparticles Tracers for Molecular Imaging, *Anal. Chem.,* 2015, *87*, 1701-1710.
61. K.A. Cychosz, R. Guillet-Nicolas, J. García-Martínez, M. Thommes, Recent advances in the textural characterization of hierarchically structured nanoporous materials, *Chem. Soc. Rev.,* 2017, *46*, 389-414.
62. M.G. Freire, P.J. Carvalho, R.L. Gardas, I.M. Marrucho, L.M.N.B.F. Santos, J.A.P. Coutinho, Mutual Solubilities of Water and the [Cnmim][Tf_2N] Hydrophobic Ionic Liquids, *J. Phys. Chem. B*., 2008, *112(6)*, 1604-1610.
63. J.C. Groen, L.A.A. Peffer, J. Pérez-Ramírez, Pore size determination in modified micro- and mesoporous materials. Pitfalls and limitations in gas adsorption data analysis, *Microporous and Mesoporous Materials*, 2003, *60*, 1-17.
64. M. Cabrejas Manchado, J. M. Guil, A. Pérez Masiá, A. Ruiz Paniego, J. M. Trejo Menayo, Adsorption of H_2, O_2, CO, and CO_2 on a γ-Alumina: Volumetric and Calorimetric Studies, *Langmuir*, 1994, *10*, 685-691.
65. C. Morterra, A. Zecchinas, S. Coluccia, A. Chiorino, IR spectroscopic study of CO_2 adsorption onto η-Al_2O_3, *J. Chem. Soc. Faraday Trans.,* 1977, *73(1)*, 1544-1560.

Experimental section

Materials

All the reactions were realized under an inert atmosphere by using the schlenk line methods.

Solvents

High purity solvents methylene chloride (CH_2Cl_2), ethanol and 2-butanol were purchased from Sigma-Aldrich. The major part of the solvents were used as received, except for CH_2Cl_2 which was dried on a silica-aluminum drying column through the PureSolv, InnovativeTechnolog device.

Chemicals

Boehmite (AlOOH, Pural SB, Condea Chemie) with good crystallinity and surface area (249 m^2/g) was supplied by CTI S.A. (Salindres, France).

Characterizations

X-ray diffraction powder patterns were recorded using a PANanalytical X'Pert PRO diffractometer at the wavelength of Cu Kα (λ = 1.5405 Å) (X-ray power: 40 kV, 20 mA) in Bragg- Brentano scanning mode. The program scanned angles (2θ) from 5 to 55° with a 0.017° step, and a step time of 40 s.

Solution NMR experiments: ^{1}H, ^{13}C and ^{31}P NMR spectra were recorded using a Bruker 300 MHz NMR spectrometer at frequencies of 300.13, 75.42 and 121.42 MHz, respectively. ^{29}Si NMR spectra was performed using a Bruker 400 MHz NMR spectrometer at a frequency of 79.46 MHz.

Solid state NMR experiments: Solid state NMR spectra were acquired on a Varian VNMRS 600 spectrometer (**^{1}H:** 599.95 MHz, **^{31}P:** 242.93 MHz, **^{27}Al:** 156.37 MHz, **^{19}F**: 564.511 MHz). A 3.2 mm Varian T3 HXY magic angle spinning (MAS) probe was used for ^{1}H, ^{27}Al One-pulse, and ^{31}P CP experiments, and a 3.2 mm Varian T3 HX magic angle spinning (MAS) probe was used for the ^{31}P and the ^{19}F One-pulse experiments. All NMR experiments were performed under temperature regulation in order to ensure that the temperature inside the rotor is 20°C.

^{1}H MAS NMR experiments: the spinning frequency was 20 kHz, and the single pulse experiments were performed with a ~90° solid pulse of 2.5 µs. A recycle delay of 5 s was used (corresponding in both cases to full relaxation of ^{1}H) and a number of scan of 16. ^{1}H chemical shifts were referenced to external Adamantane at 1.80 ppm (used as a solid reference).

^{19}F MAS NMR experiments: the spinning frequency was 20 kHz, and the single pulse experiments were performed with a ~90° solid pulse of 4 µs. A recycle delay of 5 s was used (corresponding in both cases to full relaxation of ^{19}F) and a number of scan of 16. ^{19}F chemical shifts were referenced to external PTFE at -122 ppm (used as a solid reference).

^{27}Al MAS NMR experiments: were acquired at a spinning frequency of 20 kHz. The single pulse experiments were performed with a ~15° solid pulse of 1 µs and ^{1}H decoupling during acquisition. A recycle delay of 5 s was used (corresponding in both cases to full relaxation of ^{27}Al). ^{27}Al chemical shifts were referenced to external $Al(NO_3)_3$ at 0 ppm.

^{31}P MAS NMR experiments: were recorded at spinning frequency of 20 kHz. The single pulse experiments were performed with a ~90° solid pulse of 3 µs and ^{1}H decoupling during acquisition. A recycle delay of 45 s was used (corresponding in both cases to full relaxation of ^{31}P) with a number of scan of 560 which permit to obtain a signal-to-noise ratio between 53 and 79. ^{31}P chemical shifts were referenced to external Hydroxyapatite at 2.80 ppm (used as a secondary reference).

^{31}P CP-MAS NMR experiments: were recorded at spinning frequency of 20 kHz. The number of acquisitions was 64, and the recycle delays were 7 s. A 90° pulse width of 4 µs with 1.5 ms CP contact time

was employed, the acquisition time of 20.48 ms was used and the ^{1}H channel was decoupling on this period. ^{31}P chemical shifts were referenced to external Hydroxyapatite at 2.80 ppm (used as a secondary reference).

^{13}C CP-MAS NMR spectra were recorded at spinning frequency of 12 kHz MAS. Concerning the CP-MAS experiments, a contact time of 1 ms was fixed, the acquisition time to 30 ms and the ^{1}H channel was decoupling on this period. A recycle delay of 2 s was used with a number of scan of 11450, which permit to obtain a signal-to-noise ratio between 30 and 35. ^{13}C chemical shifts were referenced to external adamantane at 38.5 ppm.

^{1}H-^{27}Al and ^{31}P-^{27}Al correlation experiments were performed using a D-HMQC sequence (Dipolar Hetero-nuclear Multiple-Quantum Coherences). A spin echo selective to the central transition was first applied on the ^{27}Al side (using ^{27}Al $\pi/2$ and π pulses of 8 and 16 µs, respectively, these pulse lengths being optimized directly on the sample). ^{1}H $\pi/2$ pulse of 2.5 µs was applied on either side of the ^{27}Al π pulse. In the case of the ^{31}P-^{27}Al correlation experiments, ^{31}P $\pi/2$ pulse of 3 µs was applied on either side of the ^{27}Al π pulse. The dipolar recoupling scheme (SR_4^{21}) was rotor-synchronized and the recoupling time, τ, are integer multiples, p, of the rotor period ($\tau = pT_R$). The recycle delay was set to 0.25 s (for the ^{1}H-^{27}Al D-HMQC) or 1 s (for the ^{31}P-^{27}Al D-HMQC), and the total number of scan acquired ranged from 1536 to 3072, depending of the experience and samples. All 2D experiments were recorded under rotor-synchronised conditions along the indirect F_1 dimension.

HR-MAS experiments

The grafted sample, ImPE-Br (8) was dried for 3h at 100°C to remove excess water. D_2O was used to swell the powder (~30 mg in X µL 99% D_2O) directly in a X µL disposable insert of a 4 mm zirconia HRMAS rotor. The resulting "pastes" was mixed with a needle and the 4 mm HRMAS rotor was sealed with a Teflon caps. The preparation of NMR samples was done rapidly on ice to avoid water air exposure.

HR-MAS NMR experiments were carried out on a Varian VNMRS 600MHz spectrometer fitted with a 4-mm inverse ^{1}H-^{13}C or ^{1}H-^{31}P HRMAS probe equipped with a Z gradient. The experiments were performed at 20°C. The probe-head was pre-cooled to 20°C before loading the sample into the instrument. The sample/probe temperature was maintained throughout the experiment (±0.1 °C) via a variable temperature control unit. The sample spinning rate was at 10 kHz except for the ^{31}P experiment which was performed at 3 kHz.

^{1}H MAS NMR experiments: a ^{1}H 90° pulse length of 10 µs and a recycling delay of 5 s were used with a number of scan of 16.

^{13}C MAS NMR experiments: The liquid NMR sequence called NOEY was used with a pulse duration of 10 µs, a recycle delay of 5 s and a number of scans of 8250.

^{31}P MAS NMR experiments: The number of acquisitions was 2800, and the recycle delays were 30 s. A 90° pulse width of 4 µs was used and the ^{1}H channel was decoupling on this period.

All the NMR spectra were referenced to D_2O (^{1}H, 1.38 ppm, internal).

Energy Dipersive X-ray spectroscopy (EDX)

The weight percentage of phosphorus in the samples was determined by EDX using a SEM EVO HD15 of Zeiss at 10 kV with the Oxford instruments software. Samples were prepared as pellets for the analysis and deposited on double sided carbon tape.

Fourier Transformed Infra Red spectroscopy (FTIR)

FTIR spectra were obtained with a Perkin-Elmer Spectrum 2 spectrophotometer and were recorded in the 4000-400 cm^{-1} range using 4 scans at a nominal resolution of 4 cm^{-1} in ATR mode (spectrum of γ-alumina as a background spectrum).

BET specific surface area measurments

The BET specific surface areas and the C_{BET} constants of the samples were obtained from N_2 adsorption experiments at 77K by using a Tristar instrument (Micromeritics) for the grafted powders and an ASAP 2020 (Micromeritics) for the pristine γ-alumina powders. Prior to measurements, samples were degassed under vacuum overnight at 100 ˚C for the grafted powders and 300°C for the pristine γ-alumina powder.

CO_2 sorption experiments

The adsorption isotherms of CO_2 were measured by using a BELSORP instrument. The grafted samples were dried and degassed at 373 K first on a BELPREP instrument during 16h and then on a BELSORP instrument during 4h with a vacuum of 2.47x 10^{-8} Pa. The CO_2 was introduced into the chamber as an adsorbate under the pressure of 1.12 kPa to 100 kPa at 298 K.

Organic synthesis

The organic synthesis of [ImPE][Br], [ImPE][Tf_2N], [ImC_{12}PE][Tf_2N] and [ImPEGPE][Tf_2N] are described in chapter II, in the experimental section.

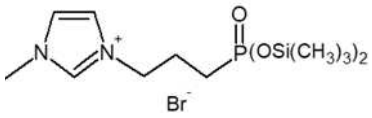

1-methyl-3-(3-((trimethoxysilyl)phosphinyl)propyl)-imidazolium bromide

The 1-methyl-3-(3-((trimethoxysilyl)phosphinyl)propyl)-imidazolium bromide ([ImTMSP][Br]) was prepared in a round-bottomed flask by the reaction of [ImPE][Br] (1 equiv) with $BrSiMe_3$ (3.5 equiv) in dry CH_2Cl_2. The following procedure is based on the procedure published by McKenna *et al.*[7]: 520 mg (1.52 mmol) of 1-methyl-3-(3-(diethylphosphinyl)propyl)-imidazolium bromide ([ImPE][Br]) was dissolved in 10 mL of dry CH_2Cl_2. Then, $BrSiMe_3$ (0.82 g, 5.35 mmol) was added dropwise and the mixture was stirred at 25°C during 17 h under argon. At the end of the reaction time, the reaction mixture was concentrated under vacuum, leading to the expected IL as a one brown-orange paste in quasi quantitative yield. (98%, 633 mg).

^{1}H NMR (300 MHz, DMSO, δ (ppm)) 9.08 (s, 1H, N–C*H*–N); 7.73 (s, 1H, N–C*H*); 7.66 (s, 1H, N–C*H*); 4.13 (t, 2H, CH_2–N); 3.79 (s, 3H,CH_3–N); 1.94-1.41 (m, 4H, CH_2–CH_2–P); 0.00 (s, 6H,O–Si–CH_3).
^{13}C NMR (300 MHz, DMSO, δ (ppm)) 137.2; 124.2; 122.7; 49.6; 36.2; 25.5; 24.4; 23.7; 2.4.
^{31P} NMR (300 MHz, DMSO, δ (ppm)) 24.7.
^{29}Si NMR (400 MHz, DMSO, δ (ppm)) 7.8.

[7] C.E. McKenna, J. Schmidhuser, Functional selectivity in phosphonate ester dealkylation with bromotrimethylsilane. *J. Chem. Soc. Chem. Commun.*, **1979**, 17, 739.

Synthesis and characterizations of the γ-alumina powder

The γ-alumina powder was prepared from the boehmite by a sol-gel process based on colloid chemistry in aqueous media according to the method reported elsewhere [1]. The boehmite (5 wt%) was placed in a beaker containing a mixture of ultrapure water and nitric acid (HNO_3/boehmite molar ratio ~0.042) as the peptizing agent. The suspension was sonicated during 15 minutes and then vigorously stirred for 2 days at room temperature. The resulting sol was centrifuged at 8500 rpm during 30 minutes in order to remove any unhydrolyzed particles. The as-obtained stable sol has been first concentrated by removing the water at temperatures under 150°C, followed by thermal treatment at 600°C/3h under ambient air (*), leading to the formation of γ-alumina powder (specific surface area of S_{BET} =220 m^2/g). All manipulation with the as-treated powder has been conducted in glovebox under an argon atmosphere.

^{27}Al solid state NMR (600 MHz, 24 kHz): δ(ppm) 10.2 (Al_{VI}); 68.2 (Al_{IV})

It must be noted that before each NMR measurement the powder has been re-calcined at 450°C/3h under nitrogen atmosphere for removing any adsorbed water on the powder surface.

(*) *Details of the thermal treatment in air:* heating ramp 10°C/min until 150°C, 1h dwelling at 150°C, second heating ramp 1°C/min until 600°C, 3h of dwell, natural cooling down to 25°C.

Grafting reactions

Standard Reaction Conditions.

The "standard" reaction parameters are summarized in Table III. 1. Typical experiments are described below.

Grafting solution with **[ImPE][Br]** was prepared by dissolving 6-fold excess (3.6 mmol) of the ionic liquid in the selected solvent. 5 mL of the grafting solution and 400 mg of the γ-alumina powder stored under argon, were mixed in a glass bottle closed with a Teflon® cap. The suspension was heated at 70 or 90°C for 3 or 12 days in an oven. After cooling down to room temperature, the suspension was then centrifuged at 8500 rpm for 5 minutes. The supernatant was removed and the remaining powder was re-dispersed in 5 mL of a (1:1) ethanol-water solution to remove the physisorbed species from the surface, and the new suspension was stirred at room temperature for 5 minutes. The ethanol-water supernatant was removed after centrifugation (8500 rpm, 5 minutes), and the washing step was repeated twice. The resulting paste was then dried under vacuum (5-10 mbar) at 70 ˚C for ~16 hours to afford the ImPE-Br (1) to (3) sample as a powder.

Grafting with **[ImTMSP][Br]** was performed directly in a round-bottomed flask in dry CH_2Cl_2, under an inert atmosphere. Typically, 3.6 mmol (6-fold excess) of **[ImTMSP][Br]** was dissolved in 14 mL of dry CH_2Cl_2 under stirring, and 400 mg of γ-alumina powder stored under argon was dispersed in the grafting solution. The suspension was kept under stirring at 25°C under argon for time periods ranging from 17h to 3 days. The suspension was then centrifuged at 8500 rpm for 5 minutes and the supernatant removed. The remaining paste was re-dispersed in 5 mL of CH_2Cl_2, and the new suspension was stirred at room temperature for 5 minutes. After centrifugation, the CH_2Cl_2 supernatant was removed and the washing step repeated once. Then, the resulting pastes were washed with a (1:1) ethanol-water solution and dried in the same conditions as above, to afford the ImTMSP-Br (1) to (2) samples as powders.

Forcing Reaction Conditions.

The "forcing" reaction conditions were applied with the **[ImPE][Br], [ImPE][Tf_2N], [ImC_{12}PE][Tf_2N]** and **[ImPEGPE][Tf_2N]** ILs. The reaction parameters are summarized in both Table III. 1, Table III. 8 and Table III. 13

Typical experiments are described below.

The IL solutions was prepared by dissolving 12-fold excess (7.2 mmol) of the pure IL in the selected solvent. Then, 10 mL of the solution and 400 mg of the γ-alumina powder stored under argon were dispersed in an autoclave which was closed with a Teflon® cap. The autoclave was sealed and the suspension was heated at 110°C or 130°C for the selected reaction time. The resulting grafted powders were washed and dried as previously described for samples prepared under standard reaction conditions. An additional washing treatment was carried out by using a Soxhlet extractor for the Tf_2N^- grafted samples. The grafted powder was placed in a cellulose thimble, closed with cotton and positioned in the extractor. 80 mL of pure ethanol was used to wash the sample; the treatment was conducted at 115°C for 24h to perform around 26 washing cycles. The resulting paste was then dried at 70 ˚C for ~16 hours, yielding samples as powders.

Chapter IV. Grafted ionic liquid-membranes for selective CO_2 transport

Stabilization of phosphonate-based ILs into the pores of a γ-Al_2O_3 ceramic membrane was achieved by applying the optimized protocol developed for grafting the ILs in the pores surface of a γ-Al_2O_3 powder (non-supported membrane). Although it was tricky to clearly demonstrate the efficiency of the grafting reaction for supported IL-membranes, their morphology and physico-chemical characteristics were investigated. The attractive performance of GILMs were evidenced through both their CO_2/N_2 ideal selectivity and CO_2 permeability.

Chapter IV. Grafted ionic liquid-membranes for selective CO_2 transport

IV.1. Introduction

The interest for the IL-based membranes for CO_2 separation applications has been demonstrated in the literature as a promising alternative to other CO_2 capture technologies (Chapter I). Among the IL-based membranes reported in the literature, the **Supported Ionic Liquid Membranes** (SILMs) composed of a ceramic membrane support received substantial attention due to their attractive CO_2 separation performances [1-3]. Such SILMs are made of a porous solid support impregnated with an IL, which is held by capillary forces within the pores and at the surface (Figure IV. 1). However, SILMs are mechanically unstable, and the IL is easily "blown out" from most support materials under pressure. To overcome these issues a new generation of SILMs has been recently developed, in which the IL is chemically grafted on the outer surface and within the pores of mesoporous or microporous ceramic supports [4] (Figure IV. 1).

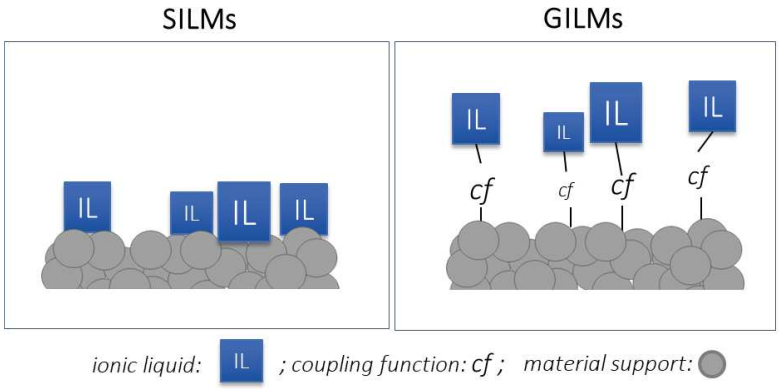

Figure IV. 1. Schematic illustration of the possible IL/support interactions in IL-based membranes: weak interaction in SILMs and strong covalent interaction in GILMs.

The preparation of **Grafted Ionic Liquid Membranes (GILMs)** requires a precise control of the covalent bonds formation between the ILs and the surface functional groups of the ceramic support. Controlling the grafting step and mechanisms is a tricky task and the literature dedicated to GILMs is very scarce [4]. In this work, the ester phosphonate coupling function was selected because it is adapted to obtain homogenous monolayers of grafted ILs. Chapter II was well dedicated to select, design and synthesize the most suitable phosphonate-ILs and to evaluate their potential for selective CO_2/light gas separation. The phosphonate-based ILs, [ImPE][Tf_2N], [ImPEGPE][Tf_2N], and [ImC_{12}PE][Tf_2N] are represented in Figure IV. 2. They are composed of the bis(trifluoromethane sulfonimide) anion and were found to provide low CO_2/CH_4 solubility selectivity but high CO_2/N_2 solubility selectivity at room temperature (cf. chapter II). The grafting protocol of these ILs has been carefully designed and optimized on γ-Al_2O_3 powders, on the basis of detailled characterization of all the hybrid phosphonate-ILs/γ-Al_2O_3 materials prepared.

In the present chapter, Grafted Ionic Liquid Membranes have been prepared by applying the optimized grafting protocol of phosphonate-based ILs to the γ-Al_2O_3 top-layer of commercial alumina discs. In order to compare the GILMs prepared in this work with the SILMs from the literature, ceramic-

based SILMs were prepared with the 1-butyl-3-methylimidazolium bis(trifluoromethanesulfonimide) ([bmim][Tf_2N]) using the same porous alumina disc as for the GILMs.

Considering the limited remaining time for achieving this final step of the PhD work, only preliminary results will be reported in this chapter, with a focus on the GILMs derived from [ImPE][Tf_2N] and [ImPEGPE][Tf_2N], in comparison with the [bmim][Tf_2N] derived SILM. The morphology, composition, and thickness of the three as-prepared membranes have been analyzed and compared together with their performance (permeance and selectivity) for gas transport.

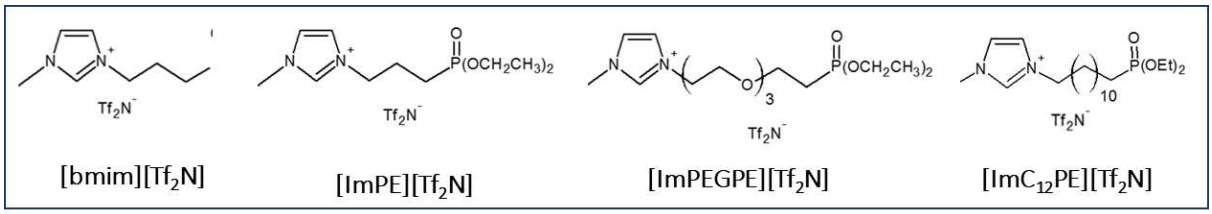

Figure IV. 2. Structure of the ILs: [bmim][Tf_2N], [ImPE][Tf_2N], [ImPEGPE][Tf_2N] and [$ImC_{12}PE$][Tf_2N].

IV.2. Results and Discussion

The preparation of the GILMs was operated by reacting the γ-Al_2O_3 top-layer with a phosphonate-based IL solution, using the optimum reaction conditions determined in chapter III. The quantity of IL and the reaction times used corresponds to the amount needed to maximize the quantity of grafted species on the γ-Al_2O_3 powder specific surface area (Table IV. 1). After grafting treatment, the GILMs were washed by immersion in an ethanol-water solution to remove the excess of IL and then dried at 70°C before analysis (cf. Experimental section). The [bmim][Tf_2N]-SILM membrane was prepared according to a procedure reported in the literature [1] (cf. Experimental section).

Table IV. 1. Details of the grafting conditions for GILM(1) and GILM(2).

sample	IL	Solvent (mL)	T(°C)	Time (h)	n (ILs) mmol
GILM(1)	[ImPE][Tf_2N]	H_2O:EtOH (20)	130	30	14.4
GILM(2)	[ImPEGPE][Tf_2N]	H_2O:EtOH (20)	130	40	6.1

Scanning Electron Microscope (SEM) observations were used to compare the morphology, location and homogeneity of the three membrane materials: [bmim][Tf_2N]-SILM, GILM(1) and GILM(2). Membrane cross-sections are shown in Figure IV. 3., with zooms in different areas of the membranes. The **pristine alumina support** is shown in Figure IV. 3. (A1, A2, and A3), the **[bmim][Tf_2N]-SILM** in (B1, B2 and B3), the **[ImPE][Tf_2N]-GILM(2)** in (C1, C2, and C3) and the **[$ImC_{12}PE$][Tf_2N]-GILM(3)** in (D1, D2, and D3). Figure IV. 3. A1 shows the pristine γ-Al_2O_3 top-layer ($Ø_{pores}$=5 nm); A2 shows the top-layer and two underlayers ($Ø_{pores}$= 100 and 800 nm) and A3 shows the external support layer ($Ø_{pores}$ =3 µm). Figure IV. 3. B1 and B2 reveal the homogeneous impregnation of the [bmim][Tf_2N] IL in both the γ-Al_2O_3 top-layer and support underlayers. On the external support layer (B3), only small amount of physisorbed IL can be observed in between the alumina grains. From SEM analysis, we can estimate the hybrid layer thickness at ~33 µm.

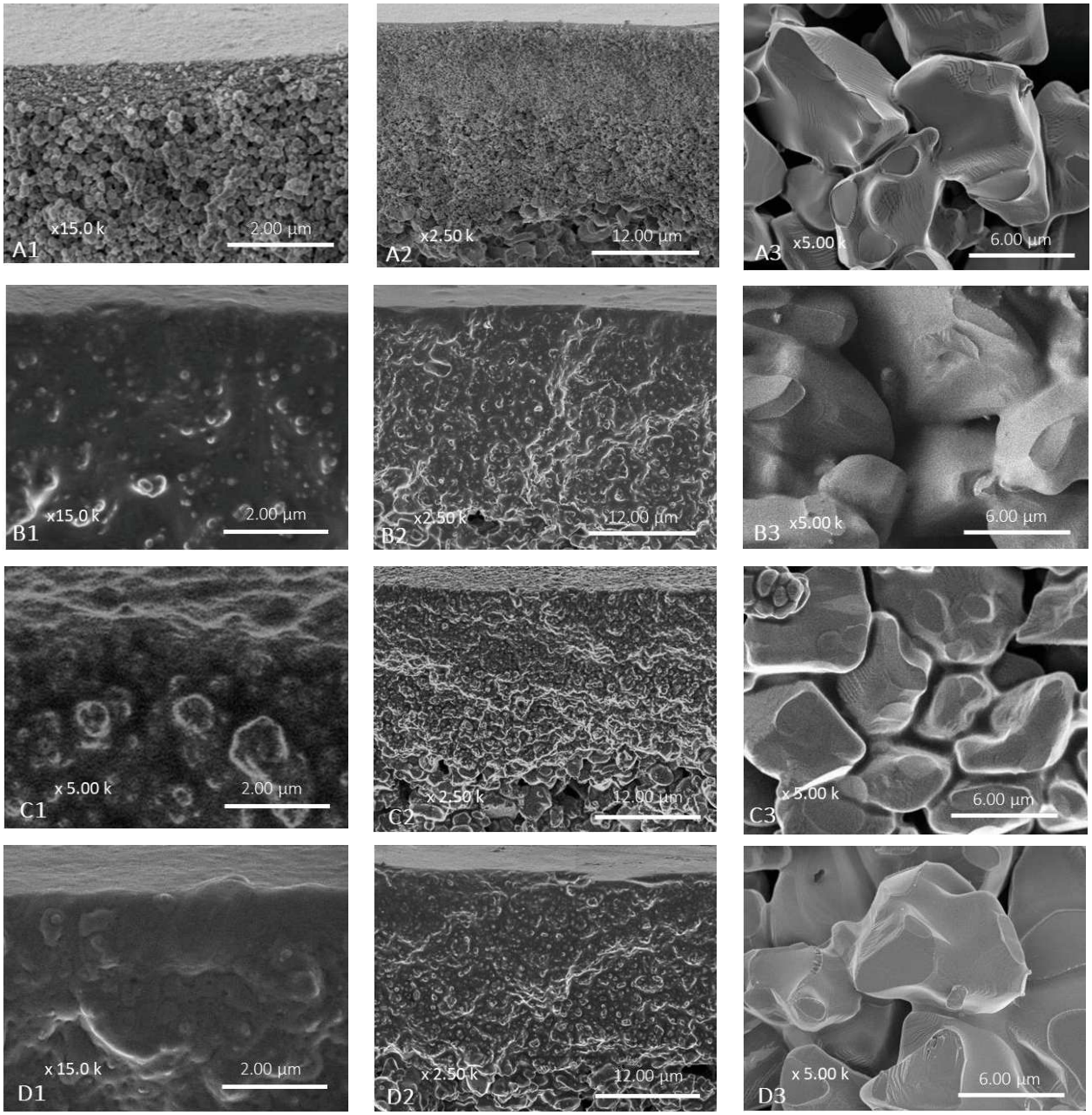

Figure IV. 3. SEM pictures showing the cross-sections of the alumina support with γ-Al_2O_3 top-layer before and after IL impregnation/grafting: A) pristine support, B) [bmim][Tf_2N]-SILM, C) [ImPE][Tf_2N]-GILM2, D) [ImPEGPE][Tf_2N]-GILM3. The numbers 1, 2 and 3 refer to different areas of the membranes: 1. γ-Al_2O_3 top-layer ($Ø_{pores}$=5 nm) and first underlayer ($Ø_{pores}$=100 nm), 2. γ-Al_2O_3 top-layer and two underlayers ($Ø_{pores}$= 100 and 800 nm), and 3. External support layer ($Ø_{pores}$ =3 µm).

The SEM observations shown in Figure IV. 3. C1, C2, and C3 relates to the [ImPE][Tf_2N]-GILM(1). When comparing to the micrographs of [bmim][Tf_2N]-SILM, the alumina grains (γ-Al_2O_3 and α-Al_2O_3) of the top-layer and internal layers are more visible in figures C1 and C2. The surface does not appear smooth like in the previous case but rather rough. The grains of the external layer seem to be coated with the [ImPE][Tf_2N] IL. The thickness of the hybrid layer was estimated at ~20 µm for [ImPE][Tf_2N]-GILM(1). Finally, the micrographs corresponding to [ImPEGPE][Tf_2N]-GILM(2) (Figure IV. 3.D1, D2, and D3) were very similar to those of [bmim][Tf_2N]-SILM except that no ILs was detected in the external layer (D3).

In order to investigate the nature and bonding modes of the phosphonate-based ILs in the GILMs, a FTIR study was achieved directly on the γ-Al_2O_3 top-layer surface of both the GILM(1) and GILM(2) samples. The FTIR spectra obtained for GILM(1) and GILM(2) in the range 1400-800 cm^{-1} are shown in Figure IV. 4 (c.) and compare with the spectra of the neat ILs (a.) and the optimized grafted powders (b.). Obviously, the FTIR spectra of both GILM(1) and GILM(2) are very similar to those of the corresponding ImPE-Tf_2N(2) and ImPEGPE-Tf_2N(2) grafted samples. In the two GILMs, we can notice the predominance of the Tf_2N^- bands at 1346-1327, 1224, 1195, 1132 and 1061 cm^{-1}. The presence of the cations is denoted by a strong vibration band at 1171 cm^{-1} typical of the =CH and $–CH_2$- deformation bands of the imidazolium ring and the organic spacers. Concerning the characteristic bands of the phosphonate coupling function, we can note in both samples a reduction of the bands related to the phosphoryl (P=O) stretching vibration near 1266 and 1235 cm^{-1}, and residual bands connected to the –POEt groups in the region 950-1050 cm^{-1}. It is important to note the presence in both GILMs of the strong P-O-Al stretching band at 1065 cm^{-1}. Thus, as concluded for the grafted samples in Chapter III, section III.2 and III.3 (ImPE-Tf_2N(2) and ImPEGPE-Tf_2N(2)), we can assume that the dominating bonding mode in the GILMs corresponds to the tridentate mode, followed by the bidentate and tridentate bonding modes.

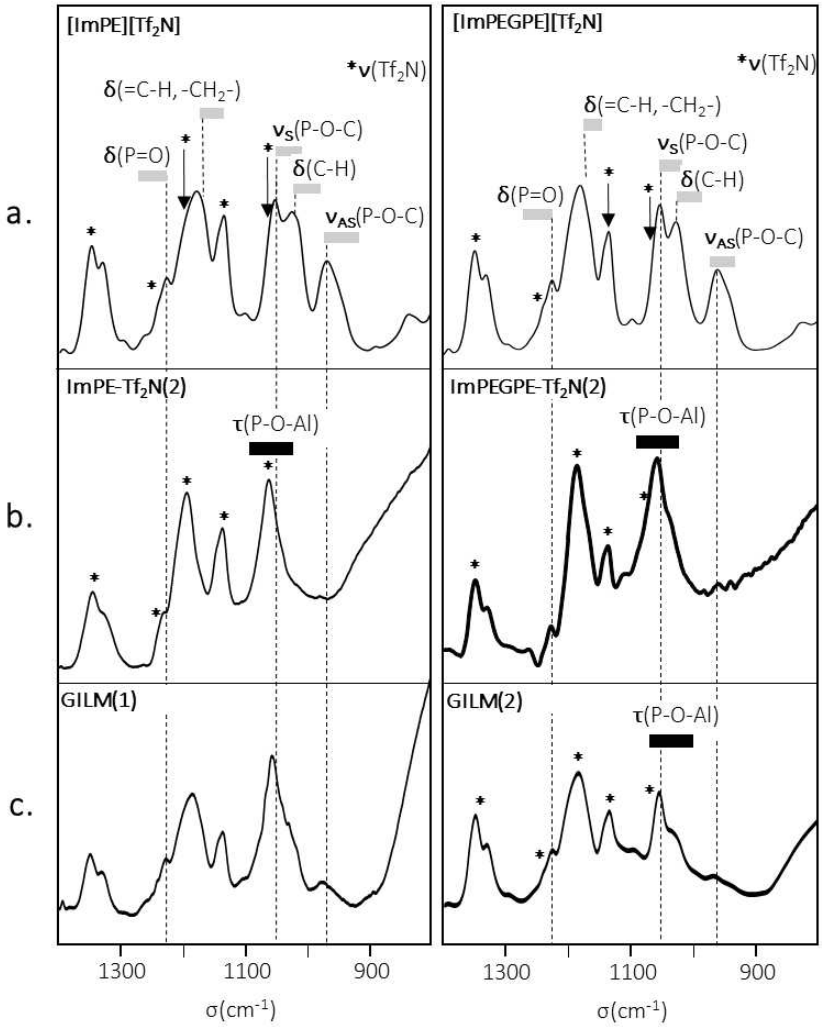

Figure IV. 4. FTIR spectra for **a.** [ImPE][Tf_2N] and [ImPEGPE][Tf_2N] ionic liquids, **b.** γ-Al_2O_3 powders grafted with ImPE-Tf_2N(2), and ImPEGPE-Tf_2N(2), **c.** Grafted ionic liquid membranes GILM(1) and GILM(2).

As already discussed in chapter I section I.3.2, the determination of the hybrid membrane thickness, δ, is required to estimate the CO_2 permeability, P^*_{CO2} (*calculated as the product of the CO_2 permeance, Π_{CO2} by the membrane thickness, δ).* In addtion, several authors highlighted the influence of the support contribution on the membrane gas separation properties [3-10]. The interactions between the IL and the different layers of the porous ceramic support are influenced by the support characteristics, *i.e., geometry, architecture, and pore structure*. Special attention has thus been devoted in this work to the evaluation of the hybrid membrane thickness in order to evidence IL/support interactions. In addition, a wrong estimation of the thickness value will impact the permeability results. Four types of methods can be found in the literature to estimate the IL membrane effective thickness: ***i)*** *the SEM thickness* δ_{SEM}, ***ii)*** *the theoretical IL membrane thickness* δ_T [5,7], ***iii)*** *the Raman thickness* δ_R [7,9]*; and* ***iv)*** *the thickness by weight measurements* δ_w [7].

- *the SEM thickness, δ_{SEM}, is* determined by analysis of the membrane cross-section. Kreiter *et al.* [3], have used this technique to control IL impregnation depth: they were able to limit the composite membrane thickness to the thickness of the mesoporous top-layer (~1.5 µm).

- *the theoretical IL membrane thickness, δ_T,* proposed by Albo *et al.* [5,7], can be expressed as follows:

$$\delta_t = \frac{P^*_{bulk}}{\Pi_{CO2}} . \frac{\varepsilon}{\tau} \qquad 4.1$$

where P^*_{bulk} is the expected CO_2 permeability in the bulk IL (*mol.µm.m^{-2}.s^{-1}.Pa^{-1}*), Π_{CO2} is the measured CO_2 permeance for the SILMs expressed in (*mol.m^{-2}.s^{-1}.Pa^{-1}*), ε is the support porosity (%), and τ is the pore network tortuosity (dimensionless approximation factor). This equation requires a determination of the values of porosity and tortuosity for the impregnated layers of the ceramic support. These parameters cannot be easily determined in multilayers materials.

- *the Raman thickness, δ_R,* proposed by Labropoulos *et al.* [7,9], is derived from the Raman spectra of the SILM along its cross-section. The intensity ratio between the stronger Raman bands of the IL and the ceramic support are compared. By plotting the values of this ratio all along the membrane cross-section, the IL infiltration profile in the SILM can be identified. The Raman thickness, δ_R, is obtained when the intensity ratio equals zero.

- *the thickness by weight measurements,* δ_w can be estimated as:

$$\delta_w = \frac{m}{S.\rho} . 10^{-4} \qquad 4.2$$

in which ρ is the IL the volumetric mass density (*g.cm^{-3}*), m the amount of IL within the SILMs (*g*) and S the surface area of the ceramic support (*cm²*). Albo *et al.* [5,7], evidenced significant difference (~50%) between δ_w and *the theoretical membrane thickness, δ_T* (*e.g., δ_w= 1.39 µm and δ_T = 0.68 µm*). The δ_w thickness fitted with SEM observations which revealed complete impregnation of the IL into all intermediate layers of the ceramic support, and partial wetting of the external layer. Consequently, the authors selected the δ_w thickness for calculating the CO_2 permeability, P^*_{CO2} of the composite membrane.

In the present work, the penetration/grafting depth of the ILs has been estimated by three methods: *i) SEM analysis*, *ii) support weight increase measurement and iii) EDX analysis of phosphorus and sulfur content along the membrane cross-section* (from the γ-Al_2O_3 top-layer to the support external layer). This last approach was used by Drobek *et al.* [11], to study the infiltration depth of oligomers in a zeolite

membrane. In the present work, phosphorus and sulfur were analysed because they are tracers of the coupling function on the cation and of the anion, respectively.

Results of thickness evaluation for GILM(1), GILM(2) and [bmim][Tf_2N]-SILM are reported in Table IV. 2 and Figure IV. 5.

Table IV. 2. Hybrid membrane thickness estimated from support weight increase (δ_w), SEM observation ($\delta_{SEM,}$) and EDX analysis (δ_{EDX}).

				Estimated thickness (µm)		
Membrane references	IL	*ρ (g.cm^{-3})*	Support weight (mg)	δ_{SEM}	δ_{EDX}	δ_w
[bmim][Tf_2N]-SILM	[bmim][Tf_2N]	1.43	44	31	28	65
GILM(1)	[ImPE][Tf_2N]	1.48	47	23	25	63
GILM(2)	[ImPEGPE][Tf_2N]	1.47	31	30	≈30	43

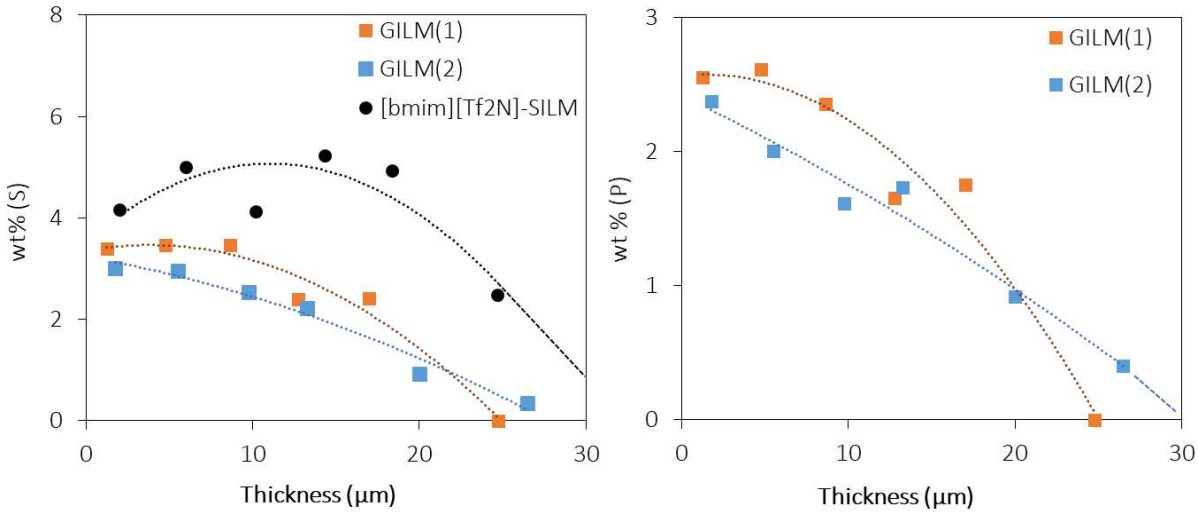

Figure IV. 5. Evolution of phosphorus (left side) and sulfur (right side) concentrations (wt% by EDX analysis) along the membrane cross-section (µm) for GILM(1), GILM(2) and [bmim][Tf_2N]-SILM.

As shown in Table IV. 2, the thickness values derived from both SEM micrographs and EDX analysis are very close. The thickness in both [bmim][Tf_2N]-SILM and GILM(2) are estimated at ~30 µm. On the other hand the hybrid membrane thickness for GILM(1) is ~23 µm from the SEM, and ~25 µm from EDX analysis. Much higher thickness values (x2 or x3) are obtained when considering the support weight increase (*e.g., for [bmim][Tf_2N]-SILM, δ_{SEM} ~31 µm while δ_w ~65 µm*). Thus, it can be concluded that, contrary to the results published by Albo *et al.* [5,7], the δ_w values derived from support weight increase does not seem to be the most relevant to evaluate the CO_2 permeability of hybrid membranes. Hence, in this work we thus used the membrane thicknesses determined by SEM (δ_{SEM}) for both [bmim][Tf_2N]-SILM and GILM(2) and EDX (δ_{EDX}) for GILM(1).

The Table IV. 3. compares the measured single gas CO_2 permeances (Π_{CO2}) and ideal CO_2/N_2 selectivities (α*) at 23°C for the 3 IL-based membranes and the pristine γ-Al_2O_3 mesoporous membrane. We have to note that all the hybrid membranes were found to be N_2-tight or at least below the system detection limit, (< 1 x 10^{-11} mol.m^{-2}.s^{-1}.Pa^{-2}). This result proves that the hybrid membranes are defect-free and continuous, with the IL blocking the pores of the γ-Al_2O_3 top-layer.

It should be noted that the values of single gas permeances through the IL-membranes developed in this work were measured in a dead-end configuration, *i.e.,* conditions favoring gas transport through

membrane defects if any. Many results reported in the literature are obtained with a Wicke-Kallenbach configuration (steady state diffusion cell) [8], which limits the contribution of defects for gas transport and thus yields high gas selectivities.

Table IV. 3. Comparison of single CO_2 permeance (Π_{CO2}) and ideal CO_2/N_2 selectivity (α^*) for three IL-based membranes, [bmim][Tf_2N]-SILM, GILM(1) and GILM(2) and for the pristine γ-Al_2O_3 mesoporous membrane. Permeances were measured at 23°C with a feed pressure of 3.5 bar. For all IL-based membranes Π_{N2} was below the system detection limit, i.e. < 1 x 10^{-11} mol.m^{-2}.s^{-1}.Pa^{-2}.

Sample	Virgin γ-Al_2O_3	[bmim][Tf_2N]-SILM	GILM(1)	GILM(2)
Π_{CO2} (mol.m^{-2}.s^{-1}.Pa^{-1})	3.30 x 10^{-6}	1.43 x 10^{-9}	6.2 x 10^{-10}	1.32 x 10^{-9}
Π_{CO2} (GPU)	9859	4.3 ± 0.5	1.8 ± 0.1	3.9 ± 1.0
δ (μm)	-	31	25	30
P^*_{CO2} (Barrer)	-	132.7 ± 5.3	47.4 ± 2.7	129.7 ± 21.2
α^* (CO_2/N_2)	0.9	143.3 ± 4.8	63.5 ± 3.7	144.1 ± 23.5

The CO_2 permeability of [bmim][Tf_2N]-SILM is remarkably low in comparison with published results for SILM prepared by impregnation of [bmim][Tf_2N] in other ceramic supports. For example, Close *et al.* [1], reported a CO_2 permeability of 2582 Barrer with a CO_2/N_2 ideal selectivity of 16 for a SILM prepared by impregnation of [bmim][Tf_2N] in alumina Anodisc support with tortuosity ~1 (parallel capillary pores). In the present work the tortuosity of the γ-Al_2O_3 top-layer is much higher than 1, thus favoring higher IL/gas contact time and thus higher ideal CO_2/N_2 selectivity (typically > 143 instead of ~16 in previous studies [1]). The same issue was observed by Labropoulos *et al*. [10], when impregnating a microporous silica top-layer ($\emptyset_{pore}$ *~1 nm*) with either [emim][TCM] or [bmim][TCM] ILs. The authors observed high CO_2/N_2 mixed gas selectivities but low CO_2 permeability for all the prepared SILMs [10]. The confinement of the IL in the micropores was invoked to generate strong increase of its viscosity and thus a decrease of the expected CO_2 permeability. In addition, the authors suggested that the confinement of [bmim][TCM] IL induces specific orientation, favoring CO_2 transport through a hopping mechanism from anion to anion, while the [emim][TCM] IL was exposed to a liquid/solid transition affecting the CO_2 diffusion. The same authors demonstrated this assumption elsewhere [9], by comparing series of ceramic-based SILMs derived from the [$C_x$mim][TCM] ILs impregnated in either microporous (silica *with* $\emptyset_{pore}$ *~1 nm*) or mesoporous (γ-Al_2O_3 with $\emptyset_{pore}$ ~ 5 or 10 nm) top-layers. Thermal analysis of the developed SILMs revealed a drastic liquid-to-solid transition upon confinement of the ILs in micropores with sizes ~1 nm. They also concluded that the IL was under different physical states depending on the pore sizes, thus yielding significant variation of the gas transport properties and CO_2 permeability. The results we obtained for the [bmim][Tf_2N]-SILM fit those reported by Labropoulos *et al*. [9,10], and could be associated to the effect of confinement.

The grafted ionic liquid membranes, GILM(1) and GILM(2), also yield relatively high CO_2/N_2 ideal selectivities (respectively > 64 and >144), similar to those measured for the [bmim][Tf_2N]-SILM in which the IL is simply physisorbed in the pores. The CO_2 permeability is also in the same range, with values of 47 Barrer for GILM(1) and 130 Barrer for GILM(2). These CO_2 permeability values fit those published by Vangeli *et al.* [4], for microporous ceramic membranes grafted with alkoxysilane imidazolium ILs. The chemical grafting of the [smmim][PF_6][8] IL was investigated by EDX elemental analysis, and was argued to explain the observed gain of stability (CO_2 permeability) obtained during 3 sequential heating/cooling

[8] [smmim][PF_6]: The 1-methyl-3-(1-trimethoxysilylmethyl) imidazolium hexafluorophosphate.

cycles up to 250°C, and 5 bar trans-membrane pressure. The highest CO_2 permeability measured at 30°C was ~226 Barrer for the modified microporous silica membrane ($Ø_{pore} \sim 1\ nm$). This permeability is close to the values obtained for both GILM(2) and [bmim][Tf_2N]-SILM. The preliminary tests on the pressure dependence of the GILMs have been conducted on GILM(2) at 20°C. They revealed a decrease of the CO_2 permeability with the increase of the pressure (cf. Figure A5. 1). This result is in adequation with those obtained by Vangeli *et al.* [4]. An investigation of the temperature dependence is also ongoing, the first results concern also GILM(2) and are presented in Figure A5. 2. Preliminary observations suggest that the temperature do not impact on the CO_2 permeability. Additional tests at higher temperature should be required to confirm this trend.

As far as nanoconfined IL-based SILMs have been shown to provide an increase of CO_2 permeability with stable CO_2 selectivity when temperature is increased [9,10,4], attractive performance are expected for the GILMs, for the separation of gas mixtures upon long term operation. This will need to be demonstrated by considering gas permeation and gas separation measurements through both SILM and GILMs for long period of time, at higher temperature and/or high pressure (ongoing work).

IV.3. Conclusion

Figure IV. 6 compares the CO_2/N_2 ideal selectivity vs. CO_2 permeability at ~25°C for series of IL-based membranes prepared in this work, with data reported in the open literature (Chapter I). The results for GILM(2) and [bmim][Tf_2N]-SILM clearly outperformed the classical upper bound limit for CO_2/N_2 ideal selectivity (Figure IV. 6).

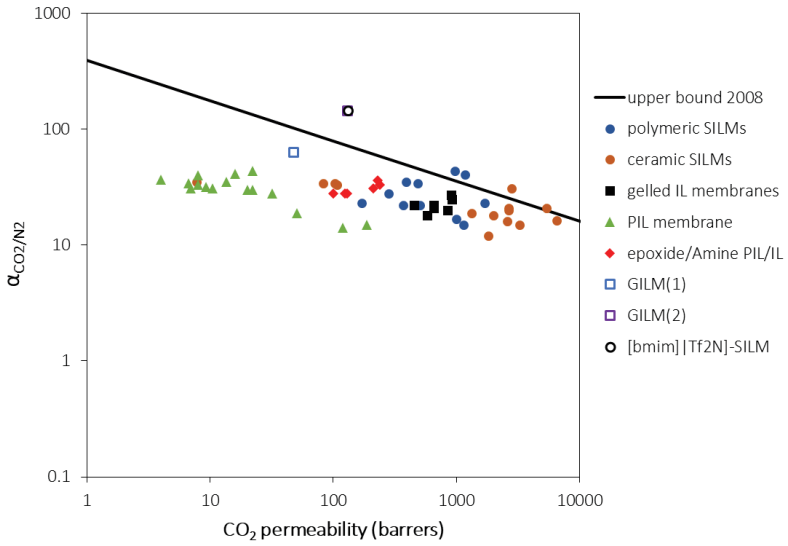

Figure IV. 6. Robeson plot comparing CO_2/N_2 ideal selectivity vs. CO_2 permeability for series of IL-based membranes studied in this chapter, in comparison with data from the literature (Note that all data points were obtained from the literature and are reported in Annex 3).

However, the CO_2 permeability values presented in Table IV. 3 shows that the highest value is limited to ~5 GPU at room temperature. According to Merkel *et al.* [12], the membranes designed to treat flue gas usually operate in a pressure-ratio-limited regime and CO_2 permeances of ~1000 GPU are typically required to reduce both the membrane area and associated capital cost. High selectivity only increases gas purity and impacts on both power requirements and operating costs, this is why a CO_2/N_2 selectivity of ~30 is often enough. Thus, application of GILMs to flue gas treatment will be possible only if higher CO_2 permeance can be reached. In addition to the application of higher temperature for activating CO_2

transport through the hybrid membrane, a controlled design of the membrane top-layer and more precise IL-deposition protocol (for limiting deep IL infiltration) will have to be considered.

References

1. J.J. Close, K. Farmer, S.S. Moganty, R.E. Baltus, CO_2/N_2 separations using nanoporous alumina-supported ionic liquid membranes: Effect of the support on separation performance, *J. Membrane. Sci.,* 2012, *390-391*, 201–210.

2. S.D. Hojniak, I.P. Silverwood, A.L. Khan, I.F.J. Vankelecom, W. Dehaen, S.G. Kazarian, K. Binnemans, Highly Selective Separation of Carbon Dioxide from Nitrogen and Methane by Nitrile/Glycol-Difunctionalized Ionic Liquids in Supported Ionic Liquid Membranes (SILMs), *J. Phys. Chem. B*., 2014, *118(26),* 7440–7749.

3. S.D. Hojniak, A.L. Khan, O. Hollo, B. Kirchner, I.F.J. Vankelecom, W. Dehaen, K. Binnemans, Separation of Carbon Dioxide from Nitrogen or Methane by Supported Ionic Liquid Membranes (SILMs): Influence of the Cation Charge of the Ionic Liquid, *J. Phys. Chem. B.,* 2013, *117(14),* 15131−15140.

4. O.C. Vangeli, G.E. Romanosa, K.G. Beltsios, D. Fokas, C. P. Athanasekou, N.K. Kanellopoulos, Development and characterization of chemically stabilized ionic liquid membranes-Part I: Nanoporous ceramic supports, *J. Membrane. Sci.,* 2010, *365,* 366–377.

5. R. Kreiter, J.P. Overbeek, L.A. Correia, J.F. Vente, Pressure resistance of thin ionic liquid membranes using tailored ceramic supports, *J. Membrane. Sci.*, 2011, *370*, 175–178.

6. J. Albo, T. Yoshioka, T. Tsuru, Porous Al_2O_3/TiO_2 tubes in combination with 1-ethyl-3-methylimidazolium acetate ionic liquid for CO_2/N_2 separation, *Sep. Purif. Technol,* 2014, *122*, 440–448.

7. J. Albo, T. Tsuru, Thin ionic liquid membranes based on inorganic supports with different pore sizes, *Ind. Eng. Chem. Res*., 2014, *53*, 8045−8056.

8. K. Soukup, P. Schneider, O. Šolcová, Comparison of Wicke–Kallenbach and Graham's diffusion cells for obtaining transport characteristics of porous solids, *Chem. Eng. Sci.,* 2008, *63*, 1003-1011.

9. O. Tzialla, A. Labropoulos, A. Panou, M. Sanopoulou, E. Kouvelos, C. Athanasekou, G. Romanos, Phase behavior and permeability of Alkyl-Methyl-Imidazolium Tricyanomethanide ionic liquids supported in nanoporous membranes; *Sep. Purif. Technol.,* 2014*, 135*, 22–34.

10. A.I. Labropoulos, G.Em. Romanos, E. Kouvelos, P. Falaras, V. Likodimos, M. Francisco, M.C. Kroon, B. Iliev, G. Adamova, T.J.S. Schubert, Alkyl-methylimidazolium Tricyanomethanide Ionic Liquids under Extreme Confinement onto Nanoporous Ceramic Membranes, *J. Phys. Chem. C.,* 2013, 117, 10114−10127.

11. M. Drobek, J. Motuzas, V. Durand, M. Duchateau, C. Charmette, A. Hertz, C. Loubat, A. Julbe, Evaluation of a new supercritical CO_2-assisted deposition method for preparing gas selective polymer/zeolite composite membranes, *J. Membrane. Sci*., 2013, *429*, 428–435.

12. T.C. Merkel, H. Lin, X. Wei, R. Baker, Power plant postcombustion carbon dioxide capture: An opportunity for membranes, *J. Membrane. Sci*., 2010, *359(1-2)*, 126−139.

Experimental section

Materials

High quality grade ethanol was purchased from Sigma-Aldrich. The 1-butyl-3-methylimidazolium bis(trifluoromethanesulfonimide) was purchased from Solvionic. All chemicals were used as received without any further purification. Porous alumina discs (25 mm diameter, 1 mm thick) with a γ-Al_2O_3 top-layer (3–5 nm pore size) were provided by Fraünhofer-IKTS (Germany) and used as supporting material for preparing the IL-based membranes (GILMs and SILM).

Description of the support

The phosphonate-based ILs were grafted in/on the mesoporous γ-Al_2O_3 top-layer supported on discs (Ø = 25 mm, 1 mm thick) provided by Fraunhofer-IKTS. They are composed of a coarse asymmetric α-alumina porous body with one side covered by γ-alumina mesoporous layer ($Ø_{pore}$ = 5 nm).

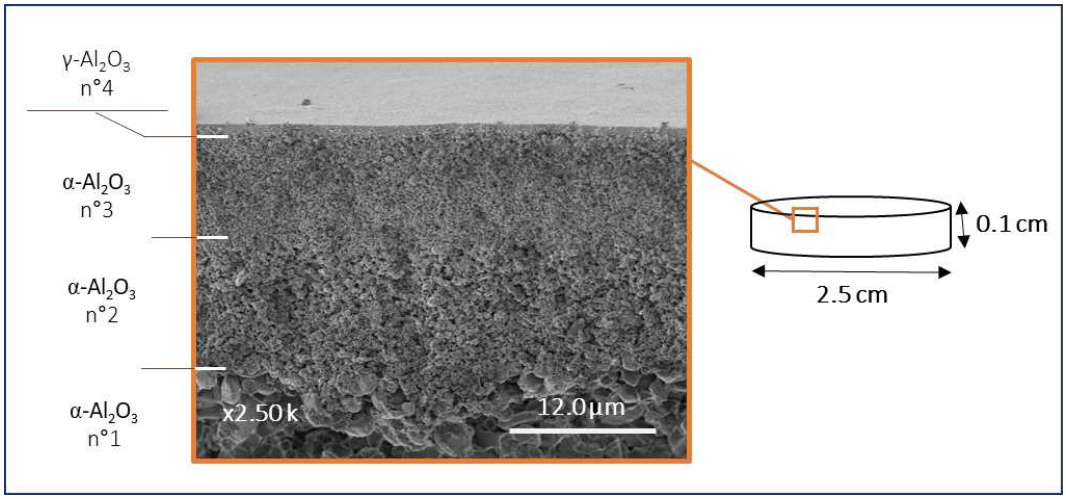

Figure IV. 7. Description of the commercial ceramic membrane discs Fraunhofer-IKTS. SEM observation of the asymmetric support microstructure with a γ-Al_2O_3 top-layer.

The asymmetric porous structure of the support, obtained by stacking layers with decreasing pore sizes, ensures both good permeability and high mechanical resistance. The characteristics of the different layers are shown in Table IV. 4. The separative top-layer governs the fluid transport mechanisms and its average pore size is often used as the membrane reference.

Table IV. 4. Main characteristics of the asymmetric ceramic membrane discs Fraunhofer-IKTS. The porosity of the different layers is in the range 30-55%.

Layer#	Material	Average pore diameter (µm)	Layer thickness (µm)
1	α-Al_2O_3	3	≈1000
2	α-Al_2O_3	0.8	11
3	α-Al_2O_3	0.1	8.5
4	γ-Al_2O_3 (top-layer)	0.005	1

Preparation of the SILM

The [bmim][Tf_2N]-SILM membrane was prepared by placing the pristine alumina disc into a container and then, drops of ILs were deposited on the γ-Al_2O_3 top-layer using a micropipette. Enough IL was added on the surface until complete support wetting, and the excess of IL was then removed from the surface with blotting papers. Samples were weighted with analytical balance before and after the coating procedure.

Preparation of the GILMs

All the GILMs were prepared by following the same experimental protocol. Experiments were conducted both on entire alumina discs and on small companion samples. The entire discs were used for dynamic characterizations (gas permeation) while the companion samples were used for static physico-chemical characterizations. The grafting solution was prepared by dissolving different proportions of the IL (either [ImPE][Tf_2N] or [ImPEGPE][Tf_2N], according to Table IV. 1) in ethanol-water media. Then, 20 mL of the grafting solution, the ceramic disc support and the companion sample were placed in a 120 mL autoclave, which was closed with a Teflon® cap. The autoclave was sealed and heated at 130°C following the grafting duration reported in Table IV. 1. The resulting Grafted Ionic Liquid Membranes (GILM(1) and GILM(2)) and companion samples were washed by immersion in 20 mL of ethanol-water solution (0.4:0.6) to remove the excess of ILs from the surface. Samples were dried for 17h at 70°C. The samples were weighted before and after the coating procedure using an analytical balance.

Characterization

Scanning electron microscopy (SEM)

SEM images were obtained with Hitachi S-4800 field-emission scanning electron microscope (Japan) using an accelerating voltage of 2 kV. Samples were metallized with platinum to favor charge release.

Energy Dispersive X-ray spectroscopy (EDX)

The weight % of phosphorus in the samples was determined by EDX using a Zeiss SEM (EVO HD15) at 10 kV with Oxford instruments software.

Fourier Transformed Infra-Red spectroscopy (FTIR)

FTIR spectra were obtained with a Perkin-Elmer Spectrum 2 spectrophotometer. Spectra were recorded in the 4000-400 cm^{-1} range using 4 scans at a nominal resolution of 4 cm^{-1} in ATR mode (γ-alumina spectrum was used as background).

Single Gas permeation measurements

The permeation of single gases (N_2, CH_4 or CO_2) through IL-based membranes was measured by using a stainless steel permeation module. Gas permeation through a pristine γ-Al_2O_3 mesoporous membrane was also evaluated. A schematic representation of the experimental set-up is shown in Figure IV. 8. The feed gas pressure was set at 3.5 bar (P_{up}) through a pressure transducer while the permeate compartment was connected to the atmosphere (P_{atm}). The tightness between the internal and external compartments was ensured by two PTFE seals (N°4. in Figure IV. 8) surrounding the alumina disc. The flow rate of the permeating gas was measured using a bubble flow meter (N°5. Figure IV. 8). The permeance (Π_A) of a single gas A (i.e. N_2, CO_2)) through the membrane ($mol.m^{-2}.s^{-1}.Pa^{-1}$ or

GPU[9]) corresponds to the ratio of the gas molar flux J_A (mol.s^{-1}.m^{-2}) (*i.e., molar flow per membrane unit area*) to the applied transmembrane pressure ($\Delta P = P_{up} - P_{atm}$).

$$\Pi_A = \frac{J_A}{\Delta P} \quad 4.3$$

The effective membrane area exposed to the gas was 2.84 cm². Prior to any measurement, membranes were outgassed under vacuum for 1h at 100°C.

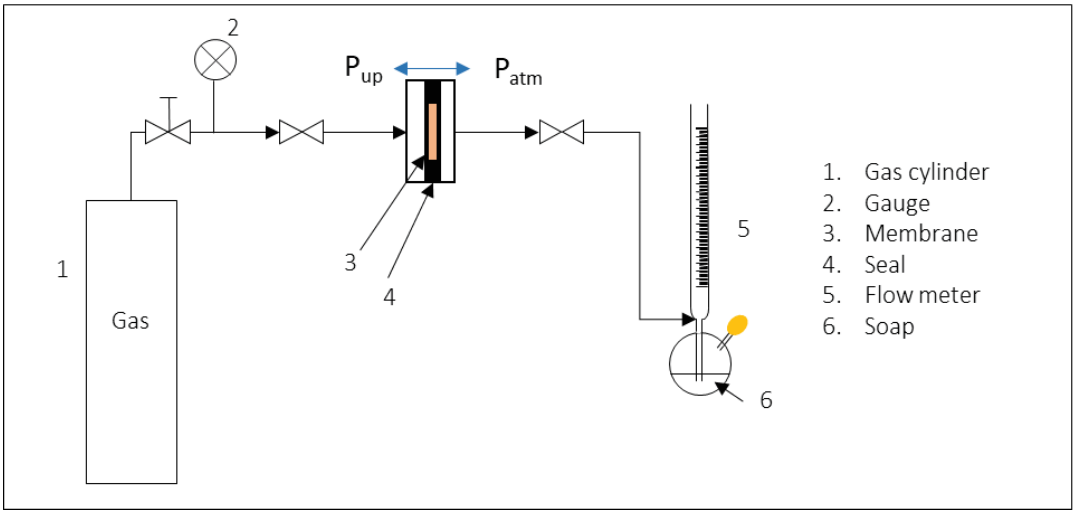

Figure IV. 8. Schematic representation of the experimental setup for measuring single gas permeation through flat membranes using dead-end configuration.

[9] 1 GPU = 3.3472 x 10^{-10} mol.m^{-2}.s^{-1}.Pa^{-1} = 10^{-6} cm^3(STP)/(cm.cmHg)

General conclusion and prospects

This work was motivated by the interest of IL-based membranes separation processes as systems for the post-combustion CO_2 capture technologies. Our contribution has been mainly focused on the development of synthesis methods adapted to the preparation of Grafted Ionic Liquid Membranes (GILMs) with both the required physicochemical characteristics, and gas transport properties in which a selected IL is confined within the pores of a mesoporous ceramic support by chemical grafting. The research work was organized in three phases:

i) Synthesis of selected ILs with relevant coupling functions ensuring their efficient grafting on the support and investigation of their CO_2 absorption properties.

ii) Grafting of these ILs on model γ-Al_2O_3 powders in order to optimize the grafting protocol, and to get a detailed insight into the complex grafting mechanism(s) as well as a quantification of its efficiency.

iii) Transfer of the optimized grafting protocol to commercial γ-Al_2O_3 ceramic membranes in order to produce Grafted Ionic Liquid Membranes (GILMs) and evaluate their performance for the selective transport of CO_2.

In the first phase (i) of the work, key parameters influencing the CO_2 separation performance of ILs were investigated to design and synthesize novel phosphonate-based ILs. The cation core of these ILs was composed of 1-methylimidazolium connected through an organic spacer *(i.e., a propyl chain, a dodecyl chain or an oligo(ethylene glycol) chain)* to a diethyl ester phosphonate coupling function. For the anion, the bis(trifluoromethanesulfonylimide) (Tf_2N^-) was selected.

Basic measurements of the CO_2, N_2, and CH_4 solubility in these ILs named respectively [ImPE][Tf_2N] [ImC_{12}PE][Tf_2N], and [ImPEGPE][Tf_2N], were performed. The CO_2 solubility values were found to be lower than those of conventional ILs analogs, although the CO_2/N_2 ideal solubility selectivity for both [ImC_{12}PE][Tf_2N] and [ImPE][Tf_2N] were high. The highest CO_2/N_2 solubility selectivity value at 20°C was provided by [ImC_{12}PE][Tf_2N], which was found to be more selective than most of the conventional ILs such as [emim][Tf_2N].

The computational study of the synthesized phosphonate-based ILs revealed the influence of both the coupling function and the organic spacer on the polarity and equilibrium conformation of the ILs. We made the assumption that the well-organized conformation and polar domains of [ImC_{12}PE][Tf_2N] contribute to lower the N_2 solubility and as a result, contribute to increase the CO_2/N_2 selectivity. Further detailed simulations and experimental studies should be required to exclude any potential chemisorption interaction between CO_2 and the ILs.

In the second phase (ii) of the work, the above synthesized phosphonate-based ILs were grafted on a γ-Al_2O_3 powder, considered as a non-supported membrane model material. The γ-Al_2O_3 powder was prepared by a sol-gel method well adapted for casting γ-Al_2O_3 layers (membranes) on porous ceramic supports. The grafting of the IL series was carried out by following a step by step approach. At each step, both the grafting efficiency and the influence of IL composition were demonstrated by using a set of characterization techniques, such as Energy Dispersive X-ray spectroscopy (EDX), N_2 physisorption measurements, Fourrier Transform InfraRed spectroscopy (FTIR) and a specific attention was paid to 1D

and/or 2D solid-state Nuclear Magnetic Resonance (NMR) spectroscopy through the study of ^{1}H, ^{13}C, ^{31}P, ^{27}Al and ^{19}F nuclei.

The first grafting study was conducted on ILs composed of a bromide anion, a 1-methylimidazolium cation containing a propyl organic spacer. The influence of the nature of the coupling function and of the grafting reaction conditions has been investigated. The diethyl ester phosphonate coupling function was found to be more efficient even using forcing conditions (water, 130°C) than the bis(trimethoxysilyl) phosphonate ester to anchor the ILs on the γ-Al_2O_3 surface.

A kinetic study of the grafting reaction was then conducted in forcing reaction conditions using two ILs having the same cation but different anions (Br^- or Tf_2N^-) ([ImPE][Br] and [ImPE][Tf_2N]). In both cases, a partial dissolution phenomenon of the γ-alumina model powder was evidenced, leading to the formation of boehmite and the formation of a bulk aluminum phosphonate phase for [ImPE][Br]. This dissolution phenomenon might be explained by the hydrolysis of the phosphonate ester moiety in pure aqueous solution and could be limited or avoided by carefully choosing the grafting reaction time and solvent.

After optimization of grafting reaction conditions for [ImPE][Tf_2N] IL, the grafting study was extended to both [ImPEGPE][Tf_2N] and [$ImC_{12}PE$][Tf_2N] ILs.

The best grafting conditions for all the IL sample series have been determined and led to the synthesis of a new variety of original phosphonate-based ILs/ γ-Al_2O_3 hybrid systems with a grafting density reaching ~60% of the full surface coverage.

Specific solid-state NMR techniques were applied for the firt time to study in details the grafted samples. D-HMQC experiments provided precious information on the nature of the ^{27}Al nuclei involved in the grafting and allowed to follow the structural transformation yielding the bulk aluminum phosphonate phase. HR-MAS NMR techniques improved the resolution of ^{1}H, ^{13}C and ^{31}P MAS NMR spectra allowing to finely ascribe the different resonances to grafted species and to highlight the difference in mobility of grafted ILs depending on their bonding mode.

N_2 physisorption experiments brought valuable information regarding the porous structure of the grafted samples and the influence of IL characteristics on the N_2/grafted surface interactions. On the other hand CO_2 sorption measurements at 25°C were useful to evidence the dominating CO_2/hybrid system physisorption interaction.

In the last phase (iii) of the work, the phosphonate-based ILs have been stabilized in the pores of γ-Al_2O_3 ceramic membranes by applying the optimized protocol developed to graft the ILs on γ-Al_2O_3 powders (non-supported membranes). At this step, it was crucial to precisely determine the best grafting conditions for the selected ILs ([ImPE][Tf_2N], [$ImC_{12}PE$][Tf_2N] and [ImPEGPE][Tf_2N]) yielding maximum grafting density and avoiding any potential γ-Al_2O_3 support dissolution phenomenon. Although it was tricky to clearly demonstrate the efficiency of the grafting reaction for supported IL-membranes, their morphology and physico-chemical characteristics were investigated.

In spite of their low CO_2 permeability (~130 Barrer) which was difficult to measure with our initial set-up/protocol, the best membranes prepared with the [ImPEGPE][Tf_2N] IL were found to posses high CO_2/N_2 ideal selectivity (~ 144) outperforming the classical Robeson upper bound limit. As far as nanoconfined IL-based SILMs have been shown to provide an increase of CO_2 permeability with stable CO_2 selectivity when temperature was increased, attractive performance is expected for the separation of gas mixtures with the GILMs, upon long term operation. This will need to be demonstrated by considering gas permeation and gas separation measurements through both SILMs and GILMs for long period of time, at high temperature and/or high pressure.

By using a multidisciplinary approach combining organic chemistry, chemical engineering, and materials science, a number of original results emerge from this research work based on both the development of new ionic liquids and the synthesis of novel grafted ILs membranes. Each of the developed ILs yielded hybrid membrane systems with specific properties which have still to be fully explored. This work also illustrates the strong impact and benefit of a multidisciplinary approach towards the development of stable hybrid membranes for CO_2 separation.

The prospects of this exploratory research work are wide, whether as a direct complement to the work already started, as complementary approaches (*e.g.,* modeling) or the extension of the strategy to other systems and applications.

The grafting of phosphonate-based ILs could be conducted on other oxide metals such as TiO_2 or ZrO_2, ZnO but also on some Hydroxide Double Lamellar (HDL) compounds, zeolites or Metal Organic Frameworks (MOFs). Different porous ceramic supports with various pore sizes/porous structures and geometries could be considered. The composition of the ILs could be also modified in order to decrease the viscosity, or change the CO_2/IL interaction by addition of amino group. Computational investigation of the grafted IL position on/in the porous support and details about grafting mechanism could be investigated.

Theoretical calculations (coupled to systematic experiments) could also help modelling the molecular-level phenomena involved in the interaction between the ILs and a controlled chemical composition of the oxide surface (reactive groups).

The complex competition between the coupling agent evolution and support surface modification/etching is clearly driven by the grafting reaction conditions (time, temperature, solvent…) and would desserve detailed computionnal investigations in order to evidence the grafting triggering factor(s).

Apart from the acidic gas separation applications, the developed IL-grafted layers could be considered for other applications in relation with the specific properties of both the selected support and the grafted IL, e.g. for antimicrobial, hydrophilic-hydrophobic surfaces, ionic conductors or hybrid electronic devices, catalysis (metallic carben).

ANNEX 1

« Design of Phosphonated Imidazolium-Based Ionic Liquids Grafted on γ-Alumina: Potential Model for Hybrid Membranes »

MA. Pizzoccaro, M. Drobek, E. Petit, G. Guerrero, P. Hesemann, A. Julbe, *Int. J. Mol Sci.,* 2016*, 17*, 1212. (doi: 10.3390/ijms17081212)

International Journal of
Molecular Sciences

MDPI

Article

Design of Phosphonated Imidazolium-Based Ionic Liquids Grafted on γ-Alumina: Potential Model for Hybrid Membranes

Marie-Alix Pizzoccaro [1], Martin Drobek [1], Eddy Petit [1], Gilles Guerrero [2,*], Peter Hesemann [2] and Anne Julbe [1,*]

[1] Institut Européen des Membranes, UMR-5635 CNRS-UM-ENSCM, Université de Montpellier (CC047), Place Eugène Bataillon, F-34095 Montpellier cedex 5, France; marie-alix.pizzoccaro@etu.umontpellier.fr (M.-A.P.); martin.drobek@umontpellier.fr (M.D.); eddy.petit@univ-montp2.fr (E.P.)

[2] Institut Charles Gerhardt, UMR-5253 CNRS-UM-ENSCM, Université de Montpellier (CC1701), Place Eugène Bataillon, F-34095 Montpellier cedex 5, France; peter.hesemann@umontpellier.fr

* Correspondence: gilles.guerrero@umontpellier.fr (G.G.); anne.julbe@umontpellier.fr (A.J.); Tel.: +33-467-144-223 (G.G.); +33-467-149-142 (A.J.)

Academic Editor: Andreas Taubert
Received: 24 June 2016; Accepted: 20 July 2016; Published: 27 July 2016

Abstract: Imidazolium bromide-based ionic liquids bearing phosphonyl groups on the cationic part were synthesized and grafted on γ-alumina (γ-Al_2O_3) powders. These powders were prepared as companion samples of conventional mesoporous γ-alumina membranes, in order to favor a possible transfer of the results to supported membrane materials, which could be used for CO_2 separation applications. Effective grafting was demonstrated using energy dispersive X-ray spectrometry (EDX), N_2 adsorption measurements, fourier transform infrared spectroscopy (FTIR), and special attention was paid to ^{31}P and ^{13}C solid state nuclear magnetic resonance spectroscopy (NMR).

Keywords: imidazolium-based ionic liquids; γ-alumina; phosphonate coupling agent; grafting; solid state NMR; hybrid membrane

1. Introduction

In competition with amines, ionic liquids are known to interact strongly and reversibly with CO_2, making supported ionic liquid (IL) materials versatile solids for use in adsorptive or membrane CO_2 separation applications [1]. The most common systems are composed of ILs either impregnated or confined in matrices, which can be porous or non-porous (i.e., polymer, ceramic or hybrid matrices). These materials can have applications, for example, in batteries [2–4], as electrolytes [5] or as CO_2 separation systems [6,7]. Imidazolium-based ILs grafted onto the surface of porous supports are promising systems for a range of applications, including catalysis [8,9], chromatography [10–12] and gas separation [13,14]. These types of systems have been defined by Fehrmann et al. [15], as supported ionic liquids (SILs), which refer to either inert or catalytically-active covalently-bound monolayers of ILs. In these materials, the IL does not act like the bulk liquid anymore, but as a surface modifier. As reported by the authors, tailoring the chemical nature of the support, as well as its microstructure (pore size, size distribution, surface area, etc.), govern the grafting of the IL and its distribution on the support surface. Covalent linking of ILs on a ceramic oxide support appears as an attractive strategy to fine-tune solids with outstanding properties for CO_2 adsorption and with improved long-term stability. Ionic liquids can be grafted on mesoporous silica-based supports, such as MCM-41 [16] or SBA-15 [17], and they also can be incorporated within a silica hybrid matrix [18].

These mixed ionic-mineral phases have been the most widely-investigated systems for applications such as heterogeneous catalysis [13,19,20], gas separation [13,14] or CO_2 sorption [21].

γ-alumina (γ-Al_2O_3) is a commonly-used ceramic support, and its hydroxylated surface is attractive for anchoring or grafting active species for either gas separation or heterogeneous catalysis [22]. In addition, this material can be cast easily as a continuous membrane film and was thus selected in this work as a relevant support for grafting imidazolium-based ionic liquids. Controlling the chemical grafting of ILs in the pores of a porous material is much more challenging than their simple impregnation in a porous support, yielding the supported ionic liquid phase (SILP). Obviously, the choice of the functionalized imidazolium-based IL is a key parameter, but the characterization of the grafting reaction is a tricky task. The efficiency of the grafting step needs to be quantified, and the spatial proximity between the grafted sites needs to be determined.

Several functionalized imidazolium-based ILs have been reported in the literature with functional groups, such as trimethoxysilyl, thiol-, ether-, carboxylic acid-, amino- and hydroxyl-groups [23]. Each of these functional groups is adapted for grafting on a pre-functionalized support. Vangeli et al. [14] selected the trimethoxysilyl group to react with the hydroxyl groups of silica-based materials pre-treated with a piranha solution. The grafting reaction has been performed in two steps: (i) grafting of a silylated precursor and (ii) quaternization with 1-methylimidazole, yielding the imidazolium species. Despite the detection of carbon by elemental analysis and the measured decrease of support specific surface area after grafting, the demonstration of both the quaternization reaction and anchoring configuration were rather unclear.

The chemical modification of γ-alumina powders with organosilanes has been largely investigated in the literature [24,25]. As an alternative, grafting reactions could also be realized with phosphonate or phosphinate coupling functions. Randon et al. [26] have linked phosphoric acid and alkyl phosphonic acid to the surface of both titania and zirconia membranes in order to improve their performance for the ultrafiltration of bovine serum albumin (BSA) proteins. Caro et al. [27] modified a γ-Al_2O_3 membrane top-layer with alkyl/aryl phosphonic acids, thus resulting in an organophobic behavior. Guerrero et al. [28,29] studied the grafting of phenylphosphonic acid and its ester derivatives on both γ-Al_2O_3 and TiO_2 powders. The surface bonding modes were investigated by both diffuse reflectance infrared spectroscopy (DRIFT) and ^{31}P solid-state magic angle spinning nuclear magnetic resonance spectroscopy (MAS NMR). The same authors also patented a process for modifying an inorganic substrate with organophosphorus coupling agents, relevant for antibacterial applications. In this work, imidazolium-based ILs with phosphonyl functional groups were used for their intrinsic antimicrobial properties [30].

The aim of the present work was to develop an optimized γ-Al_2O_3/imidazolium-based ILs system able to serve as a preliminary study for developing efficient gas separation hybrid membrane in which the IL will be effectively grafted on the pore surface. The approach involves the synthesis and characterizations of both the γ-Al_2O_3 support and the functionalized IL, followed by the investigation of the grafting reaction and the quantitative analysis of both the grafting step and the derived hybrid material. Two organophosphorus functionalized imidazolium-based ILs were selected (Figure 1): the 1-methyl-3–(3–(diethylphosphinyl)propyl)-imidazolium bromide (ImPE) and the 1-methyl-3–(3–((trimethoxysilyl)phosphinyl)propyl)-imidazolium bromide (ImTMSP). The synthesis of ImPE was carried out following the procedure described by Mu et al. [31], while the synthesis of ImTMSP was performed for the first time by adapting the work of McKenna et al. [32]. The modification of the γ-Al_2O_3 surface under either standard or forcing conditions was investigated by energy dispersive X-ray spectrometry (EDX) and N_2 adsorption measurements. In addition, key information was derived from fourier transform infrared spectroscopy (FTIR) and ^{31}P, ^{13}C solid state NMR analysis.

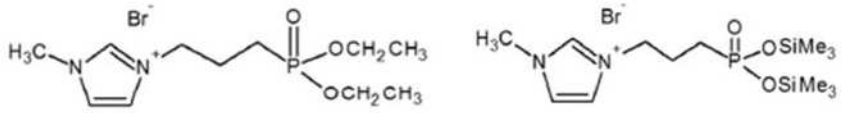

(a) (b)

Figure 1. Representation of the structures of ImPE (1-methyl-3–(3–(diethylphosphinyl)propyl)-imidazolium bromide) (**a**) and ImTMSP (1-methyl-3–(3–((trimethoxysilyl)phosphinyl)propyl)-imidazolium bromide) (**b**).

2. Results and Discussion

γ-alumina (γ-Al_2O_3) was prepared from boehmite using a sol-gel process described by Leenaars et al. [33] and followed by a 3-h thermal treatment in air at 600 °C. As revealed by ^{1}H MAS NMR, hydroxyl groups are present on the alumina surface, and they are involved in the grafting reaction mechanism by condensation with ester functions (P-OX) of the organophosphonate coupling agent [34].

The surface of γ-Al_2O_3 powders was modified by treatment with an organic or aqueous grafting solution containing n-fold excess of either ImPE or ImTMSP ionic liquid. The quantity of IL used corresponds to the amount needed for a full surface coverage of the γ-Al_2O_3 particles (0.6 mmol, assuming an area of 25 Å^2 per ionic liquid molecule). Depending on the ILs used, different reaction conditions were applied (Table 1). In order to evidence the spectroscopic characteristics of physisorbed phases or unreacted species on the surface of γ-Al_2O_3, a grafting experiment was first performed with ImPE in "physisorption conditions". Secondly, in standard reaction conditions, grafting with ImPE was achieved during several days in an alcoholic solvent, while grafting with ImTMSP was realized during either one night or three days in dry methylene chloride. Otherwise, as reported for the grafting of diethyl phenylphosphonate coupling agents on γ-Al_2O_3, the use of forcing reaction conditions (i.e., excess of coupling agent relative to full surface coverage, and high temperature) did not lead to dissolution-precipitation mechanism (no formation of bulk aluminum phos phonate phases) and improved the surface grafting density [28,35]. Therefore, finally, forcing reaction conditions were also tested with ImPE in aqueous medium for one night by increasing the reaction temperature up to 130 °C. After the grafting treatment, samples were centrifuged, washed with an ethanol-water solution to remove unreacted and physisorbed species and dried at 70 °C under vacuum before analysis (see Materials and Methods).

Table 1. Standard and forcing conditions for grafting the γ-alumina powders with organophosphonate imidazolium-based ionic liquids (ILs).

	IL	Solvent (mL)	T (°C)	Time (h)	N-Fold Excess	N (ILs) mmol	Sample
Standard conditions	ImPE	2-butanol (5)	90	288	6	3.6	ImPE1
	ImTMSP	CH_2Cl_2 (14)	25	17	2	1.2	ImTMSP1
	ImTMSP	CH_2Cl_2 (14)	25	72	2	1.2	ImTMSP2
	ImTMSP	CH_2Cl_2 (14)	25	17	6	3.6	ImTMSP3
	ImTMSP	CH_2Cl_2 (14)	25	72	6	3.6	ImTMSP4
Forcing conditions	ImPE	water (10)	130	17	2	1.2	ImPE2
	ImPE	water (10)	130	17	6	3.6	ImPE3
	ImPE	water (10)	130	17	12	7.2	ImPE4

The characteristics of unmodified and grafted γ-Al_2O_3 powders are summarized in Table 2. Average phosphorus weight percentages (wt % P) obtained from EDX showed the presence of phosphorus in all of the grafted samples. The proportions do not exceed a full surface coverage (i.e., 3.2 wt % P), which is coherent with the surface reactions of the ILs coupling agents on γ-Al_2O_3. The sample modified with a six-fold excess of ImPE in forcing reaction condition (ImPE3) exhibited a slight increase of P contents by comparison with the sample obtained with a six-fold excess in standard condition (ImPE1). This result suggests that a higher temperature with a short reaction time tends to

increase the rate of the surface modification reaction. For ImPE samples in forcing reaction conditions, an enhancement of ILs coupling agent excess in solution leads to an increase of the γ-Al_2O_3 surface coverage. In the case of ImTMSP samples, the P contents measured on modified γ-Al_2O_3 were in the range of the values obtained for the samples modified by ImPE. Nevertheless, no heat activation was needed with ImTMSP, suggesting a difference of reactivity, while the –PO($OSiMe_3$) function is known to be more reactive [28]. Finally, the efficiency of grafting reactions with ImTMSP did not seem to depend on reaction times, but was rather sensitive to the excess value of the IL coupling agent in solution.

Table 2. Characteristics of the γ-alumina powders before and after grafting reactions.

Sample	C_{BET}	wt% P [a]	P nm^{-2} [b]
γ-Al_2O_3	82	0	/
ImPE1	60	0.90 ± 0.05	0.9
ImPE2	63	0.62 ± 0.02	0.6
ImPE3	59	1.12 ± 0.04	1.1
ImPE4	55	1.42 ± 0.03	1.4
ImTMSP1	70	0.92 ± 0.04	0.9
ImTMSP2	66	0.92 ± 0.02	0.9
ImTMSP3	64	1.16 ± 0.10	1.1
ImTMSP4	63	1.00 ± 0.10	1.0

[a] From EDX analysis; [b] average number of coupling molecules per nm^2.

Nitrogen adsorption experiments did not reveal any important variation of the specific surface area values between the crude γ-Al_2O_3 powder and the grafted samples series, which is consistent with only the surface modification. The results of adsorption measurements gave also access to the BET constant (C_{BET}) related to the affinity of the solid with N_2 molecules ans so which is characteristic of the adsorbate/material surface interactions, as reported by Galarneau et al. [36]. The decrease of the C_{BET} value reflects a reduction of the enthalpy of adsorption of N_2 molecules on the surface and thus gives qualitative information about surface modification. All of the grafted samples showed a lower C_{BET} constant than the starting γ-Al_2O_3 powders (Table 2). For each kind of coupling agent, the increase of the weight percentage of phosphorus measured on the modified samples correlates with a decrease of the C_{BET} constant. In addition, from the weight percentage of phosphorus and the specific surface area, we can estimate the grafting density (P nm^{-2}) on the surface of the γ-Al_2O_3 powders, assuming an area of 25 $Å^2$ per phosphonate molecule (Table 2). Therefore, a full surface coverage of the alumina particles should not exceed 4 P atoms by nm^2. In all of the grafted samples, values from 0.6 to 1.4 of the grafting density were obtained, suggesting that the surface coverage does not exceed about 30% of the full monolayer in all cases.

In comparison with the literature, it has been demonstrated that the grafting on Degussa γ-Al_2O_3 in organic media with the diethyl phenylphosphonate coupling molecule resulted in a 50% surface coverage [28]. Moreover, in the same study, the authors have also evidenced that the grafting with bis(trimethylsilyl)ester phenylphosphonate coupling agent led to a higher percentage of phosphorus atoms, consistent with the formation of bulk aluminum phosphonate phases. It was also pointed out that the use of the dialkyl ester derivatives in organic media allowed the control of the grafting and excluded the formation of phosphonate phases even under prolonged heating. The partial surface coverage obtained in this study with the diethyl imidazolium phosphonate coupling molecule could result from a possible steric hindrance effect on the γ-Al_2O_3 surface (due to both the alkyl chain and the imidazolium ring) and also from the low reactivity of the coupling function. Furthermore, the results obtained with ImTMSP showed that the control of the reaction condition parameters can allow the incorporation of coupling agent quantities consistent with sole surface coverage without any evidence of the formation of bulk aluminum phosphonate phases. Thus, additional grafting parameters have to be tested (i.e., grafting duration, concentration, temperature, etc.) in order to optimize the reaction conditions and maximize the γ-alumina surface coverage.

The reaction of organophosphorus derivatives on the γ-Al_2O_3 surface is supposed to involve both coordination of the oxygen of the phosphoryl groups (P=O) to Lewis acid sites and the condensation reactions of P-OX functions (X could be Et or $SiMe_3$) with Al-OH surface groups. According to the literature, there are several possible bonding modes for phosphonate coupling molecules on an oxide surface [34]. In the case of phosphonyl imidazolium-based ILs, the possible bonding modes can be mono-, bi- or tri-dentate (Figure 2).

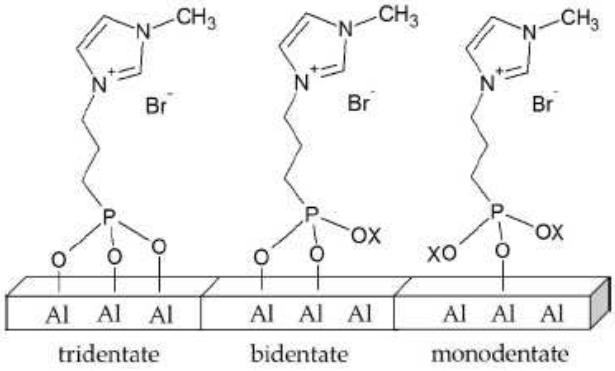

Figure 2. Schematic representation of some possible bonding modes for phosphonate coupling imidazolium-based ionic liquids on a γ-Al_2O_3 surface (X could be Et or $SiMe_3$).

The FTIR spectra between 1400 and 800 cm^{-1} of the two organophosphonate functionalized imidazolium bromide-based ILs are presented in Figure 3I. ImPE and ImTMSP showed P=O stretching vibrations at 1230 cm^{-1} and 1251 cm^{-1}, respectively, and C–H deformation vibrations at 956 cm^{-1} for ImPE and 1035 cm^{-1} for ImTMSP. Asymmetric and symmetric P-O-C stretching vibrations are present only for ImPE at 1042 and 958 cm^{-1} [28,37]. In addition, the spectra of ImTMSP present a P-O-Si deformation vibration at 833 cm^{-1}. Starting from the ionic liquid structure, DFT calculation is useful to estimate the different vibration modes of the coupling agents (Figure S10 in the Supplementary Information) and to identify some of the deformation bands, such as the =C-H imidazolium band and the -CH_2- spacer alkyl chain band present at about 1165 cm^{-1} for both ILs. In all grafted samples, we can notice the disappearance of the phosphoryl (P=O) stretching bands near 1230 and 1251 cm^{-1}, suggesting that the phosphoryl oxygen is strongly bonded to Lewis acid surface sites by coordination (Figure 3IIa–c). Moreover, the IR spectra are dominated by an absorption band at 1171 cm^{-1}, typical of the =C-H and –CH_2– deformation bands of the imidazolium ring and the spacer alkyl chain. The PO regions of the grafted samples between 950 and 1250 cm^{-1} differ depending on both the IL and the applied reaction parameters. The IR spectra of samples treated in forcing reaction conditions with ImPE (Figure 3IIb) present a strong absorption band at 1065 cm^{-1}, tentatively ascribed to the P-O-Al stretching vibration [37]. It can be noted that this band became gradually broader when increasing the quantity of grafted species. Therefore, the presence of weak absorption bands at about 1040 and 950 cm^{-1} (region of P-O-C stretching bands) does not preclude the existence of some P-OEt residual groups.

The FTIR spectrum of the sample modified with ImPE under standard reaction conditions (Figure 3IIa) shows a broader absorption band around 1050 cm^{-1} corresponding to the P-O group stretching mode. This band could be attributed to P-O surface species in organophosphonate/metal oxide systems according to Quiñones et al. [38]. In addition, the presence of strong residual P-O-C stretching bands at about 1040 cm^{-1} cannot be excluded. The IR spectra of samples prepared with ImTMSP (Figure 3IIc) in standard conditions are quite similar to the ImPE1 spectrum. The most important difference comes from the presence of residual P-O-Si deformation vibration between ~1000 and 800 cm^{-1}, which suggests that all of the coupling functions have not reacted with the alumina surface [28]. To conclude, IR spectroscopy of samples grafted in standard reaction conditions

clearly reveals the presence of residual P-O-C or P-O-Si vibrations, stating that phosphonate units are preferentially linked to the alumina surface through bidentate (or monodentate) binding modes. In the case of samples prepared in forcing conditions, weak residual P-O-C stretching modes may be present on the infrared spectra, indicating that the dominating bonding mode of the phosphonate groups seems to involve tridentate PO_3 units.

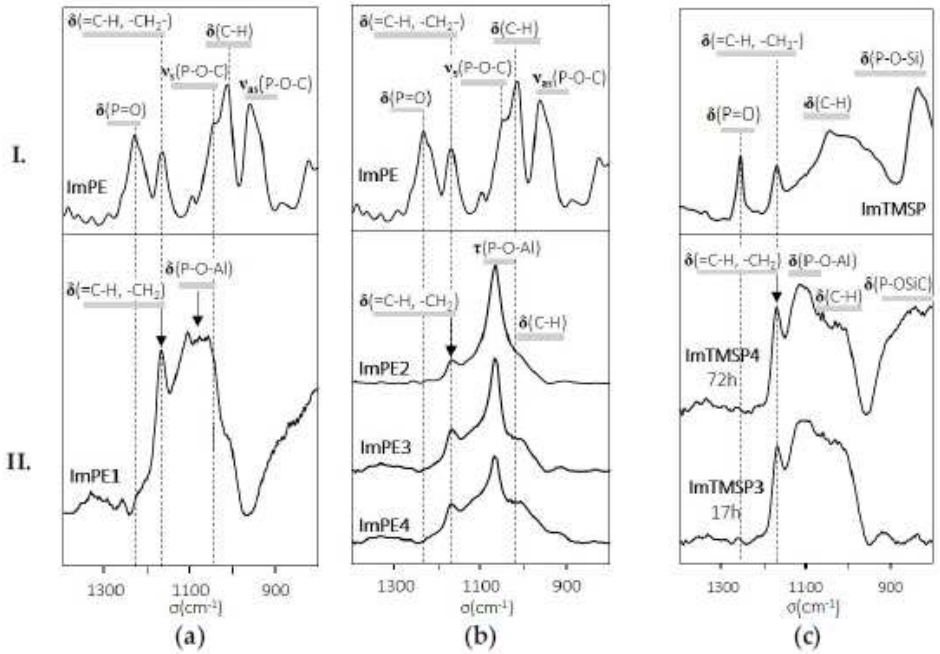

Figure 3. Experimental FTIR spectra of ImPE (**Ia**,**b**) and ImTMSP (**Ic**) and respective grafting on γ-Al_2O_3 prepared under different reaction conditions: (**IIa**) with ImPE under standard condition (ImPE1), (**IIb**) with ImPE under forcing conditions (130 °C, 17 h) at different concentration (ImPE2 to ImPE4: two- to 12-fold excess) and (**IIc**) with ImTMSP under standard conditions (25 °C, six-fold excess).

^{13}C cross polarization magic angle spinning (CP-MAS) liquid NMR spectra of ImPE and ImTMSP display both the specific chemical shifts (Figure 4Ia,b) of the 1-methyl-3-propylimidazolium group, numbered from C_1 to C_7, and those of the coupling functions, numbered from C_8 to C_9 for $-POCH_2CH_3$ and C_8 only for $-POSiMe_3$. In comparison, the ^{13}C CP-MAS solid state NMR spectra of the grafted samples ImPE4 (Figure 4IIa) and ImTMSP4 (Figure 4IIb) show a slightly upfield shift for all of the atoms, principally due to the spatial proximity and chemical bonds with the γ-Al_2O_3 surface. Whatever the coupling function, the integrity of the organic molecule structure was conserved during the grafting process. In both grafted samples' spectra, we can notice the presence of weak peaks attributed to residual -$POCH_2CH_3$ and -$POSiMe_3$ functions, confirming the conclusions derived from the FTIR spectra (Figure 3) and supporting our hypothesis concerning the presence of multimodal bonding modes (i.e., tridentate, bidentate, monodentate).

Additional information was provided by the ^{31}P MAS NMR spectra of the grafted γ-Al_2O_3. The powder treated under physisorption reaction conditions allows identification of the chemical shift corresponding to physisorbed species, with a sharp resonance at 32.1 ppm (Figure S11). The ^{31}P MAS NMR spectra of all of the grafted samples (Figure 5a,b) did not reveal this peak, indicating that only grafted phosphonate species were present on the alumina surface. Moreover, we did not notice any additional upfield sharp resonance peak resulting from a dissolution/precipitation phenomenon and the formation of aluminum phosphonate bulk phases. This was confirmed by powder X-ray diffraction patterns (XRD) highlighting the amorphous structure of all of the grafted samples (Figure S12).

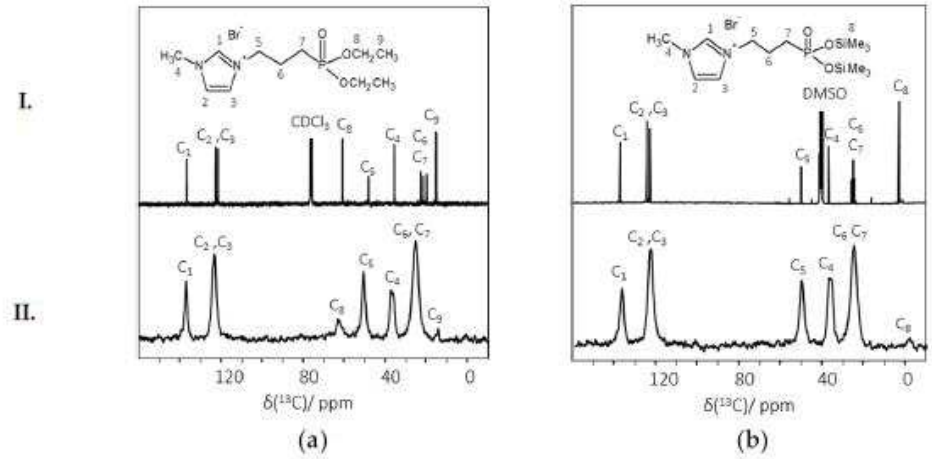

Figure 4. ^{13}C CP-MAS NMR spectra of pure ionic liquids (I) and the γ-Al_2O_3 grafted samples (II) prepared under the different reaction conditions. Comparison between: (**a**) pure ImPE and ImPE4 (130 °C, 17 h, 12-fold excess); (**b**) pure ImTMSP and ImTMSP4 (six-fold excess, 72 h).

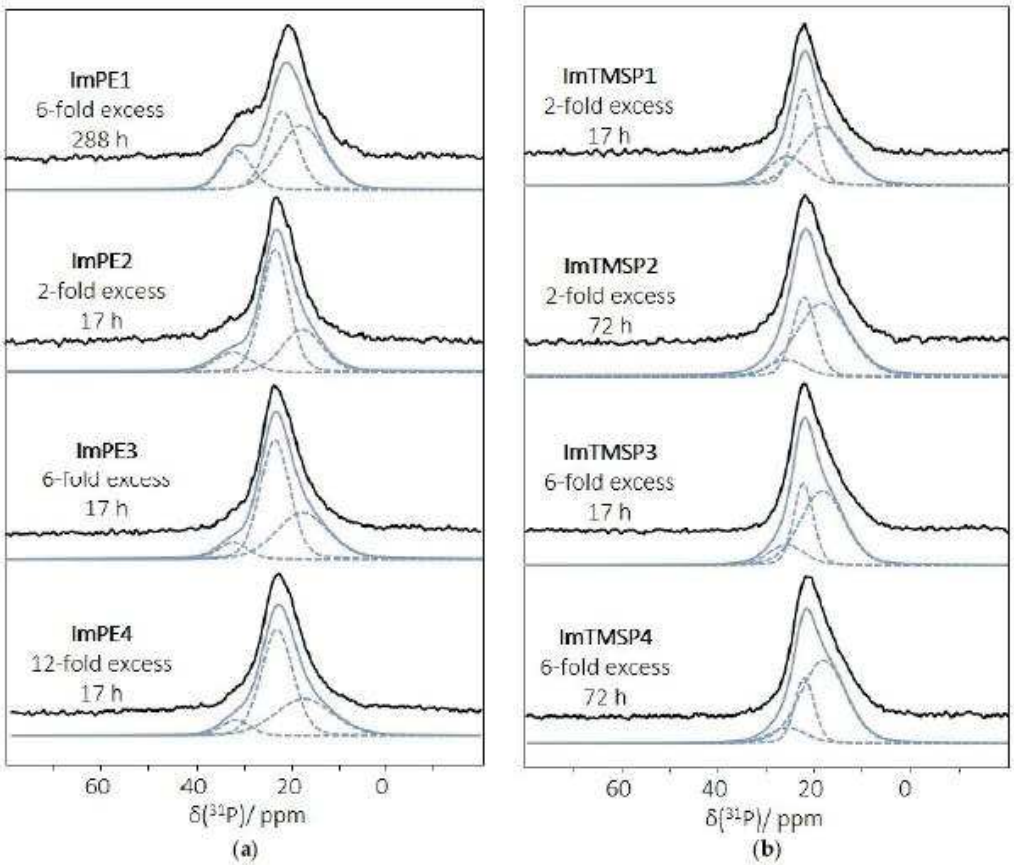

Figure 5. ^{31}P MAS NMR spectra of γ-Al_2O_3 grafted samples prepared under different reaction conditions: (**a**) standard conditions with ImPE (90 °C, 288 h) (ImPE1) and forcing conditions with ImPE (130 °C, 17 h) at different concentrations (ImPE2 to ImPE4: two- to 12-fold excess); (**b**) standard conditions with ImTMSP (25 °C) at various reaction times and concentrations: twofold excess, ImTMSP1 (17 h); ImTMSP2 (72 h); and six-fold excess, ImTMSP3 (17 h); ImTMSP4 (72 h).

The ^{31}P MAS NMR spectra of the γ-Al_2O_3 powder modified with ImPE under forcing reaction conditions are displayed in Figure 5a (ImPE2, ImPE3 and ImPE4). All three spectra present a broad resonance centered at about 23.6 ppm. The simulation of the spectra indicated the presence of at least three sites (signals at 32.4, 23.6 and 17.9 ppm (Figure 5, Table 3)) revealing the presence of multiple bonding modes (Figure 2) for the phosphonate units as already discussed for the IR spectra. As reported by Brodard-Severac et al. [39], the interaction of the P=O groups with surface Lewis or Brønsted acidic sites should lead to a downfield shift. On this basis, the signal at 32.4 ppm, integrating from 7% to 13%, could be tentatively ascribed to the minor monodentate bonding mode (Figure 2). ^{13}C CP MAS NMR indicated the presence of residual P-OEt functions, and IR spectra showed also weak residual P-O-C stretching modes, stating that the dominating bonding mode of the phosphonate groups seems to involve tridentate PO_3 units. Therefore, we propose to ascribe the major signal at 23.6 ppm, integrating from 55% to 58%, to tridentate phosphonate PO_3 units grafted on the γ-Al_2O_3 surface. The third resonance at 17.9 ppm, integrating from 29% to 38%, was then attributed to grafted phosphonate functions in a bidentate mode. For both ImPE3 and ImPE4, it is interesting to notice that the increase of the proportion of this bonding mode correlates well with the increasing intensity of the IR stretches of residual P-OEt functions. Consequently, by increasing the n-fold excess of coupling agents during the grafting reaction in forcing reaction conditions, both tridentate and bidentate bonding modes of the phosphonate units were favored.

Table 3. Parameters used for the simulation of ^{31}P MAS NMR spectra of γ-Al_2O_3 grafted with ImPE under either standard (ImPE1) or forcing (ImPE2, ImPE3 and ImPE4) reaction conditions.

Sample	ImPE1			ImPE2			ImPE3			ImPE4		
δ (ppm)	31.6	22.1	18.1	32.4	23.6	17.9	32.4	23.6	17.9	32.4	23.6	17.9
Width (ppm)	7.5	7.6	11.5	9.1	6.9	10.0	7.4	7.4	13.0	7.4	8.0	14.4
Integration (%)	18	37	45	13	58	29	7	55	38	7	57	36

The ^{31}P MAS NMR spectrum of the γ-Al_2O_3 powder modified with ImPE under standard reaction conditions is also displayed in Figure 5a (ImPE1). It consists of a broad resonance centered at about 21.6 ppm with an important downfield asymmetrical shape. The simulation of the ImPE1 spectrum using a minimum number of resonances with a Gaussian–Lorentzian shape indicates the presence of at least three sites (Figure 5a, Table 3) at 31.6, 22.1 and 18.1 ppm, evidencing the presence of multiple bonding modes, as for ImPE2 to 4 (Figure 2). On the basis of the IR results, a higher number of residual P-OEt functions was detected when using standard rather than forcing reaction conditions. This implies an increasing proportion of monodentate and/or bidentate bonding modes of the phosphonate units. Thus, by comparison with the ImPE2 to 4 samples, we noticed a raising in the integration of the signals at 31.6 (18%) and 18.1 (45%) ppm, respectively ascribed to monodentate and bidentate bonding modes (Figure 2), which is in a good agreement with FTIR data. The signal corresponding to tridentate bonding mode at 22.1 ppm became minor with 37% integration.

The above results suggest that the grafting of γ-Al_2O_3 with diethyl phosphonate coupling agent strongly depends on the surface modification reaction conditions. Soft standard reaction conditions mainly promote bidentate and monodentate bonding modes on the surface with a minority of tridentate phosphonate units. Conversely, forcing conditions lead rather to tridentate bonding modes on the alumina surface, with a smaller proportion of the other bonding modes.

Figure 5b displays the ^{31}P MAS NMR spectra of γ-Al_2O_3 grafted under standard conditions (25 °C) using ImTMSP at different reaction times and quantities of IL (two- and six-fold excess). The spectra of ImTMSP1 to 4 samples are qualitatively similar and present a broader peak in comparison with the spectra of γ-alumina grafted with ImPE in forcing reaction conditions, centered at 22.1 ppm. In all cases, the NMR signals present an asymmetrical shape. According to the simulated spectra, three chemical shifts at 25.6, 22.1 and 18.1 ppm were identified with a major resonance for the latter (Table 4). As for the ImPE sample in standard condition with the presence of P-OEt groups, the IR

spectra of ImTMSP1 to 4 revealed important residual P-OSiMe$_3$ functions, implying an increasing proportion of monodentate and/or bidentate bonding modes of the phosphonate units. The liquid state ^{31}P NMR spectrum of ImTMSP (Figure S8) indicated an upfield chemical shift at 24.7 ppm (to be compared with 29.8 ppm for pure ImPE (Figure S5)) in good agreement with the P-OEt to P-OSiMe$_3$ conversion [29]. On this basis, the signal at 25.6 ppm, integrating from 9% to 18%, could be tentatively ascribed to the minor monodentate bonding mode with two P-OSiMe$_3$ functions (Figure 2). As for the ImPE1 sample in standard reaction conditions, the major resonances attributed to phosphonate units in bidentate bonding mode correspond to the upfield chemical shifts located at 18.2 ppm and integrating from 47% to 67%. The last signal at 22.1 ppm could be ascribed to tridentate phosphonate units. By using ImTMSP as the coupling agent, we cannot correlate unambiguously the influence of the reaction parameters (excess of coupling agent, reaction duration) with the proportion of the different bonding modes.

Table 4. Parameters used for the simulation of ^{31}P MAS NMR spectra of γ-Al_2O_3 grafted with ImTMSP.

Sample	ImTMSP1			ImTMSP2			ImTMSP3			ImTMSP4		
δ (ppm)	25.6	22.1	18.2	25.6	22.1	18.2	25.6	22.1	18.2	25.6	22.1	18.2
Width (ppm)	9.6	5.5	12	9	5.8	12.6	9	4.9	11.2	9	4.9	10.8
Integration (%)	18	35	47	9	30	62	10	23	67	13	29	58

The above results suggest that the reaction of γ-Al_2O_3 with either ImPE or ImTMSP in respective standard conditions promotes the grafting of phosphonate units with mainly a bidentate configuration. An increase of the temperature of the grafting reaction with ImPE favors the tridentate bonding mode of the phosphonate units on the γ-Al_2O_3.

3. Materials and Methods

3.1. Starting Materials

Triethyl phosphite (98%), 1-methylimidazole (≥99%) and bromotrimethylsilane (BrSiMe$_3$) (>97%) were purchased from Sigma-Aldrich (Saint-Quentin-Fallavier, France) and were used as received. 1,3-dibromopropane (98%) was provided by Fisher Chemical (Illkirch, France). Boehmite (Pural type) with a high crystallinity and surface area (249 m^2/g) was supplied by CTI S.A. (Salindres, France).

A batch of γ-Al_2O_3 powder was prepared by a sol-gel process based on colloid chemistry in aqueous media with a specific surface area of 220 $m^2 \cdot g^{-1}$. The γ-alumina powder batch was separated in small samples containing equal amounts of powder (400 mg) into an argon glovebox. This step avoided the presence of water on the alumina surface and yielded comparable conditions for the grafting reactions.

ImPE was obtained as a yellow oil in a high yield by the corresponding nucleophilic substitution of 1-methylimidazole with diethyl(3-bromopropyl)phosphonate in tetrahydrofuran (THF) (δ ^{31}P = 29.80 ($CDCl_3$)).

ImTMSP was synthetized in a round-bottomed flask by the reaction of the ionic liquid ImPE with BrSiMe$_3$ (3 equiv) in dry methylene chloride (CH_2Cl_2) (δ ^{31}P = 24.70 (DMSO d_6)).

THF and CH_2Cl_2 were provided by Sigma-Aldrich and dried with the PureSolv, Innovative Technology device.

3.2. Grafting Reactions

Standard Reaction Conditions: The "standard" reaction conditions are summarized in Table 1. Typical experiments are described below.

Grafting solution with ImPE was prepared by dissolving n-fold excess of the IL in the selected solvent. Five milliliters of the grafting solution and 400 mg of the γ-Al_2O_3 powder stored under argon were mixed in a glass bottle closed with a Teflon cap. The suspension was heated at 90 °C for 12 days.

After cooling down to room temperature, the suspension was then centrifuged at 8500 rpm for 5 min using a Sigma 3-16P centrifuge equipped with a Sigma 12150-H rotor. The supernatant was removed, and the remaining powder was re-dispersed in 5 mL of a (1:1) ethanol-water solution to remove the physisorbed species from the surface, and the new suspension was stirred at room temperature for 5 min. The ethanol-water solution supernatant was removed after centrifugation (8500 rpm, 5 min), and this washing step was repeated twice. The resulting paste was then dried under vacuum (5 to 10 mbar) at 70 °C for ~16 h to afford the sample ImPE1 as a powder.

Grafting with ImTMSP was performed directly in the grafting round-bottomed flask in dry CH_2Cl_2. Typically, ImTMSP (1.2 to 3.6 mmol, corresponding to a 2- or 6-fold excess relative to the amount necessary for a full surface coverage on the γ-Al_2O_3 particles) was dissolved in 15 mL of dry CH_2Cl_2 under stirring, and 400 mg of γ-Al_2O_3 powder stored under argon were dispersed in the grafting solution. The suspension was kept under stirring at 25 °C under argon for time periods ranging from 17 h to 3 days. The suspension was then centrifuged at 8500 rpm for 5 min and the supernatant removed. The remaining paste was re-dispersed in 5 mL of CH_2Cl_2, and the new suspension was stirred at room temperature for 5 min. After centrifugation, the CH_2Cl_2 supernatant was removed and the washing step repeated once. Then, the resulting pastes were washed with a (1:1) ethanol-water solution and dried in the same conditions as above, to afford the samples ImTMSP1 to 4 as powders.

Forcing Reaction Conditions: The "forcing" reaction conditions are summarized in Table 1. Typical experiments are described below.

Grafting ImPE solutions was prepared in water by dissolving the pure ImPE at different proportions (2-, 6- or 12-fold excess). Ten milliliters of the grafting solution and 400 mg of the γ-Al_2O_3 powder stored under argon were dispersed in an autoclave, which was closed with a Teflon cap. The autoclave was sealed and the suspension heated at 130 °C for 17 h. The resulting grafted powders were washed and dried as previously described for ImPE samples grafted under standard reaction conditions to afford the samples ImPE2 to 4 as powders.

3.3. Characterization

The BET specific surface areas and the C_{BET} constants of the samples were obtained from nitrogen adsorption experiments at 77 K by using a Tristar instrument (Micromeritics) for the grafted powders and a ASAP 2020 (Micromeritics) for the γ-Al_2O_3 powders. Prior to measurements, samples were degassed under vacuum overnight at 100 °C for the grafted powders and 300 °C for the γ-Al_2O_3 powder. The weight percentage of phosphorus in the samples was determined by EDX using a Zeiss scanning electron microscope (SEM) EVO HD15 at 10 kV equipped for EDX analysis with the AZtecEnergy analysis software (Oxford instruments. Abindong, UK). Samples were prepared as pellets for the analysis and deposited on double-sided carbon tape. FTIR spectra were obtained with a Perkin-Elmer Spectrum 2 spectrophotometer and were recorded in the 4000 to 400 cm^{-1} range using 32 scans at a nominal resolution of 4 cm^{-1} in ATR mode (spectrum of γ-Al_2O_3 as a background spectrum).

Solution NMR experiments: ^{13}C and ^{31}P NMR spectra were recorded using a Bruker 300-MHz NMR spectrometer at frequencies of 150.86 and 242.94 MHz, respectively.

Solid state NMR experiments: Solid state NMR experiments were performed using a Varian VNMRS 600 MHz (14.1 T) NMR spectrometer. A 3.2-mm Varian T3 HX MAS probe was used for ^{1}H, ^{13}C and ^{31}P experiments. The operating frequencies for ^{1}H, ^{13}C and ^{31}P were 599.95, 150.86 and 242.86 MHz, respectively. All NMR experiments were performed under temperature regulation in order to ensure that the temperature inside the rotor is 20 °C.

^{13}C CP-MAS solid state NMR spectra were recorded at a spinning frequency of 12 kHz MAS. Concerning the CP-MAS experiments, a contact time of 1 ms was fixed, the acquisition time to 30 ms, and the ^{1}H channel was decoupling on this period. A recycle delay of 2 s was used with a number of scans of 11,450, which permit to obtain a signal-to-noise ratio between 30 and 35. ^{13}C chemical shifts were referenced to external adamantane at 38.5 ppm.

^{31}P MAS solid state NMR spectra were recorded at a spinning frequency of 20 kHz. The single pulse experiments were performed with a ~90° solid pulse of 3 µs and ^{1}H decoupling during acquisition. A recycle delay of 45 s was employed (corresponding in both cases to full relaxation of ^{31}P) with a number of scans of 56 for obtaining a signal-to-noise ratio between 53 and 79. ^{31}P chemical shifts were referenced to external hydroxyapatite at 2.80 ppm (used as a secondary reference).

4. Conclusions

One important outcome of this study bears on the possibility to perform the grafting with imidazolium bromide-based ILs bearing phosphonate functions (ImPE or ImTMSP) on γ-Al_2O_3 powders, either in dry methylene chloride solvent (for ImTMSP) or in aqueous and alcoholic solvents (for ImPE). Compared to previous studies published in the literature describing the grafting of phenylphosphonic acid or its bis(trimethylsilyl)ester derivative, no bulk aluminum phosphonate phases were evidenced in the present work. Moreover, this study confirmed that the use of the diethyl imidazolium phosphonate coupling molecule allowed the control of the grafting reaction by using either prolonged heating or high temperature. Surprisingly, the same behavior was demonstrated with the bis(trimethylsilyl)imidazolium ester derivative.

FTIR and solid state NMR spectroscopy (^{31}P, ^{13}C) demonstrated that γ-Al_2O_3 surface modification with diethyl phosphonate coupling agent strongly depends on the grafting conditions.

Soft standard reaction conditions mainly promote bidentate and monodentate bonding modes on the surface, with a minority of tridentate phosphonate units. Conversely, the forcing reaction conditions mainly lead to the formation of tridentate bonding modes on the alumina surface, with a smaller proportion of the other ones. In addition, the grafting of ImTMSP in standard conditions seems also to promote the alumina surface modification by phosphonate units in a mostly bidentate configuration.

However, in all cases, the surface coverage does not exceed about 30% of the full monolayer. The results obtained in this study for ImPE and ImTMSP could result from a possible sterically-hindered effect on the γ-Al_2O_3 surface (due to both the alkyl chain and the imidazolium ring) and to the low reactivity of the coupling function. Furthermore, the results obtained with ImTMSP suggest that additional grafting parameters have still to be tested (i.e., grafting duration, concentration, temperature, etc.) in order to optimize the reaction conditions and maximize the γ-Al_2O_3 surface coverage.

This work allowed establishing the optimized synthesis and characterization protocols for the development of imidazolium phosphonate-grafted γ-Al_2O_3 hybrid materials with controlled bonding modes and grafting rates. As a perspective on this fundamental work, the preparation and testing of the corresponding gas separation hybrid membranes will now be investigated.

Supplementary Materials: The synthesis procedures and characterizations of γ-Al_2O_3 powder, the bulk 1-methyl-3–(3–(diethylphosphinyl)propyl)-imidazolium (ImPE), 1-methyl-3–(3–((trimethoxysilyl)phosphinyl)propyl)-imidazolium bromide (ImTMSP), as well as the details on XRD analysis, the synthesis procedure of the physisorbed sample, FTIR and DFT spectra of the ionic liquids, including DFT detailed calculations. The following are available online at Supplementary materials can be found at http://www.mdpi.com/1422-0067/17/8/1212/s1.

Acknowledgments: Philippe Gaveau (Ingénieur de Recherche CNRS) and Bertrand Ribière (Assistant ingénieur CNRS) from the Institute Charles Gerhardt in Montpellier are sincerely acknowledged for their useful technical contributions in respectively solid state NMR and EDX analysis.

Author Contributions: Gilles Guerrero and Anne Julbe were the idea source and writers of the manuscript. Marie-Alix Pizzoccaro is the co-writer and responsible for the synthesis and characterizations. Eddy Petit contributed to FTIR spectra attributions and the DFT calculus. Martin Drobek and Peter Hesemann contributed to this article by bringing their scientific expertise, on respectively inorganic (synthesis and characterizations of the γ-Al_2O_3) and organic chemistry (synthesis of ionic liquids).

Conflicts of Interest: The authors declare no conflict of interest.

References

1. Dai, Z.; Noble, R.D.; Gin, D.L.; Zhang, X.; Deng, L. Combination of Ionic Liquids with Membrane Technology: A New Approach for CO_2 Separation. *J. Membr. Sci.* **2016**, *497*, 1–20. [CrossRef]

2. Nair, J.R.; Porcarelli, L.; Bella, F.; Gerbaldi, C. Newly Elaborated Multipurpose Polymer Electrolyte Encompassing RTILs for Smart Energy-Efficient Devices. *ACS Appl. Mater. Interfaces* **2015**, *7*, 12961–12971. [CrossRef] [PubMed]
3. Park, H.; Choi, Y.S.; Kim, Y.; Hong, W.H.; Song, H. 1D and 3D Ionic Liquid–Aluminum Hydroxide Hybrids Preparedvia an Ionothermal Process. *Adv. Funct. Mater.* **2007**, *17*, 2411–2418. [CrossRef]
4. Porcarelli, L.; Gerbaldi, C.; Bella, F.; Nair, J.R. Super Soft All-Ethylene Oxide Polymer Electrolyte for Safe All-Solid Lithium Batteries. *Sci. Rep.* **2016**, *6*, 19892. [CrossRef] [PubMed]
5. Zehbe, K.; Kollosche, M.; Lardong, S.; Kelling, A.; Schilde, U.; Taubert, A. Ionogels Based on Poly(methyl methacrylate) and Metal-Containing Ionic Liquids: Correlation between Structure and Mechanical and Electrical Properties. *Int. J. Mol. Sci.* **2016**, *17*, 391. [CrossRef] [PubMed]
6. Scovazzo, P.; Kieft, J.; Finan, D.A.; Koval, C.; Dubois, D.; Noble, R. Gas separations using non-hexafluorophosphate $[PF_6]^-$ anion supported ionic liquid membranes. *J. Membr. Sci.* **2004**, *238*, 57–63. [CrossRef]
7. Albo, J.; Yoshioka, T.; Tsuru, T. Porous Al_2O_3/TiO_2 tubes in combination with 1-ethyl-3-methylimidazolium acetate ionic liquid for CO_2/N_2 separation. *Sep. Purif. Technol* **2014**, *122*, 440–448. [CrossRef]
8. Mehnert, C.P. Supported ionic liquid catalysis. *Chem. Eur. J.* **2004**, *11*, 50–56. [CrossRef] [PubMed]
9. Van Doorslaer, C.; Wahlen, J.; Mertens, P.; Binnemans, K.; de Vos, D. Immobilization of molecular catalysts in supported ionic liquid phases. *Dalton Trans.* **2010**, *39*, 8377–8390. [CrossRef] [PubMed]
10. Qiu, H.; Takafuji, M.; Liu, X.; Jiang, S.; Ihara, H. Investigation of π–π and ion-dipole interactions on 1-allyl-3-butylimidazolium ionic liquid-modified silica stationary phase in reversed-phase liquid chromatography. *J. Chromatogr. A* **2010**, *1217*, 5190–5196. [CrossRef] [PubMed]
11. Pino, V.; Afonso, A.M. Surface-bonded ionic liquid stationary phases in high-performance liquid chromatography-A review. *Anal. Chim. Acta* **2012**, *714*, 20–37. [CrossRef] [PubMed]
12. Wang, Y.; Tian, M.; Bi, W.; Row, K.H. Application of Ionic Liquids in High Performance Reversed-Phase Chromatography. *Int. J. Mol. Sci.* **2009**, *10*, 2591–2610. [CrossRef] [PubMed]
13. Perdikaki, A.V.; Vangeli, O.C.; Karanikolos, G.N.; Stefanopoulos, K.L.; Beltsios, K.G.; Alexandridis, P.; Kanellopoulos, N.K.; Romanos, G.E. Ionic Liquid-Modified Porous Materials for Gas Separation and Heterogeneous Catalysis. *J. Phys. Chem. C* **2012**, *116*, 16398–16411. [CrossRef]
14. Vangeli, O.C.; Romanos, G.E.; Beltsios, K.G.; Fokas, D.; Kouvelos, E.P.; Stefanopoulos, K.L.; Kanellopoulos, N.K. Grafting of imidazolium based ionic liquid on the pore surface of nanoporous materials—Study of physicochemical and thermodynamic properties. *J. Phys. Chem. B* **2010**, *114*, 6480–6491. [CrossRef] [PubMed]
15. Fehrmann, R.; Haumann, M.; Riisager, A. Introduction. In *Supported Ionic Liquids: Fundamentals and Applications*, 1st ed.; Fehrmann, R., Riisager, A., Haumann, M., Eds.; Wiley-VCH Verlag GmbH & Co. KGaA: Weinheim, Germany, 2014; pp. 1–9.
16. Gadenne, B.; Hesemann, P.; Moreau, J.J.E. Supported ionic liquids: Ordered mesoporous silicas containing covalently linked ionic species. *Chem. Commun.* **2004**, 1768–1769. [CrossRef] [PubMed]
17. Motos-Pérez, B.; Roeser, J.; Thomas, A.; Hesemann, P. Imidazolium functionalized SBA-15 type silica: Efficient organocatalysts for Henry and cycloaddition reactions. *Appl. Organomet. Chem.* **2013**, *27*, 290–299. [CrossRef]
18. Nguyen, T.P.; Hesemann, P.; Moreau, J.J.E. I-Silica: Nanostructured silica hybrid materials containing imidazolium groups by hydrolysis-polycondensation of disilylated bis-*N*,*N*′-alkyl-imidazolium halides. *Microporous Mesoporous Mater.* **2011**, *142*, 292–300. [CrossRef]
19. Zhang, Q.; Luo, J.; Wei, Y. A silica gel supported dual acidic ionic liquid: An efficient and recyclable heterogeneous catalyst for the one-pot synthesis of amidoalkyl naphthols. *Green Chem.* **2010**, *12*, 2246–2254. [CrossRef]
20. Kotadia, D.A.; Soni, S.S. Silica gel supported-SO_3H functionalized benzimidazolium based ionic liquid as a mild and effective catalyst for rapid synthesis of 1-amidoalkyl naphthols. *J. Mol. Catal. A Chem.* **2012**, *353–354*, 44–49. [CrossRef]
21. Zhu, J.M.; Xin, F.; Sun, Y.C.; Dong, X.C. Phosphonium-based ionic liquids grafted onto silica for CO_2 sorption. *Theor. Found. Chem. Eng.* **2014**, *48*, 787–792. [CrossRef]
22. Julbe, A.; Farrusseng, D.; Guizard, C. Porous ceramic membranes for catalytic and reactors and overview and new ideas. *J. Membr. Sci.* **2001**, *181*, 3–20. [CrossRef]
23. Xin, B.; Hao, J. Imidazolium-based ionic liquids grafted on solid surfaces. *Chem. Soc. Rev.* **2014**, *43*, 7171–7187. [CrossRef] [PubMed]

24. Alami-Younssi, S.; Kiefer, C.; Larbot, A.; Persin, M.; Sarrazin, J. Grafting γ-alumina microporous membranes by organosilanes: Characterisation by pervaporation. *J. Membr. Sci.* **1998**, *143*, 27–36. [CrossRef]
25. Leger, C.; De Lira, H.L.; Paterson, R. Preparation and properties of surface modified ceramic membranes. Part III. Gas permeation of 5 nm alumina membranes modified by trichloro-octadecylsilane. *J. Membr. Sci.* **1996**, *120*, 187–195. [CrossRef]
26. Randon, J.; Blanc, P.; Paterson, R. Modification of ceramic membrane surfaces using phosphoric acid and alkyl phosphonic acids and its effects on ultrafiltration of BSA protein. *J. Membr. Sci.* **1995**, *98*, 119–129. [CrossRef]
27. Caro, J.; Noack, M.; Kölsch, P. Chemically modified ceramic membranes. *Microporous Mesoporous Mater.* **1998**, *22*, 321–332. [CrossRef]
28. Guerrero, G.; Mutin, P.H.; Vioux, A. Organically modified aluminas by grafting and sol–gel processes involving phosphonate derivatives. *J. Mater. Chem.* **2001**, *11*, 3161–3165. [CrossRef]
29. Guerrero, G.; Mutin, P.H.; Vioux, A. Anchoring of Phosphonate and Phosphinate Coupling Molecules on Titania Particles. *Chem. Mater.* **2001**, *13*, 4367–4373. [CrossRef]
30. Mutin, P.H.; Guerrero, G.; Almaric, J. Preparation of An Inorganic Substrate Having Antimicrobial Properties. Patent No. US 8586758 B2, 19 November 2013. CNRS (FR); Université Montpellier II (FR).
31. Mu, Z.; Zhou, F.; Zhang, S.; Liang, Y.; Liu, W. Preparation and Characterization of New Phosphonyl-Substitued Imidazolium ionic Liquids. *Helv. Chim. Acta* **2004**, *87*, 2549–2555. [CrossRef]
32. McKenna, C.; Schmidhauser, J. Functional Selectivity in Phosphonate Ester Dealkylation with Bromotrimethylsilane. *J. Chem. Soc. Chem. Commun.* **1979**, *17*, 739. [CrossRef]
33. Leenaars, A.F.M.; Keizer, K.; Bruggraaf, A.J. The reparation and characterization of alumina membrane with ultra-fine pores. *J. Mater. Sci.* **1984**, *19*, 1077–1088. [CrossRef]
34. Guerrero, G.; Alauzun, J.G.; Granier, M.; Laurencin, D.; Mutin, P.H. Phosphonate coupling molecules for the control of surface/interface properties and the synthesis of nanomaterials. *Dalton Trans.* **2013**, *42*, 12569–12585. [CrossRef] [PubMed]
35. Mutin, P.H.; Guerrero, G.; Vioux, A. Hybrid material from organophosphorus Coupling Molecules. *J. Mater. Chem.* **2005**, *15*, 3761–3768. [CrossRef]
36. Galarneau, A.; Abid, Z.; Said, B.; Didi, Y.; Szymanska, K.; Jarzębski, A.; Tancret, F.; Hamaizi, H.; Bengueddach, A.; Di Renzo, F.; et al. Synthesis and Textural Characterization of Mesoporous and Meso-/Macroporous Silica Monoliths Obtained by Spinodal Decomposition. *Inorganics* **2016**, *4*, 9. [CrossRef]
37. Thissen, P.; Vega, A.; Peixoto, T.; Chabal, J.Y. Environment-Controlled Tethering by Aggregation and Growth of Phosphonic Acid Monolayers on Silicon Oxide. *Langmuir* **2012**, *28*, 8046–8051.
38. Quiñones, R.; mariea, S.; Gawalt, E. Study of the Formation of Self-Assembled Monolayers on Nitinol. *Langmuir* **2007**, *23*, 10123–10130. [CrossRef] [PubMed]
39. Brodard-Severac, F.; Guerrero, G.; Maquet, J.; Florian, P.; Gervais, C.; Mutin, P.H. High-Field ^{17}O MAS NMR Investigation of Phosphonic Acid Monolayers on Titania. *Chem. Mater.* **2008**, *20*, 5191–5196. [CrossRef]
40. Taoufik, M.; Szeto, K.C.; Merle, N.; Del Rosal, I.; Maron, L.; Trébosc, J.; Tricot, G.; Gauvin, R.M.; Delevoye, L. Heteronuclear NMR spectroscopy as a surface-selective technique: A unique look at the hydroxyl groups of γ-alumina. *Chem. Eur. J.* **2014**, *20*, 4038–4046. [CrossRef] [PubMed]
41. Hewitt, D.W.; Newland, G.L. Organophosphorus compounds. P-Arylated perhydro-1,2-azaphosphorines. *Aust. J. Chem.* **1977**, *30*, 579. [CrossRef]

Int. J. Mol. Sci. **2016**, *17*, 1212; doi 10.3390/ijms17081212

Supplementary Materials: Design of Phosphonated Imidazolium-Based Ionic Liquids Grafted on γ-Alumina: Potential Model for Hybrid Membranes

Marie-Alix Pizzoccaro, Martin Drobek, Eddy Petit, Gilles Guerrero, Peter Hesemann and Anne Julbe

Summary

Int. J. Mol. Sci. **2016**, *17*, 1212; doi:10.3390/ijms17081212

1. Characterizations

X-ray diffraction powder patterns were recorded using a PANanalytical X'Pert PRO diffractometer at the wavelength of Cu Kα (λ = 1.5405 Å) (X-ray power: 40 kV, 20 mA) in Bragg-Brentano scanning mode. The program scanned angles (2θ) from 4° to 50° with a 0.017° step, and a step time of 40 s.

Solution NMR experiments: ^{1}H, ^{13}C and ^{31}P nuclear magnetic resonance NMR spectra were recorded using a Bruker 300 MHz NMR spectrometer at frequencies of 300.13, 75.42 and 121.42 MHz, respectively. ^{29}Si NMR spectra was performed using a Bruker 400 MHz NMR spectrometer at frequencies of 79.46 MHz.

Solid state NMR experiments: Solid state NMR spectra were acquired on a Varian VNMRS 600 spectrometer (^{1}H: 599.95 MHz, ^{31}P: 242.86 MHz, ^{27}Al: 156.33 MHz). A 3.2 mm Varian T3 HXY magic angle spinning (MAS) probe was used for ^{1}H and ^{27}Al experiments, and a 3.2 mm Varian T3 HX magic angle spinning (MAS) probe was used for ^{1}H and ^{31}P experiments All NMR experiments were performed under temperature regulation in order to ensure that the temperature inside the rotor is 20 °C.

For ^{1}H experiments, the spinning frequency was 24 kHz, and the single pulse experiments were performed with a ~90° solid pulse of 2.5 μs. A recycle delay of 5 s was used (corresponding in both cases to full relaxation of ^{1}H). ^{1}H chemical shifts were referenced to external Adamantane at 1.80 ppm (used as a solid reference).

^{27}Al MAS NMR spectra at 14.1 T were acquired at a spinning frequency of 24 kHz. The single pulse experiments were performed with a ~15° solid pulse of 1 μs and ^{1}H decoupling during acquisition. A recycle delay of 5 s was used (corresponding in both cases to full relaxation of ^{27}Al). ^{27}Al chemical shifts were referenced to external $Al(NO_3)_3$ at 0 ppm.

^{31}P MAS solid state NMR spectra were recorded at spinning frequency of 20 kHz. The single pulse experiments were performed with a ~90° solid pulse of 3 μs and ^{1}H decoupling during acquisition. A recycle delay of 45 s was used (corresponding in both cases to full relaxation of ^{31}P) with a number of scan of 56 which permit to obtain a signal-to-noise ratio between 53 and 79. ^{31}P chemical shifts were referenced to external Hydroxyapatite at 2.80 ppm (used as a secondary reference).

2. Synthesis and Characterizations of the γ-Alumina Powder

The γ-alumina powder was prepared from the boehmite by a sol-gel process based on colloid chemistry in aqueous media according to the method reported elsewhere [33]. The boehmite (5 wt %) was placed in ultrapure water containing nitric acid (HNO_3/boehmite molar ratio ~0.042) as the peptizing agent. The suspension was sonicated during 15 min and then vigorously stirred for 2 days at room temperature. The resulting sol was centrifuged at 8500 rpm during 30 min in order to remove any unhydrolyzed particles. The as-obtained stable sol has been first concentrated by removing the water at temperatures under 150 °C, followed by thermal treatment at 600 °C/3 h in air, leading to the formation of γ-alumina powder (specific surface area of S_{BET} = 220 m^2/g).

^{1}H solid state NMR measurements (600 MHz, 24 kHz): δ (ppm) −0.2 (μ^1-Al_{IV}); 0.5–2.8 (μ^2-Al_{VI}); 2.5–4 (μ^2-Al_{IV}, μ^3-Al_n); ^{27}Al solid state NMR (600 MHz, 24 kHz): δ (ppm) 10.2 (Al_{VI}); 68.2 (Al_{IV}). Attributions were assigned from the work of Taoufik et al. [40].

It must be noted that before each NMR measurement the powder has been re-calcined at 450 °C/3 h under nitrogen for removing any adsorbed water on the powder surface. All manipulation with the as-treated powder has been conducted in glovebox under an argon atmosphere.

Int. J. Mol. Sci. **2016**, *17*, 1212; doi:10.3390/ijms17081212

3. Synthesis and Characterizations of Phosphonyl Imidazolium-Based Ionic Liquids

The diethyl(3-bromopropyl)phosphonate was synthesized via Arbuzov reaction from triethylphosphite and 1,3-dibromopropane, as described in [41]; its physicochemical constants coincided with the literature data. ^{1}H NMR (300 MHz, $CDCl_3$): δ (ppm) = 4.05 (m, 4H, –PO(CH_2CH_3)$_2$); 3.41 (t, 2H, Br–CH_2–CH_2); 2.07 (m, 2H, –CH_2–CH_2–P); 1.80 (m, 2H, –CH_2–CH_2–P); 1.27 (t, 6H, –PO(CH_2CH_3)$_2$). ^{31}P NMR (300 MHz, $CDCl_3$): δ (ppm) = 30.8.

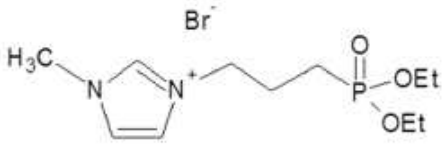

Figure S1. 1-methyl-3–(3–(diethylphosphinyl)propyl)-imidazolium bromide.

The 1-methyl-3–(3–(diethylphosphinyl)propyl)-imidazolium bromide (**ImPE**) was obtained as a yellow oil in high yield from the corresponding nucleophilic substitution of 1-methylimidazole with diethyl(3-bromopropyl)phosphonate adapted from the procedure published by Mu et al. [31]. The diethyl(3-bromopropyl)phosphonate precursor (27.00 g, 107 mmol) was dissolved in 50 mL of dry tetrahydrofuran (THF). Then, 1-methylimidazole (8.80 g, 107 mmol) was added dropwise and the mixture was heated to reflux at 70 °C during 3 days under argon. After cooling to room temperature and decanting, two phases could be distinguished as a yellow oil phase and a liquid phase. The two phases was separated and the yellow oil was washed twice with 50 mL of THF, then separated by liquid-liquid extraction with CH_2Cl_2 and H_2O. The combined organic fractions were solubilized in absolute ethanol, dried with anhydrous $MgSO_4$ and concentrated under vacuum to afford **ImPE** as a yellow oil with a 88% yield (32 g).

IR (ATR, cm^{-1}) ν: 3384, 3143, 3072, 2978, 1573, 1447, 1392, 1237, 1171, 1026, 965, 789, 475, 403.

^{1}H NMR (300 MHz, DMSO): δ (ppm) 10.53 (s, 1H, N–C*H*–N); 7.54 (s, 1H, N–C*H*); 7.36 (s, 1H, N–C*H*); 4.57 (t, 2H, CH_2–N); 4.06 (m, 4H, O–CH_2–CH_3); 4.06 (s, 3H,CH_3–N); 2.17-1.77 (m, 4H, CH_2–CH_2–P); 1.34 (t, 6H,O–CH_2–CH_3).

^{13}C NMR (300 MHz, $CDCl_3$): δ (ppm) 137.5; 123.7; 122.5; 62.0; 49.3; 36.7; 23.9; 22.8; 20.9; 16.5.

^{31}P NMR (300 MHz, $CDCl_3$): δ (ppm) 29.8.

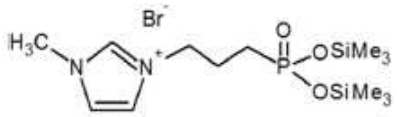

Figure S2. 1-methyl-3–(3–((trimethoxysilyl)phosphinyl)propyl)-imidazolium bromide.

The 1-methyl-3–(3–((trimethoxysilyl)phosphinyl)propyl)-imidazolium bromide (**ImTMSP**) was prepared in a round-bottomed flask by the reaction of the ionic liquid **ImPE** with $BrSiMe_3$ (3.5 equiv) in dry CH_2Cl_2. The following procedure is based on the procedure published by McKenna et al. [32]: 520 mg (1.52 mmol) of 1-methyl-3–(3–(diethylphosphinyl)propyl)-imidazolium bromide (**ImPE**) was dissolved in 10 mL of dry CH_2Cl_2. Then, $BrSiMe_3$ (0.82 g, 5.35 mmol) was added and the mixture was stirred at 25°C during 17 h under argon. At the end of the reaction time, the reaction mixture was concentrated under vacuum, leading to the expected IL as a one brown-orange paste in quasi quantitative yield. (98%, 633 mg).

Int. J. Mol. Sci. **2016**, *17*, 1212; doi:10.3390/ijms17081212

IR (ATR, cm^{-1}) ν: 3153, 3064, 2956, 2894, 1563, 1448, 1251, 1164, 1045, 998, 835, 754, 728, 694, 646, 619, 505, 428.

^{1}H NMR (300 MHz, DMSO): δ (ppm) 9.08 (s, 1H, N–C*H*–N); 7.73 (s, 1H, N–C*H*); 7.66 (s, 1H, N–C*H*); 4.13 (t, 2H, CH_2–N); 3.79 (s, 3H,CH_3–N); 1.94-1.41 (m, 4H, CH_2–CH_2–P); 0.00 (s, 6H,O–Si–CH_3).

^{13}C NMR (300 MHz, DMSO): δ (ppm) 137.2; 124.2; 122.7; 49.6; 36.2; 25.5; 24.4; 23.7; 2.4.

^{31}P NMR (300 MHz, DMSO): δ (ppm) 24.7.

^{29}Si NMR (400 MHz, DMSO): δ (ppm) 7.8.

4. ^{1}H, ^{13}C and ^{31}P NMR Spectra of the Ionic Liquids ImPE and ImTMSP

ImPE

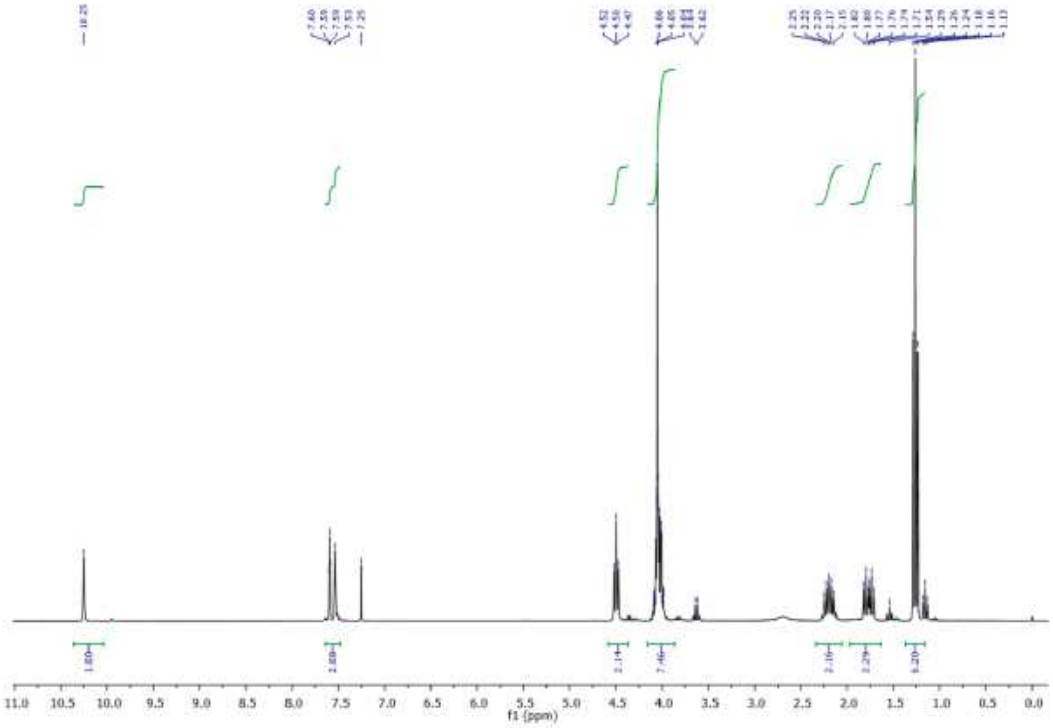

Figure S3. ^{1}H NMR spectra of ImPE.

Int. J. Mol. Sci. **2016**, *17*, 1212; doi:10.3390/ijms17081212

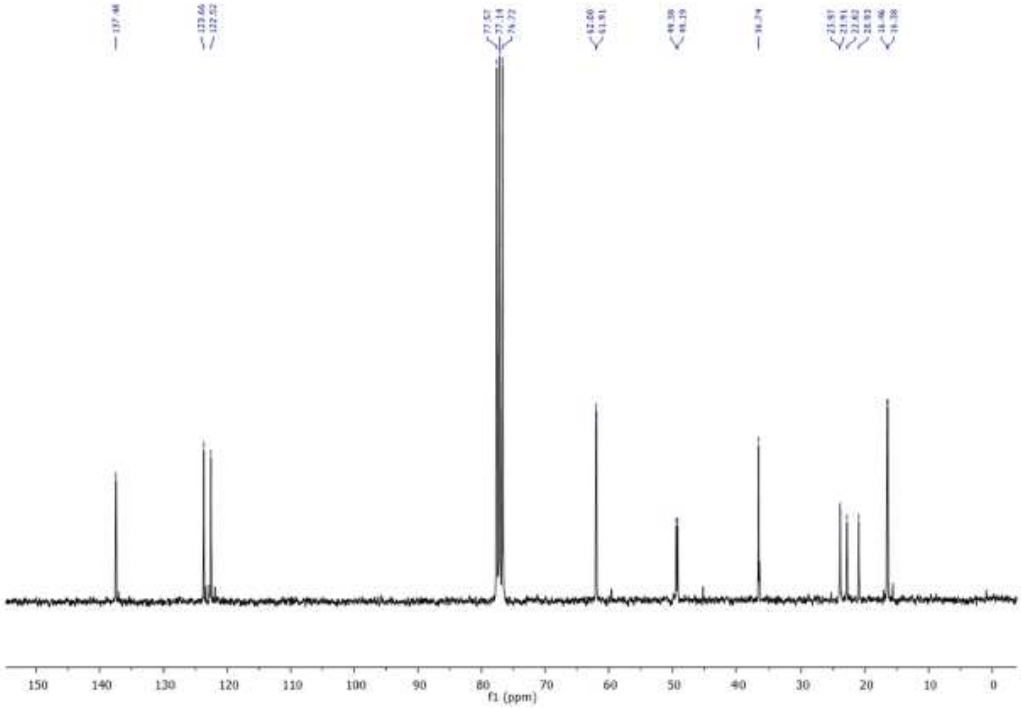

Figure S4. ^{13}C NMR spectra of ImPE.

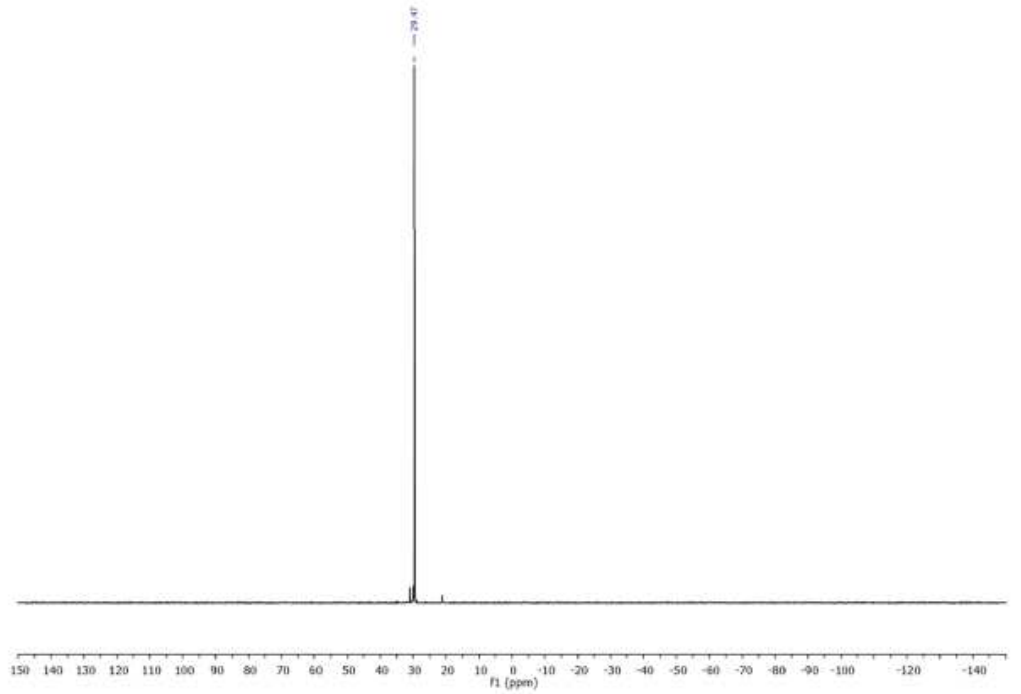

Figure S5. ^{31}P NMR spectra of ImPE.

Int. J. Mol. Sci. **2016**, *17*, 1212; doi:10.3390/ijms17081212

ImTMSP

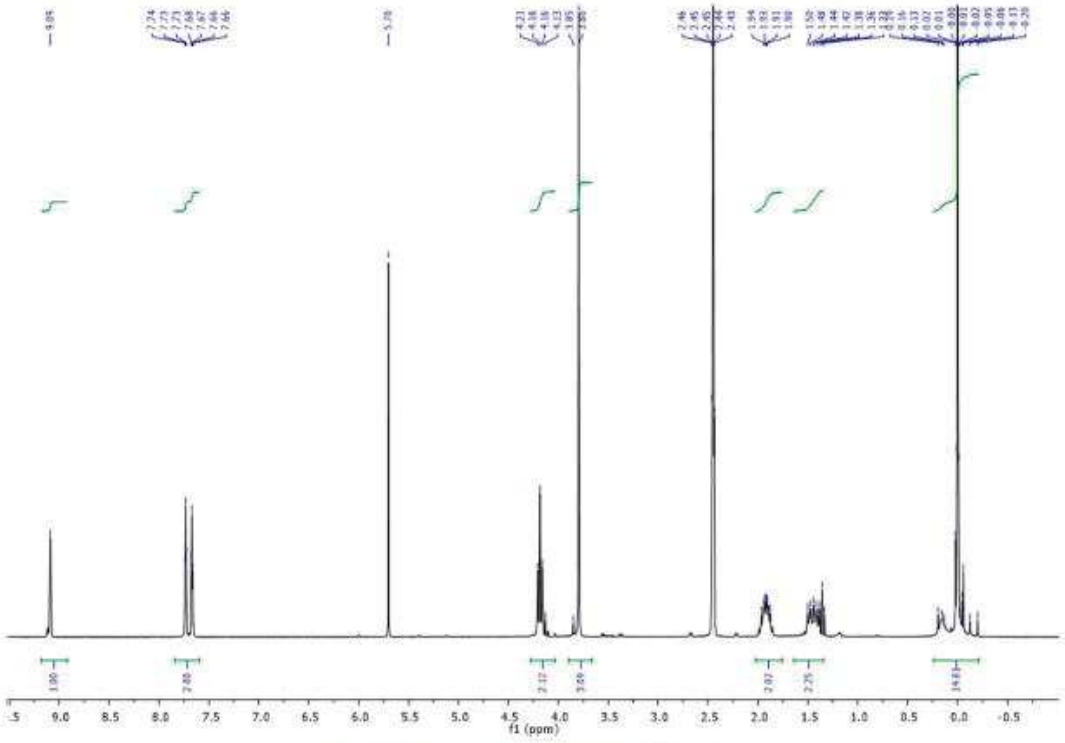

Figure S6. ^{1}H NMR spectra of ImTMSP.

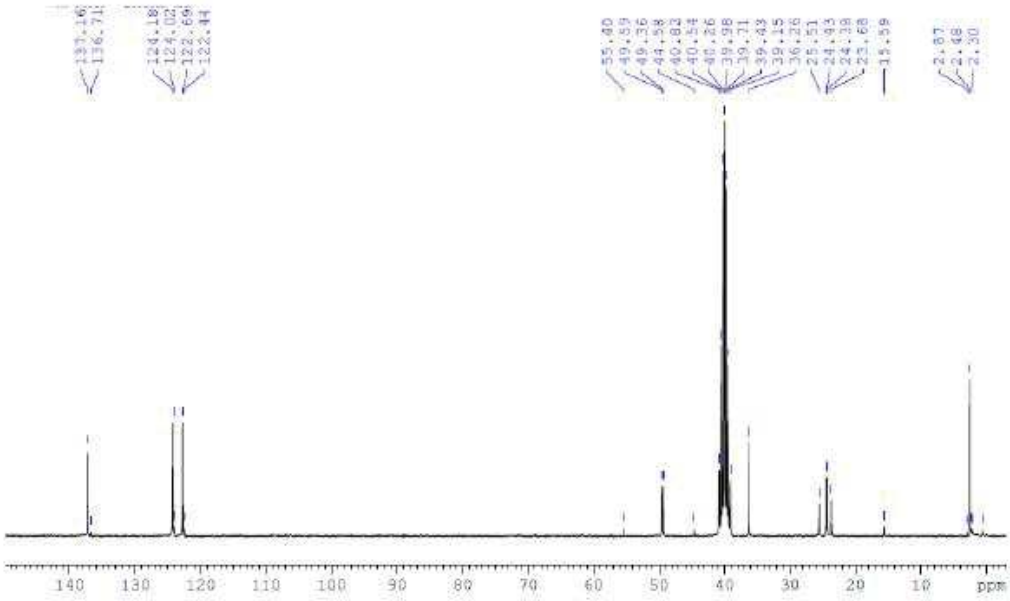

Figure S7. ^{13}C NMR spectra of ImTMSP.

Int. J. Mol. Sci. **2016**, *17*, 1212; doi:10.3390/ijms17081212

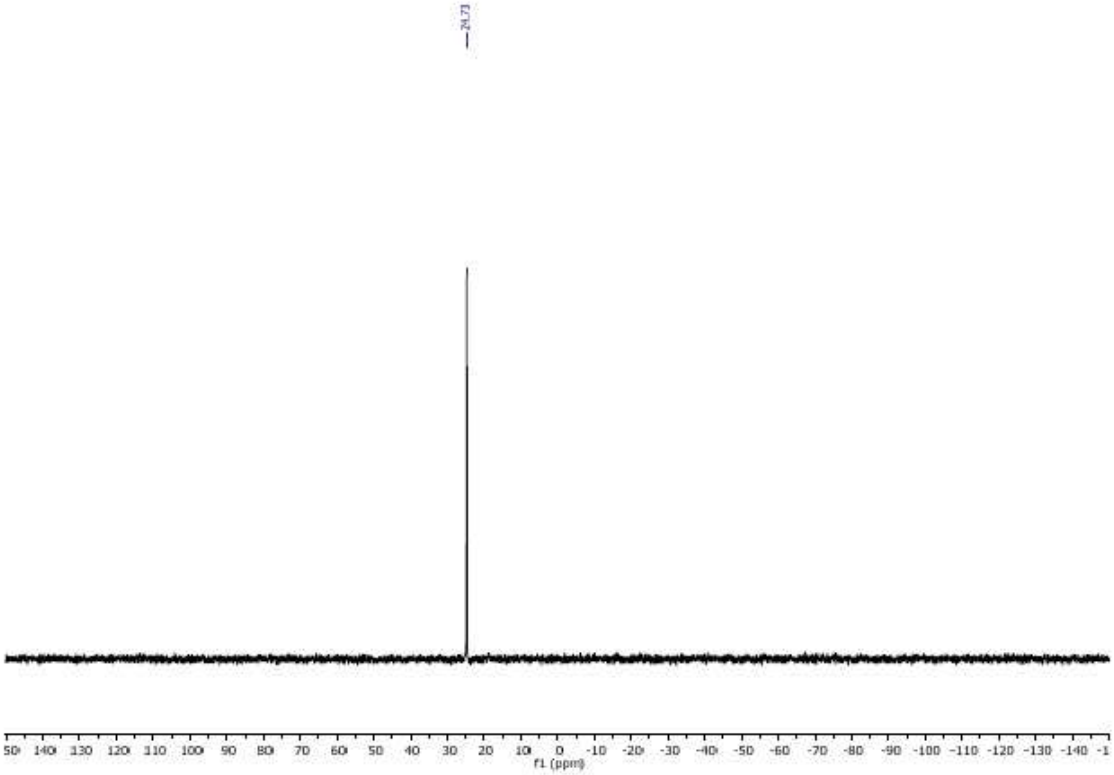

Figure S8. ^{31}P NMR spectra of ImTMSP.

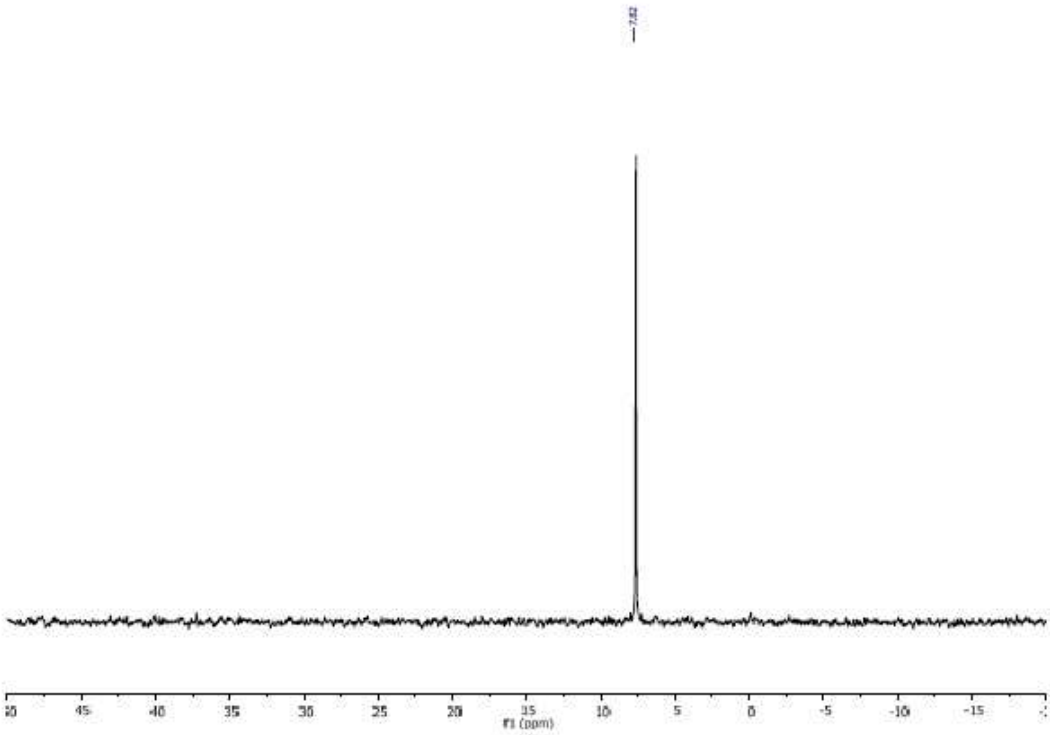

Figure S9. ^{29}Si NMR spectra of ImTMSP.

Int. J. Mol. Sci. **2016**, *17*, 1212; doi:10.3390/ijms17081212

5. FTIR Spectra of the Ionic Liquids in ATR Mode and DFT Calculated Spectra

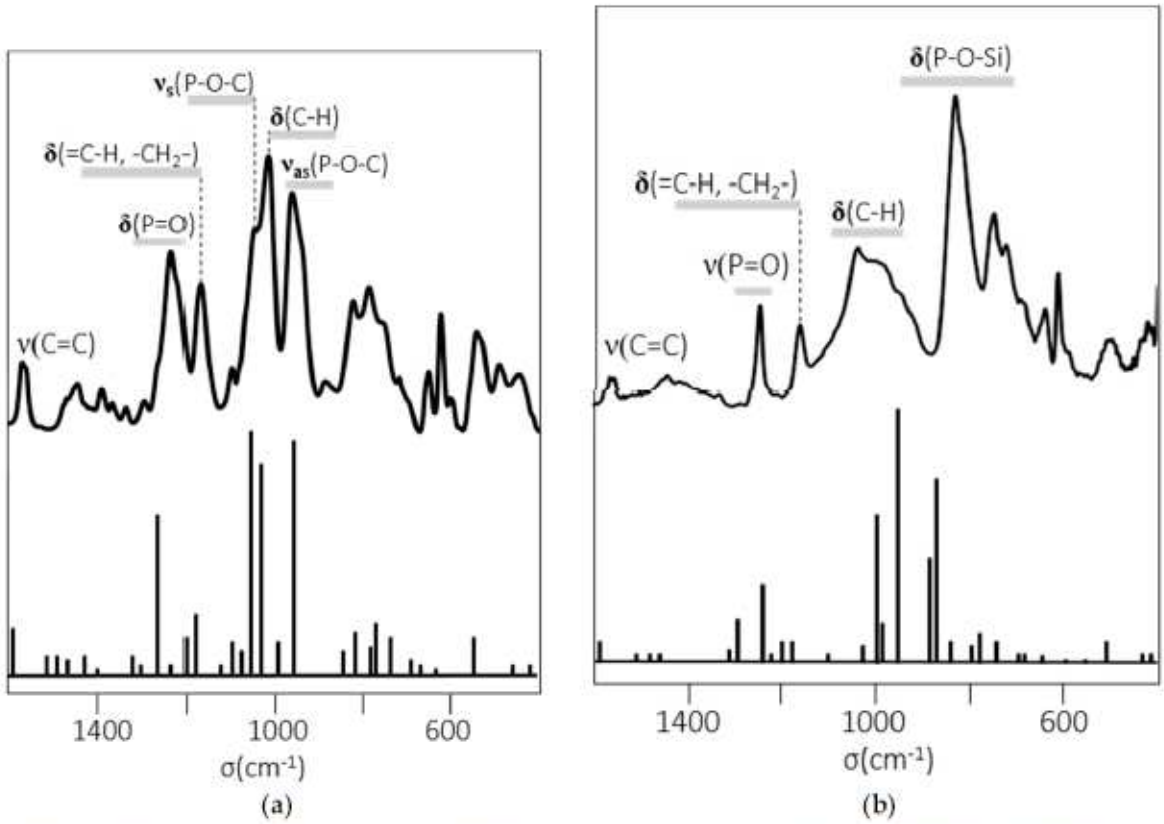

Figure S10. Portion of the experimental IR spectra of the ionic liquid (IL): (**a**) ImPE; (**b**) ImTMSP and representation of the DFT-calculated frequencies for these ILs.

Computational Method:

The calculations were performed with the help of Density Functional Theory (DFT) with B3LYP levels, using 6-311G(2d,p) as basis set on Gaussian 09 program package.Geometry optimization and harmonic vibrational frequencies were calculated at the same level DFT. The predicted wavenumbers correspond to the isolated molecular state (the experimental wavenumbers correspond to a liquid state spectrum). No scaling factors were applied. A detailed interpretation of the vibrational spectra of these compounds have been made.

6. Physisorbed Sample

Physisorption Conditions. The "physisorption" conditions of modification is summarized in Table 1. Grafting solutions of ImPE was prepared in CH_2Cl_2 by dissolving 0.6 mmol of the phosphorus ionic liquid, which corresponds to a 1-fold excess. 5 mL of the grafting solution was placed in a glass bottle. 400 mg of γ-alumina powder stored under argon was added and the bottle was closed with a Teflon caps. The suspension was maintained at 30 °C during 1h30. Then, the supernatant was removed and the resulting powder was dried under vacuum (5–10 mbar) at 70°C for ~16 h. The sample was called **ImPE-Ph** (wt % P: 1.6 ± 0.04)

Int. J. Mol. Sci. **2016**, *17*, 1212; doi:10.3390/ijms17081212

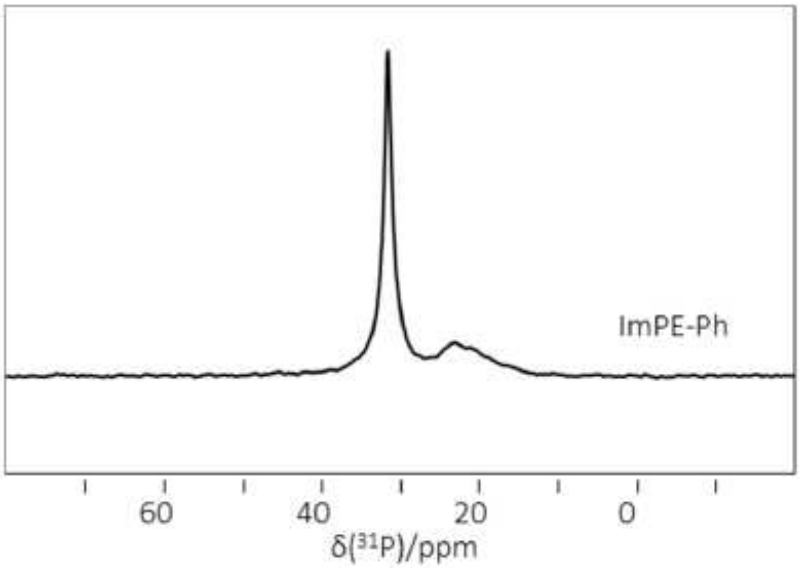

Figure S11. ^{31}P solid-state NMR spectra of ImPE-Ph.

7. XRD of γ-Alumina and Grafted Powders

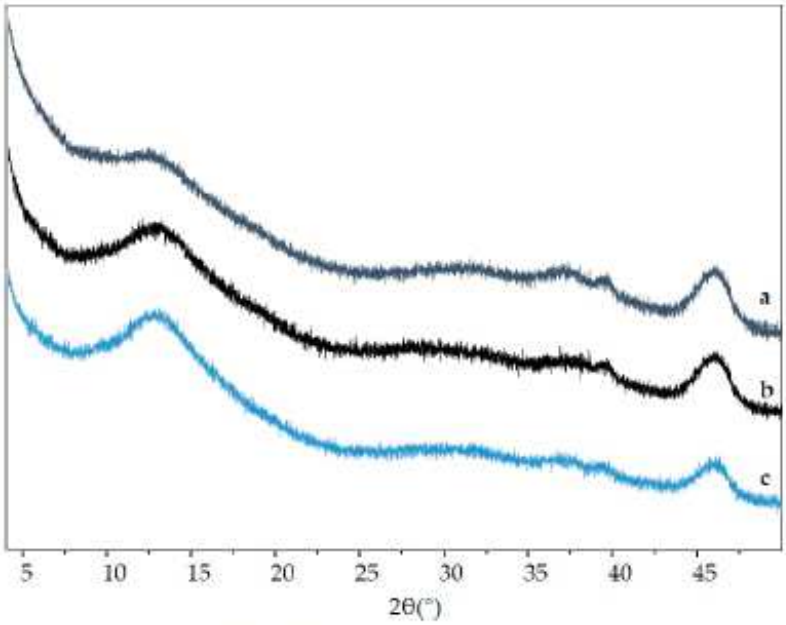

Figure S12. Examples of powder XRD diffractograms: (a) starting γ-alumina powder; and grafted sample realized in: (b) forced condition (ImPE4); (c) standard condition (ImTMSP4).

ANNEX 2

Contains information related to Chapter III.

^{27}Al NMR spectra of different pristine γ-Al_2O_3

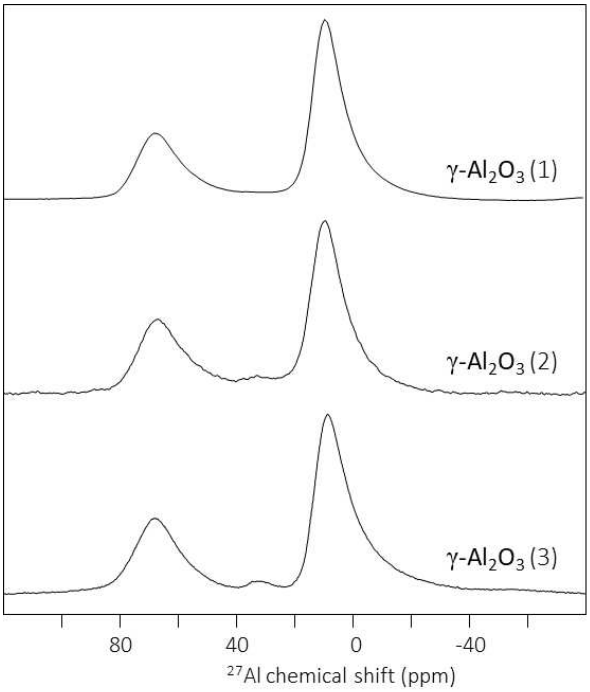

Figure A2. 1. Comparison of the ^{27}Al NMR spectra for the different pristine γ-alumina batches used.

FTIR spectra of the ILs in ATR mode and DFT calculated spectra

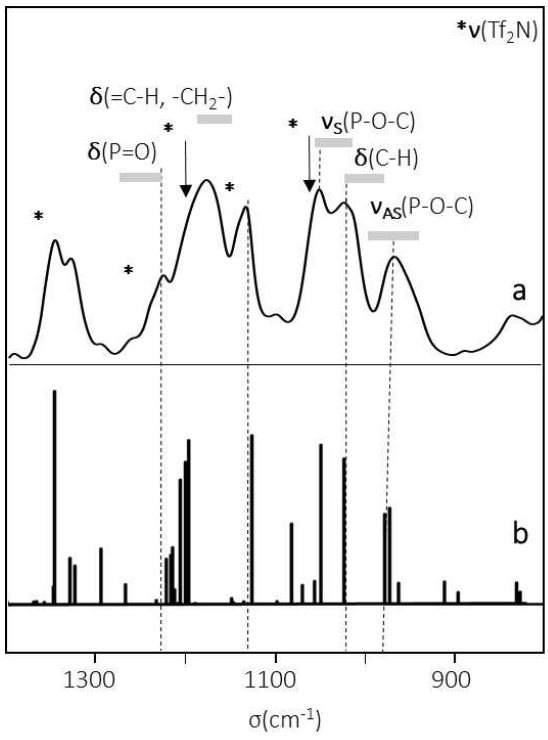

Figure A2. 2. Portion of the FTIR spectra of [ImPE][Tf_2N]: a) experimental, b) model.

Physisorbed sample

Physisorption Conditions

A grafting solution of [ImPE][Tf_2N] was prepared in EtOH:H_2O by dissolving 7.2 mmol of the phosphonate-based ionic liquid, which corresponds to a 12-fold excess. 10 mL of the grafting solution were placed in a glass bottle. 400 mg of γ-alumina powder stored under argon were added in the bottle which was closed with a Teflon cap. The suspension was maintained at 130°C during 1h. Then, the supernatant was removed and the resulting powder was dried under vacuum at 70°C for ~16 h. The sample was called ImPE-Tf_2N (Ph) (wt % P: 1.8 ± 0.18).

Samples analysis

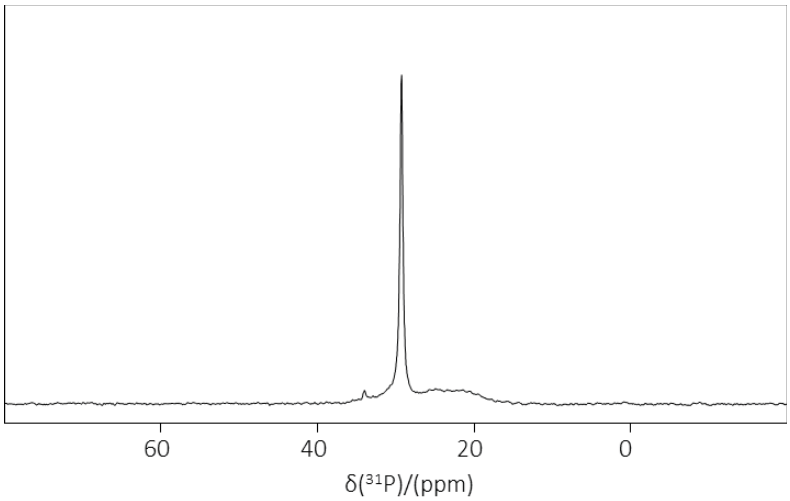

Figure A2. 3. ^{31}P ssNMR spectrum of ImPE-Tf_2N (Phy).

TEM analysis of the pristine γ-Al_2O_3

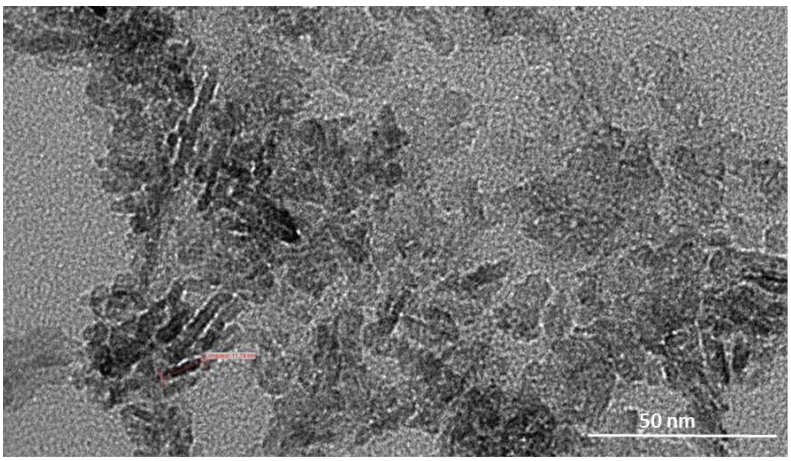

Figure A2. 4. TEM picture of the *pristine γ-Al_2O_3 material.*

N_2 adsorption-desorption isotherms

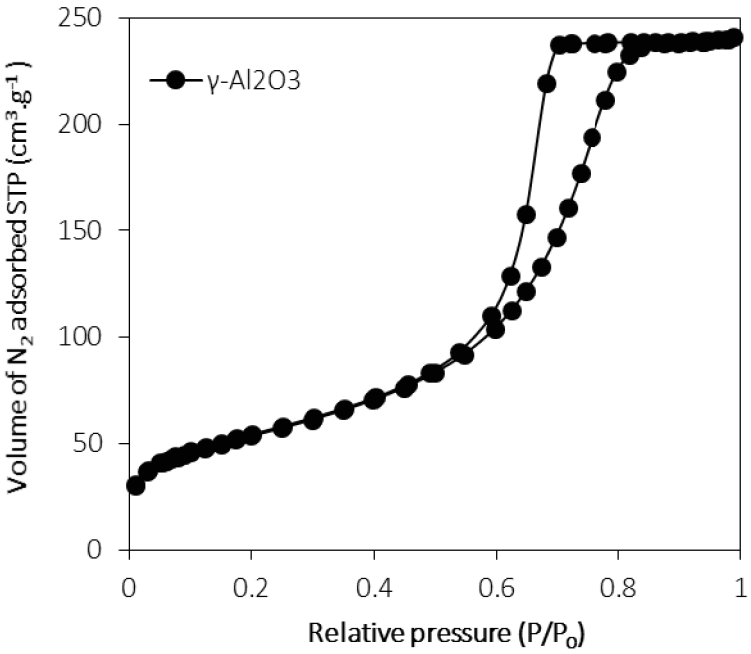

Figure A2. 5. N_2 adsorption-desorption isotherm of γ-Al_2O_3 at 77K.

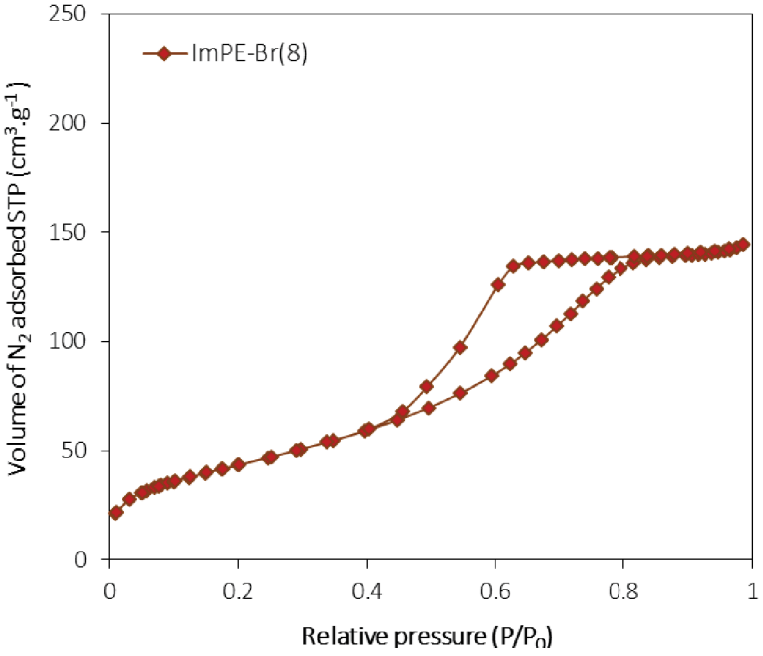

Figure A2. 6. N_2 adsorption-desorption isotherm of ImPE-Br (8) at 77K.

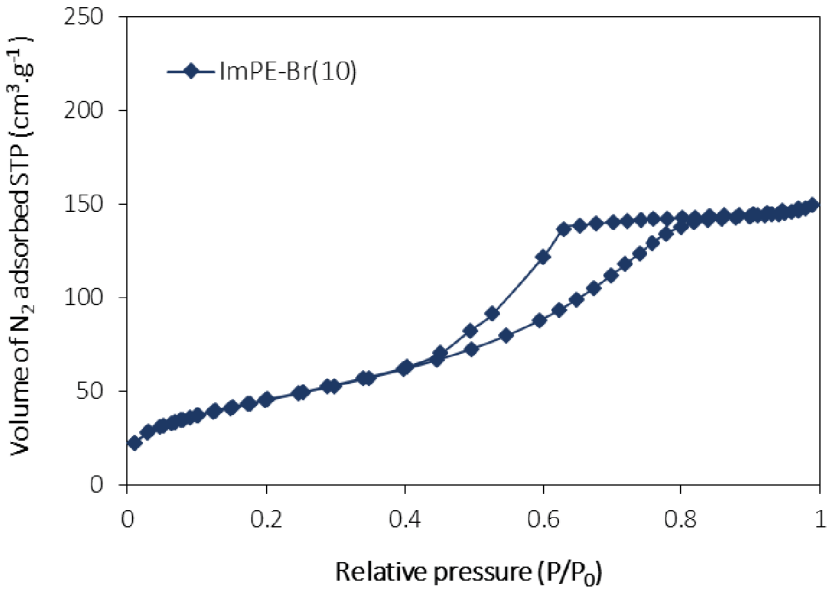

Figure A2. 7. N_2 adsorption-desorption isotherm of ImPE-Br (10) at 77K.

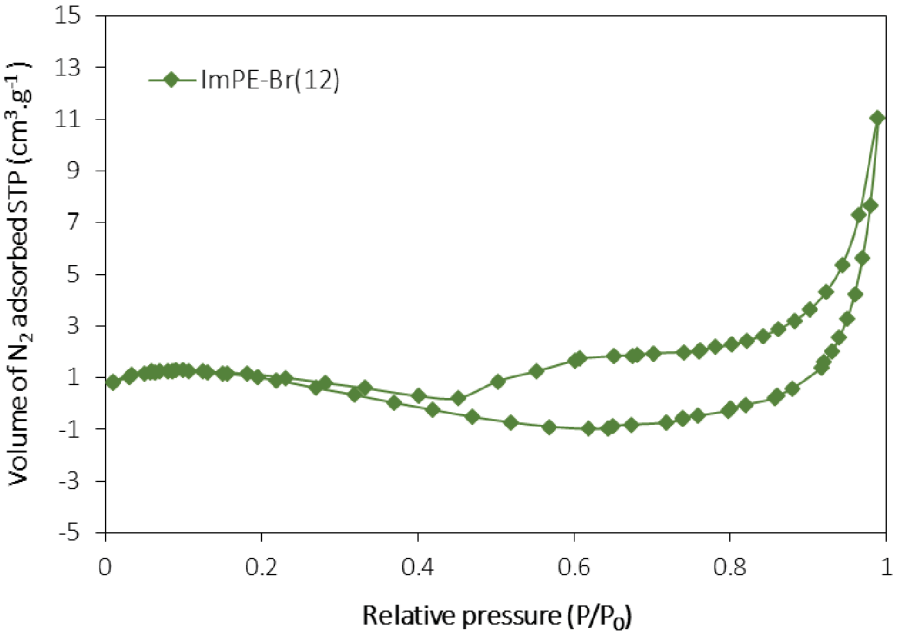

Figure A2. 8. N_2 adsorption-desorption isotherm of ImPE-Br (12) at 77K.

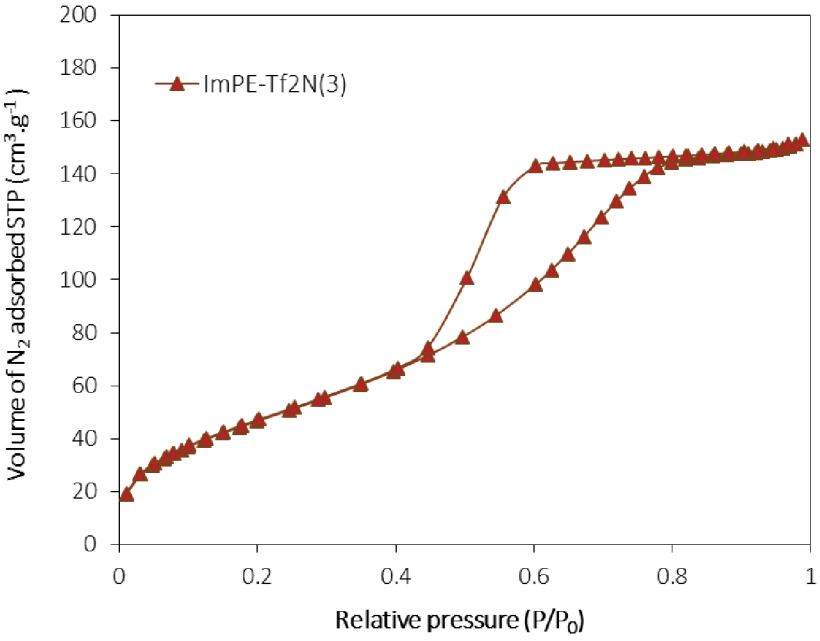

Figure A2. 9. N_2 adsorption-desorption isotherm of ImPE-Tf_2N (3) at 77K.

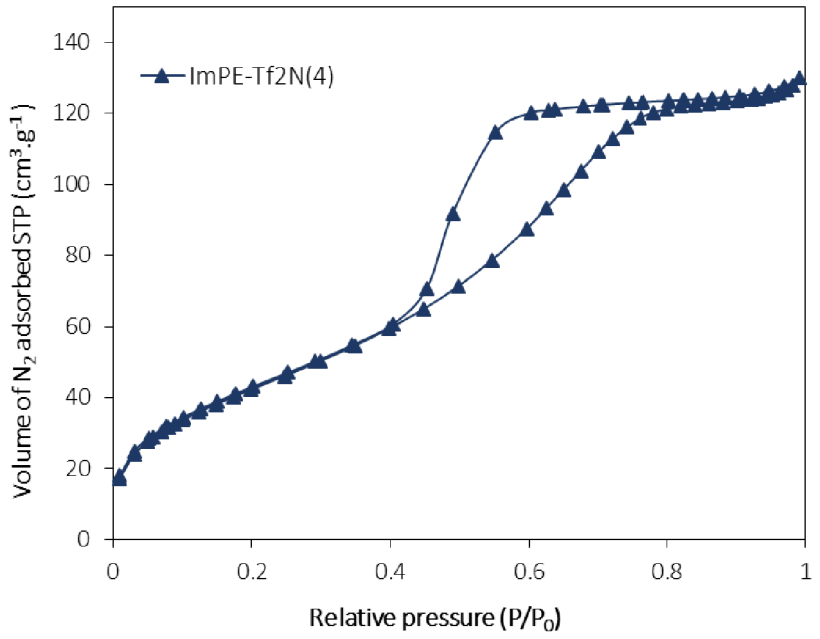

Figure A2. 10. N_2 adsorption-desorption isotherm of ImPE-Tf_2N (4) at 77K.

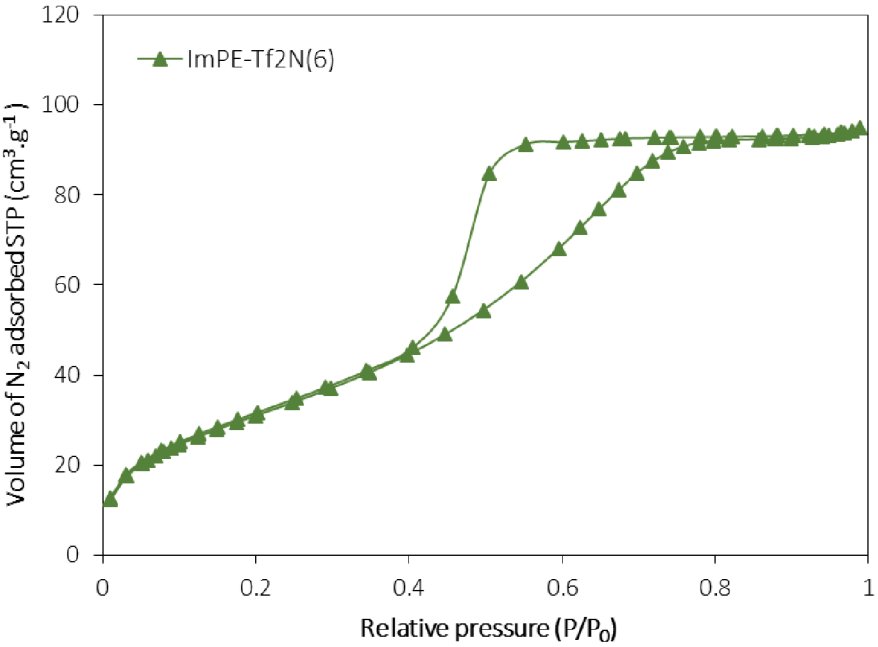

Figure A2. 11. N_2 adsorption-desorption isotherm of ImPE-Tf_2N (6) at 77K.

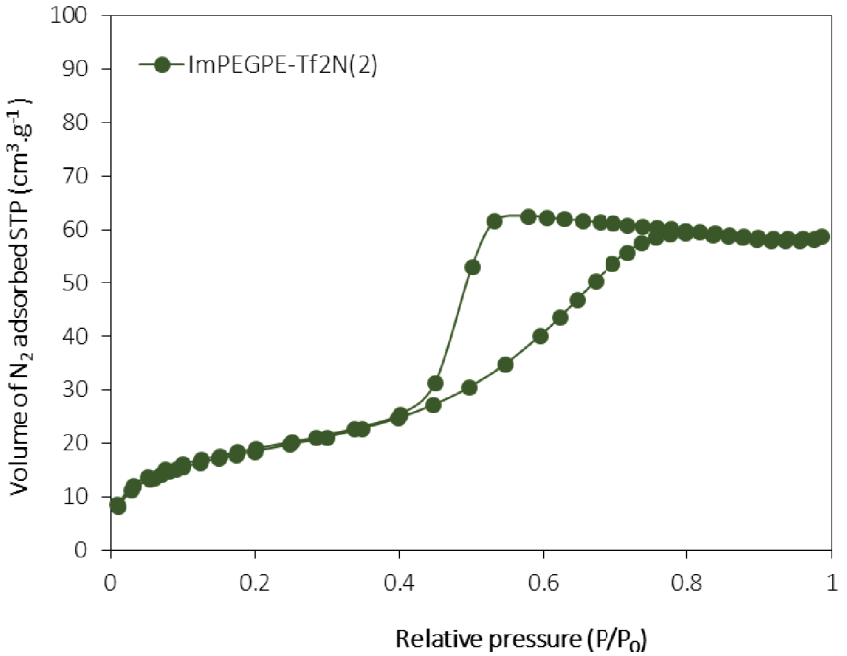

Figure A2. 12. N_2 adsorption-desorption isotherm of ImPEGPE-Tf_2N (2) at 77K.

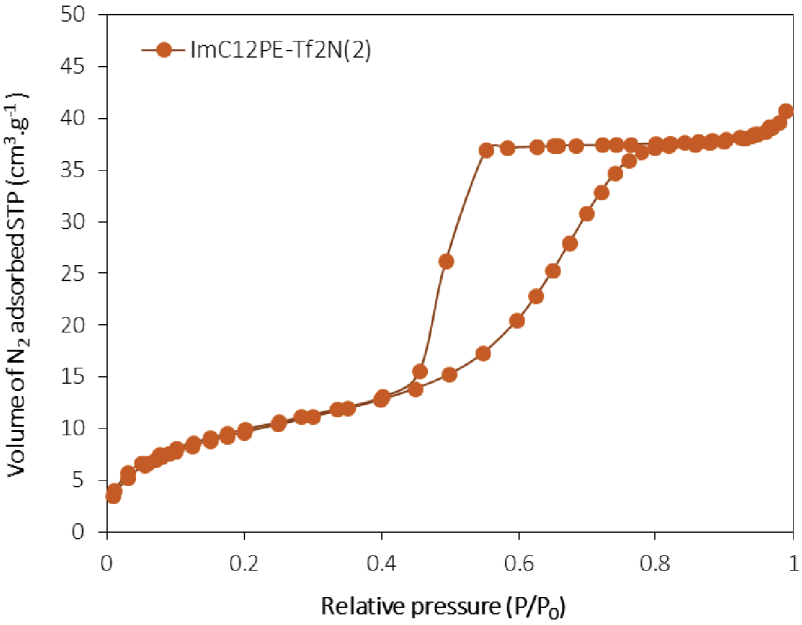

Figure A2. 13. N_2 adsorption-desorption isotherm of $ImC_{12}PE\text{-}Tf_2N$ (2) at 77K.

ANNEX 3

Information on the data points used for the Robeson plot.

Ceramic-based SILMs

ILs	Type of support	Measurement conditions	CO_2 Permeability (Barrer)	CO_2/N_2 Selectivity	Ref.
[emim][Ac]	ZrO_2/SiO_2 tubular ($Ø_{pore}$ = 1 nm)	25°C, 2 bar*, single gas	83	34	a.
[emim][Ac]	TiO_2 tubular ($Ø_{pore}$ = 2.5 nm)		103	34	
[emim][Ac]	TiO_2 tubular ($Ø_{pore}$ = 20 nm)		107	33	
[bmim][BF_4]	TiO_2 tubular ($Ø_{pore}$ = 20 nm)	25°C, 2 bar, single gas	8	35	b.
[decmim][BF_4]			2807	31	
[emim][Tf_2N]	Al_2O_3 Anodisc ($Ø_{pore}$ = 20 nm)	23°C, 1.15 bar, single gas	2642	20	c.
[bmim][[Tf_2N]			2582	16	
[pmmim][Tf_2N]			2642	21	
[hmim][Tf_2N]			1802	12	
[bbim][Tf_2N]			3243	15	
[bmim][Ac]			1321	19	
[emim][TFA]			1982	18	
[emim][Tf_2N]			5405	21	
[glymIm][TsO]	γ-Al2O3 disc (Øpore = 5 nm)	25°C, single gas	6466	16	d.

Table A3. 1. CO_2 permeability, CO_2/N_2 selectivity and measurement conditions for selected polymeric-based SILMs reported in the literature (* feed pressure).

Reference

a. J. Albo, T. Tsuru, Thin ionic liquid membranes based on inorganic supports with different pore sizes, *Ind. Eng. Chem. Res*., 2014, *53*, 8045–8056.

b. J. Albo, T. Yoshioka, T. Tsuru, Porous Al_2O_3/TiO_2 tubes in combination with 1-ethyl-3-methylimidazolium acetate ionic liquid for CO_2/N_2 separation, *Sep. Purif. Technol,* 2014, *122*, 440-448.

c. J.J. Close, K. Farmer, S.S. Moganty, R.E. Baltus, CO_2/N_2 separations using nanoporous alumina-supported ionic liquid membranes: Effect of the support on separation performance, *J. Membrane. Sci.,* 2012, *390-391*, 201–210.

d. S.D. Hojniak, A.L. Khan, O. Hollo, B. Kirchner, I.F.J. Vankelecom, W. Dehaen, K. Binnemans, Separation of Carbon Dioxide from Nitrogen or Methane by Supported Ionic Liquid Membranes (SILMs): Influence of the Cation Charge of the Ionic Liquid, *J. Phys. Chem. B.,* 2013, *117(14),* 15131–15140.

Polymeric-based SILMs

ILs	Type of support	Measurement conditions	CO_2 Permeability (Barrer)	CO_2/N_2 Selectivity	References
[bmim][PF_6]	Hydrophobic PVDF	30°C, 0.5 bar*, single gas	171	23	a.
[hmim][PF_6]			281	28	
[omim][PF_6]			370	22	
[bmim][BF_4]	Hydrophobic PVDF	30°C, 0.7 bar*, single gas	390	35	b.
[decmim][BF_4]			506	22	
[emim][BF_4]	PES	30°C, 2 bar*, single gas	968	44	c.
[emim][CF_3SO_3]			1171	40.5	
[emim][Tf_2N]			1702	23	
[hmim][Tf_2N]			1136	15	
[bmim][beti]			991	16.7	
[emim][CF_3SO_3]	Hydrophobic PVDF	30°C, 2 bar*, single gas	486	34	d.

Table A3. 2. CO_2 permeability, CO_2/N_2 selectivity and measurement conditions for selected polymeric-based SILMs reported in the literature (* feed pressure).

Reference

a. L.A. Neves, N. Nemestóthy, V.D. Alves, P. Cserjési, K. Bélafi-Bakó, I.M. Coelhoso, Separation of biohydrogen by supported ionic liquid membranes, *Desalination*, 2009, *240(1-3)*, 311-315.

b. L.A. Neves, J.G. Crespo, I.M. Coelhoso, Gas permeation studies in supported ionic liquid membranes, *J. Membrane. Sci.,* 2010, 357, 160-170.

c. P. Scovazzo, D. Havard, M. McShea, S. Mixon, D. Morgan, Long-term, continuous mixed-gas dry fed CO_2/CH_4 and CO_2/N_2 separation performance and selectivities for room temperature ionic liquid membranes, *J. Membrane. Sci.,* 2009, *327(1-2),* 41-48.

d. P. Cserjési, N. Nemestóthy, K. Bélafi-Bakó, Gas separation properties of supported liquid membranes prepared with unconventional ionic liquids, *J. Membrane. Sci.,* 2010, *349(1-3)*, 6-11.

Gelled-IL membranes

ILs	Type of gelator/support	Measurement conditions	CO_2 Permeability (Barrer)	CO_2/N_2 Selectivity	Ref.
[hmim][Tf_2N]	LMOG/PTFE	22°C, 1.5 bar*, single gas	650	22	a.
[hmim][Tf_2N]	LMOG/PTFE	22°C, 1 bar*, single gas	450	22	b.
[hmim][Tf_2N]			580	18	
[hmim][Tf_2N]			650	21	
[emim][Tf_2N]			850	20	
[emim][Tf_2N]			900	27	
[emim][Tf_2N]			920	25	

Table A3.3. CO_2 permeability, CO_2/N_2 selectivity and measurement conditions for selected gelled-IL membranes reported in the literature (* feed pressure).

Reference

a. B.A. Voss, J.E. Bara, D.L. Gin, R.D. Noble, Physically gelled ionic liquids: solid membrane materials with liquid like CO_2 gas transport, *Chem. Mater.,* 2009, *21*, 3027–3029.

b. P.T. Nguyen, B.A. Voss, E.F. Wiesenauer, D.L. Gin, R.D. Noble, Physically Gelled RTIL-based Thin-film Composite Membranes for CO_2/N_2 Separation: Effect of Composition and Thickness on Membrane Properties and Performance, *Ind. Eng. Chem. Res.,* 2013, *52(26)*, 8812–8821.

Ion gel membranes

ILs	% of free IL	bis(epoxide) imidazolium IL monomer/TAEA#	Measurement conditions	CO_2 Permeability (Barrer)	CO_2/N_2 Selectivity	Ref.
[emim][Tf_2N]	50	3:1	22°C, 2 bar*, single gas	125	28	a.
[emim][Tf_2N]	50	3:2		100	28	
[emim][Tf_2N]	50	3:2		130	28	
[emim][Tf_2N]	60	3:1		230	36	
[emim][Tf_2N]	60	3:2		210	31	
[emim][Tf_2N]	60	3:2		240	33	

Table A3.4. CO_2 permeability, CO_2/N_2 selectivity and measurement conditions for selected ion gel membranes reported in the literature (#tris(2-aminoethyl)amine) (* feed pressure).

Reference

a. W.M. McDanel, M.G. Cowan,J.A. Barton,D.L. Gin, R.D. Noble, Effect of Monomer Structure on Curing Behavior, CO_2 Solubility, and Gas Permeability of Ionic Liquid-Based Epoxy–Amine Resins and Ion-Gels, *Ind. Eng. Chem. Res.,* 2015, 54, 4396−4406.

PIL membranes

ILs	monomer/support	Measurement conditions	CO_2 Permeability (Barrer)	CO_2/N_2 Selectivity	Ref.
$[Im_{1VB}][Tf_2N]$	Styrene/PES (Øpore = 200 nm)	22°C, ~2 bar*, single gas	9.2	32	a.
$[Im_{4VB}][Tf_2N]$			20	30	
$[Im_{6VB}][Tf_2N]$			32	28	
$[Im_{1VA}][Tf_2N]$	Acrylate/PES (Øpore = 200 nm)		7	31	
$[Im_{4VA}][Tf_2N]$			22	30	
$[Im_{P1VB}][Tf_2N]$	Styrene/PES (Øpore = 200 nm)	20°C, ~2 bar*, single gas	16	41	b.
$[Im_{P2VB}][Tf_2N]$			22	44	
$[Im_{C4NVB}][Tf_2N]$			4	37	
$[Im_{C6NVB}][Tf_2N]$			8	40	
$[Im_{isopropylVB}][Tf_2N]$	Styrene/Nylon (Øpore = 200 nm)	20°C, 3 bar*, single gas	10.4	31	c.
$[Im_{secbutylVB}][Tf_2N]$			13.6	35	
$[Im_{methylcyclopropylIVB}][Tf_2N]$			7.94	33	
$[Im_{cyclopentylVB}][Tf_2N]$			6.65	34	

Table A3.5. CO_2 permeability, CO_2/N_2 selectivity and measurement conditions for selected PIL membranes reported in the literature (* feed pressure).

References

a. J.E. Bara, S. Lessmann, C.J. Gabriel, E.S. Hatakeyama, R.D. Noble, D.L. Gin, Synthesis and Performance of Polymerizable Room-Temperature Ionic Liquids as Gas Separation Membranes, *Ind. Eng. Chem. Res.,* 2007, *46*, 5397–5404.

b. J.E. Bara, C.J. Gabriel, E.S. Hatakeyama, T.K. Carlisle, S. Lessmann, R.D. Noble, D.L. Gin, D. L. Improving CO_2 selectivity in polymerized room-temperature ionic liquid gas separation membranes through incorporation of polar substituents, *J. Membrane. Sci.,* 2008, *321*, 3–7.

c. W.J. Horne, M.A. Andrews, M.S. Shannon, K.L. Terrill, J.D. Moon, S.S. Hayward, J.E. Bara, Effect of branched and cycloalkyl functionalities on CO_2 separation performance of poly(IL) membranes, *Sep. Purif. Technol.,* 2015, *155*, 89–95.

ANNEX 4

Hydrothermal-assisted hydrolysis of dialkylphosphonate ester ILs.

Hydrothermal-assisted hydrolysis of dialkylphosphonate ester ILs

The chemical nature of the coupling agent is important to avoid the dissolution-precipitation process. The grafting of alumina with phosphonic acids and their parent trimethylsilyl esters has already been described in the literature[a,b] and led to bulk phosphonate aluminum phases even if soft conditions. The use of the diethylester phosphonate coupling function in organic medium only led to surface modified alumina, the diethylester phosphonate coupling function being known to be stable. Thus, in order to evaluate the stability of the diethyl ester phosphonate function in aqueous medium, we studied the influence of the forcing reaction conditions on the both pure ILs *[ImPE][Tf_2N] and [ImPE][Br]*.at different duration times (*i.e. 20, 48 and 92h*). ^{1}H and ^{31}P liquid NMR were used to conclude on the phosphonate function nature for both ILs during the grafting treatment.

On the basis of the chemical shifts in ^{31}P liquid NMR related to the ester or acid form of the coupling functions, we were able to quantify the proportion of diethylester after the different treatment in forcing conditions. As presented in Figure A4.1, and 2, after 20h of treatment, only 1% of [ImPE][Br] is still present. The major part of the IL has been transformed into his phosphonic acid form (82%) or into its monoester. Concerning the [ImPE][Tf_2N] coupling agent, after a 20h treatment, 85% of the diethyl ester phosphonate IL is still present and a 15% proportion has been converted to the monoester form (Figure A4.3). After a 48h treatment, the conversion proportion increases with only 48% of the initial ester present and only 15% for the monoester. Thus, the [ImPE][Tf_2N] IL is much more stable than [ImPE][Br] toward hydrolysis in aqueous medium confirming that the formation of bulk aluminium phosphonate phases is strongly related to the chemical nature of the coupling agent.

To conclude, the hydrolysis of the ILs in aqueous medium has not been precluded and is surprising, the classical way to form phosphonic acids in aqueous medium being a strong acidic treatment (HCl 6M) under reflux.

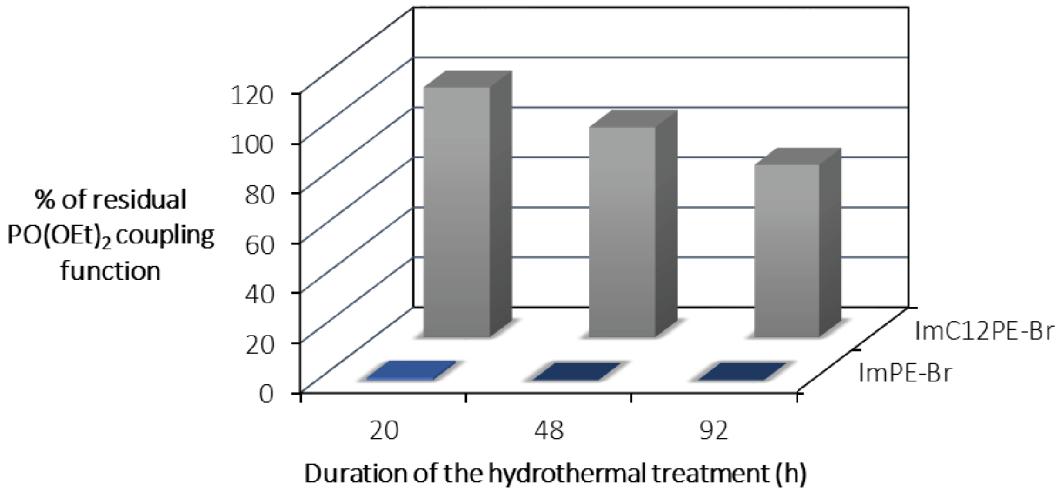

Figure A4. 1. Evolution of the -P(O)(OEt)$_2$ coupling function vs. hydrothermal treatment duration (h) in H_2O.

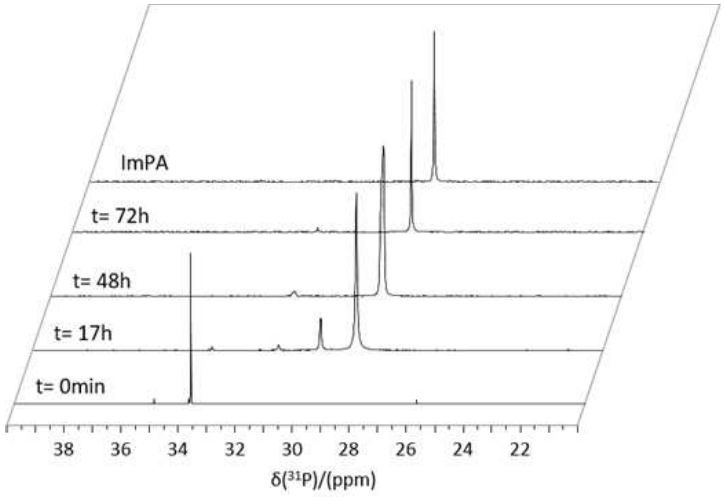

Figure A4. 2. ^{31}P-NMR spectra at different times of the ionic liquids ImPE-Br in hydrothermal conditions.

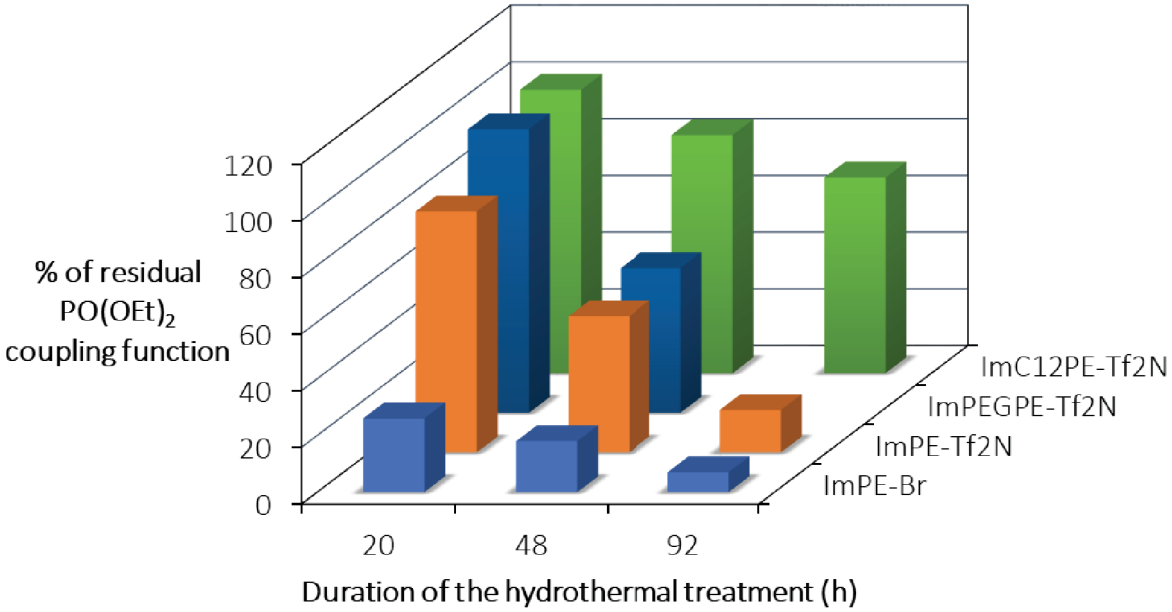

Figure A4. 3. Evolution of the -P(O)(OEt)$_2$ coupling function vs. hydrothermal treatment duration (h) in H_2O:EtOH.

Experimental section

Protocol

All the hydrothermal-assisted hydrolysis of dialkylphosphonate ester ILs were carried out by following the same experimental protocol. 100 mg of the IL were dissolved in 20 mL of the selected solvent (either H_2O or H_2O:EtOH mixture). Then, the solution was placed in a 90 mL autoclave, which was closed with a Teflon® cap. The autoclave was sealed and heated at 130°C for a reaction time of 20h, 48h or 92h. At the end, the solvent was removed under reduced pressure (0.1 bar) at 80°C for 2h and a viscous liquid vas recovered.

Table A4. 1. Details of the reaction tests carried out (*not soluble in water)

Cation	Anion	Abbreviation	Solvent	Temperature (°C)	δ (*-P(O)(OEt)₂*) / ppm	Deuterium solvent
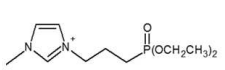	Br^-	ImPE-Br	H_2O H_2O:EtOH	130	33.83	D_2O
	Tf_2N^-	ImPE-Tf_2N*	H_2O:EtOH	130	30.41	DMSO
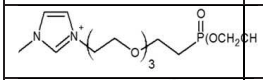	Tf_2N^-	ImPEGPE-Tf_2N*	H_2O:EtOH	130	28.68	DMSO
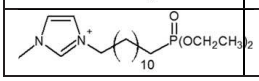	Tf_2N^-	ImC_{12}PE-Tf_2N*	H_2O:EtOH	130	32.08	DMSO

Characterization

Liquid NMR experiments: ^1H, ^{13}C, ^{31}P, and ^{19}F NMR spectra were recorded using a Bruker 300 MHz NMR spectrometer at frequencies of 300.13, 75.42, 121.49 and 282.4 MHz, equipped with a 5 mm QNP probe. Chemical shift data, given in δ ppm, were calibrated to TMS on the basis of the relative chemical shift of the solvent as an internal standard.

References

a. G. Guerrero, P.H. Mutin, A. Vioux, Organically modified alumina by grafting and sol–gel processes involving phosphonate derivatives, *J.Mater.Chem.,* **2001**, 11(12), 3161–3165.

b. G. Guerrero, P.H. Mutin, A. Vioux, Anchoring of Phosphonate and Phosphinate Coupling Molecules on Titania Particles. *Chem. Mater.,* **2001**, 13(11), 4367-4373.

ANNEX 5

Contains information related to Chapter IV.

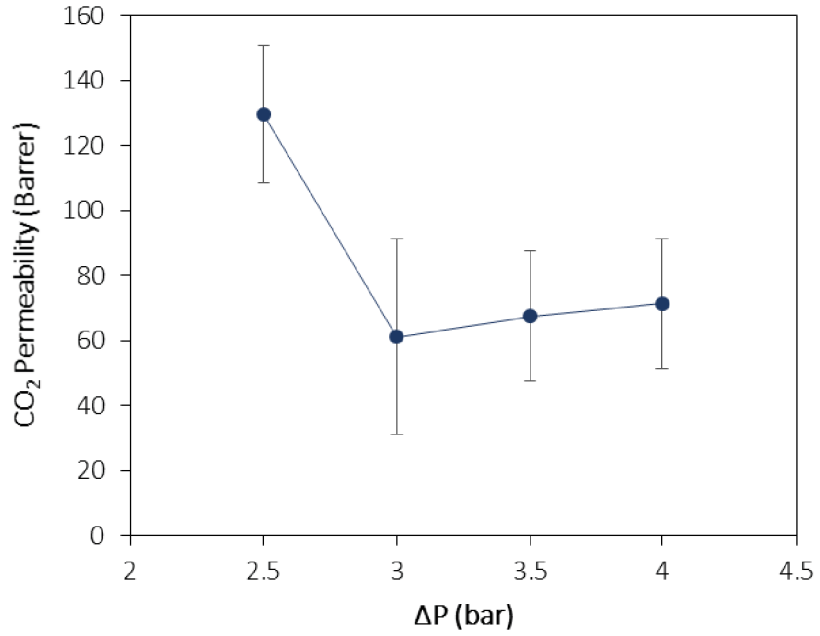

Figure A5. 1. Evolution of CO_2 permeability vs. transmembrane pressure for GILM(2) at 20°C.

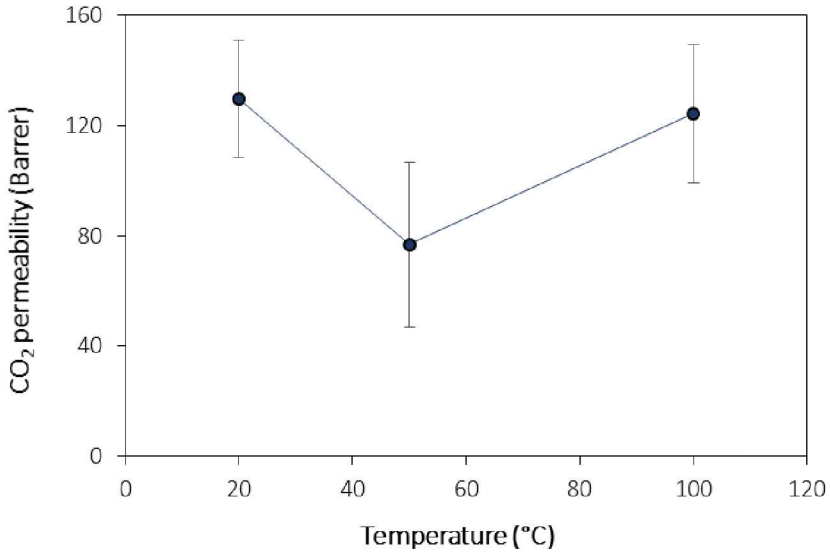

Figure A5. 2. Evolution of CO_2 permeability vs. temperature for GILM(2).